Armin Traußnig, DI(FH)

A framework for model based development and assessment of vehicle thermal control

DOCTORAL THESIS

to achieve the university degree of

Doktor der technischen Wissenschaften

submitted to

Graz University of Technology

Supervisor

Univ.-Prof. Dipl.-Ing. Dr.techn. Martin Horn

Institute of Automation and Control

Univ.-Doz. Dipl.-Ing. Dr.techn. Theodor Sams

Graz, October 2016

AFFIDAVIT

I declare that I have authored this thesis independently, that I have not used other than the declared sources/resources, and that I have explicitly indicated all material which has been quoted either literally or by content from the sources used. The text document uploaded to TUGRAZonline is identical to the present doctoral thesis.

_____

Date   Signature

```
+---------------------------------------+
|                                       |
|     _____ _         _      _ _        |
|    |_   _| |_  ___ | |  ( ) |__       |
|      | | | ' \/ -_) |__| | '_ \       |
|      |_| |_||_\___|___|_|_|.__/       |
|                                       |
|    Thermo-Fluid  Library  v2016.2     |
+---------------------------------------+
```

Vorwort

Der größte Dank gilt meiner Familie die in den letzten Jahren und Monaten eine Vielzahl an Entbehrungen auf sich nehmen musste. Ohne den Beistand, die Geduld und die Rücksichtnahme meiner Frau Kathrin wäre es wohl nicht möglich gewesen.

Graz im Oktober 2016,

Armin Traußnig

In Zusammenarbeit mit

Unterstützt von

Zusammenfassung

Aufgrund bevorstehender Änderungen im Bereich der Fahrzeug Typenzulassung hinsichtlich Erfassung der Emissionen und Verbrauch im praktischen Fahrbetrieb (engl. RDE - real driving emissions) liegt der Fokus dieser Arbeit auf der Entwicklung einer Methodik zur modellbasierten Entwicklung und Bewertung von Steuer- und Regelungsstrategien für thermische Fahrzeugsysteme im Kontext realitätsnaher Fahrzeugnutzung. Der Schwerpunkt der Tätigkeiten liegt dabei auf der Schließung methodischer Lücken in den Bereichen Thermo-Fluid Simulation, Steuergeräte Softwarearchitektur und der Auswahl geeigneter Fahrzyklen zur Bewertung von Energieeffizienz und Lebensdauer.

Eine Gesamtfahrzeugsimulation wird verwendet, um die komplexen thermischen, mechanischen und elektrischen Wechselwirkungen zwischen den einzelnen Fahrzeugteilsystemen zu berücksichtigen. Dazu wird für ein Plug-in-Hybrid-Elektrofahrzeug das Fahrzeuglängsdynamikmodell inklusive Hybrid Steuergerät mithilfe der Software AVL CRUISE abgebildet und mit einem Thermo Management Controller (TMC) sowie einem thermischen Fahrzeugmodell (beides abgebildet in MATLAB/Simulink), co-simuliert.

Im Zuge dieser Arbeit wird eine MATLAB/Simulink Library - genannt Thermo-Fluid Library (TheLib) - zur Simulation komplexer Fluidkreisläufe (thermisch und hydraulisch) sowie thermischer Punktmassen Netzwerke entwickelt. Dabei liegt der Schwerpunkt der Arbeit auf der Entwicklung eines benutzerfreundlichen Werkzeugs, welches:

- die Simulation von Wärmeübergängen in stehenden Fluidkreisläufen ermöglicht;
- eine hohe Rechengeschwindigkeit aufweist;
- gut für die Entwicklung vom Steuergerätefunktionen und Reglern geeignet ist und
- die Möglichkeit der Codegenerierung für Zielhardware (z.B. HiL Prüfstand) bietet.

Des Weiteren wird eine Steuergeräte-Architektur entwickelt und zwar mit dem Ziel, ein möglichst einfaches und universell einsetzbares Grundgerüst für die Regelung und Steuerung der Aktuatoren im Kühl- und Schmiersystem des Fahrzeugs zu schaffen.

Die Methode der Nutzungsraumanalyse wird verwendet, um aus einer Vielzahl an Fahrzeugmessdaten kundenspezifische Fahrzyklen abzuleiten, die sowohl das durchschnittliche als auch das extreme Konsumentenverhalten berücksichtigen. Zudem werden statistisch aussagekräftige Temperaturprofile ermittelt, um die unterschiedlichen klimatischen Bedingungen während eines Jahres in den relevanten Nutzungsorten zu berücksichtigen.

Zusammenfassend kann gesagt werden, dass durch die Verwendung von TheLib ein Gesamtfahrzeugsimulationsmodell erstellt wird, welches das thermische Verhalten des Fahrzeugs detailliert und korrekt wiedergibt und eine beachtlichen Rechengeschwindigkeit aufweist. Die generische Struktur des TMC wird genutzt, um eine Auswahl unterschiedlicher

Regelstrategien zu entwickeln und im Gesamtfahrzeugmodell zu integrieren. Schließlich wird die erarbeitet Methodik zur Bewertung des thermischen Fahrzeugverhaltens angewandt, um für unterschiedliche Hardware- und Regler-Konfigurationen Aussagen bezüglich Jahresenergieverbrauch und Batteriealterung zu treffen.

Schlagwörter: Fahrzeug Thermo Management, Regelung und Steuerung, Jahresenergiebedarf, thermische Simulation, Hybridfahrzeug

Abstract

Based on the background of upcoming changes in the vehicle type approval regarding real world driving emissions (RDE), this doctoral thesis is dedicated to the development of a framework for model based development and assessment of vehicle thermal control in the context of realistic vehicle usage. The emphasis of the work lies on closing methodological gaps in the areas of thermo-fluid simulation, control unit software architecture and the selection of suitable drive cycles for the assessment of energy efficiency and lifetime.

The methodology of global vehicle simulation is used to consider the complex thermal, electrical and mechanical interactions among the individual vehicle subsystems. For this purpose the longitudinal dynamics and hybrid control unit of a plug-in hybrid vehicle are modeled in the software AVL CRUISE and co-simulated with a Thermal Management Controller (TMC) and a plant model of the thermal vehicle system (both created in MATLAB/Simulink).

In course of this work a MATLAB/Simulink Library - called Thermo-Fluid Library (TheLib) - which is developed for the simulation of complex fluid circuits (thermal and hydraulical) as well as for analysis of lumped mass thermal networks. The work mainly focuses on the development of a user-friendly tool, which:

- allows the simulation of heat transfer in stagnant fluid circuits;
- features a high computing speed;
- supports the development of control system software functions and controllers and
- enables the possibility of code generation for hardware targets (e.g. HiL testbed).

Furthermore a control system architecture is developed, with the aim of providing a simple and generic framework for the control of vehicle cooling and lubrication system actuators.

A methodology called usage space analysis is used to extract custom drive cycles from real world driving measurements. Resulting reference drive cycles consider not only the average customer but also the extreme customer vehicle usage behavior. In addition, statistically representative temperature profiles are derived to consider the annual climatic conditions at selected vehicle usage locations.

In summary, it can be stated that by using TheLib for the build up of the global vehicle simulation model a detailed and accurate representation of the thermal vehicle behavior is achieved with considerably high computing speeds. The generic structure of the TMC is used for testing and development of a number of control strategies and for integration into the global vehicle simulation model. Finally, the developed methodology is used for the assessment of the vehicle thermal performance in order to evaluate important vehicle attributes like energy consumption and battery aging.

Contents

Introduction

This chapter introduces the background and the field of application of the present work. The basic physical principles of Vehicle Thermal Management Systems (VTMS) analysis are explained as well as the high level objectives. Since the emission legislation is an important driver for the introduction of new technologies and improvements within the development process, the relevant upcoming changes in the vehicle certification test are discussed. Based on the state of research for thermal control and thermo-fluid simulation future needs and challenges are identified which form the basis for the objectives and contributions of this thesis.

1.1. Vehicle thermal management

In average people in Europe are using their car twice a day for a total driving range of around 30 kilometers. The trip length has a large impact on Carbon Dioxide (CO_2) and pollutant emissions because a vehicle has it's maximum efficiency at an ambient temperature of around 20 °C with all powertrain components at their optimal operating temperature. Comparison of fuel consumption results for the same ambient temperature but with the powertrain in cold start condition shows a CO_2 consumption increase of around 15-20% for a conventional car [1]. This means that the vehicle is in the less efficient warm-up operation mode twice a day. The assessment of possible improvements regarding the vehicle warm-up is one of the core elements in VTMS simulation.

For a hybrid vehicle it is slightly different because the cold start behavior is depending on the hybrid powertrain configuration, battery size, cell type and initial State of Charge (SoC). Nevertheless components like a multi mode hybrid vehicle gearbox also have a strong temperature dependent efficiency curve. Therefore the gearbox warm-up is also influencing the vehicle efficiency. Depending on the drive cycle, approximately 6% to 10% of the overall power consumption in an EV is used for thermal conditioning (cooling) of power electronics, battery and motor [2]. Based on that, the second objective of VTMS is the efficient control of all thermal system actuators.

In order to meet current and future pollutant and greenhouse gas emission targets, an efficient vehicle thermal management system is one of the key factors in conventional as well as in electrified powertrains. The steadily growing number of vehicle variants with increasing modularity and variability in its systems and functions are representing a large

challenge to the vehicle development process. Global vehicle simulation is already a well-established tool to support the vehicle development process [3, 4, 5, 6]. This particularly holds for the vehicle thermal management: The required needs in development strongly exceed the definition of the cooling system alone. Actually all energy fluxes have to be distributed among the subsystems of the vehicle as efficiently as possible, in order to provide a minimized consumption of primary energy. Exemplary the energy flows within a hybrid vehicle in blended hybrid operation mode are shown in Fig. 1.1. By means of VTMS simulation the wall heat losses (28.5% of combustion gas enthalpy), friction losses (11.3% of indicated power) and the mechanical as well as electrical auxiliary energy consumption are targeted. With the introduction of certain VTMS measures (split cooling, smart valves, active grill shutter,...) a shifting of energy flows towards a reduction of friction losses and energy consumption can be performed.
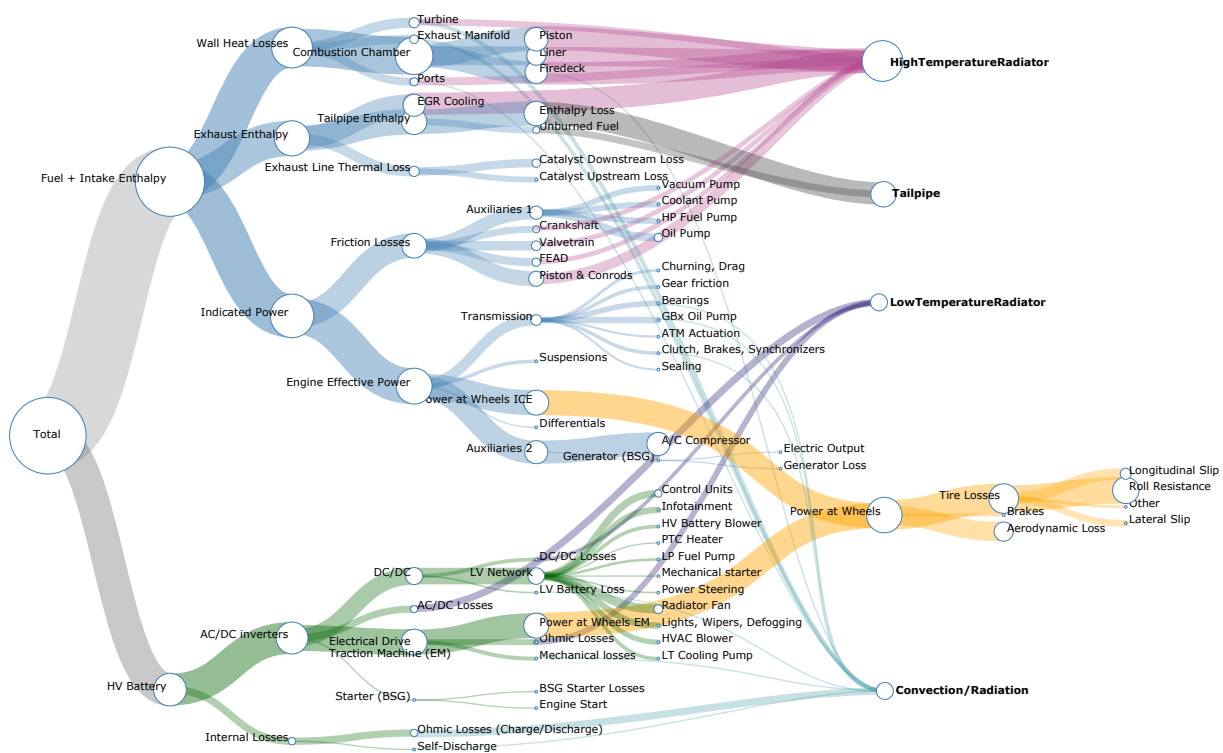
Figure 1.1.: Energy flow chart for a hybrid vehicle in blended operation mode [7].

Apart from the main aspect of fuel consumption, also the reduction of vehicle emissions is deeply connected to the optimization of the thermal management. In order to meet the demands of the restrictive emission legislation in the future, the introduction of new thermal management features is required. As depicted in Fig. 1.2 the levers and physical effects used to reach the objectives are either aiming faster warm-up and therefore decreased friction or the reduction of actuator power consumption by deployment of a situation- and needs-based control. For an increase in durability a balance between energy consumption for cooling and aging effects e.g. for the battery has to be found. The impact of the features on fuel consumption and durability is largely depending on the applied thermal control strategy.

A major development target is the global optimization of vehicle efficiency with respect to the overall vehicle performance. Decoupled optimization of single components or subsystems (e.g.: engine cooling or lubrication system) is no longer sufficient to meet these objectives. This is due to the strong and complex interactions among these functions, which very often lead to non-predictable overcompensations of individual improvements on system level.
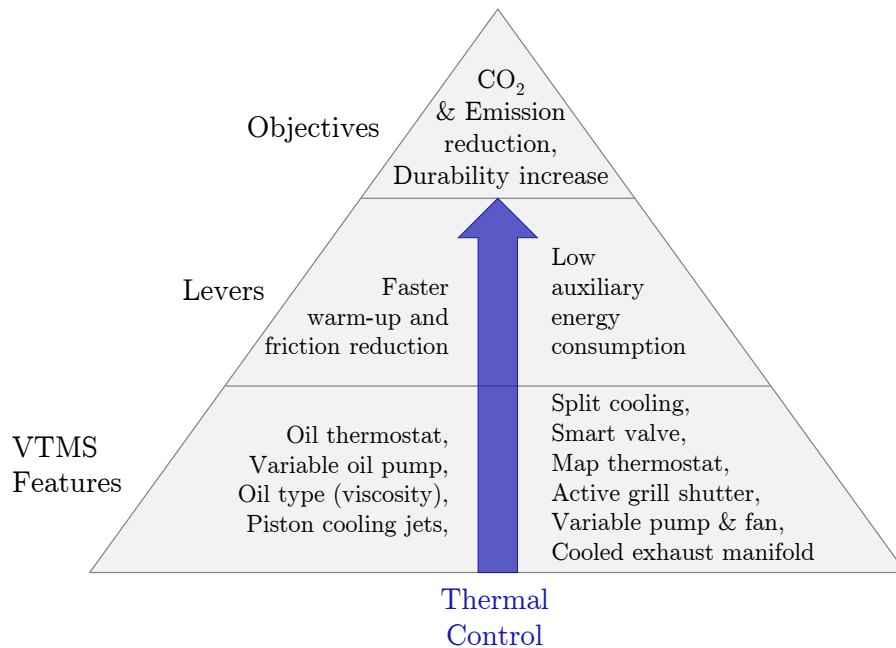
Figure 1.2.: Overview on VTMS measures, levers and objectives.

For a combination of different features into vehicle variants, as depicted in Fig. 1.3, the selection of the control concept hast a significant influence on the outcome. Due to the strong mutual influenc of certain VTMS measures the fuel saving potential for a combination of features cannot be calculated as the sum of individual CO_2 reduction potentials.

Many of the current emission reduction concepts (e.g. exhaust gas recirculation at high engine load, two-stage turbo charging, etc.) imply an increase of the overall heat rejection. For the minimization of the fuel consumption and for the reduction of the vehicle emissions, which are the major development targets, two opposite effects become evident: on the one hand all efforts have to be taken to keep the parasitic energy losses as small as possible by economic engine concepts and on the other hand a steadily increasing amount of rejected heat is required, in order to assure the light-off and the operation of exhaust-aftertreatment. The solution of this conflict can only be found in an active design of a sophisticated thermal management concept, which takes all subsystems and components within the vehicle into account.

This especially applies for the development of control strategies, which definitely require a holistic and vehicle related approach [8].

Variant 3

[Heat pump]

[Waste heat recovery]

[Phase change material]

[Split cooling]

[Smart water valve]

[Latent heat storage]

[Active grill shutters]

Variant 2

Variant 1

{Smart valve control}

{WHR control}
{Predictive heat pump control}
{Pre conditioning control}
{Model based fan and grill shutter control}
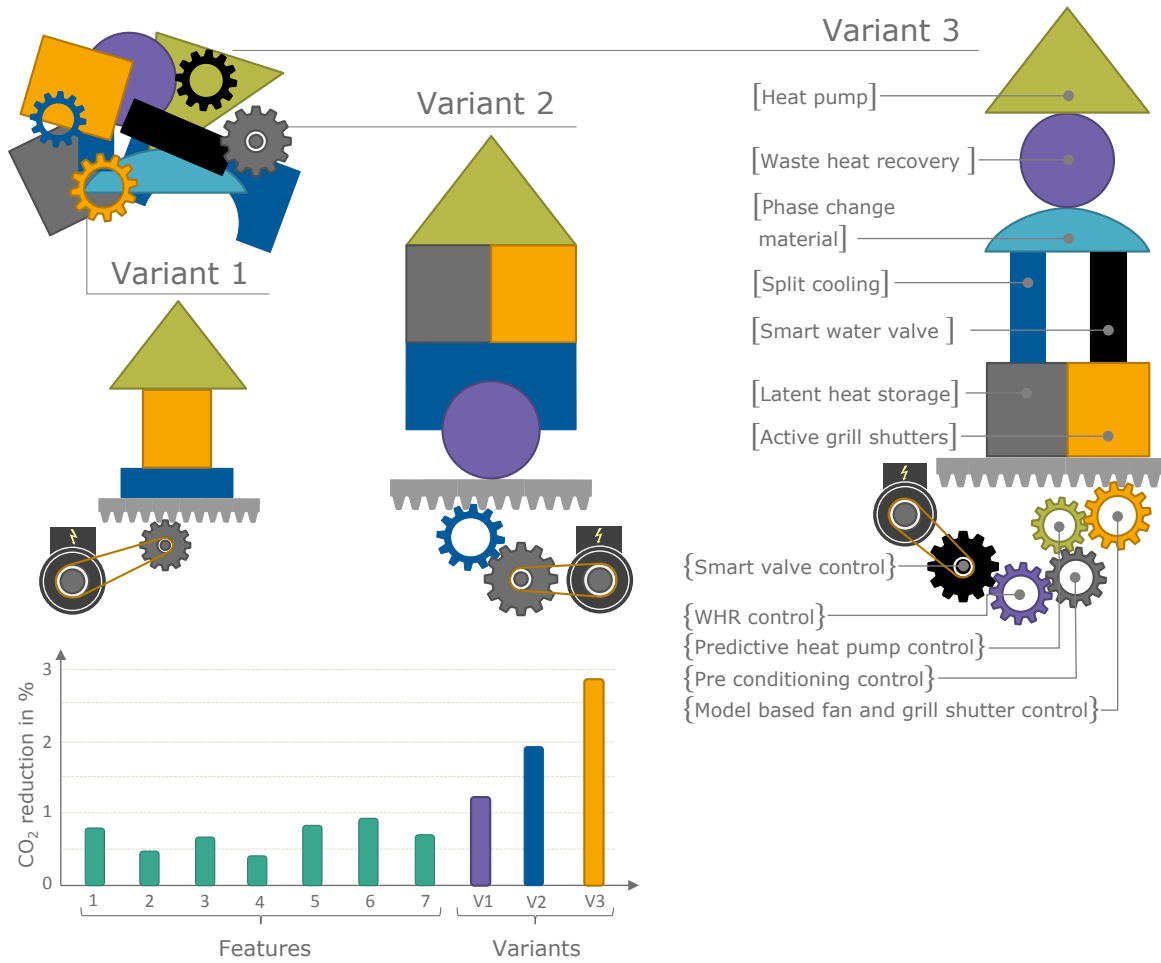
Figure 1.3.: Possible combinations of thermal management features and control thereof

The virtual world challenges and requirements are similar: the simulation model has to consider the entire vehicle including all relevant systems, which have an impact on energy distribution (with respect to electrical, mechanical, chemical as well as thermal energy). The main vehicle systems, which have to be coupled and interlinked, are illustrated in Fig. 1.4.
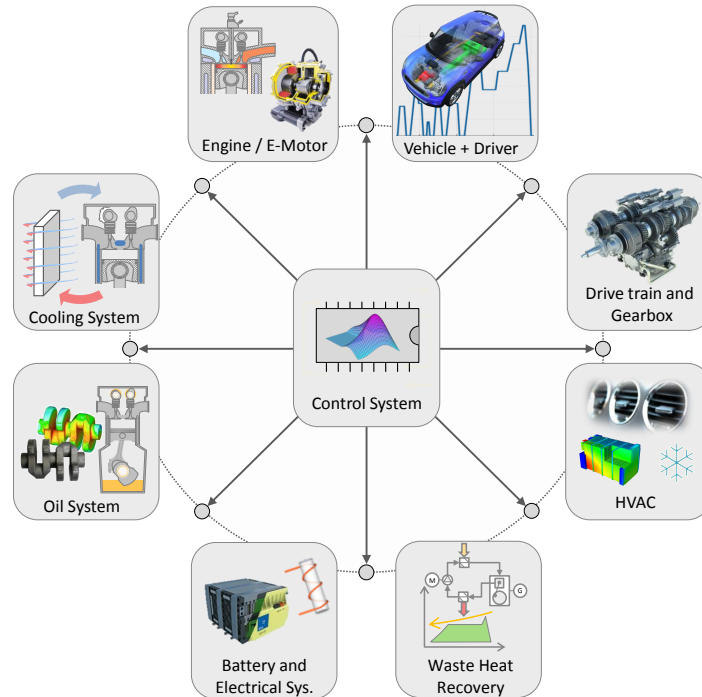
Figure 1.4.: Systems to be considered in a global VTMS simulation model.

1.2. Emission legislation

At the time of writing the European Union considers the Real Driving-Emissions (RDE) legislation as the key to a reliable measurement of vehicle pollutants and greenhouse gas emission [9]. There are a number of reasons that required this step towards a more realistic vehicle certification.

Air quality measurements conducted by Austrian environment agency for the last 15 years showed that efforts towards the particle emissions were quite successful and show a reduction of 20 percent [10]. Contrary, the trend for Nitrogen Oxide (NO_X) emission is showing a stagnation since the introduction of EURO 1 emission legislation in 1992. Measurements conducted at the Graz University of Technology with a Portable Emission Measurement System (PEMS) show that especially EURO 3 and 4 vehicles show even higher NO_2 emissions than EURO 1 vehicles and that the respective New European Drive Cycle (NEDC) limits were exceeded by far [9].

Regarding greenhouse gas emissions, there has been a significant reduction of one percent per year from 2005 till 2007 and four percent per year from 2007 till 2014, as shown in Fig. 1.5. Since 2005 CO_2 emission levels of new cars in the EU decreased by 24 percent. As emissions are directly related to fuel consumption, this reduction is equivalent to a decrease in fuel consumption from approximately 6.7 liters per 100 kilometers (l/100 km) to 5.1 l/100 km. According to the data, all major manufacturers have achieved the 2015 target at least one year early, with average fleet emissions amounting to 123.3 g/km [11]. This results are based on the NEDC type-approval data.
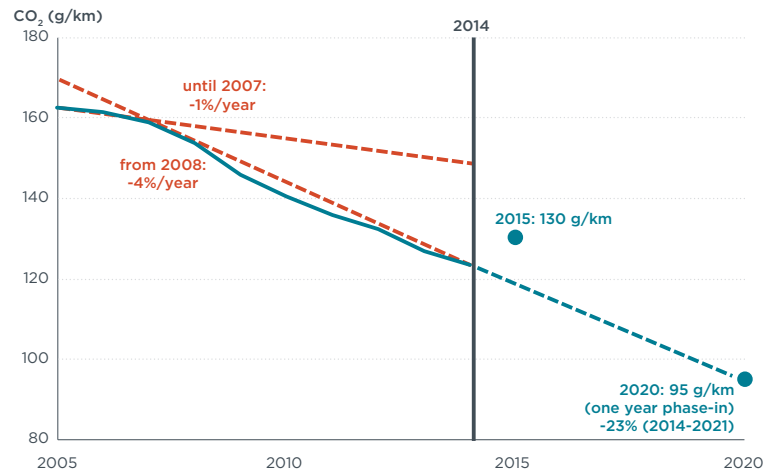
Figure 1.5.: Historical development and future targets for CO_2 emission levels of new passenger cars in the EU [11].

The EU vehicle efficiency regulations rely on results obtained from certification tests, also called type-approval tests, conducted in vehicle testing laboratories and not on the road. For fleet CO_2 emission targets to be effective, laboratory test results should translate accurately into real-world performance. Nevertheless, a study conducted by the International Council on Clean Transportation (ICCT) [12] using data on almost 0.6 million vehicles shows that this is not the case. The study reveals that the gap between real-world and official CO_2 emissions is huge and continues to increase, as shown in Fig. 1.6. For conventional cars the divergence grew from 8% in 2001 to as much as 40% in 2014.
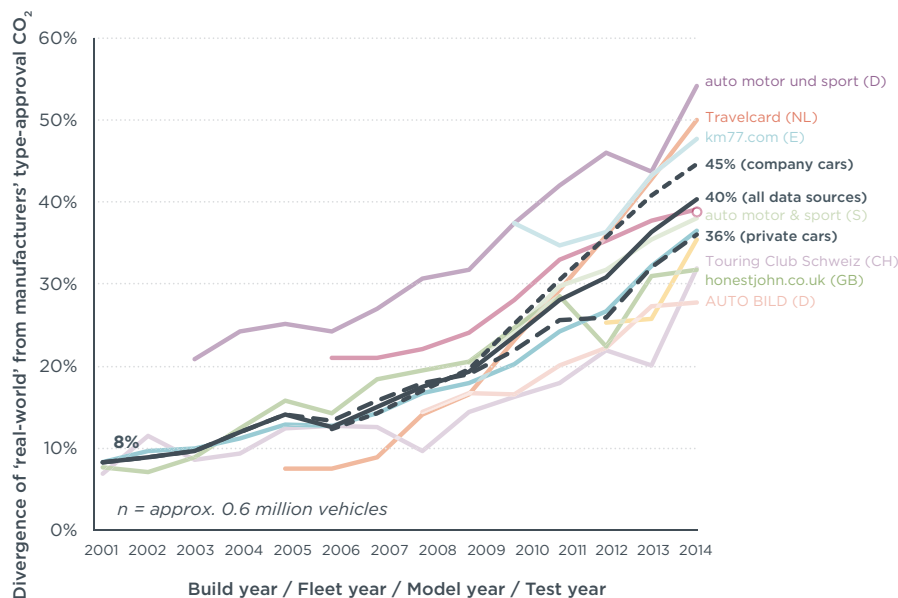
Figure 1.6.: Divergence between real-world and manufacturers' type-approval CO_2 emissions for various real-world data sources, including average estimates for private cars, company cars, and all data sources [12].

The divergence for Plug-in hybrid electric vehicles (PHEVs) is even higher. As shown in Fig. 1.7 the divergence from certified emission values is over 200 percent and reveals the shortcomings of the current test procedure in evaluating hybrid vehicle efficiency.
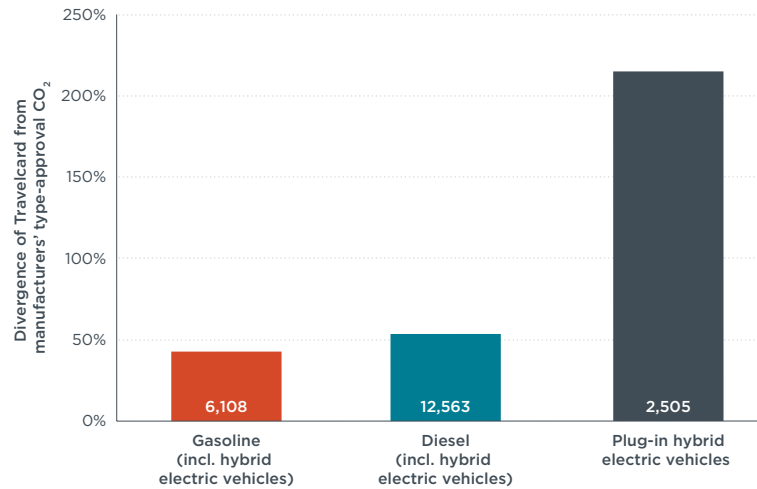
Figure 1.7.: Divergence between real-world and manufacturers' type-approval CO_2 emissions [12].

The reason for the large gap between the certified emission and the real-world emissions becomes evident when looking at the current certification test and calculation procedure. Hybrid Electric Vehicle (HEV) fuel consumption (FC) is calculated based on the NEDC fuel consumption with full battery (M_A), which is zero if the electric driving range (D_E) is larger than 11 kilometers and the NEDC FC with minimum SoC (M_B) [13]:

$$FC = \frac{M_A D_E + M_B 25}{25 + D_E}. \tag{1.1}$$

Eq. 1.1 indicates that with the current type-approval tests the vehicle manufacturers can "tune" the certification fuel consumption with the electric driving range D_E and thus with the battery size as illustrated in Fig. 1.8. This explains why the Audi A3 e-tron with 252 hp for propulsion and an electric range of 50 km has a significant lower FC (1.5 l/100km) than a Prius Plug-in (2.1 l/100km) with only 136 hp and an electric driving range of 20 km.
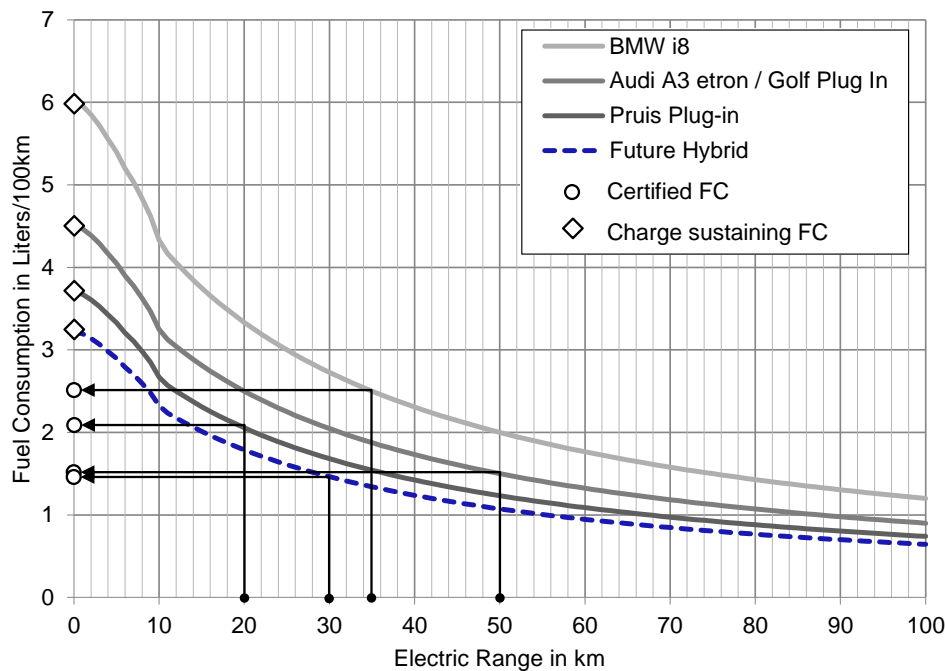
Figure 1.8.: HEV type-approval CO_2 emissions calculation procedure for four different PHEVs and variable battery size [14].

Apart from the mentioned shortcomings in the certification procedure for PHEVs the following causes for the growing discrepancies can be identified [12]:

1. **Road load determination:** Preceding the lab test a vehicle road load has to be determined on a test track. This offers the manufacturer a number of flexibilities to influence the road load. As example, preparation of the test track, selection of tires and tire pressure, ambient conditions and pre-conditioning of the vehicle. Regarding the thermal boundary conditions the NEDC test is limited to ambient temperatures ranging from 20 to 30°C. Operation of the vehicles at the maximum allowable ambient temperature and initial engine temperature decreases friction losses and hence increases the vehicle efficiency;

2. **Chassis dynamometer testing:** The laboratory test offers a number of tolerances that can be exploited by the vehicle manufacturer. These include break-in period of the test vehicles, usage of pre series parts and variation of battery SoC. As the test is always conducted under controlled laboratory conditions the test situation is easily detected and so called "defeat devices" can be triggered [15];

3. **Technology deployment:** A number of recently introduced technologies, on average, are more effectively reducing the CO_2 emissions during laboratory test than under real-world driving conditions. Examples include stop-start, hybrid technologies and automatic transmissions. For hybrid vehicles the hybrid control strategy, responsible for the coordination of the torque split between combustion engine and e-motor, can be optimized towards the reduction of cycle emissions, rather than improving overall real-word driving efficiency;

    4. Auxiliary consumers: Auxiliary system such as Heating Ventilation and Air Conditioning (HVAC) and entertainment system are increasing the fuel consumption during real world driving. Nonetheless these devices were either switched off or not fully taken into account.

This discrepancies between legislation cycle emissions and emissions in real driving are the main driver for the EU to introduce a new emission certification standard. Even if not all details of the RDE legislation are determined so far, the certification procedure of vehicles in Europe will change. The main novelties of the Real Driving Emissions (RDE) test procedure will include among others [9]:

1. Measurement of emissions in real-world traffic situations with a PEMS. This makes it hard to detect if an emission test is running.

2. A valid test run is required to cover the full spectrum of normal driving situations. Hence the full vehicle operating range, including full load, is take into consideration. Optimization of the vehicle towards a specific test case is no longer successful.

3. Ambient conditions are clusterd into moderate and extended conditions. With moderate conditions ranging from 0 till 30°C and an altitude below 700m, and extended conditions ranging from -2 till 35°C and an altitude below 1300m.

4. Results from RDEs measurements are getting normalized $\|RDE\|$ and compared relative to a limiting value. This ratio is called Conformity Factor (CF)

   $CF = \frac{\|RDE\|}{LimitValue}$.

   Fixed maximum values for the CF will be part of the legislation. The normalization algorithm is still subject to ongoing discussions.

1.3. State of research and future needs

1.3.1. Vehicle thermal management and thermal control

Electric Vehicles (EVs) and PHEVs are currently gaining increasing popularity. Almost all major vehicle OEMs introduced such kind of vehicles to reduce the fleet CO_2 emissions in order to meet the stringent targets that where proposed by the legislation. Exemplary, the Volkswagen group has announced to introduce as much as 20 additional electric or PHEV vehicle models until 2020 [16].

Together with the powertrain architecture of the EVs also the vehicle thermal system has to be adapted accordingly. In contrast to conventional vehicles where most of the thermal actuators are actuated mechanically, electrified vehicles are equipped with electrically controlled actuators. Therefore the degrees of freedom and complexity of the vehicle thermal management systems has increased drastically.

Fig. 1.9 gives an overview of the involved cooling and lubrication systems and the associated electric controllable actuators for a PHEV. A total number of *16* actuators is required to enable thermal management features like split cooling, gearbox heating, cabin heating with or without combustion engine and combined cabin and battery refrigerant cooling. From that it is evident that the effort for calibration and testing of such systems is very high and demands for a sophisticated development process and tools to derive a high level of maturity before first vehicle tests.

The increasing amount of hybrid vehicle variants together with many involved subsystems with high interactions and electric controllable actuators in the thermal system leads to a strong need for a generic thermal system control architecture.

Actuator Name	#
Variable Pumps	6
Compressor	1
Bypass Valves	4
Shut-off Valves	2
Fans	2
Map-Thermostat	1
Sum of Actuators:	16

AC… Air condition
LT… Low Temperature
HT… High Temperature
OC… Oil Cooler
EM… Electric Motor
SOV… Shut-off valve
BV… Bypass valve
TXV… Expansion valve
TH…Thermostat
CH… Cabin Heater
EVAP… Evaporator
HV… High Voltage
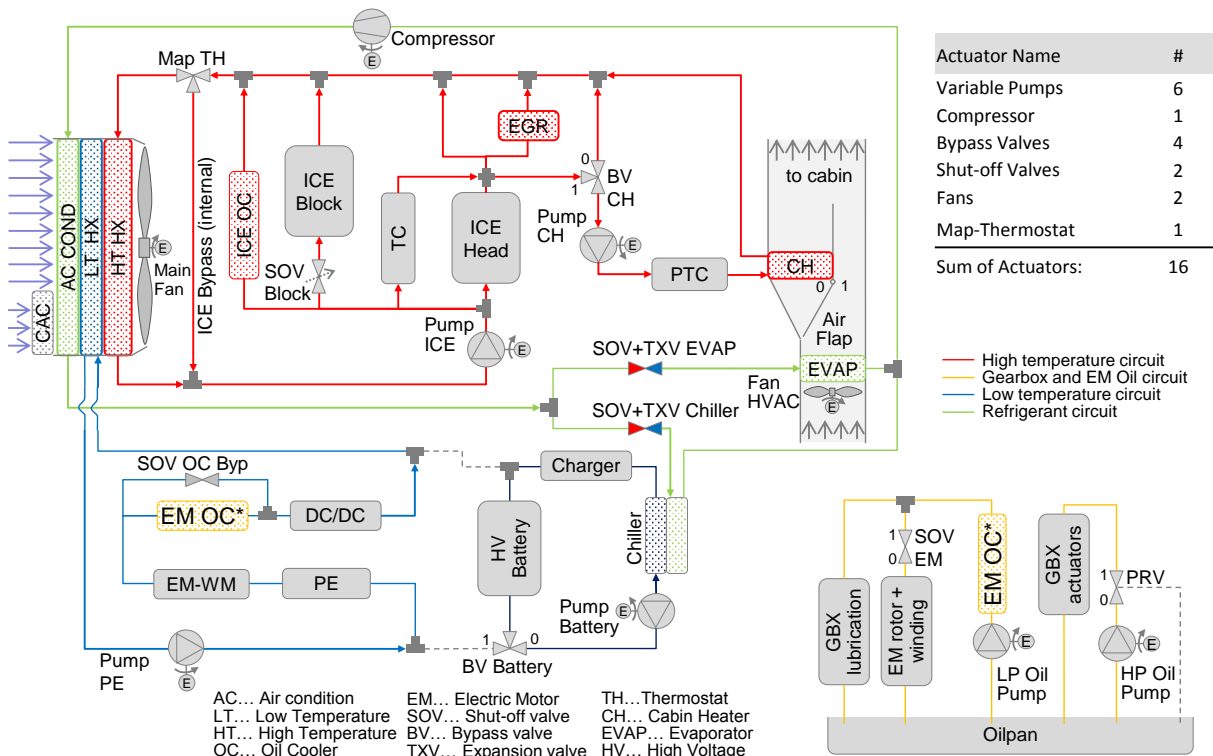
Figure 1.9.: Thermal systems and actuators in a PHEV.

Regarding the state of research towards thermal management control architecture, results from literature survey and patent research show that Ford owns patents covering cabin conditioning [17] and power electronics cooling [18] based on bang-bang temperature control. A more generic approach under patent law is owned by Daimler [19]. Specified therein is a cabin heating *mode selection concept* that controls the actuators dependent on the currently active heating mode for HEVs/PHEVs/BEVs. Apart from the mentioned patents the field of thermal management control architecture is so far not broadly covered by other publications, which is in contradiction to the hybrid control unit (HCU) architecture.

Towards control laws applied for thermal system actuators many methods are proposed to track and regulate a coolant temperature within a safety range. Therefore mainly linear PID control [20, 21, 22] and nonlinear Lyapunov stability theorem based control algorithms [23, 24, 25, 26, 27, 28] are used. Control laws that are taking fuel consumption into consideration are mainly using dynamic programming which is a well-known method for solving optimal control problems [29]. This approach inherits large computational cost and is therefore not suited for a microprocessor implementation [30]. Nevertheless dynamic programming can be used to provide a reference solution for the control problem. A model predictive controller that can take the actuator limitations and system thermal boundary conditions into account is favorable for fuel and energy consumption optimization. Exemplary, a set of linear Model Predictive Control (MPC) controllers is used in [31], while a nonlinear MPC was developed in [32, 33]. It is noteworthy that beside lab buildups of single cooling circuits an implementation of a model based thermal control algorithm in a series production vehicle has not been found. This is probably due to the fact that for the development of model based controllers comprehensive insight into the entire vehicle system is required. Therefore a mathematical plant model is required which is able to describe all relevant interdependencies in a sufficient granularity. Additionally, if control problems are formulated in terms of temperature tracking it is strongly recommended to show that the temperature tracking has a positive effect on fuel consumption or emissions, compared to baseline bang-bang control [24]. This evidence is typically performed by experiment or thorough simulations studies covering the entire area of application.

In contrast to conventional vehicles, electrified powertrains offer an additional challenge to the thermal conditioning: the durability of e-components is not only influenced by temperature peaks but also by the duration and amplitude of temperature swings as well as temperature gradients within the components during their lifetime. Keeping all components always at the preferred lowest temperature level to avoid aging under any conditions (driving, parking, etc.) will result in very high energy consumption which is in contradiction to the efficiency targets.

The layout of the thermal system and its control strategy is always a compromise between *efficiency* and component *durability* under consideration of a *representative annual usage profile*.

A methodology supporting the development and assessment of control algorithms towards fuel and energy consumption together with durability, is missing so far.

1.3.2. Thermo-fluid simulation

For simulation modeling of thermo fluid vehicle systems, such as the Internal Combustion Engine (ICE) cooling circuit including the connected thermal network, a number of commercial available software solutions exist. The most popular are:

- KULI[1] from Engineering Center Steyr,
- Flowmaster[2] from Mentor Graphics,
- GT Suite[3] from Gamma Technologies.

Concerning the current NEDC type-approval focused approach those tools performed well as a part in the global vehicle simulation tool chain. But things change with the introduction of real-world drive cycles. Needs arise for a consistent integration of the thermal system simulation and control into the vehicle development process. Subsequently, the future requirements for thermo fluid simulation can be formulated as:

(a) **Stagnant flow:** Technologies like split cooling, stop-start, engine warm-up without active cooling and the simulation of real-world drive cycles offer challenges to thermo fluid simulation tools. The crucial point is the simulation of zero/stagnant flow conditions. Therefore the fluid flow solver has to be disabled and reactivated. Additionally, it is required to treat heat transfer in different manner. For instance, commonly used fluid mass flow dependent heat transfer correlations fail to describe the cool down of a heat exchanger at zero coolant flow and nonzero air mass-flow conditions;

(b) **Simulation speed:** With the introduction of RDE it is mandatory to simulate the entire area of vehicle operation. Therefore the simulation task moves from a 11 kilometers and 1180 seconds long NEDC simulation to a number of more realistic drive cycles. These drive cycles have to cover all possible ambient conditions and driving situations. Consequently the number and length of simulation runs will increase dramatically. A simulation real time factor (RTF)[4] of 0.7-2 is typical for a global vehicle model [3, 34, 35]. Because the thermo fluid simulation is consuming a large portion of the required calculation time an improvement in terms of computing performance is required;

(c) **Development process:** After concept evaluation and layout of the thermal system the thermal control functionality is developed. The thermal management controller and the comprehensive global vehicle simulation model are coupled together in order to perform offline optimization of control strategies and pre-calibration of threshold values. Model based control development requires full system insight and the exchange of physical models rather than black box models. Since software and control development is commonly done by different departments an efficient collaboration requires a flexible and straight forward exchange of plant models;

---

[1] http://www.kuli-software.com/
[2] https://www.mentor.com/products/mechanical/flowmaster/
[3] https://www.gtisoft.com/
[4] The RTF is defined as the ratio of the simulation time to the time of the real process

(d) **Hardware target:** After office control and function development Hardware in the Loop (HiL) tests are often conducted to test certain control functionalities and actuator behavior. For that a so called HiL simulator has to provide all necessary sensor stimulations and boundary conditions. Hence, a real-time capable version of the thermo fluid simulation tool is required. Solutions using commercial software involve extensive simulation studies and an ensuing mathematical model fit (e.g.: Neuronal Networks [34] or Response Surfaces [36]).

Based on the challenges in thermo fluid simulation it can be stated that there is so far no commercial tool available that:

- allows the simulation of heat transfer in stagnant fluid circuits;
- supports the development process in terms of flexible model exchange;
- has a high computing performance and
- has a native support for target code generation.

1.4. Objectives and contributions

Based on the future needs described in chapter 1.3 the main objective of the thesis is a *methodology* for model based development of *vehicle thermal control.* This methodology reaches from the coupled simulation of all relevant vehicle subsystems over the development of a generic thermal control architecture till the exemplary assessment of model based control algorithms. The high level development objective of vehicle thermal management, and therefore also for the control development, is the reduction of CO_2 and pollutant emissions together with durability aspects. Thus, the objectives span the assessment of the developed control architecture and thermal control algorithms under real-world driving conditions with respect to the upcoming RDE legislation (section 1.2).

To accomplish these objectives, contributions to the following subjects, as shown in Fig. 1.10, will be made in course of this work:

1. **Thermo Fluid Simulation:** For lifetime analysis one of the key requirements are short simulation run-times without sacrificing the model accuracy and fidelity. Therefore an approach for thermo-fluid simulation that allows: stagnant flow simulation; high computing performance (RTF $<< 0.1$); flexible model exchange and hardware target code generation is proposed in chapter 3;

2. **Control Architecture:** The present work provides a generic approach for a thermal management controller, that is flexible in change of powertrain architecture and functionality, as shown in section 5.1.2. This means the thermal control of a conventional car can be handled as well as a complex hybrid vehicles with numerous involved thermal systems and actuators;

3. **Assessment of fuel and energy consumption:** In the presented approach custom drive cycles and ambient temperature conditions are extracted from real-world driving measurements. These drive cycles are a statistically significant representation of the real vehicle usage behavior and therefore valid for statements regarding the annual energy consumption and durability, as described in section 6.3.

Model based development
and assessment of vehicle thermal control

Chapter 4	*Chapter 5*	*Chapter 6*
Global vehicle simulation	Control system architecture	Assessment

Main contributions

Chapter 3	*Section 5.1.2*	*Section 6.3*
Thermo-Fluid simulation tool	Generic thermal management controller	Usage space analysis
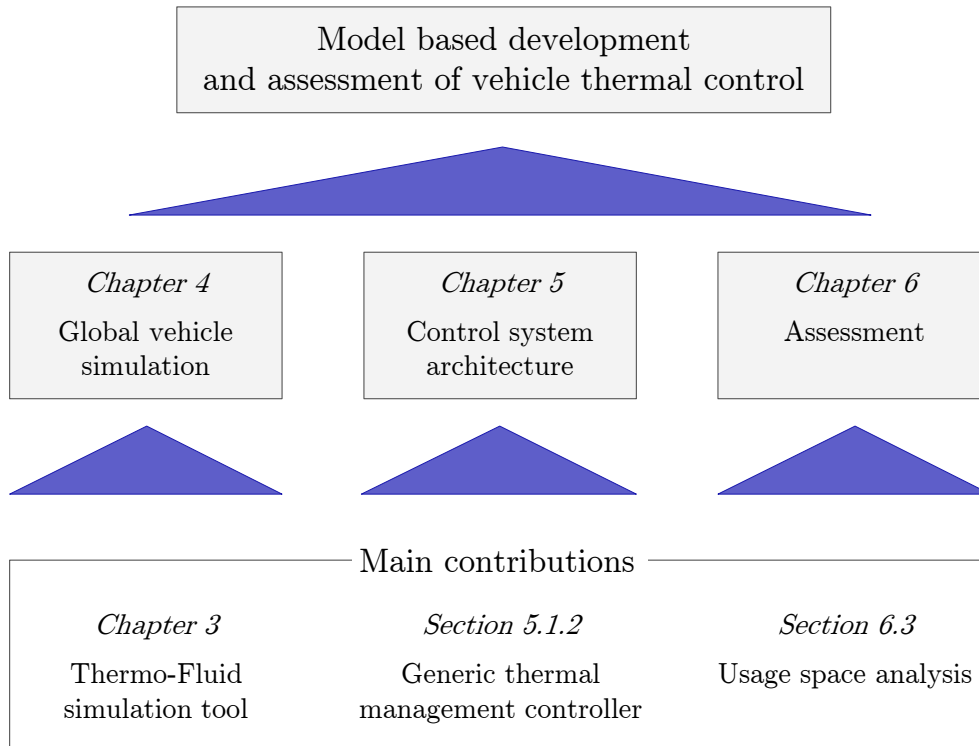
Figure 1.10.: Outline of chapter structure and main contributions to reach the objectives

2

Heat transfer and fluid mechanics fundamentals

This chapter gives an overview of the first principle laws that are used in thermo fluid analysis. Descriptions will focus on simplifying first principle laws towards a convenient 1D representation to enable the usage in system simulations and control development. Since simplifications are necessary the boundary conditions and areas of utilization for the given equations are stated. First, the fundamental law of thermodynamics is introduced to describe the transient thermal behavior of open and closed systems. After that, the mechanisms of heat conduction and convection, especially in pipes and channels, are discussed. The second part of this chapter focuses on the fundamentals of fluid mechanics. Equations for the conservation of mass, momentum and energy are introduced, since they play an important role in describing fluid flow characteristics, friction losses, pressure sources and, finally, thermo fluid networks.

2.1. Energy conservation and heat transfer

2.1.1. Energy conservation

The first law of thermodynamics is a fundamental expression of the energy conservation principle, and it asserts that energy is a thermodynamic property. According to [37] it simply states that the change in energy of a system ΔE_{system} is equal to the difference between the total energy entering and the total energy leaving the system (E_{in}, E_{out}) as

$$\Delta E_{system} = E_{in} - E_{out}. \tag{2.1}$$

The energy of a system is presumed to be some function of the measurable properties of the system so it can be stated that

$$E_{system} = U(T, p, etc.) \tag{2.2}$$

where U is called the *internal energy function* which usually depends on the thermodynamic states temperature T and pressure p. Change in internal energy ΔU is often denoted as

$$\Delta U = Q - W \tag{2.3}$$

where Q and W are called *heat* and *work*, respectively. Heat input and work output are are defined as positive quantities. For engineering purpose the equation above shall be used to calculate Q and W therefore the internal energy function $U(T, p)$ must be known before calculation. For common fluids this function is available from engineering reference tools ([38], [39]), otherwise, it has to be derived from experiments. The specific heat is such quantity which is defined as the energy required to raise the temperature of a unit mass of a substance by one degree. It is used to describe the internal energy of a system and is defined as

$$c_v = \left(\frac{\partial u}{\partial T}\right)_v \quad \text{at constant volume, or} \quad c_p = \left(\frac{\partial h}{\partial T}\right)_p \quad \text{at constant pressure.} \quad (2.4)$$

For solids and fluids it can be shown [40] that constant volume and constant pressure specific heats are identical

$$c_p = c_v = c. \tag{2.5}$$

Like those of ideal gases, the specific heats of incompressible substances depend on temperature only. Thus, the partial differentials in equation 2.4 can be replaced by ordinary differentials, which yields after rearranging

$$du = c(T)\, dT. \tag{2.6}$$

The change in internal energy between states 1 and 2 is then obtained by integration

$$u = \int_1^2 c(T)\, dT. \tag{2.7}$$

For the analysis of certain processes the combination of internal energy and pressure p times volume V is commonly used. Therefore they are combined into a property called *enthalpy H*

$$H = U + pV \quad \text{or, } \textit{specific enthalpy} \text{ per unit mass:} \quad h = \frac{H}{m} = u + pv \tag{2.8}$$

The differential form can be determined by differentiation to be

$$dH = dU + p\, dV + dp\, V. \tag{2.9}$$

With a constant volume V under the assumption of a constant pressure process ($dp = 0$), as in heaters, it can be stated that the enthalpy equals the internal energy

$$dH = dU \quad \text{or, per unit mass:} \quad dh = du. \tag{2.10}$$

Substitution into equation 2.6 and integration from state 1 to state 2 results in the specific enthalpy

$$h = \int_1^2 c(T)\, dT. \tag{2.11}$$

Energy can be transferred to or from a system in three forms: *heat flow* $\dot{Q}$, *work* $\dot{W}$ or *enthalpy flow* $\dot{H}$. Changes in energy are balanced at the system boundary of a c*ontrol volume*[1] as shown in Fig. 2.1. The internal energy balance can also be written in time derivative form as

$$\frac{dH}{dt} = \sum \dot{Q} + \sum \dot{W} + \Delta \dot{H} \tag{2.12}$$

where $\Delta \dot{H}$ is the *enthalpy flow difference* that describes the difference between the energy of the in- and outflowing fluid as

$$\Delta \dot{H} = \sum \dot{H}_{out} - \sum \dot{H}_{in} = \sum (\dot{m}\, h)_{out} - \sum (\dot{m}\, h)_{in} \,. \tag{2.13}$$
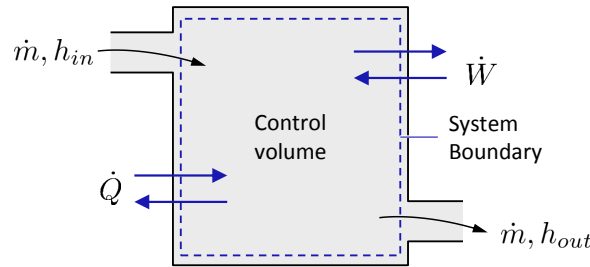
Figure 2.1.: Energy change in an open system control volume by means of heat $\dot{Q}$, work $\dot{W}$ or mass flow $\dot{m}$ [41]

Closed System:

The only two forms of energy interactions associated with a fixed mass or *closed system* are heat and work.
For the energy balance of *solids* (e.g. ICE, Electric Motor (EM) structure) the energy transfer from work and mass flow can be neglected. Thus, under assumption of constant heat capacity, equation 2.12 yields

$$\frac{dH}{dt} = m\, c\, \frac{dT}{dt} = \sum \dot{Q} \tag{2.14}$$

where $\dot{Q}$ can be any heat source or sink ranging from heat transfer via *conduction* (as in section 2.1.2) over *convection* (as in section 2.1.3) till *radiation.*

Open System:

Open systems involve mass flow in and out of a system and are modeled as *control volumes* (as in Fig. 2.1). For the energy balance of *open systems* (for example a control volume in a coolant or oil circuit), it is also assumed that no work is performed. Hence, equation 2.12 simplifies to

$$\frac{dH}{dt} = \sum \dot{Q} + \Delta \dot{H}. \tag{2.15}$$

---

[1]A control volume is a specific region of interest within a system to which physical laws can be easily applied.

Combining Eq. 2.11 and 2.13, the sum of heat transferred via fluid mass flow can be calculated as

$$\Delta \dot{H} = \dot{m} \int_{T_{in}}^{T_{out}} c(T) \, dT. \tag{2.16}$$

Note that this equation is only valid for a control volume with one inlet and one outlet.

2.1.2. Conductive heat transfer

Heat conduction in a medium, in general, is three-dimensional and time dependent. It is driven by temperature gradients within a material. The temperature in a medium varies with position x, y, z as well as time t

$$T = T(x, y, z, t). \tag{2.17}$$

From experimental research it is proven that a *linear relation* between heat flux $\dot{\mathbf{Q}}$ and temperature gradient $(\text{grad}(T))$ exists. It can be described by *Fourier's law of heat conduction* [42] as

$$\dot{\mathbf{Q}}_{cond} = -k \, A \, \text{grad}(T) \tag{2.18}$$

where k is the thermal conductivity of the material, and A is the heat transfer area that is normal to the direction of heat flux. Solution of equation 2.18 for the temperature field given in 2.17 is subject to application of the first law of thermodynamics and leads to a inhomogeneous partial differential equation of second order. Analytical solution of this equation is in many cases non trivial or even impossible, therefore the following *simplifications* are made towards a more convenient application:

- When the direction of heat transfer has only one predominant direction the heat conduction problem is considered as *one dimensional*;
- The thermal conductivity of a material is a measure of the ability of a material to conduct heat, which in general is a function of temperature and pressure $k = k(T, p)$. For simplicity it is obtained by using a *constant value* at an average temperature;
- Heat transfer problems are often classified as being *steady* (no change with time) or *transient* (variation with time). Although most heat transfer problems are transient they are usually analyzed under some presumed steady conditions since steady processes are easier to analyze and capable of providing the answers to most questions.

Fourier's law of heat conduction (Eq. 2.18) for one-dimensional, steady state heat conduction with constant thermal conductivity, as shown in Fig. 2.2, simplifies to

$$\dot{Q}_{cond} = -k \, A \frac{dT}{dx}. \tag{2.19}$$

Separation of variables and integrating for the heat conduction length x from zero to length L and temperature from T_1 to T_2 yields

$$\dot{Q}_{cond} = \frac{k}{L} A(T_1 - T_2). \tag{2.20}$$
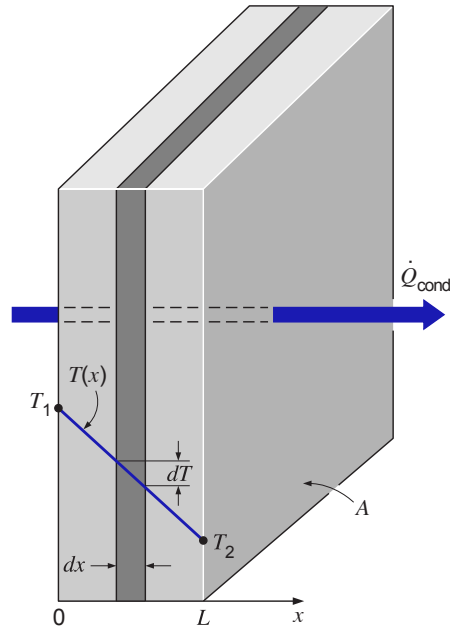
Figure 2.2.: Wall temperature profile at steady state heat conduction [40]

The heat conductivity k (with SI units $\frac{W}{m\,K}$) is in general high in solids and low in gases. Typical values lie somewhere in between

$$
\begin{aligned}
0.015 \leq k_{gas} &\leq 0.15, \\
0.1 \leq k_{liquid} &\leq 0.65, \\
1 \leq k_{solid} &\leq 450.
\end{aligned}
\tag{2.21}
$$

2.1.3. Convective heat transfer

Convective heat transfer occurs between a fluid and a solid surface that have a relative velocity and a temperature difference. The resulting heat flux is strongly depending on the material properties and flow conditions. Conductive heat flux as well as heat flux from fluid motion has to be considered. The faster the fluid motion, the better the convective heat transfer. Convection is called *forced convection* if the fluid is forced to flow over the surface by external means such as a fan, a pump or the wind. In contrast, convection is called *natural* (or *free*) *convection* if the fluid motion is caused by buoyancy forces that are induced by density differences due to the variation of temperature in the fluid. Heat transfer processes that involve *change of phase* of a fluid are also considered as *convection* because of the fluid motion induced during the process (e.g. boiling).

Flow boundary layer

For the heat transfer calculation that occurs between a fluid and it's boundary, e.g. a wall, the characteristics of the fluid close to the wall is significant. In Fig. 2.3 the near wall flow (left) and temperature (right) profile of a fluid that is flowing parallel to the wall is shown. Where y is the distance from the wall and u_∞, T_∞ are the flow velocity

and temperature far from the wall. Fluids have the tendency to adhere to the wall while they pass by it which is mainly influenced by the *viscosity* of the fluid. Therefore a region with variable fluid velocity must exist between zero velocity close to the surface and the free stream velocity u_∞. This region is called *flow boundary layer*. The boundary layer thickness δ_u is depending on the flow regime, as depicted in Fig. 2.4. It defines the separation line between the boundary layer region and the inviscid flow region.
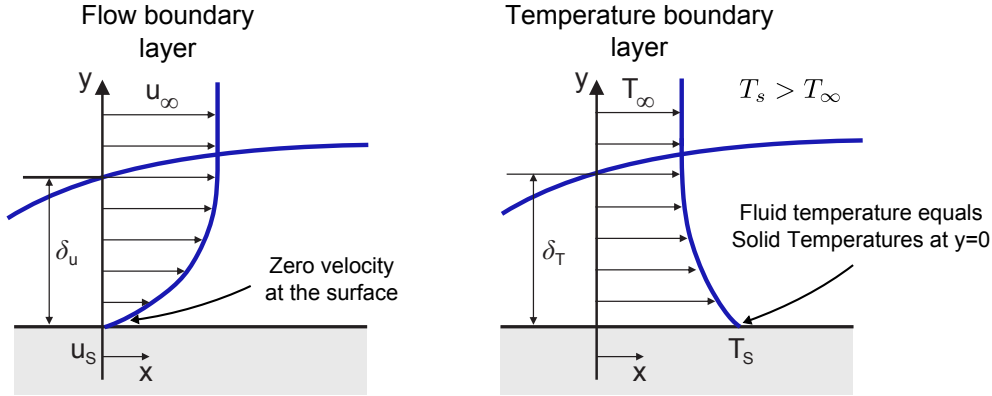
Figure 2.3.: Flow and temperature boundary layers [43].

A mathematical description of the flow boundary layer thickness can be given by the dimensional function

$$\delta_u = f(u_\infty, \rho, \mu, x) \tag{2.22}$$

where ρ is the fluid density and μ is the dynamic viscosity. Applying the Buckingham Π theorem [44] for dimensional analysis of the five variables yields

$$Re_x \equiv \frac{u_\infty \, \rho \, x}{\mu} = \frac{u_\infty \, x}{\nu}. \tag{2.23}$$

where ν is the kinematic viscosity, x is the characteristic length for the considered heat transfer problem and Re_x is called the *Reynolds number*[2]. The characteristic length for external (free) flow is the distance from the leading edge until a length x in flow direction. The Reynolds number characterizes the relative influence of inertial and viscous forces in a fluid flow. It can be used to describe the flow regime and the development of the boundary layer, as depicted in Fig. 2.4:

- **Laminar flow** develops at low Reynolds numbers ($Re_x \leq Re_L$) where viscous forces are dominant, and can be characterized by steady and smooth streamlines and highly-ordered motion;
- **Turbulent flow** develops at high Reynolds numbers ($Re_x \geq Re_T$) where inertial forces are dominant, and can be characterized by unsteady turbulent flow with velocity fluctuations and highly-disordered motion;
- **Transition** from laminar to turbulent flow does not occur suddenly. It develops over a Reynolds number region ($Re_L \leq Re_x \leq Re_T$) in which the flow fluctuates between laminar and turbulent flows before it becomes fully turbulent.

---

[2]Subscript x indicates the length on which it is based upon.
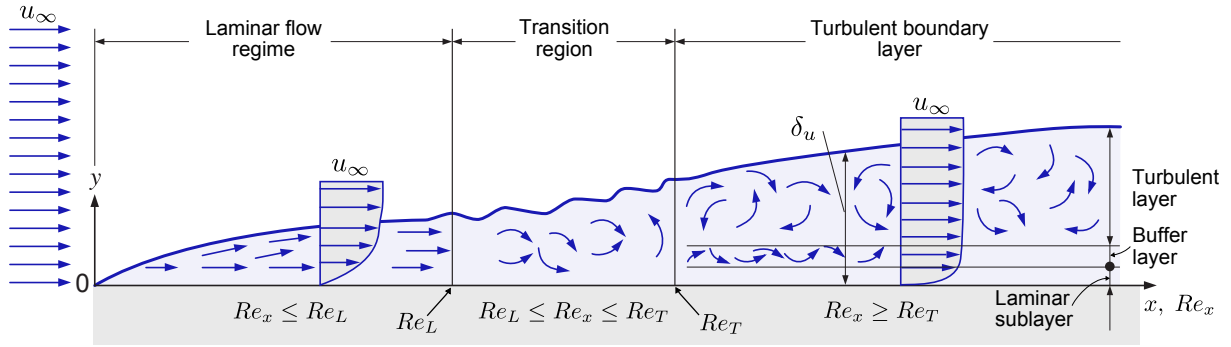
Figure 2.4.: The development of the boundary layer for flow over a flat plate, and the different flow regimes [40].

The Reynolds number is significantly relevant for describing the influence of the flow on forced convective heat transfer. From Fig. 2.5 it can be observed that the kinematic viscosity varies over temperature (by a factor of ten for coolant compared at 0 and 90 °C) and that water has a significantly lower kinematic viscosity than the water glycol mixture. Thus, the Reynolds number is higher for water compared to a water glycol mixture at a similar flow speed.
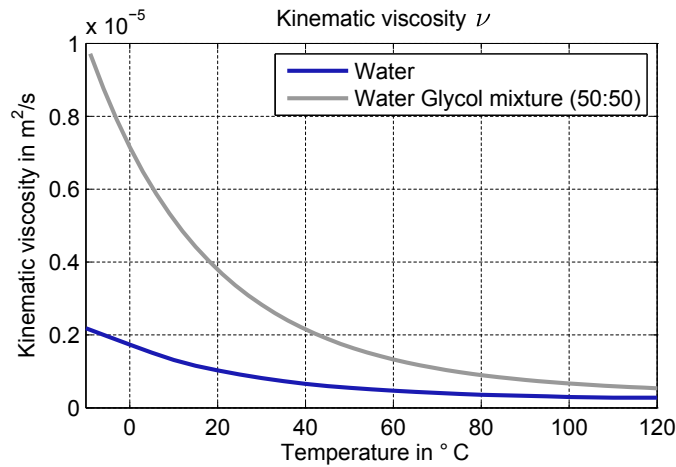
Figure 2.5.: Kinematic viscosity for water and water glycol mixture (50:50).

For the description of the flow characteristics at *natural convection* the *Grashof number* is used, which is defined as

$$Gr = \frac{x^3 \ g \ \beta \ (T_s - T_\infty)}{\nu^2} \tag{2.24}$$

where β is the thermal expansion coefficient and g is the acceleration due to gravity. The Grashof number represents the ratio of the *lifting force* to the *viscous force* acting on the fluid.

21

Temperature boundary layer

If the temperature of the surface T_s is different from the temperature of the free stream T_∞ a temperature boundary layer δ_T exists that is, in general, different from the flow boundary layer[3]. The thermal boundary layer for the case $T_s > T_\infty$ (cooling of a solid) is shown in Fig. 2.3.

For a fluid that is forced to flow over a solid surface the flow velocity becomes zero at the wall surface (known as *no-slip condition* [43]). This implies that directly at the surface of a body the convective heat transfer can be neglected and the heat flux can be described as in Eq. 2.19

$$\dot{Q}_{conv} = \dot{Q}_{cond} = -k_f \, A \frac{dT}{dy}\bigg|_{y=0} \tag{2.25}$$

where dT/dy is the fluid temperature gradient directly at the surface of a body and k_f is the thermal conductivity of the fluid layer. The temperature gradient of the fluid depends on the flow conditions and fluid properties and can be described by momentum, mass and energy conservation laws. Despite the complexity of the analytical solution, the rate of convection heat transfer is observed to be proportional to the temperature difference, and is conveniently expressed by *Newton's law of cooling* [40]

$$\dot{Q}_{conv} = h \, A \, (T_s - T_\infty) \tag{2.26}$$

where h is the *heat transfer coefficient (HTC)* in $\frac{W}{m^2 \, K}$, A is the effective heat transfer area in m^2, T_s is the surface temperature in °C and T_∞ is the temperature of the fluid outside of the temperature boundary layer in °C.

When two bodies at different temperatures are brought into contact, heat transfer occurs until both bodies reach the same temperature at the point of contact. Therefore, the fluid and the solid will have the same temperature at the point of contact. This is known as the *no-temperature-jump condition* [43]. Under consideration of the *no-slip* and *no-temperature-jump* condition the conducted heat (Eq. 2.25) equals the convected heat (Eq. 2.26) at the wall surface, as shown in Fig. 2.6, which yields

$$\dot{Q}_{cond} = \dot{Q}_{conv}$$
$$-k_f \, A \frac{dT}{dy}\bigg|_{y=0} = h \, A \, (T_s - T_\infty). \tag{2.27}$$

From 2.27 the *heat transfer coefficient h* results in

$$h = -k_f \, \frac{A \frac{\partial T}{\partial y}}{(T_s - T_\infty)}\bigg|_{y=0} . \tag{2.28}$$

---

[3]If the *Prandtl number* is equal to one, the temperature and flow boundary layer thickness is identical.
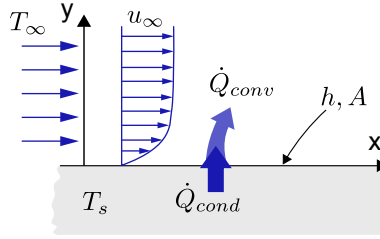
Figure 2.6.: Forced convection heat transfer mechanisms for a straight wall [40].

If the fluid temperature profile in wall proximity $\frac{\partial T}{\partial y}$ is known the heat transfer coefficient can be calculated. This is generally not the case. Therefore for many practical relevant problems *heat transfer correlations*, which are commonly called *Nusselt correlations*, are derived base on heat flux $\dot{Q}$ and temperature (T_s, T_∞) measurements.

Prandtl Number Pr

Based on the similarity law approach it can be shown that the convective heat transfer is a function of kinematic viscosity ν and *thermal diffusivity a*. The nondimensional relation between the kinematic viscosity and thermal diffusivity is called *Prandtl number*.

$$Pr = \frac{\nu}{a} = \frac{\nu \, \rho \, c}{k_f} \tag{2.29}$$

where a is the thermal diffusivity which can be expressed as $a = k_f/(\rho \, c)$. In Eq. 2.29 the kinematic viscosity ν accounts for the friction induced momentum transport (flow boundary layer) and the thermal conductivity k_f represents the conductive heat transfer in the temperature boundary layer. Therefore, the Prandtl number is a measure of the ratio between flow and temperature boundary layer thickness. It can also be considered as a characteristic *non dimensional fluid property*.

Nusselt Number Nu

For the formulation of heat transfer correlations it is common practice to use similarity laws in order to nondimensionalize the governing equations and combine the variables together in groups.
Multiplying both sides of Eq. 2.28 with the characteristic length L and dividing by the fluid thermal conductivity k_f gives a non dimensional representation of the heat transfer coefficient h which is called *Nusselt number*

$$Nu_x = \frac{h \, L}{k_f} = -\frac{L \, A \frac{\partial T}{\partial y}}{(T_s - T_\infty)}\bigg|_{y=0}. \tag{2.30}$$

Subscript x indicates that it is a local property, valid for position x in flow direction.
The Nusselt number is viewed as a dimensionless convection heat transfer coefficient. From a physics point of view, the Nusselt number represents the *enhancement of heat transfer* through a fluid layer as a result of *convection* relative to *conduction* across the same fluid layer. Nu_x can also be expressed as

$$Nu_x = \frac{\dot{Q}_{conv}}{\dot{Q}_{cond}} = \frac{h \, A \, \Delta T}{k_f \, / L \, A \, \Delta T} = \frac{h \, L}{k_f}.$$

The larger the Nusselt number, the better the convective heat transfer. A Nusselt number of $Nu_x = 1$ means that heat is transfered across the fluid layer by *pure conduction.*
With the Reynolds number Re for the description of the flow characteristics and Prandtl Pr number for consideration of the fluid properties the dimensionless heat transfer coefficient, the Nusselt number, can be described by a function f as

$$Nu_x = f(Re, Pr). \tag{2.31}$$

In case of natural convection the Grashof number Gr is used instead of the Reynolds number, which yields

$$Nu_x = f(Gr, Pr). \tag{2.32}$$

With the four introduced dimensionless numbers it is possible to solve geometrical similar problems under certain boundary conditions in a straight forward manner.

2.1.4. Heat transfer in pipe and channel flow

An important practical engineering problem is the heat transfer for flow in pipes and channels. Piping systems occur in almost every engineering design an thus a large amount of experimental data is available with a smaller amount of theory.

Hydraulic diameter

In pipe and channel flow a characteristic length is used to calculate the Reynolds number, Nusselt number and the Darcy friction factor[4]. For circular or non circular pipes and channels the characteristic length is the *hydraulic diameter* d_h that is defined as

$$d_h = \begin{cases} \dfrac{4\,A_f}{p} & \text{for noncircular tubes} \\ d & \text{for circular tubes} \end{cases} \tag{2.33}$$

where A_f is the channel free flow area, p is the perimeter and d is the circular tube diameter.

Nusselt correlations for pipe and channel flow

In this work *Nusselt correlations* are used for the calculation of the convective heat transfer coefficient in *forced pipe and channel flow* (as in Eq. 2.31).
Since the variable flow and fluid property conditions at pipe entrance region, as shown in Fig. 2.7, have significant influence *only* for high diameter to length ratios d/L it is convenient to use *mean* Nusselt number correlations that are valid for the entire pipe. This correlations are available in [43, 46] for a large number of technical relevant heat transfer problems. The symbol Nu, without subscript, indicates a *mean* Nusselt number. In tube flow heat transfer analysis usually a mean Reynolds number for *fully developed*

---

[4]The Darcy friction factor is used to describe surface roughness induced pressure losses in pipes, as described in section 2.2.2.
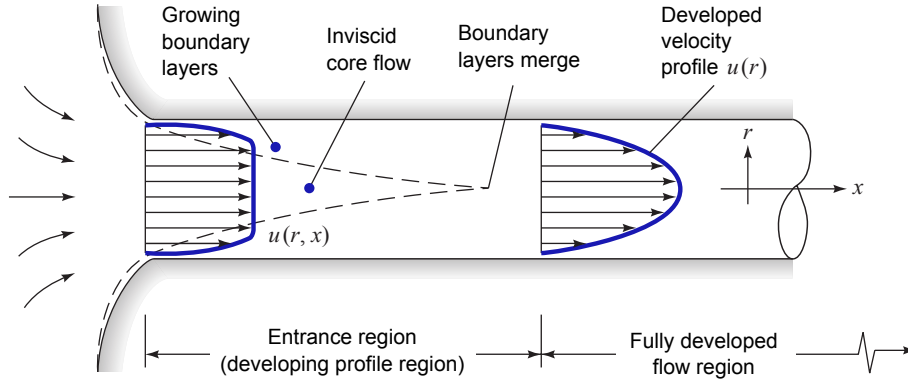
Figure 2.7.: Pipe flow velocity profile and boundary layer development [45]

flow is considered, therefore the subscript x is skipped and the hydraulic diameter is used as characteristic length for the heat transfer problem:

$$x = d_h.$$

Accordingly we may write for the mean Nusselt and Reynolds number in forced pipe or channel flow

$$Nu = \frac{h \, d_h}{k_f} \quad \text{and} \quad Re = \frac{v \, d_h}{\nu} \tag{2.34}$$

where h is the *mean* heat transfer coefficient and v is the mean fluid velocity. Most of the correlations are only valid in a certain Reynolds number range. Thus following cases need to be considered to cover the entire range of operation (also compare with Fig. 2.4):

$$Nu = \begin{cases} Nu_L & \text{for} & Re < 2300 & \text{laminar flow} \\ Nu_{tr} & \text{for} & 2300 \leq Re \leq 10000 & \text{transitional flow} \\ Nu_T & \text{for} & Re > 10000 & \text{turbulent flow.} \end{cases} \tag{2.35}$$

Nusselt correlation for laminar flow Nu_L

Under consideration of the *hydrodynamic* and *thermal entrance region*[5] a mean Nusselt correlation for laminar flow that is valid for all pipe diameter D and pipe length L ratios is given in [47, 46] as

$$Nu_L = \left\{ \underbrace{3.66^3 + 0.7^3}_{\text{Lower Asymptote}} + \underbrace{\left[1.615 \left(Re \, Pr \, \frac{d_h}{L} \right)^{\frac{1}{3}} - 0.7 \right]^3}_{\text{Low d/L ratio influenc}} + \right.$$

$$\left. + \underbrace{\left[\left(\frac{2}{1 + 22 \, Pr} \right)^{\frac{1}{6}} \left(Re \, Pr \frac{d_h}{L} \right)^{\frac{1}{2}} \right]^3}_{\text{Prandtl number influence}} \right\}^{\frac{1}{3}}. \tag{2.36}$$

---

[5]The region from the tube inlet to the point at which the boundary layer merges at the centerline is called the hydrodynamic entrance region and the region of flow over which the thermal boundary layer develops and reaches the tube center is called the thermal entrance region [40].

Nusselt correlations for turbulent flow Nu_T

Fully developed turbulent pipe flow can be assumed at Reynolds numbers $\geq$ 1e4. The following equation represents a general form of the well-known *Dittus Boelter* equation [48] that can be used for a broad range of convective heat transfer problems

$$Nu_T = a\ Re^b\ Pr^c \tag{2.37}$$

where a, b, c are tunable parameters that are usually fitted in least squares sense according to component data sheets or measurements. If no further information is given the coefficients proposed by Dittus and Boelter can be used:

$$a = 0.023; \qquad b = \frac{4}{5}; \qquad c = \begin{cases} 0.4 & \text{for heating of the fluid} \\ 0.3 & \text{for cooling of the fluid.} \end{cases} \tag{2.38}$$

Especially for flows in the lower turbulent area the *Gnielinski* [46, 49] equation may be used alternatively. It is defined as

$$Nu_T = \frac{(f/8)\ Re\ Pr}{1 + 12.7\ \sqrt{f/8}\ (Pr^{2/3} - 1)} \left[1 + \left(\frac{d_h}{L} \right)^{2/3} \right] \tag{2.39}$$

with a simplified Darcy friction factor f for smooth pipes, as presented by Konakov [50]

$$f = (1.8\ \log_{10}(Re)\ - 1.5)^{-2}\,. \tag{2.40}$$

The analytical derivation of the accurate friction factor f correlation for the full Reynolds number range is given in section 2.2.2.

Nusselt correlation for flow in the transitional area Nu_{tr}

For the transition area between laminar and turbulent flow ($2300 \leq \mathrm{Re} \leq$ 1e4) a linear interpolation between the correlations for turbulent and laminar flow is applied using an intermittency factor γ, as shown by Gnielinski in [49]

$$\gamma = \frac{Re - 2300}{1e4 - 2300} \quad \text{with} \quad 0 \leq \gamma \leq 1. \tag{2.41}$$

The intermittency factor together with the laminar and turbulent Nusselt numbers at their validity boundaries $Nu_{L,2300} = Nu_L(Re = 2300)$ and $Nu_{T,1e4} = Nu_L(Re = 1e4)$ are used to define the transitional Nusselt number as

$$Nu_{tr} = (1 - \gamma)Nu_{L,2300} + \gamma Nu_{T,1e4}. \tag{2.42}$$

With the equations 2.36 till 2.42 the convective heat transfer coefficient in forced channel flow for a broad range of applications is covered and heat flow from convection can be calculated. As shown in Fig. 2.8 the *full Reynolds number range* can be covered, including the case with stagnant fluid.
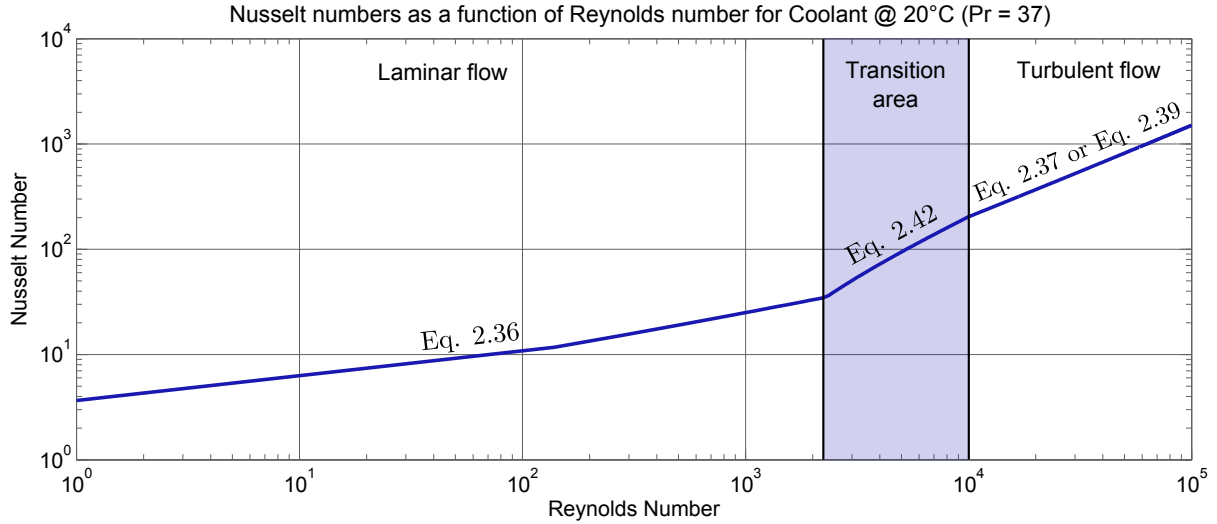
Figure 2.8.: Pipe and channel flow Nusselt numbers for the entire Reynolds number range

Nusselt correlation for heat exchangers with louvered fins

To describe the air side heat transfer for heat exchangers with a louvered fin geometry the Nusselt correlation found by Chang and Wang [51] is frequently used. This approach relies on the geometric details of the heat exchanger tubes, fins and louvers, as depicted in Fig. 2.9. It is given by

$$Nu = \frac{h_a\, l_p}{k_a} = j\, Re_{lp}\, Pr^{1/3} \tag{2.43}$$

with the Coleburn j factor defined as

$$j = Re_{lp}^{-0.49} \left(\frac{l_a}{90}\right)^{0.27} \left(\frac{f_p}{l_p}\right)^{-0.14} \left(\frac{f_h}{l_p}\right)^{-0.29} \left(\frac{f_d}{l_p}\right)^{-0.23} \left(\frac{l_l}{l_p}\right)^{0.68} \left(\frac{f_h + t_t}{l_p}\right)^{-0.28} \left(\frac{f_t}{l_p}\right)^{-0.05} \tag{2.44}$$

and with the local air velocity u_{lp} and the Reynolds number at the louvered pitch (Re_{lp}) given as

$$u_{lp} = \frac{\dot{m}_a}{\rho_a A_{ff}} \quad \text{and} \quad Re_{lp} = \frac{u_{lp}\, l_p}{\nu_a}, \tag{2.45}$$

where l_a is the louver angle, l_p is the louver pitch, f_p is the fin pitch, f_h is the fin height, f_d is the fin depth, f_t is the fin thickness, l_l is the louver length, t_t is the tube thickness, A_{ff} is the free flow area and ν_a and ρ_a are the kinematic viscosity and the density of the air.

27
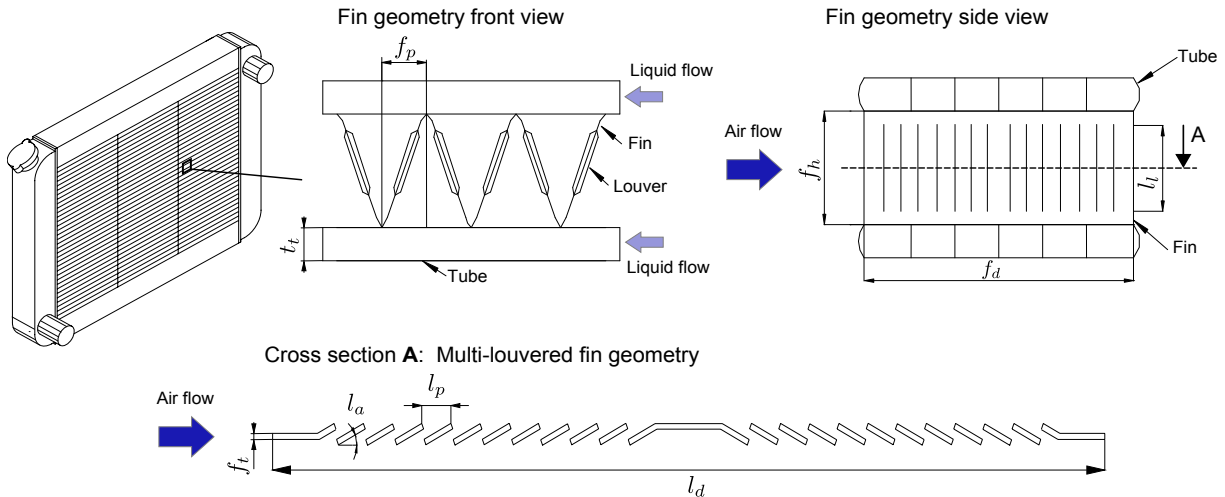
Figure 2.9.: Automotive louvered fin heat exchanger geometry details [52].

Mean temperature difference ΔT_m

For the calculation of the convective heat transfer in pipes two common boundary conditions must be considered;

- Constant surface heat flux: $\dot{q}_s = $ constant and
- Constant surface temperature: $T_s = $ constant.

In both cases Newtons law of cooling is used to calculate the heat flux which can be recalled as

$$\dot{Q} = h \, A \, \Delta T_m \tag{2.46}$$

where the average temperature difference between wall and fluid ΔT_m differers for the two cases.

Constant surface heat flux boundary condition:
In the case of a constant heat flux the fluid temperature increases *linearly* in the flow direction as shown on the left side of Fig. 2.10. Therefore under consideration of the rate of heat transfer equation

$$\dot{q}_s = h(T_s - T_f) \tag{2.47}$$

and the definition for the temperature difference

$$\Delta T_m = T_s - T_f \tag{2.48}$$

the mean temperature difference yields

$$\Delta T_m = \frac{\dot{q}_s}{h} \tag{2.49}$$

where T_s is the surface temperature, T_f is the *mean* fluid temperature and h is the heat transfer coefficient.

Constant surface temperature boundary condition:

Since the surface temperature is constant over the length of the pipe the fluid temperature change in flow direction must be considered by calculation of a mean temperature difference ΔT_m as shown on the right side of Fig. 2.10. With Newtons law of cooling and the energy balance on a differential control volume it can be shown that the mean temperature difference between the wall and the fluid can be described by

$$\Delta T_m = \Delta T_{ln} \equiv \frac{\Delta T_i - \Delta T_e}{ln\left(\frac{\Delta T_i}{\Delta T_e}\right)} \tag{2.50}$$

with

$$\Delta T_i = T_s - T_i \quad \text{and} \quad \Delta T_e = T_s - T_e$$

where T_i is the fluid temperature at pipe inlet and T_e is the fluid at pipe exit. ΔT_{ln} is the *logarithmic mean temperature difference* which sufficiently describes the mean temperature difference between the surface and the fluid.
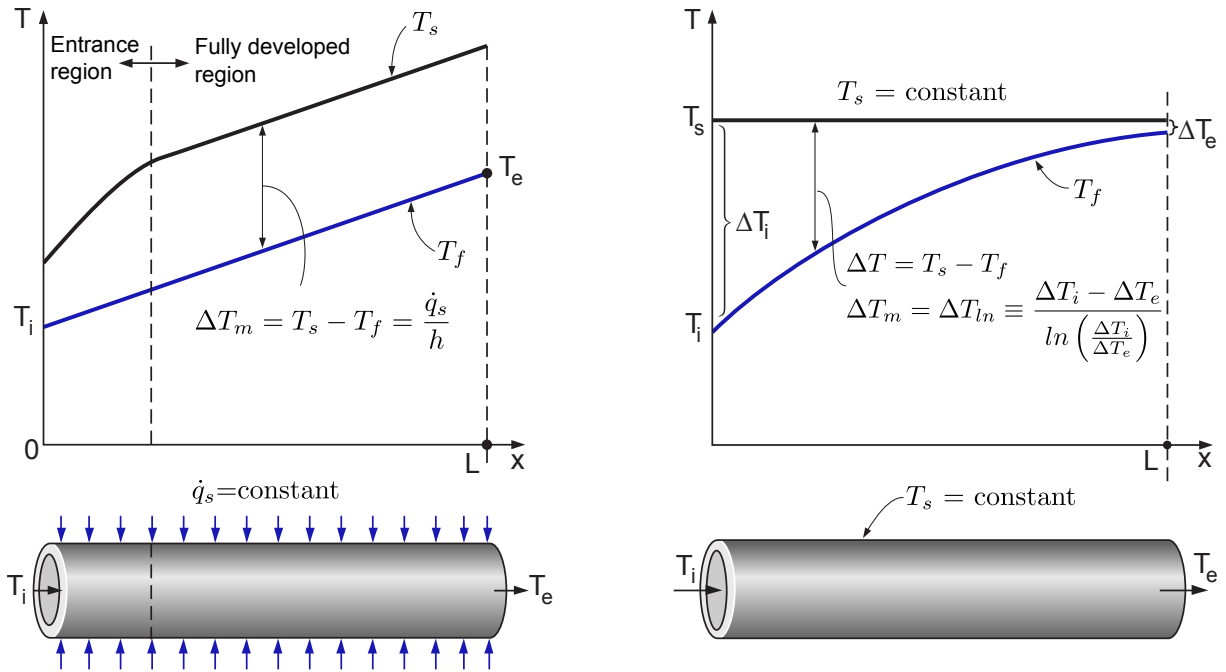
Figure 2.10.: Mean temperature difference for heat transfer calculation at constant rate of heat transfer (left) and constant wall temperature boundary condition (right) as in [40].

2.1.5. Thermal networks

Until now heat transfer phenomena have been considered isolated from each other. This is in general not the case. Often networks with multiple interlinked structures, that are subject to conductive and convective heat transfer, need to be analyzed. Therefor the thermal resistance concept or the electrical analogy is used to describe the heat transfer, as depicted in Fig. 2.11.

Figure 2.11.: Electrical and thermal resistance analogy [40]

The heat flow $\dot{Q}$ is analogous to the relation for current flow I. Thereby the temperature difference $T_1 - T_2$ across a thermal resistance R corresponds to a voltage difference across an electrical resistance R_e.

Newton's law of cooling (Eq. 2.26) and Fourier's law of heat conduction (Eq. 2.19) can be rearranged in thermal resistance form as

$$\dot{Q}_{conv} = \frac{\Delta T_m}{R_{conv}} \qquad \text{with} \qquad R_{conv} = \frac{1}{h\,A} \quad \text{and}$$
$$\dot{Q}_{cond} = \frac{T_1 - T_2}{R_{conv}} \qquad \text{with} \qquad R_{cond} = \frac{L}{k\,A}, \tag{2.51}$$

where R_{conv} and R_{cond} are the convection and conduction resistances, respectively. The electric analogy is also valid for configurations with multiple thermal resistances in *series* or *parallel*. In general, it can be stated that the rate of steady heat flux between two surfaces is equal to the temperature difference divided by the *total thermal resistance* between those surfaces. Exemplary, for a combined series and parallel thermal resistance network, as shown in Fig. 2.12, the total thermal resistance R_{tot} is calculated as

$$R_{tot} = \frac{R_1\,R_2}{R_1 + R_2} + R_3 + R_{conv} \tag{2.52}$$

where R_1, R_2 and R_3 are conduction resistances.

Figure 2.12.: Combined serial and parallel thermal resistances of a multi layer structure.

Two assumptions are commonly used in solving complex multidimensional heat transfer problems by treating them as one-dimensional:

(a) The temperature varies only in one direction (x-direction), and interfaces normal to this direction are *isothermal* (no temperature variations);

(b) Interfaces normal to direction of heat transfer (y-direction) are treated adiabatic.

It is often convenient to formulate the total heat transfer resistance analogous to Newtons law of cooling as

$$\dot{Q} = U A \, \Delta T \quad \text{with} \quad U A = \frac{1}{R_{total}} \tag{2.53}$$

where U is the *overall heat transfer coefficient* in $W/(m^2\,K)$.

Lumped System Analysis

During transient heat transfer, the temperature normally varies with time as well as position $(T = T(x, y, z, t))$. In a special case the temperature of the body changes uniformly with time. Here, the temperature (T) of the body stays uniform and can be expressed as function of time only $(T = T(t))$. Analysis of the heat transfer by utilization of this idealization is called *lumped systems analysis*. Considering a body of mass m (also called *lumped mass*) with a constant specific heat capacity c that is subject to heat transfer with its environment at temperature T_∞ with a constant heat transfer coefficient h, the energy balance can be expressed as

$$m \, c \frac{dT}{dt} = h \, A \, (T - T_\infty). \tag{2.54}$$

Separation of variables and integrating from time $t = 0$, where $T = T_i$ to any time t, at which $T = T(t)$ gives after rearranging

$$T(t) = T_\infty + (T_i - T_\infty) \, e^{-b\,t} \tag{2.55}$$

where

$$b = \frac{h \, A}{m \, c} \quad \text{in} \quad \frac{1}{s}. \tag{2.56}$$

The reciprocal of this term $(1/b)$ is called *time constant*. From the time constant we can determine the duration the body takes to reach the ambient temperature and that it reaches the ambient temperature exponentially with time. In general, the higher the time constant the longer it takes to reach the ambient temperature.

Biot Number Bi

Lumped system analysis is a highly convenient approach for transient thermal network and heat transfer analysis. The *Biot number* is a criterion that can be used to determine if it is appropriate to make such simplifications or not. It is defined as

$$Bi = \frac{hL_c}{k} \tag{2.57}$$

where L_c it the characteristic length which is defined as

$$L_c = \frac{V}{A}, \tag{2.58}$$

where V is the volume of the body, A is the surface area of the body and k is the thermal conductivity of the solid. Alternatively it can be expressed as:

$$Bi = \frac{\text{Convection at the surface}}{\text{Conduction inside the body}} = \frac{h \, A \, \Delta T}{(k/L_c) \, A \, \Delta T} = \frac{h \, L_c}{k}, \tag{2.59}$$

or by utilization of the thermal resistance analogy the Biot number yields

$$Bi = \frac{\text{Conduction resistance within the body}}{\text{Convection resistance at the surface}} = \frac{\dfrac{L_c}{A \, k}}{\dfrac{1}{h \, A}} = \frac{h \, L_c}{k}. \tag{2.60}$$

The Biot number and time dependency of a temperature profile within a solid wall, which is exposed to convective heat transfer, is depicted in Fig. 2.13. Consequently, it can be stated that for a small Biot number Bi the temperature gradient within the wall is very small. Therefore it can be treated as *lumped mass* and *lumped system analysis* is applicable. With an increasing Biot number (lower convection resistance in this case) the temperature profile shows a large variation in x direction $T = T(x,t)$. The lumped mass simplification is not applicable for this cases.
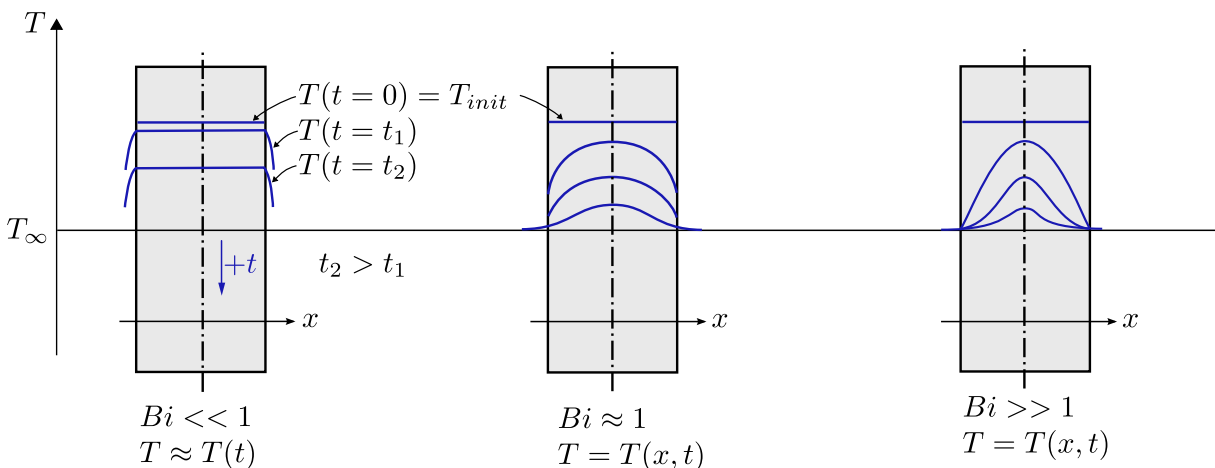
Figure 2.13.: Temperature profile within a solid wall cooled by convection at different times dependent on the *Biot number* [53].

2.2. Fluid mechanics

2.2.1. Mass, momentum and energy conservation

In mechanics and thermodynamics all the fundamental laws for the conservation of mass, energy and momentum are stated for a *system* which has an arbitrary quantity of mass of fixed identity. Conversely, in fluid mechanics this fundamental laws are translated into a *control volume* form. The conversion law is called *Reynolds transport theorem* [54] and it can be applied to all basic laws of thermodynamics and mechanics.

Mass conservation:

Application of the Reynolds transport theorem to the fundamental law of mass conservation in a control volume (CV) with a number of one dimensional in- and outlets i, as shown in [45], yields:

$$\int_{CV} \frac{\partial \rho}{\partial t} dv + \sum_i (\rho_i \, A_i \, v_i)_{out} - \sum_i (\rho_i \, A_i \, v_i)_{in} = 0 \tag{2.61}$$

where ρ is the density, A is the flow area and v is the mean flow velocity at in- or outlet. Under the assumption of *steady flow* the expression $\frac{\partial \rho}{\partial t} = 0$ and Eq. 2.61 simplifies to

$$\sum_i (\rho_i \, A_i \, v_i)_{out} = \sum_i (\rho_i \, A_i \, v_i)_{in}. \tag{2.62}$$

Expressed in terms of volume flow $\dot{V}$ or mass flow $\dot{m}$ the above equation yields

$$\sum_i (\dot{V}_i \, \rho_i)_{out} = \sum_i (\dot{V}_i \, \rho_i)_{in} \tag{2.63}$$

or

$$\sum_i (\dot{m}_i)_{out} = \sum_i (\dot{m}_i)_{in} \tag{2.64}$$

which are widely used formulations in engineering problems.

Momentum conservation:

According to [45] the application of the Reynolds transport theorem to Newton's second law under the assumption of following simplifications

- *One dimensional in- and outlets:* uniform flow and density over the area;
- *Steady flow:* no variation of momentum over time;

reduces the momentum equation for a control volume to

$$\sum F = \sum (\dot{m}_i \, v_i)_{out} - \sum (\dot{m}_i \, v_i)_{in} \tag{2.65}$$

where $\sum F$ is the resulting force from the vector sum of outlet momentum fluxes minus the vector sum of inlet fluxes.

Energy conservation:

The form of the energy equation that can be used for a large variety of internal flow problems can be derived by application of the *Reynolds transport theorem* to the *first law of thermodynamics.*

The energy equation for *incompressible*, *steady flow* in a pipe or duct with one inlet and one outlet under consideration of *friction* and *shaft work*, as derived in [45], yields

$$
\left(\underbrace{\underbrace{\frac{p}{\rho\,g}}_{\text{Pressure head}} + \underbrace{z}_{\text{Elevation head}}}_{\text{Static head}} + \underbrace{\frac{v^2}{2\,g}}_{\text{Velocity head}} \right)_{in} + h_p = \left(\frac{p}{\rho\,g} + z + \frac{v^2}{2\,g} \right)_{out} + h_f + h_t \quad (2.66)
$$

where

p	is the pressure in Pa,
v	is the flow velocity in m/s,
ρ	is the density of the fluid in kg/m^3,
z	is the elevation in m,
g	is the acceleration due to gravity m/s^2,
h_f	is the friction head loss in m,
h_p	is the pump head in m,
h_t	is the turbine head loss in m.

All elements in the equation are either a length or a *head*. *Head* is used in fluid mechanics to express the internal energy of a fluid due to pressure. *Pressure head* together with *elevation head* it is called *static head.* The energy due to fluid bulk motion is called *velocity head.*

The friction loss h_f is always positive in real (viscous) flows, a pump adds energy h_p (increases the left-hand side), and a turbine h_t extracts energy from the flow. Losses from friction and fittings have to be correlated with the head from pump and turbine which is treated in section 3.2.2.

Alternatively, the energy equation can be written in pressure notation by simply multiplying Eq. 2.66 with density ρ and acceleration due to gravity g which leads to

$$
\left(\underbrace{\underbrace{p + \rho\,g\,z}_{\text{Static pressure}} + \underbrace{\frac{\rho}{2}\,v^2}_{\text{Velocity pressure}}}_{\text{Total pressure}} \right)_{in} + \Delta p_p = \left(p + \rho\,g\,z + \frac{\rho}{2}\,v^2 \right)_{out} + \Delta p_f + \Delta p_t. \quad (2.67)
$$

Now all elements in the equation represent pressures or pressure differences where

Δp_p	is the pressure difference due to pump or fan in Pa,
Δp_f	is the pressure difference due to friction losses in Pa,
Δp_t	is the pressure difference due to turbine shaft work in Pa.

By using the energy equation one always has to be aware of the restrictive assumptions that were used to derive it [45]:

1. *Steady flow:* With this common simplification non gravitational accelerative effects that are acting on the fluid are neglected $\dfrac{\partial v}{\partial t} = 0$;

2. *Incompressible flow:* The density of liquids is nearly constant, therefore they can be treated analytically as incompressible. Also gas flows can be treated as if they were incompressible, particularly if the gas velocity is less than about 30 percent of the speed of sound ($\approx 370\ km/h$ for air at 20 °C).

2.2.2. Friction losses for viscous flow in ducts

Correlations for the friction head losses h_f, mentioned in course of the energy equation, shall be derived in this subsection. In general it is distinguish between two different loss types can be distinguished:

- **Wall friction losses**: Losses due to shear forces acting on the pipe walls,
- **Minor losses**: Losses due to fittings, bends and changes in pipe diameter.

Wall friction losses

Wall friction losses shall now be described with a classic fluid flow example in a pipe as shown in Fig. 2.14. Considering constant fluid properties (adiabatic pipe) the continuity equation 2.61 simplifies to

$$\dot{V}_1 = \dot{V}_2 = \text{const}$$
$$\text{or} \qquad v_1 = \frac{\dot{V}_1}{A_1} = v_2 = \frac{\dot{V}_2}{A_2}, \tag{2.68}$$

because the pipe has a constant diameter. In the absence of any shaft work and heat transfer effects, the energy equation 2.66 simplifies to a simple expression for the friction-head loss h_f given as

$$h_f = \left(z_1 + \frac{p_1}{\rho\ g} \right) - \left(z_2 + \frac{p_2}{\rho\ g} \right). \tag{2.69}$$

Thus the pipe head loss equals the change in sum of pressure Δp and elevation head Δz (static head) as

$$h_f = \Delta z + \frac{\Delta p}{\rho\ g}. \tag{2.70}$$
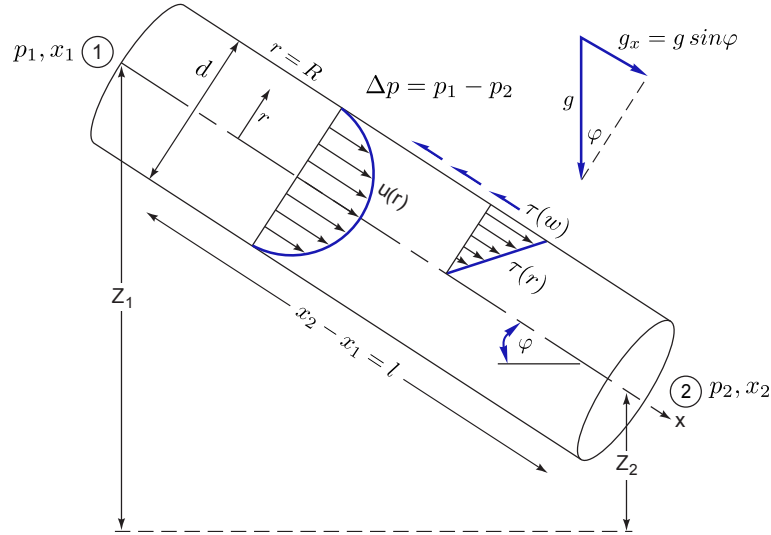
Figure 2.14.: Control volume of steady, fully developed flow between two sections in an inclined pipe [45].

Applying the momentum relation to the control volume in Fig. 2.14 accounts for applied forces due to pressure, gravity and shear yields

$$\underbrace{\Delta p \; R^2 \; \pi}_{\text{Pressure Force}} + \underbrace{\rho \; g \; \pi \; R^2 \; l \; sin(\varphi)}_{\text{Gravity Force}} - \underbrace{\tau_w \; 2 \; \pi \; R \; l}_{\text{Shear Force}} = 0 = \sum F = \dot{m}(v_2 - v_1). \tag{2.71}$$

Expressing h_f from Eq. 2.69 and combining with Eq. 2.71, where we used $\Delta z = l \; sin(\varphi)$, gives for the friction-head loss

$$h_f = \Delta z + \frac{\Delta p}{\rho \; g} = \frac{2 \; \tau_w \; l}{\rho \; g \; R}. \tag{2.72}$$

This equation correlates the head loss and shear forces. The missing part is the correlation to flow conditions which can be established by dimensional analysis based on the functional relation for the wall shear stress that can be assumed as the function

$$\tau_w = F(\rho, \; v, \; \mu, \; R, \; \epsilon) \tag{2.73}$$

where ϵ is the wall-roughness height. From dimensional analysis the dimensionless parameter f, called *Darcy friction factor* was derived by Henry Darcy as

$$\frac{8 \; \tau_w}{\rho \; v^2} = f = F \left(Re, \frac{\epsilon}{d} \right). \tag{2.74}$$

Expressing τ_w from Eq. 2.74 and combining with Eq. 2.72 leads to the well known *Darcy-Weisbach equation* which allows to correlate the effect of pipe roughness and length for flows through ducts of any cross section and for turbulent as well as laminar flow as

$$h_f = f \; \frac{l}{d} \frac{v^2}{2 \; g} \quad . \tag{2.75}$$

Note that R was replaced by $d/2$.
The only missing part is to find a Darcy friction factor function of the form $F(Re, \epsilon/d)$.

Laminar pipe flow

For laminar duct flow the Darcy friction factor function was derived analytically by *Hagen and Poisseuille* as

$$f_L = \frac{64}{Re}. \tag{2.76}$$

Combination of equation 2.75 and 2.76 with $v = 4\dot{V}/(d^2\,\pi)$ and $Re = (v\,d\,\rho)/\mu$ gives

$$h_{f,lam} = \frac{128\,\mu\,l\,\dot{V}}{\pi\,\rho\,g\,d^4}. \tag{2.77}$$

Equation 2.77 indicates that the laminar head loss is proportional to the volume flow $\dot{V}$ but correlates with the *fourth power* of the tube diameter. Hence, halve diameter means a 16 times higher friction head loss.

Transitional and turbulent pipe flow

For transitional and turbulent flow the friction factor relation is much more complex due to the degree of turbulence and the thickness of the boundary layer. That is why it has been determined by experiment.

Colebrook developed an empirical interpolation formula that combines friction factor correlations for hydraulically smooth and rough pipes into one equation (frequently called *Colebrook* or *Colebrook–White* equation):

$$\frac{1}{\sqrt{f_T}} = -2\log_{10}\left(\frac{\frac{\epsilon}{d}}{3.7} + \frac{2.51}{Re\,\sqrt{f_T}}\right). \tag{2.78}$$

This phenomenological equation expresses the Darcy friction factor f_T as a function of Reynolds number Re and pipe relative roughness ϵ/d. For turbulent pipe flow friction Eq. 2.78 represents the broadly accepted design formula. It can be used to (iteratively) solve for the Darcy–Weisbach friction factor f_T. The Colebrook equation was first plotted by Moody [55], therefore the chart in Fig. 2.15 is called *Moody chart*. Solving equation 2.78 for the friction factor f in turbulent flow usually requires using the moody chart or several iterative calculation steps. Alternatively, simplified and less accurate formulations, as shown in [56, 57, 58], can be used to explicitly solve for f_T.

A robust, fast, and accurate method for solving the Colebrook-like equations is presented in [59]. The computations are not more demanding than simplified approximations, but they are much more accurate. Therefore this solution approach will be used in this work.

Since the friction factor for the critical and transition zone is not defined, an intermittency factor γ is used to interpolate between the laminar and turbulent friction factor at the respective boundaries. Under the assumption that laminar flow exists up to a Reynolds number $Re = 2300$ and that the complete turbulent flow exists from $Re = 1e4$ we can define the intermittency factor γ as

$$\gamma = \frac{Re - 2300}{1e4 - 2300} \quad \text{where} \quad 0 \le \gamma \le 1. \tag{2.79}$$

The intermittency factor together with the laminar and turbulent friction factors at their validity boundaries $f_{L,2300} = f_L(Re = 2300)$ and $f_{T,1e4} = f_L(Re = 1e4)$ are used to define the transitional friction factor as

$$f_{tr} = (1 - \gamma) f_{L,2300} + \gamma f_{T,1e4}. \tag{2.80}$$

Finally, we may give the Darcy friction factor f for the full Reynolds number range, for smooth and rough pipes with any length and diameter combination as

$$f = \begin{cases} f_L & Re \leq 2300 \\ f_{tr} & 2300 < Re < 1e4 \\ f_T & Re \geq 1e4 \end{cases} . \tag{2.81}$$

With $\Delta p = \rho \, g \, h_f$ the Darcy-Weisbach equation (Eq. 2.75) expressed in terms of pressure drop yields

$$\Delta p = f \, \frac{\rho \, l \, v^2}{2 \, d} \quad \text{and with} \quad v = \frac{4 \, \dot{m}}{\rho \, d^2 \, \pi} \quad \text{we get} \quad \Delta p = f \, \frac{8 \, l}{d^5 \, \pi^2 \, \rho} \dot{m}^2. \tag{2.82}$$
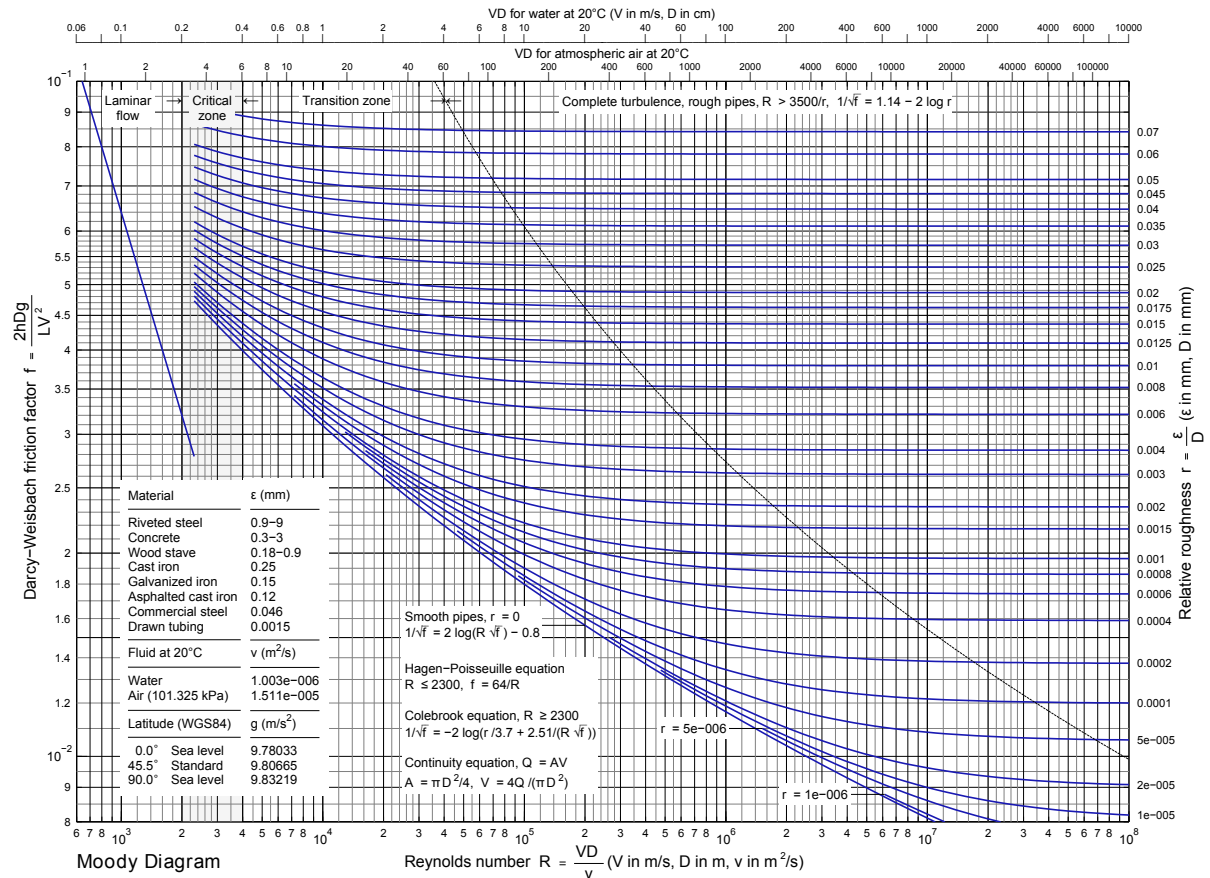

Figure 2.15.: Moody chart for the determination of the pipe friction factor f for pipes with smooth and rough walls [60].

Minor Losses

In addition to the losses that occur as a result of the pipe geometry and surface roughness (Moody type losses), additional so-called *minor losses* may occur due to:

1. Sudden expansion and contraction;
2. Gradual expansion and contraction;
3. Bends, elbows, tees and other fittings;
4. Valves from open to fully closed.

Despite the name, *minor losses* can have a much greater influence on the overall head loss than due to pipe friction (e.g. a closed valve). Because of the complicated flow patterns that occur the theory for flow resistance calculation in minor losses is weak. The losses are typically measured experimentally and correlated with flow parameters. Measures for the minor losses are usually given as a ratio of head loss $h_m = \Delta p/(\rho\,g)$ to velocity head $v^2/(2\,g)$ as

$$\zeta = \frac{h_m}{v^2/(2\,g)} = \frac{\Delta p}{\frac{1}{2}\rho\,v^2} \tag{2.83}$$

where ζ is the dimensionless *pressure loss coefficient*. Dimensionless pressure loss coefficients, derived from experiment, for a great variety of technical relevant problems can be found in [56] and [57].

Minor losses in series: In a common pipe system multiple minor losses may occur. If all are correlated to the same fluid velocity, and thus to the same pipe diameter, the total loss yields the sum of the minor losses h_m plus the friction loss h_f

$$h_{tot} = h_f + \sum h_m = \frac{v^2}{2\,g}\left(\frac{f\,l}{d} + \sum\zeta\right). \tag{2.84}$$

For convenience the losses are often expressed as pressure differences Δp which correlate to the head loss h with

$$\Delta p = \rho\,g\,h \tag{2.85}$$

where ρ is the fluid density and g is the acceleration due to gravity. From the friction head loss correlation (Eq. 2.75) and the minor head loss calculation approach (Eq. 2.83) we have seen that the head, respectively pressure loss in the turbulent flow regime scales quadratically with the flow speed v. Therefore, pressure differences measurements are frequently approximated with a second order polynomial as

$$\Delta p = a_2\,v^2 + a_1\,v + a_0 \tag{2.86}$$

or under consideration of the density ρ as a function of the fluid mass flow $\dot{m} = v\,A\,\rho$

$$\Delta p = a_2\,\dot{m}^2 + a_1\,\dot{m} + a_0 \tag{2.87}$$

or in vector notation

$$\Delta p = \mathbf{K}\,\dot{\mathbf{m}}^2 \quad \text{with} \quad \dot{\mathbf{m}}^2 = \dot{m}^{[2\ 1\ 0]^T} = \begin{bmatrix} \dot{m}^2 \\ \dot{m}^1 \\ \dot{m}^0 \end{bmatrix} \quad \text{and} \quad \mathbf{K} = [a_2\ a_1\ a_0] \tag{2.88}$$

where the coefficients a_2, a_1 and a_0 are derived from fitting the measurement data in a least squares sense. K is the pressure coefficient that contains all information about the diameter, length, pipe roughness and minor losses. **K** is the related pressure coefficient vector.

Note that for describing minor losses a sole quadratic correlation of the form

$$\Delta p = K \, \dot{m}^2 \tag{2.89}$$

is sufficient, with

$$K = \frac{1}{2} \frac{\zeta}{A^2 \, \rho}. \tag{2.90}$$

2.2.3. Pressure sources

Within piped fluid networks there are three kinds of pressure or head sources:

1. Static head from elevation,
2. Velocity head,
3. Head h_p from turbo machinery e.g.: pump or fan.

Handling of the first two pressure sources was already discussed in course of the energy equation (Eq. 2.66). The missing part is the variable head increase by turbo machinery. Regardless of the fact that the theory for analytical performance description of turbo machinery is quite strong, this section will only focus on *similarity laws* that allow a comfortable representation of existing pump or fan curve measurements.

As shown in [61] the performance of a pump can be expressed in terms of flow variables, geometric variables and fluid properties. For the hydraulic pump it is convenient to regard the net energy transfer $g\,h$ and power supplied P, as dependent variables and to write the two functional relationships as

$$g\,h_p = f_1(\dot{V}, n, D, \rho, \mu, \epsilon), \tag{2.91a}$$
$$P = f_2(\dot{V}, n, D, \rho, \mu, \epsilon). \tag{2.91b}$$

From dimensional analysis the following dimensionless groups can be identified

$$\text{Head coefficient} \qquad \Psi = \frac{g\,h_p}{n^2\,D^2} \;= f_3\left(\frac{\dot{V}}{n\,D^3}, \frac{\rho\,n\,D^2}{\mu}, \frac{\epsilon}{D}\right), \tag{2.92a}$$

$$\text{Power coefficient} \qquad \hat{P} = \frac{P}{\rho\,n^3\,D^5} = f_4\left(\frac{\dot{V}}{n\,D^3}, \frac{\rho\,n\,D^2}{\mu}, \frac{\epsilon}{D}\right), \tag{2.92b}$$

where the group

$$\phi = \frac{\dot{V}}{n\,D^3} \tag{2.93}$$

is called volumetric flow coefficient ϕ. The group $\dfrac{\rho\,n\,D^2}{\mu}$ is a form of the Reynolds number and ϵ/D is called roughness ratio. At high Reynolds number operating conditions of

turbo machinery the influence of the surface roughness and the Reynolds number on the performance are expected to have a constant effect on similar pumps, therefore they are neglected. With this simplifications the functional relationships for geometrically similar hydraulic turbo machines reduces to,

$$\Psi = f_3 \left(\frac{\dot{V}}{n\, D^3} \right) \quad \Rightarrow \quad \Psi = \Psi(\phi), \tag{2.94a}$$

$$\hat{P} = f_4 \left(\frac{\dot{V}}{n\, D^3} \right) \quad \Rightarrow \quad \hat{P} = \hat{P}(\phi). \tag{2.94b}$$

This allows us to express the head coefficient Ψ and the power coefficient $\hat{P}$ as a function of the flow coefficient ϕ. The actual form of the functions f_3 and f_4 must be found by experiment. Non-dimensional representation of performance data has the important practical advantage of generating only a single curve as results that would otherwise require a multiplicity of curves if plotted dimensionally, as shown in Fig. 2.16 and Fig. 2.17. The non-dimensional results shown in Fig. 2.16 have been obtained for a particular pump. They would also be approximately valid for a range of different pump sizes so long as all these pumps are geometrically similar and cavitation is absent. The dynamically similar results can be applied to predict the dimensional performance of a given pump for a series of required speeds.

From Fig. 2.16 we see that the missing function $f_3 = \Psi(\phi)$ can be adequately approximated with a second order polynomial. The recalculated pump performance at different pump speeds (indicated with suffix rc in Fig. 2.17) is showing good overall accordance with the measurement data.
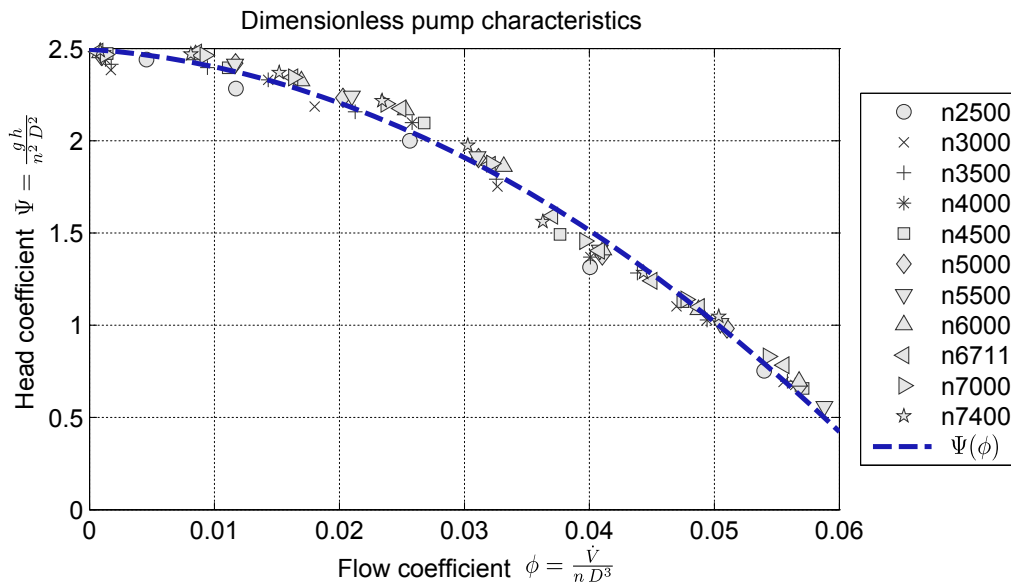
Figure 2.16.: Dimensionless head vs. flow coefficient for an automotive centrifugal pump.
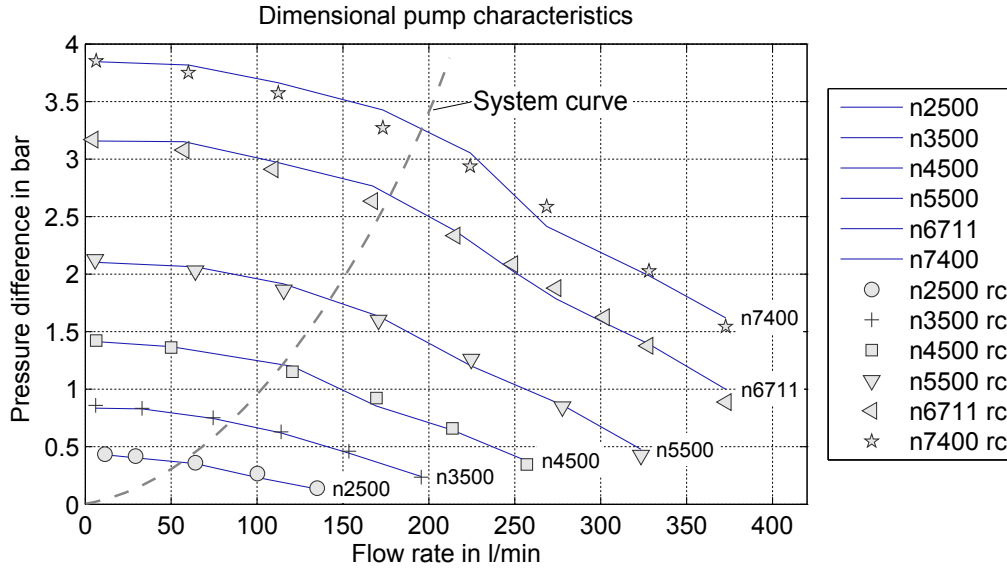
Figure 2.17.: Dimensional pump characteristics for an automotive centrifugal pump. The solid line represents measurement data and the markers represent the recalculation from function $f_3 = \Psi(\phi)$, as shown in Fig. 2.16.

Note that we can rearrange the presented similarity correlation to fit the general pressure difference form $\Delta p = \mathbf{K}\,\dot{\mathbf{m}}^2$ of Eq. 2.88. Starting with the function

$$\frac{g\,h}{n^2\,D^2} = f\left(\frac{\dot{V}}{n\,D^3}\right) = f_2\left(\frac{\dot{V}}{n\,D^3}\right)^2 + f_1\left(\frac{\dot{V}}{n\,D^3}\right) + f_0 \tag{2.95}$$

multiplication with ρ and $(n^2\,D^2)$ gives for the left hand side of the equation $\Delta p = \rho\,g\,h$ and replacing $\dot{V}$ with $\dot{m}/\rho$ on the right hand side yields

$$\Delta p = f_2\,\rho\,n^2\,D^2\left(\frac{1}{n\,D^3\,\rho}\right)^2 \dot{m}^2 + f_1\,\rho\,n^2\,D^2\left(\frac{1}{n\,D^3\,\rho}\right)\dot{m} + f_0\,\rho\,n^2\,D^2. \tag{2.96}$$

From Eq. 2.96 we can derive the pressure coefficient vector $\mathbf{K}$ according to the dimensionless pump law as

$$\mathbf{K} = [a_2 \mid a_1 \mid a_0] = \left[\; f_2\rho\,n^2\,D^2\left(\tfrac{1}{n\,D^3\,\rho}\right)^2 \mid f_1\rho\,n^2\,D^2\left(\tfrac{1}{n\,D^3\,\rho}\right)^2 \mid f_0\rho n^2\,D^2 \;\right]. \tag{2.97}$$

The power consumption for a pressure source with power coefficient polynomial $\hat{P}(\phi)$ for any given speed can be calculated by rearranging Eq. 2.94 and Eq. 2.92 towards

$$\hat{P} = \frac{P}{\rho\,n^3\,D^5} = p_3\left(\frac{\dot{V}}{n\,D^3}\right)^3 + p_2\left(\frac{\dot{V}}{n\,D^3}\right)^2 + p_1\left(\frac{\dot{V}}{n\,D^3}\right) + p_0,$$

$$P = p_3\,\rho\,n^3\,D^5\left(\frac{1}{n\,D^3\,\rho}\right)^3 \dot{m}^3 + p_2\,\rho\,n^3\,D^5\left(\frac{1}{n\,D^3\,\rho}\right)^2 \dot{m}^2 + p_1\,\rho\,n^3\,D^5\left(\frac{1}{n\,D^3\,\rho}\right)\dot{m} +$$

$$+ p_0\,\rho\,n^3\,D^5 \tag{2.98}$$

where the coefficients p_3, p_2, p_1 and p_0 are coefficients of a third order polynomial that can be fitted from the dimensionless power coefficient $(\hat{P})$, which is a function of the flow coefficient $(\hat{P} = \hat{P}(\phi))$.

2.2.4. Fluid network hydraulics

In the fluid network hydraulics analysis all previously separately described parts come together in one interconnected network. A typical fluid network consists of multiple pipes, nodes, fittings, minor losses and pressure sources. The task of the flow network analysis is to solve the fluid network in terms of energy, momentum and mass conservation in order to derive the pressure distribution in the network together with the fluid flow in each branch of the network.

Simple networks

Simple pipe networks may only consist of a couple of flow resistances in series or parallel. Under the assumption of steady, one dimensional and incompressible flow simple networks can be solved by applying the mass conservation law to the network nodes and the energy conservation law (see Eq. 2.67) to the network branches.

For pipes in series, as shown exemplary in Fig. 2.18, we can write for the mass conservation at node A

$$\dot{m}_A = \dot{m}_B = \dot{m}_1 = \dot{m}_2 = \dot{m}_3$$

and for the energy equation

$$p_A - p_B = \Delta p_1 + \Delta p_2 + \Delta p_3$$

where p_A and p_B are the total pressures at location A and B, respectively. With the individual pressure differences given by $\Delta p = K \, \dot{m}^2$ as in Eq. 2.89 the total pressure difference Δp_{tot} yields:

$$\Delta p_{tot} = \sum_{n=1}^{3} K_n \, \dot{m}^2 \tag{2.99}$$

where K_n are the flow resistance coefficients as shown in Eq. 2.90.

For the flow network with *parallel branches*, as shown on the right hand side of Fig. 2.18, we can write for the mass conservation at the nodes A and B (under the assumption of steady incompressible flow):

$$\dot{m}_A = \dot{m}_B = \dot{m}_1 + \dot{m}_2 + \dot{m}_3 \tag{2.100}$$

and for the pressure difference Δp_{tot} between entrance A and exit B

$$\Delta p_{tot} = \Delta p_1 = \Delta p_2 = \Delta p_3. \tag{2.101}$$

With $\dot{m} = \sqrt{\frac{\Delta p}{K}}$ equation 2.100 yields

$$\left(\frac{1}{K_{tot}}\right)^{1/2} = \left(\frac{1}{K_1}\right)^{1/2} + \left(\frac{1}{K_2}\right)^{1/2} + \left(\frac{1}{K_3}\right)^{1/2} = \sum_{n=1}^{3} \left(\frac{1}{K_n}\right)^{1/2} \tag{2.102}$$

where K_{tot} is the overall pressure coefficient for the hydraulic network. With K_{tot} we can write for the total network pressure drop

$$\Delta p_{tot} = K_{tot}\,\dot{m}_{tot}^2.$$

The presented approach for the solution of simple flow networks will be used for the description of the air flow through the vehicle cooling package and underhood.
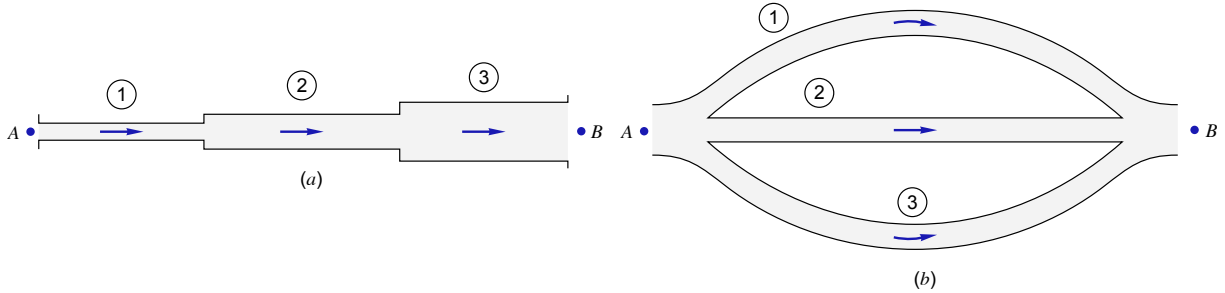

Figure 2.18.: Simple pipe network with flow resistance is series and parallel.

Complex networks

Conservation of mass at network nodes for parallel pipes and conservation of energy can be extend towards a general formulation for networks in steady state condition. The resulting set of equations can be solved for pipe flows and pressures at the nodes in steady state or in quasi dynamic (from one steady state condition to the other) manner.

For the description of the flow network, equations for mass conservation and energy conservation are reformulated for an efficient handling of multiple nodes and pipes.

Conservation of mass: The energy conservation equation for junctions of two or more pipes, called *nodes*, can be given as

$$\sum_{l \in J_{in}} \dot{m}_l - \sum_{l \in J_{out}} \dot{m}_l = q_i \tag{2.103}$$

where q_i is flow leaving or entering the system at the node i, J_{in} and J_{out} are the set of pipes that are supplying and removing flow from node, respectively, and $l \in J_{in}$ indicates that l is in the set of pipes in J_{in}. This equation can be applied to any node of a given flow network.

Conservation of energy: The conservation of energy must be conserved between any two points in the network. For a branch with equal inlet and outlet pipe diameter that connects two points and contains only one pressure loss component (e.g. pipe friction or minor loss) the energy conservation equation Eq. 2.67 simplifies to

$$p_A - p_B = \Delta p_f \quad \text{with} \quad \Delta p_f = K_l \lfloor \dot{m}_l \rfloor^n \quad \text{and} \quad \lfloor \dot{m}_l \rfloor^n \equiv |\dot{m}|^n \, \mathrm{sgn}(\dot{m}) \tag{2.104}$$

where $\lfloor \dot{m}_l \rfloor^2$ is a short form notation which states that the *absolute value* of the mass flow for component l raised to the power of n and that the *sign* of the term is based on the flow direction. Similar can be done in vector notation, as in Eq. 2.88:

$$p_A - p_B = \mathbf{K} \lfloor \dot{\mathbf{m}}_l \rfloor^n \qquad \text{with} \qquad \lfloor \dot{\mathbf{m}}_l \rfloor^n \equiv |\dot{m}_l|^{[n \ \ n\text{-}1 \ \ n\text{-}2]^T} \, \mathrm{sgn}(\dot{m}_l). \tag{2.105}$$

Solution of the equation system

The unknowns in a hydraulic network are the flows $\dot{m}$ for each component and the pressure p at the nodes. Thus, in a system with *nnode* (number of nodes) and *ncomp* (number of components), the total number of unknowns is *nnode + ncomp.* All sets of equations are *nonlinear* due to the nonlinear energy loss relation ship and need an iterative solution. The Newton-Raphson approach is the most widely used method for the iterative solution of flow networks. In principal four different solution approaches exist to solve the network for the unknowns:

(a) **Loop Equations:** This approach uses the smallest set of equations - the loop equations. This method first determines mass flow corrections for each loop independently until mass conservation is ensured then applies the corrections to compute the new pipe flows. With the new flow distribution, another set of corrections is computed.
This approach is also known as the Hard Cross method [62]. It is less efficient than algorithms that consider the entire system simultaneously. Also the definition of loops is required which can be time consuming.

(b) **Node loop Equations:** Wood and Rayes used a Newton's type method to solve directly for the pipe flow rates rather than the loop equation approach that solves for loop flow corrections. It is more efficient than the loop equation approach but still requires the loop definitions.

(c) **Node Equations:** It is possible to substitute each in and outgoing branch flow rate of the system nodes with the transformed energy equation expression

$$\dot{m}_l = \left(\frac{\lfloor p_A - p_B \rfloor}{K_l} \right)^{1/n} .$$

This combines the mass conservation equation with the energy equation. Shamir and Howard solved these equations using the Newton-Raphson method.

(d) **Pipe Equations:** The previous methods solve for the pipe flows, $\dot{m}$, or nodal pressures, p, in a nonlinear solution scheme. Then the energy conservation law is applied to determine the other set of unknowns. Haman and Brameller (1972) and Todini and Pilati (1988) [63] developed a method to solve for $\dot{m}$ and p *simultaneously.* They used the node equations (Eq. 2.103) with respect to the pipe flows and the pipe equation (Eq. 2.104) for each pipe including both the pipe flows and the nodal heads. Although the number of equations (nnode + npipe) is larger than for other methods, the solution times and the convergence are similar or better. Additionally, the algorithm does not require the definition of loops.

For the present work the author chose the pipe equations approach from Todini and Pilati because of it's good convergence and convenience in terms of network definition and equation formulation.

<div style="text-align: right; font-size: 4em;">3</div>

Thermo-Fluid Library

This chapter describes a toolbox for modeling and simulation of liquid cooling systems and thermal networks within vehicles. First the toolbox requirements regarding simulation modeling and control development purposes are discussed. Then the concept for solving thermo fluid networks is presented. Afterwards the hydraulic network solver and the thermo solver equations are discussed in detail. Further explanations are given based on a demonstration example. Finally the chosen modeling approach and the equations used within the Simulink library components are given.

3.1. Requirements and methodology

Besides the new requirements and challenges outlined in section 1.3.2, the following key requirement for the toolbox in terms of *simulation modeling* can be identified:

1. **Genericity**: Thermal system architecture, arrangement of components and components itself may vary a lot during the development process, therefore flexibility and modularity of the tool is required. It should be flexible enough to simulate any given vehicle and powertrain configuration.

2. **Physical based:** Thermo-fluid systems are inherently non-linear due to the fact that heat transfer and pressure drop show a nonlinear characteristics. A physically based modeling approach allows to describe the system with good accuracy before it is build. This model can predict the impact of design changes, so controller design and model identification can be done *offline* with a minimum amount of hardware tests required (sometimes called *front-loading*).

3. **User-friendliness:** A large amount of information is required to describe the thermo-fluid network configurations, components, interconnections and boundary conditions. Hence, the tool should be easy to use and to setup. Also the representation of the thermo fluid network in the software has to be clear, such that the structure of the system can be straightforward identified.

If the toolbox is also used for control *development purposes* some additional requirements apply:

1. **Link to control system design tools:** A native link to the control system development tools in the common coding language (MATLAB® Simulink in this case) is

required.

2. **Real-time capability:** To run the model on hardware like HiL simulator or a Control Unit (xCU) it is prerequisite that it runs faster than real-time.

3. **Code generation:** To support on-board control and diagnostics the software has to be coded in or translated to C code (e.g. MATLAB® Coder)

4. **Stable:** For use on real time hardware the solvers and used equations must be numerically robust.

5. **Cost efficient:** If the code is intended to run in production vehicles additional license fees for thermal functions should be avoided.

Compliance with the additional requirements enables the application of the Thermo Fluid Library during the entire product development process. For the buildup of the thermo fluid simulation library the tool and coding language choice is made based on the requirements towards automatic target code generation and plant model interchangeability, respectively applicability for control development. Simulink® from The MathWorks, is a graphical programming environment for modeling, simulating and analyzing multi domain dynamic systems. It is chosen because of the following reasons:

- Widespread usage within automotive industry;

- Established tool for control development;

- Code generation capability [64].

With the Simulink environment simulation modeling, control development and automatically C source code generation for real-time implementation can be done in a single tool. Since the software is commonly used interchangeability represents no obstacle - as long as no additional toolboxes are required.

Toolbox structure

In general, each cooling/lubrication system can be described by three main subsystems that can be identified as follows:

- **Fluid Network:** Description of the heat transfer (between fluid $\leftrightarrow$ air, fluid $\leftrightarrow$ solid and fluid $\leftrightarrow$ fluid), heat distribution and heat storage for fluids like coolant and oil as well as the pressure drop and flow distribution in complex pipe networks;

- **Solid network:** Heat storage, heat balancing and distribution within solid component structures (e.g.: ICE or EM) based on thermal resistances and lumped mass analysis;

- **Airpath:** Vehicle velocity and fan speed dependent calculation of the air mass flow through the vehicle underhood, and thus through the radiators.

To describe the dynamic behavior of the components within the Thermo-Fluid Library (TheLib), physical laws for describing heat storage, heat transfer, pressure drop and pressure source are used as shown in Fig. 3.1. Underlying fundamentals and equations were described in chapter 2.

The Thermo Fluid Library is build up from plain Simulink block-sets which is beneficial from a performance point of view. But, writing rather complex numerical solver routines is not feasible with the standard Simulink block-sets. Therefore, the Thermo Fluid Solver,
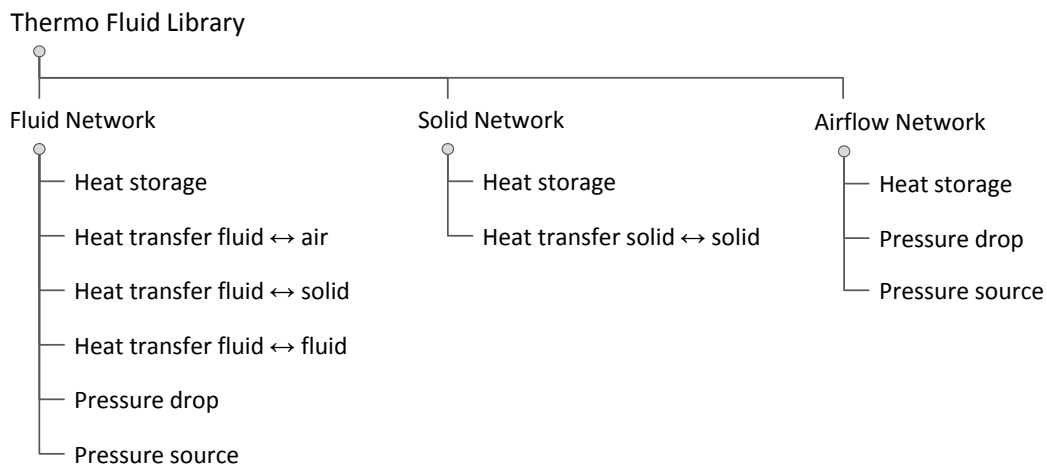
Figure 3.1.: Structure of the simulation tool components and required sub-models to describe the thermal and hydraulic behavior of vehicle cooling and lubrication systems.

that is responsible for the solution of a given fluid network towards component mass flows and temperatures, is implemented as C/C++ code[1]. This code is interfaced to the thermo fluid network. Even tough the C/C++ code integration is quite efficient the overall calculation time is dominated by the iterative flow network solution. Detailed insight into the solver is given in section 3.2.2. For a real time hardware implementation (e.g.. for HiL applications) of the thermal system simulation, including the thermo fluid solver, the mentioned automatic source code generation functionality is used [64].
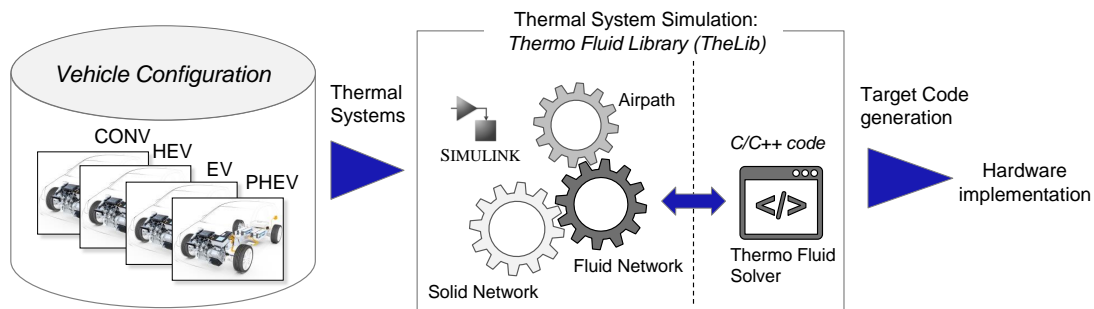

Figure 3.2.: Methodology for thermal system simulation and code generation with Simulink®.

---

[1]Automatically created from MATLAB® code using a so called *MATLAB function* subsystem in Simulink.

3.2. Thermo hydraulic solver

3.2.1. Causality

Since MATLAB Simulink was chosen as software environment limitations arising from the causal nature of the tool have to be addressed in an appropriate manner. Challenging is the change in fluid flow direction e.g. caused by changed pressure levels due to valve switching as depicted in Fig. 9. In Situation 1 the pressure at component A and B is higher than at component C. Thus, component A and B are defining component C mass flow ($\dot{m}_C$) and inlet temperature $T_{C,i}$. If the pressure at node C is higher than at nodes A and B the direction of the flow changes (Situation 2) and component C defines component A and B inlet temperatures and mass flows. That is why flow direction change does also cause a change of the information flow and signal propagation direction - in this case from $A + B \rightarrow C$ to $C \rightarrow A + B$.
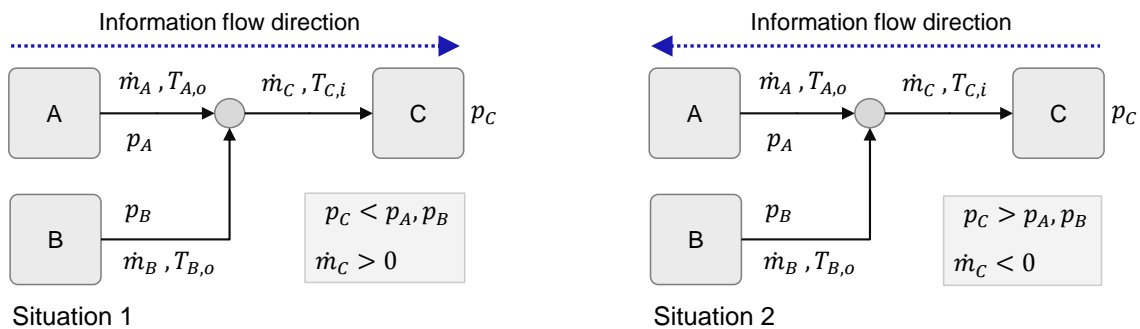
Figure 3.3.: Information and flow direction change in a flow network based on component A, B and C pressure levels

Flow direction changes can be treated in Simulink via two possible ways:

(a) Switching systems or

(b) Custom thermo flow solver.

Switching systems

Solving the causality problem via switching between systems requires having a dedicated simulation model for all possible flow network configurations. Switching between this simulation models is required. In this case the pressure of the nodes is essential for the switching behavior. Therefore commonly used causal flow and thermal solver can be used. Unfortunately there are two grave disadvantages:

- Complex systems with many possible network configurations require a huge amount of different models;

- Switching between the systems requires the exchange of state information (Temperatures, Flows) and initial conditions. This is a non-trivial task since all possible combinations have to be considered.

Custom thermo flow solver

Because of the disadvantages of the described switchable systems approach a custom build thermo hydraulic flow solver is used in the present work. The basic functionality is shown in Fig. 3.4. Solution of the hydraulic network requires information about the flow network layout and the flow directions which is stored in the network connectivity matrix A_{21}. The matrix has i rows and j columns, where i symbolizes the number of components and j the number of nodes in the system. Minus one (-1) symbolizes flow out of a node towards the component and plus one (1) symbolizes that the component is delivering positive flow input to a certain node. E.g.: component A is receiving flow from node one (N1) and is delivering flow to node three (N3), hence in the first row of the network connectivity matrix minus one (-1) is reflecting the source node (N1) and plus one (1) is defining the sink node (N3) as depicted in Fig. 3.4. Together with the mass flow dependent pressure drop polynomials $\Delta p(\dot{m}_c)$ provided by each component the hydraulic network is solved for continuity at each node (N) and energy conservation for each component (C) via the method of global gradient similar to the approach shown in [63]. Symbols (C) and (N) are denoting all the components and nodes in the flow system respectively. Results from the thermo flow solver are the individual component fluid mass flows $\dot{m}_C$, component pressure differences Δp_C and nodal pressure levels p_N.

The solution of the thermal system requires adjusting the network connectivity matrix according to current flow direction. Note that changes in flow direction are respected by changing the signs in the connectivity matrix for components with a negative mass flow. Component coolant mass flows and outlet temperatures $(\dot{m}, T_o)$ are used to calculate the mixing temperatures at the nodes under the assumption of perfect (isentropic) mixing. Node temperatures are then mapped towards component inlet temperatures $T_{c,i}$ using only the negative parts of the network connectivity matrix.
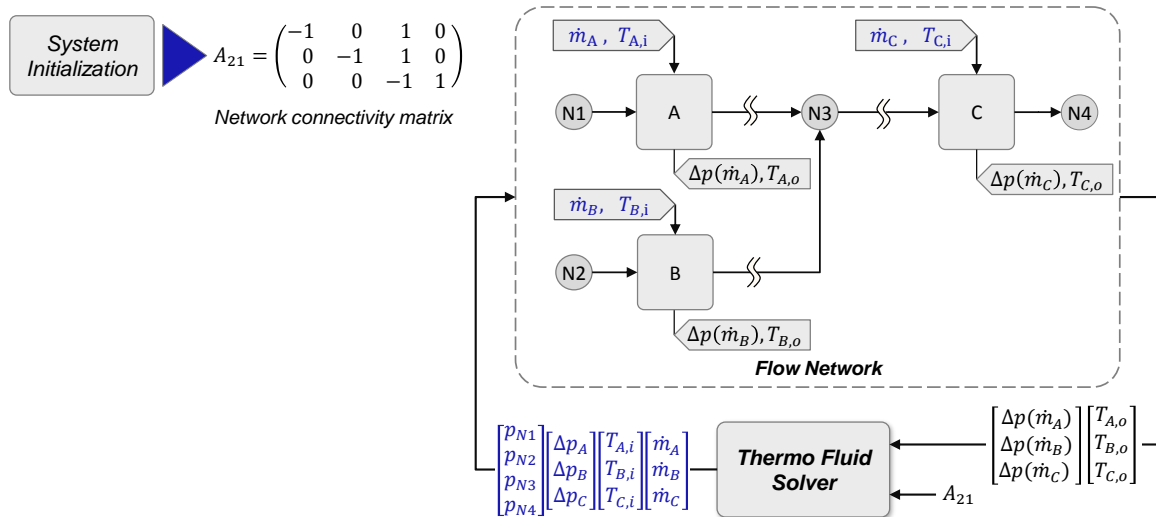
Figure 3.4.: Methodology for a flow direction independent solution of flow and thermodynamic state in a closed fluid circuit.

3.2.2. Flow solver

In this section the *pipe equations* solution scheme, or *global gradient* method, from Todini and Pilati [63, 58] is used as baseline for the flow network solution (as introduced in section 2.2.4). Further extension and modification are necessary to support the simulation of close loop and open loop cooling systems including variable pressure sources (pumps) and variable flow resistances (valves). An important difference to the original formulation is the usage of *mass flow* rather than *volume flow* in both the mass conservation and energy equation. This is necessary to consider the temperature and density variations within the network. Modeling of pressure sources and valves required extending the sole n_{th} order pressure difference formulation $p_A - p_B = K_l \lfloor \dot{m}_l \rfloor^n$ given by Todini and Pilati to the full vector notation form $p_A - p_B = \mathbf{K} \lfloor \dot{\mathbf{m}}_l \rfloor^n$ that considers all polynomial coefficients.

On the following pages a *modified pipe equation solution algorithm* is described and applied to a demonstration example. For the hydraulic network in Fig. 3.5 we can write one mass conservation equation for each of the three nodes and one energy conservation equation for each of the five components in the network. The pressure at the reservoir p_1 and at the sink p_5 as well as the pump speed are assumed to be known for this example. In terms of mass flow conservation we can write for the nodes N[2]:

$$
\begin{aligned}
\mathrm{F_{m1}}: \quad & +\dot{m}_1 - \dot{m}_2 - \dot{m}_3 && = 0 && \{\mathrm{N2}\} \\
\mathrm{F_{m2}}: \quad & +\dot{m}_2 - \dot{m}_5 && = 0 && \{\mathrm{N3}\} \\
\mathrm{F_{m3}}: \quad & +\dot{m}_3 + \dot{m}_5 - \dot{m}_4 && = 0 && \{\mathrm{N4}\}
\end{aligned}
\tag{3.1}
$$

In terms of energy conservation we can write for each of the components C in the network:

$$
\begin{aligned}
\mathrm{F_{p1}}: \quad & +\mathbf{K}_1 \lfloor \dot{\mathbf{m}}_1 \rfloor^n + p_2 - p_1 && = 0 && \{\mathrm{C1}\} \\
\mathrm{F_{p2}}: \quad & +\mathbf{K}_2 \lfloor \dot{\mathbf{m}}_2 \rfloor^n + p_3 - p_2 && = 0 && \{\mathrm{C2}\} \\
\mathrm{F_{p3}}: \quad & +\mathbf{K}_3 \lfloor \dot{\mathbf{m}}_3 \rfloor^n + p_4 - p_2 && = 0 && \{\mathrm{C3}\} \\
\mathrm{F_{p4}}: \quad & +\mathbf{K}_4 \lfloor \dot{\mathbf{m}}_4 \rfloor^n + p_5 - p_4 && = 0 && \{\mathrm{C4}\} \\
\mathrm{F_{p5}}: \quad & +\mathbf{K}_5 \lfloor \dot{\mathbf{m}}_5 \rfloor^n + p_4 - p_3 && = 0 && \{\mathrm{C5}\}
\end{aligned}
\tag{3.2}
$$
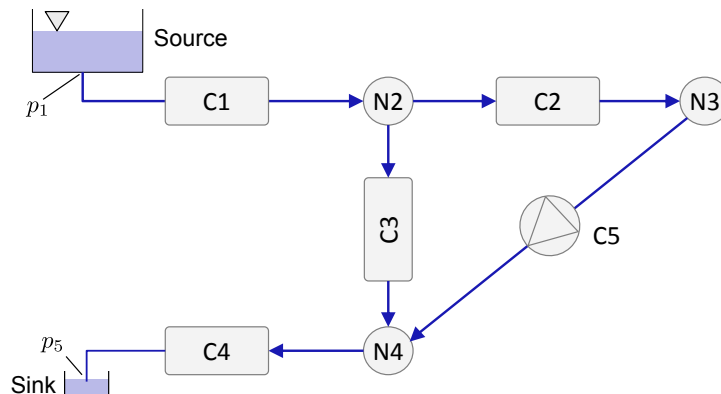
Figure 3.5.: Flow network example with static pressure source, pump C5 and flow resistances C1-C4.

---

[2] mass flow input is accounted positive, output negative

Note that the group $\lfloor \dot{\mathbf{m}} \rfloor^n$ in the energy equation represents that the mass flow vector is raised to the power of $[n\ n{-}1\ n{-}2]$ as shown in Eq. 2.105 and the sign of the pipe flow is applied to the head loss equation term, as shown in Eq. 2.104. The direction of the flow is also considered in the node equations. Thus, a negative flow is acceptable and defines a flow that is in the opposite direction from the initial assumption.

To solve for the unknown flow rates and node pressures the *node equation* (Eq. 2.103) is expanded to a Taylor series which is truncated at the first order term:

$$F_m^k = F_m^{(k-1)} + \sum_{l\,\in\,J_{in},J_{out}} \left(\dot{m}_l^k - \dot{m}_l^{k-1} \right) \frac{\partial F_m}{\partial \dot{m}_l} \tag{3.3}$$

where l indicates a component from the set of in and outgoing flows (J_{in}, J_{out}) and $\frac{\partial F_m}{\partial \dot{m}_l}$ is the derivative of the node equation with respect to the lth component. The superscript k represents the iteration count.

With $\Delta \dot{m}_l \equiv \dot{m}_l^k - \dot{m}_l^{k-1}$ and with $F_m^k = 0$ at the root of the linear function given in Eq. 3.3 we can express the change of mass flow as

$$\Delta \dot{m}_l = \frac{-F_m^{(k-1)}}{\sum\limits_{l\,\in\,J_{in},J_{out}} \left.\frac{\partial F_m}{\partial \dot{m}_l}\right|_{\Delta \dot{m}_l=0}} \tag{3.4}$$

which is equivalent to the *Newton-Raphson* method [65] except that $\Delta \dot{m}$ is calculated rather than the updated flow $\dot{m}^{(k)}$. Rearranging towards a convenient linear system of equations form ($A\,x = y$) yields for the mass conservation equation at the nodes:

$$\sum_{l\,\in\,J_{in},J_{out}} \left.\frac{\partial F_m}{\partial \dot{m}_l}\right|_{\Delta \dot{m}_l=0} \Delta \dot{m}_l = -F_m^{(k-1)}. \tag{3.5}$$

Applying the Newton Raphson method to the *energy equation* (Eq. 3.2) for pipe l that connects nodes i and j gives:

$$\left.\frac{\partial F_p}{\partial p_i}\right|_{\Delta p=0} \Delta p_i + \left.\frac{\partial F_p}{\partial p_j}\right|_{\Delta p=0} \Delta p_j + \left.\frac{\partial F_p}{\partial \dot{m}_l}\right|_{\Delta \dot{m}=0} \Delta \dot{m}_l = -F_p^{(k-1)}. \tag{3.6}$$

The right hand sides are computed by substituting the present estimate of the flow rate and head into the network defining equations (Eq. 3.1 and Eq. 3.2, respectively). $F_m^{(k-1)}$ can be interpreted as the current mass flow error at the node and $F_p^{(k-1)}$ can be seen as the current energy error for the component. For convenience we define $dm \equiv F_m^{(k-1)}$ and $dE \equiv F_p^{(k-1)}$.

For the nodes in the example network Eq. 3.5 becomes

$$\begin{aligned}
(+1)\Delta \dot{m}_1 + (-1)\Delta \dot{m}_2 + (-1)\Delta \dot{m}_3 &= -(\dot{m}_1 - \dot{m}_2 - \dot{m}_3) &= -dm_2 && \{N2\} \\
(+1)\Delta \dot{m}_2 + (-1)\Delta \dot{m}_5 &= -(\dot{m}_2 - \dot{m}_5) &= -dm_3 && \{N3\} \\
(+1)\Delta \dot{m}_3 + (+1)\Delta \dot{m}_5 + (-1)\Delta \dot{m}_4 &= -(\dot{m}_3 + \dot{m}_5 - \dot{m}_4) &= -dm_4 && \{N4\}
\end{aligned} \tag{3.7}$$

and for the components Eq. 3.6 becomes

$$
\begin{aligned}
(-1)\Delta p_1 + (+1)\Delta p_2 + \mathbf{K}_1 \, \mathbf{N} \, \lfloor \dot{\mathbf{m}}_1 \rfloor^{n-1} \Delta \dot{m}_1 \quad &= -(p_2 - p_1 + \mathbf{K}_1 \lfloor \dot{\mathbf{m}}_1 \rfloor^n) \quad &= -dE_1 \quad \{C1\} \\
(-1)\Delta p_2 + (+1)\Delta p_3 + \mathbf{K}_2 \, \mathbf{N} \, \lfloor \dot{\mathbf{m}}_2 \rfloor^{n-1} \Delta \dot{m}_2 \quad &= -(p_3 - p_2 + \mathbf{K}_2 \lfloor \dot{\mathbf{m}}_2 \rfloor^n) \quad &= -dE_2 \quad \{C2\} \\
(-1)\Delta p_2 + (+1)\Delta p_4 + \mathbf{K}_3 \, \mathbf{N} \, \lfloor \dot{\mathbf{m}}_3 \rfloor^{n-1} \Delta \dot{m}_3 \quad &= -(p_4 - p_2 + \mathbf{K}_3 \lfloor \dot{\mathbf{m}}_3 \rfloor^n) \quad &= -dE_3 \quad \{C3\} \\
(-1)\Delta p_4 + (+1)\Delta p_5 + \mathbf{K}_4 \, \mathbf{N} \, \lfloor \dot{\mathbf{m}}_4 \rfloor^{n-1} \Delta \dot{m}_4 \quad &= -(p_5 - p_4 + \mathbf{K}_4 \lfloor \dot{\mathbf{m}}_4 \rfloor^n) \quad &= -dE_4 \quad \{C4\} \\
(-1)\Delta p_3 + (+1)\Delta p_4 + \mathbf{K}_5 \, \mathbf{N} \, \lfloor \dot{\mathbf{m}}_5 \rfloor^{n-1} \Delta \dot{m}_5 \quad &= -(p_4 - p_3 + \mathbf{K}_5 \lfloor \dot{\mathbf{m}}_5 \rfloor^n) \quad &= -dE_5 \quad \{C5\}
\end{aligned}
\tag{3.8}
$$

where the product $\mathbf{K}_l \, \mathbf{N} \, \lfloor \dot{\mathbf{m}}_l \rfloor^{n-1}$ results from $\left. \frac{\partial F_p}{\partial \dot{m}_l} \right|_{\Delta \dot{m}=0}$ with $\mathbf{N}$ defined as

$$
\mathbf{N} = \mathrm{diag}(n \; n-1 \; n-2)
$$

thus,

$$
\mathbf{K}_l \, \mathbf{N} \, \lfloor \dot{\mathbf{m}}_1 \rfloor^{n-1} = n K_{l,2} \, \dot{m}_l^{n-1} + (n-1) K_{l,1} \, \dot{m}_l^{n-2} + (n-2) K_{l,0} \, \dot{m}_l^{n-3}
$$

where $K_{l,*}$ represents a coefficient within the component l pressure coefficient vector. The eight equations, given in Eq. 3.7 and Eq. 3.8, can now be solved for the changes in node mass flow and component pressure difference. For the next iteration the unknowns can be computed by:

$$
\begin{aligned}
p^{(k)} &= p^{(k-1)} \quad + \Delta p^{(k)}, \\
\dot{m}^{(k)} &= \dot{m}^{(k-1)} \quad + \Delta \dot{m}^{(k)}.
\end{aligned}
\tag{3.9}
$$

Todini and Pilati presented a generalization of this procedure in matrix form. This formulation is adopted in order to consider temperature variations in the system and to support the pressure coefficient implementation in *vector notation* which is required to consider pressure sources. After modification, the conservation of mass in the nodes and conservation of energy equations (Eq. 3.1 and 3.2) can be written in matrix form as

$$
\begin{aligned}
\mathbf{F}_p(\dot{\mathbf{M}}, \mathbf{p}) &= \mathbf{A}_{11}\dot{\mathbf{M}}^{(k)} + \mathbf{A}_{12}\mathbf{p}^{(k)} + \mathbf{A}_{10}\mathbf{p}_0 \quad = \mathbf{0} \\
\mathbf{F}_m(\dot{\mathbf{M}}, \mathbf{p}) &= \mathbf{A}_{21}\dot{\mathbf{M}}^{(k)} - \mathbf{q} \quad\quad\quad\quad\quad = \mathbf{0}
\end{aligned}
\tag{3.10}
$$

where $\dot{\mathbf{M}}$ is the component mass flow vector, $\mathbf{p}$ is the node pressure vector, $\mathbf{A}_{10}$ is the fixed node pressure connectivity matrix and $\mathbf{p}_0$ is the fixed node pressure vector. They are defined as

$$
\dot{\mathbf{M}} = \begin{bmatrix} \dot{m}_1 \\ \dot{m}_2 \\ \vdots \\ \dot{m}_{ncomp} \end{bmatrix} \in \mathbb{R}^{[ncomp \times 1]}, \quad
\mathbf{p} = \begin{bmatrix} p_1 \\ p_2 \\ \vdots \\ p_{nnodes} \end{bmatrix} \in \mathbb{R}^{[nnodes \times 1]}, \quad
\mathbf{q} = \begin{bmatrix} q_1 \\ q_2 \\ \vdots \\ q_{nnodes} \end{bmatrix} \in \mathbb{R}^{[nnodes \times 1]}.
$$

Looking at the node and the component equations from the beginning of the example reveals that coefficients of the flows entering and leaving node 2 are 1, -1, -1, for components 1-3 respectively and 0 for the components 4 and 5. These coefficients are identical

to the coefficients that occur for the node pressure p_2 in the component equation for corresponding mass flow. They comprise the matrices, $\mathbf{A}_{12}$ and $\mathbf{A}_{21}$. $\mathbf{A}_{21}$ is the connectivity or topological matrix and $\mathbf{A}_{12} = \mathbf{A}_{21}^T$. The coefficients in the matrix define the network connections and can take on values 1, -1 and 0. Each column in $\mathbf{A}_{21}$ corresponds to a component and each row corresponds to a node. Looking at the rows (nodes), values of 1 are assigned to components that deliver input to the node, -1 indicates components that get input from the node and 0 is assigned if the node and the component are not connected at all. Consequently, the connectivity matrix for the example network in Fig. 3.5 can be given as

$$\mathbf{A}_{21} = \begin{bmatrix} 1 & -1 & -1 & 0 & 0 \\ 0 & 1 & 0 & 0 & -1 \\ 0 & 0 & 1 & -1 & 1 \end{bmatrix} \quad \text{and} \quad \mathbf{A}_{12} = \mathbf{A}_{21}^T = \begin{bmatrix} 1 & 0 & 0 \\ -1 & 1 & 0 \\ -1 & 0 & 1 \\ 0 & 0 & -1 \\ 0 & -1 & 1 \end{bmatrix}. \quad (3.11)$$

Note that the rows in the *nnodes* × *ncomp* matrix $\mathbf{A}_{21}$ correspond to the nodes 2, 3 and 4 respectively. The fixed node pressure connectivity matrix $\mathbf{A}_{10}$ and fixed node pressure vector $\mathbf{p}_0$ for the example can be given as

$$\mathbf{A}_{10} = \begin{bmatrix} -1 & 0 \\ 0 & 0 \\ 0 & 0 \\ 0 & 1 \\ 0 & 0 \end{bmatrix} \in I\!\!R^{[ncomp \times n0nodes]} \quad \text{and} \quad \mathbf{p}_0 = \begin{bmatrix} 201300 \\ 101300 \end{bmatrix} \in I\!\!R^{[n0nodes \times 1]}, \quad (3.12)$$

where *n0nodes* is the number of known static pressure nodes. $\mathbf{A}_{11}$ is a diagonal matrix containing the pressure coefficient vector $\mathbf{K}$ of the components multiplied with the flow raised only to the power of $n-1$, because the matrix is then multiplied with $\dot{\mathbf{M}}$ (as shown in 3.10). It is defined as:

$$\mathbf{A}_{11} = \begin{bmatrix} \mathbf{K}_l |\dot{\mathbf{m}}_l|^{\mathbf{n-1}} & & \mathbf{0} \\ & \ddots & \\ \mathbf{0} & & \mathbf{K}_{ncomp} |\dot{\mathbf{m}}_{ncomp}|^{\mathbf{n-1}} \end{bmatrix} \in I\!\!R^{[ncomp \times ncomp]} \quad (3.13)$$

or written in vector notation this equation yields

$$\mathbf{A}_{11} = \text{diag}\left(\overline{\mathbf{K}}\,\overline{\mathbf{M}}\right) \quad (3.14)$$

where $\mathbf{n} = [n \; n-1 \; n-2]^T$, $\mathbf{n-1} = [n-1 \; n-2 \; n-3]^T$ and with the diagonal matrix $\overline{\mathbf{M}}$ defined as

$$\overline{\mathbf{M}} = \begin{bmatrix} m_1^{n-1} & m_1^{n-2} & m_1^{n-3} \mid m_2^{n-1} & \dots & m_{ncomp}^{n-3} \end{bmatrix} \in I\!\!R^{[(n+1)\,ncomp \times 1]}. \quad (3.15)$$

For the vector computation all pressure coefficient vectors are combined as block diagonals in matrix $\overline{\mathbf{K}}$ which is defined as

$$\overline{\mathbf{K}} = \begin{bmatrix} \mathbf{K}_1 & & & \\ & \mathbf{K}_2 & & \\ & & \ddots & \\ & & & \mathbf{K}_{ncomp} \end{bmatrix} \in I\!\!R^{[ncomp \times (n+1)\,ncomp]}.$$

Applying now the Newton-type solution scheme to the equation system (Eq. 3.10) yields:

$$\begin{aligned}
n\mathbf{A}_{11}\Delta\dot{\mathbf{m}}^{(k)} + \mathbf{A}_{12}\,\Delta\mathbf{p}^{(k)} &= -\mathbf{dE} \\
\mathbf{A}_{21}\Delta\dot{\mathbf{m}}^{(k)} &= -\mathbf{dm}
\end{aligned} \tag{3.16}$$

and the full matrix equation, without the iteration index (k), is

$$\begin{bmatrix} n\mathbf{A}_{11} & \mathbf{A}_{12} \\ \hline \mathbf{A}_{21} & \mathbf{0} \end{bmatrix} \begin{bmatrix} \Delta\dot{\mathbf{m}} \\ \hline \Delta\mathbf{p} \end{bmatrix} = \begin{bmatrix} -\mathbf{dE} \\ \hline -\mathbf{dm} \end{bmatrix} \tag{3.17}$$

which is equivalent to the formulations found for the example network nodes and components (Eq. 3.7 and 3.8). In Eq. 3.16 $\mathbf{dm} \equiv \mathbf{F}_m(\dot{\mathbf{M}}, \mathbf{p})$ and $\mathbf{dE} \equiv \mathbf{F}_p(\dot{\mathbf{M}}, \mathbf{p})$ is defined for convenience, in accordance with Eq. 3.10. The right hand side is a $ncomp + nnodes \times 1$ vector that contains the residuals of the mass and energy conservation equations at iteration $(k-1)$ which are defined as

$$\mathbf{dE} = \begin{bmatrix} dE_1 \\ dE_2 \\ \vdots \\ dE_{ncomp} \end{bmatrix} \in I\!R^{[ncomp \times 1]} \quad \text{and} \quad \mathbf{dm} = \begin{bmatrix} dm_1 \\ dm_2 \\ \vdots \\ dm_{nnodes} \end{bmatrix} \in I\!R^{[nnodes \times 1]}. \tag{3.18}$$

The left hand side consists of a $nnodes + ncomp \times nnodes + ncomp$ matrix with the matrix $n\mathbf{A}_{11}$ defined as

$$n\mathbf{A}_{11} = \begin{bmatrix} \mathbf{K}_1\left(\left|\dot{\mathbf{m}}_1\right|^{\mathbf{n-1}} \cdot \mathbf{n}\right) & & \mathbf{0} \\ & \ddots & \\ \mathbf{0} & & \mathbf{K}_{ncomp}\left(\left|\dot{\mathbf{m}}_{ncomp}\right|^{\mathbf{n-1}} \cdot \mathbf{n}\right) \end{bmatrix} \in I\!R^{[ncomp \times ncomp]} \tag{3.19}$$

or in matrix notation

$$n\mathbf{A}_{11} = \mathrm{diag}\left(\overline{\mathbf{K}}\,\overline{\mathbf{N}}\,\overline{\mathbf{M}}\right) \tag{3.20}$$

with

$$\overline{\mathbf{N}} = \mathrm{diag}\left([n\ n\text{–}1\ n\text{–}2 \mathrel{\vdots} n\ n\text{–}1\ \dots n\text{–}2]\right) \in I\!R^{[(n+1)\,ncomp \times (n+1)\,ncomp]}. \tag{3.21}$$

The left hand side matrix in equation 3.17 is multiplied with the unknown update variable vectors for change in mass flow $\Delta\dot{\mathbf{m}}$ and pressure $\Delta\mathbf{p}$ which are defined as

$$\Delta\dot{\mathbf{m}} = \begin{bmatrix} \Delta\dot{m}_1 \\ \Delta\dot{m}_2 \\ \vdots \\ \Delta\dot{m}_{ncomp} \end{bmatrix} \in I\!R^{[ncomp \times 1]}, \quad \Delta\mathbf{p} = \begin{bmatrix} \Delta p_1 \\ \Delta p_2 \\ \vdots \\ \Delta p_{nnodes} \end{bmatrix} \in I\!R^{[nnodes \times 1]}. \tag{3.22}$$

The matrix equation 3.17 can now be solved for $\Delta\dot{\mathbf{m}}$ and $\Delta\mathbf{p}$. Pressure at the nodes and component mass flows are then updated by

$$\begin{aligned}
\mathbf{p}^{(k)} &= \mathbf{p}^{(k-1)} + \Delta\mathbf{p}^{(k)} \\
\dot{\mathbf{M}}^{(k)} &= \dot{\mathbf{M}}^{(k-1)} + \Delta\dot{\mathbf{m}}^{(k)}.
\end{aligned} \tag{3.23}$$

For the given flow network example (Fig. 3.5) and under the assumption that components C1, C3 and C4 are pipes of the same length and diameter, application of the *Colebrook equation* (see Eq. 2.78) gives for the pressure coefficient vectors $\mathbf{K}_1 = \mathbf{K}_3 = \mathbf{K}_4 = [255870 \ 0 \ 0]$. Component C2 represents a higher minor loss with $\mathbf{K}_2 = [723430 \ 0 \ 0]$. The pump component C5 has a rotation speed dependent pressure coefficient vector $\mathbf{K}_5$ (as shown in Eq. 2.97) that can be given as:

$$\mathbf{K}_5 = \begin{cases} [0 \ 0 \ 0] & \text{Pump off} \\ [144762 \ -33525 \ -72775] & \text{Pump at rated speed} \end{cases}.$$

An initial mass flow of 0.2 kg/s, a pressure at the source of $p_1 = 2.013$ bar and a pressure at the sink of $p_2 = 1.013$ bar, is assumed. Density is calculated from the initial system fluid temperature which is 20 °C.

Consequently, we get for the matrix equation (Eq. 3.17) after the first iteration with *active pump*:

$$\left[\begin{array}{ccccc:ccc} 102348 & 0 & 0 & 0 & 0 & 1 & 0 & 0 \\ 0 & 289372 & 0 & 0 & 0 & -1 & 1 & 0 \\ 0 & 0 & 102348 & 0 & 0 & -1 & 0 & 1 \\ 0 & 0 & 0 & 102348 & 0 & 0 & 0 & -1 \\ 0 & 0 & 0 & 0 & 24380 & 0 & -1 & 1 \\ \hdashline 1 & -1 & -1 & 0 & 0 & 0 & 0 & 0 \\ 0 & 1 & 0 & 0 & -1 & 0 & 0 & 0 \\ 0 & 0 & 1 & -1 & 1 & 0 & 0 & 0 \end{array}\right] \left[\begin{array}{c} \Delta\dot{m}_1 \\ \Delta\dot{m}_2 \\ \Delta\dot{m}_3 \\ \Delta\dot{m}_4 \\ \Delta\dot{m}_5 \\ \hdashline \Delta p_1 \\ \Delta p_2 \\ \Delta p_3 \end{array}\right] = \left[\begin{array}{c} 78116 \\ -23556 \\ 664 \\ -9484 \\ 79207 \\ \hdashline 0.2 \\ 0 \\ -0.2 \end{array}\right].$$

Solving for $\Delta\mathbf{p}$ and $\Delta\dot{\mathbf{m}}$ yields

$$[\Delta\dot{\mathbf{m}} \vdots \Delta\mathbf{p}]^T = \begin{bmatrix} 0.34 & 0.16 & -0.02 & 0.34 & 0.16 & \vdots & 42438.7 & -29933.5 & 45160.9 \end{bmatrix}^T.$$

Substituting this into Eq. 3.23 gives for the flow and pressure for the next iteration step

$$[\dot{\mathbf{M}} \vdots \mathbf{p}]^T = \begin{bmatrix} 0.54 & 0.36 & 0.18 & 0.54 & 0.36 & \vdots & 155388 & 77635 & 147212 \end{bmatrix}^T.$$

Repeating the process for the second iteration gives

$$[\dot{\mathbf{M}} \vdots \mathbf{p}]^T = \begin{bmatrix} 0.45 & 0.32 & 0.13 & 0.45 & 0.32 & \vdots & 152978 & 80601 & 149622 \end{bmatrix}^T.$$

Repeated for another iteration gives the final solution of the problem as

$$[\dot{\mathbf{M}} \vdots \mathbf{p}]^T = \begin{bmatrix} 0.43 & 0.32 & 0.11 & 0.43 & 0.32 & \vdots & 153069 & 80640 & 149530 \end{bmatrix}^T.$$

The final solution of the problem with the *pump deactivated* results in

$$[\dot{\mathbf{M}} \vdots \mathbf{p}]^T = \begin{bmatrix} 0.40 & 0.15 & 0.25 & 0.40 & 0.15 & \vdots & 159515 & 143084 & 143084 \end{bmatrix}^T.$$

As stopping criteria the change in pipe mass flow and pressure at the nodes as well as the overall pressure (energy) and mass flow error are used. The solver stops when the maximum number of iterations is reached or if all of the following conditions are met:

- $\left(\dot{\mathbf{M}}^{(k)} - \dot{\mathbf{M}}^{(k-1)}\right)^T \times \left(\dot{\mathbf{M}}^{(k)} - \dot{\mathbf{M}}^{(k-1)}\right) < dm_{res}$ change in flow in kg/s;

- $\left(\mathbf{dm}^{(k)}\right)^T \times \left(\mathbf{dm}^{(k)}\right) < m_{res}$ continuity error in kg/s;

- $\left(\mathbf{p}^{(k)} - \mathbf{p}^{(k-1)}\right)^T \times \left(\mathbf{p}^{(k)} - \mathbf{p}^{(k-1)}\right) < dp_{res}$ change in pressure in Pa;

- $\left(\mathbf{dE}^{(k)}\right)^T \times \left(\mathbf{dE}^{(k)}\right) < E_{res}$ energy conservation error in Pa,

where dm_{res}, m_{res}, dp_{res} and E_{res} are the respective residual values.

The overall procedure for solving the hydraulic network can be summarized as:

1. Form the network connectivity matrix $\mathbf{A}_{12}$ as shown in Eq. 3.11;

2. Initialize iteration count $k = 0$ and define starting set of nodal pressures, $\mathbf{p}^{(0)}$, and initial pipe flows, $\dot{\mathbf{M}}^{(0)}$. If the solver function call count is greater than zero use the converged solution from the last time step as initial condition, otherwise take the user defined initial conditions;

3. Calculate pressure coefficient matrix $\overline{\mathbf{K}}^{(0)}$;

4. Increase the iteration count and set $k = k + 1$;

5. Build matrix $n\mathbf{A}_{11}$ using Eq. 3.19;

6. Compute mass balance error $\mathbf{F}_m = -\mathbf{dm}$ at the nodes and component energy error $\mathbf{F}_p = -\mathbf{dE}$ as in Eq. 3.10;

7. Solve the system of equation (Eq. 3.17) for $\Delta\dot{\mathbf{m}}$ and $\Delta\mathbf{p}$;

8. Update the node pressure $\mathbf{p}$ and component mass flows $\dot{\mathbf{M}}$ according to Eq. 3.23;

9. Check the residuals. If all are satisfied, output the solution and increase the solver function call count. Else, if maximum number of iterations is reached go to step 2 an restart with different initial condition. Otherwise, go to step 4 and continue with next iteration.

3.2.3. Thermal network solver

The task of the thermal network solver is to compute the temperature distribution in a pipe interconnected fluid network. Changes in temperature and energy level can occur due to heat input from heat sources like electric resistance or combustion losses or due to heat sinks like heat exchangers. Also heat storages influent the warm-up or cool-down behavior of the system.

The presented approach for solving the thermal network is such that each component in the network calculates a fluid outlet temperature based on fluid inlet temperature and fluid mass flow from the flow solver. Consequently, the thermal network solver receives the individual component outlet temperatures together with the fluid mass flows from the hydraulic network solver and calculates mixing temperature at the nodes. Under the assumption of a node control volume with steady, perfect mixing of the incoming enthalpy fluxes $\dot{H}_{in}$, the first law of thermodynamics reduces to a difference between the enthalpy of the in- and outgoing fluid flows (as introduced in Eq. 2.13):

$$\Delta \dot{H} = 0 = \sum_{l \in J_{out}} \dot{H}_{out} - \sum_{l \in J_{in}} \dot{H}_{in} = \sum_{l \in J_{out}} (\dot{m}\,h)_{out} - \sum_{l \in J_{in}} (\dot{m}\,h)_{in} \qquad (3.24)$$

where J_{in} and J_{out} represent a set of components which are connected as input or output to this node, respectively. For convenience, we define $\dot{H}_n$ as the sum of the incoming enthalpy fluxes and h_n as the specific enthalpy at the outlet of the node that are given as

$$\dot{H}_n = \sum_{l \in J_{in}} \dot{H}_{in} \qquad \text{and} \qquad h_n = \frac{\dot{H}_n}{\sum\limits_{l \in J_{in}} \dot{m}_{in}}. \qquad (3.25)$$

Note that the specific enthalpy is a known property of the fluid that can be converted into a temperature with the help of fluid property tables, as given in [39, 38].

For the formulation of thermal network equations in vector notation we continue to use the *network connectivity matrix* $\mathbf{A}_{21}$, as introduced in course of the hydraulic network solver (Eq. 3.11). Subsequently, we will use it to compute the node outlet temperatures.

To account for a possible *flow direction change* (e.g.: the direction of the flow is not equal to the initial assumption) the signs of the connectivity matrix have to be corrected. The sign is corrected by multiplication of the $\mathbf{A}_{21}$ matrix with the sign vector of the current component mass flows $\mathrm{sign}(\dot{\mathbf{M}})$. This modified connectivity matrix is called $\mathbf{A}_{s21}$ and can be build from

$$\mathbf{A}_{s21} = \mathbf{A}_{21} \, \mathrm{diag}\left(\mathrm{sign}(\dot{\mathbf{M}})\right) \qquad (3.26)$$

and for the static temperature sources we reuse the fixed node connectivity matrix $\mathbf{A}_{10}$ and define the flow direction adjusted connectivity matrix $\mathbf{A}_{s10}$ as

$$\mathbf{A}_{s10} = \mathrm{diag}\left(\mathrm{sign}(\dot{\mathbf{M}})\right) \, \mathbf{A}_{10}. \qquad (3.27)$$

From $\mathbf{A}_{s21}$ and $\mathbf{A}_{s10}$ we can identify the components that are providing positive enthalpy flow (input) to the node by the identifier $+1$. These components are collected in the node input matrix $\mathbf{A}_{in}$ which contains all positive elements of matrix $\mathbf{A}_{s21}$:

$$\mathbf{A}_{in} = \mathbf{A}_{s21}(\mathbf{A}_{s21} > 0). \qquad (3.28)$$

Components that receive an enthalpy flux from the connecting node can be identified by a -1 in the connectivity matrix. They are collected in the node output matrix $\mathbf{A}_{out}$ which is defined as

$$\mathbf{A}_{out} = \mathbf{A}_{s21}(\mathbf{A}_{s21} < 0) \tag{3.29}$$

and for components that are connected to static nodes we get

$$\mathbf{A}_{out0} = \mathbf{A}_{s10}(\mathbf{A}_{s10} < 0). \tag{3.30}$$

For the calculation of the enthalpy at the node, the component enthalpy fluxes are required. They are collected in the enthalpy flux vector $\dot{\mathbf{H}}$ and specific enthalpy vector $\mathbf{h}$, which may be calculated from

$$\dot{\mathbf{H}} = \mathbf{h}(T)\,\dot{\mathbf{M}} \quad \text{with} \quad \mathbf{h}(T) = \begin{bmatrix} h_1 & & & \\ & h_2 & & \\ & & \ddots & \\ & & & h_{ncomp} \end{bmatrix} \in \mathbb{R}^{[ncomp \times ncomp]} \tag{3.31}$$

where $\mathbf{h}(T)$ indicates that the specific component outlet enthalpy vector $\mathbf{h}$ is a temperature dependent fluid property. The sum of the incoming enthalpy fluxes from the connected components divided by the sum of the incoming mass flows yields the specific enthalpy at the node outlet:

$$h_n = \frac{\displaystyle\sum_{l \in J_{in}} \dot{H}_l}{\displaystyle\sum_{l \in J_{in}} \dot{m}_l}$$

where J_{in} is the set of incoming pipes for this node. In vector notation we can write for the equation above

$$\mathbf{h}_n = \mathrm{diag}\Big(\mathbf{A}_{in}\,\dot{\mathbf{H}}\Big)\,\mathrm{diag}\Big(\mathbf{A}_{in}\,|\dot{\mathbf{M}}|\Big)^{-1}\underbrace{[1\ 1\ \ldots\ 1]^T}_{\in \mathbb{R}^{[nnodes \times 1]}}. \tag{3.32}$$

The specific enthalpy vector at node outlet $\mathbf{h}_n$ is translated to a fluid temperature vector τ_n with the help of fluid property tables or polynomials that are typically a function of temperature:

$$\tau_n = \mathrm{f}(\mathbf{h}_n).$$

Finally, the unknown component inlet temperature vector τ_c for the next time step can be calculated from

$$\tau_i = \mathbf{A}_{out}^T\,\tau_n + \mathbf{A}_{out0}\,\tau_0 \tag{3.33}$$

where τ_0 is the static temperature source vector with the dimension $nstatic \times 1$.

The hydraulic flow network example shown in Fig. 3.5 is considered again, with some extensions as shown in Fig. 3.6, to demonstrate the thermal network solver functionality.

Components C1, C3 and C4 are assumed to be static adiabatic components with no thermal inertia. This means that no heat is leaving or entering the system within this components and that the temperature does not change over time ($T_{out} = T_{in}$). Component C2 is considered as heat source with a thermal inertia represented by 1 liter of water. The transient thermal behavior of the component *outlet* temperature is described by application of the first law of thermodynamics for open systems, as shown in Eq. 2.15. As heat input a constant prescribed heat flux of $\dot{Q} = 10kW$ is assumed at component C2. The static temperature source (and also the sink in case of flow direction change) is assumed to deliver water with a temperature of $T = 20$ °C which defines the static temperature vector as

$$\tau_0 = [20\ 20]^T \quad \text{in} \quad °C$$
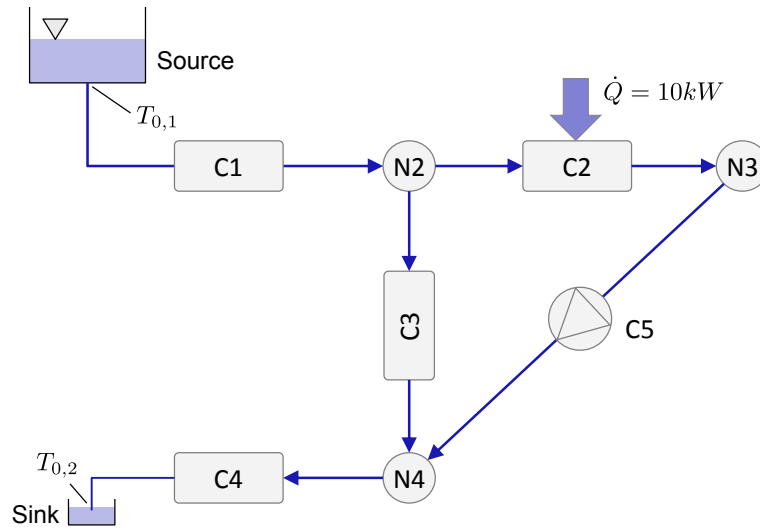
Figure 3.6.: Thermo network example with static source and sink nodes an constant heat input.

For the presented example, under consideration of the resulting fluid mass flows, for the case with running pump, the matrices $\mathbf{A}_{in}$, $\mathbf{A}_{out}$ and $\mathbf{A}_{out0}$ can be derived from Eq. 3.28, 3.29 and 3.30 and may be given as

$$\mathbf{A}_{in} = \begin{bmatrix} 1 & 0 & 0 & 0 & 0 \\ 0 & 1 & 0 & 0 & 0 \\ 0 & 0 & 1 & 0 & 1 \end{bmatrix}, \qquad \mathbf{A}_{out} = \begin{bmatrix} 0 & 1 & 1 & 0 & 0 \\ 0 & 0 & 0 & 0 & 1 \\ 0 & 0 & 0 & 1 & 0 \end{bmatrix}, \qquad \mathbf{A}_{out0} = \begin{bmatrix} 1 & 0 \\ 0 & 0 \\ 0 & 0 \\ 0 & 0 \\ 0 & 0 \end{bmatrix}. \quad (3.34)$$

Note that because the flow direction corresponds to the initial assumption the sign of the connectivity matrices did not change. The dimensions of the matrices are equal to $\mathbf{A}_{21}$ and $\mathbf{A}_{10}$, respectively. Assuming an initial component temperature of 20 °C the component enthalpy flux vector for the first time-step yields

$$\dot{\mathbf{H}} = \begin{bmatrix} 36417 & 26543 & 9874 & 36417 & 26543 \end{bmatrix}^T. \quad (3.35)$$

After 50 seconds the system is in steady state condition, as shown in Fig. 3.7, hence the component enthalpy flux vector can be given as

$$\dot{\mathbf{H}} = \begin{bmatrix} 36414 & 36519 & 9895 & 46414 & 36519 \end{bmatrix}^T. \tag{3.36}$$

From this enthalpy flux vector we can use the fluid properties to calculate the specific enthalpy at the node outlet, as shown in Eq. 3.32. This specific enthalpy is equivalent to a node outlet temperature vector τ_n, which is calculated as

$$\tau_n = \begin{bmatrix} 20 & 27.6 & 25.5 \end{bmatrix}^T \quad \text{in } °C. \tag{3.37}$$

Note that the first value corresponds to the node N2 outlet temperature, as depicted in Fig. 3.6, which is equivalent to the source temperature because component C1 is treated adiabatic. With the component outlet temperatures and the application of Eq. 3.33 we get for the component inlet temperature vector τ_i:

$$\tau_i = \begin{bmatrix} 20 & 20 & 20 & 25.5 & 27.6 \end{bmatrix}^T \quad \text{in } °C. \tag{3.38}$$

For comparison the steady state component inlet temperature after 50 seconds is also given for the case with *deactivated pump*:

$$\tau_i = \begin{bmatrix} 20 & 20 & 20 & 25.9 & 35.9 \end{bmatrix}^T \quad \text{in } °C. \tag{3.39}$$
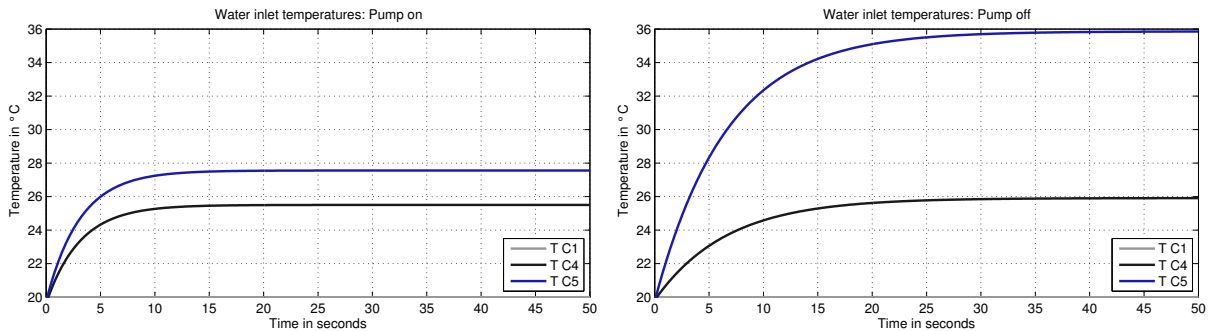
Figure 3.7.: Transient component inlet temperatures for activated and deactivated pump (left, right).

The overall procedure for solving the thermal network can be summarized as:

1. Initialize the component outlet temperatures and receive the fluid mass flow vector $\dot{\mathbf{M}}$ and network connectivity matrices $\mathbf{A}_{21}$ and $\mathbf{A}_{10}$ from the fluid network solver according to Eq. 3.11 and Eq. 3.12;

2. Adjust the network connectivity matrix for the current flow direction and form the matrices $\mathbf{A}_{s12}$, $\mathbf{A}_{s10}$, $\mathbf{A}_{in}$, $\mathbf{A}_{out}$ and $\mathbf{A}_{out0}$ as shown in equations 3.26 - 3.30;

3. Calculate component outlet enthalpy flux vector $\dot{\mathbf{H}}$ according to Eq. 3.31;

4. Compute the specific node outlet enthalpy $\mathbf{h}_n$ as shown in Eq. 3.32;

5. Derive the node outlet temperature vector τ_n from (4) and given fluid properties;

6. Calculate the component inlet temperature τ_i according to Eq. 3.33;

7. Output the component inlet temperatures and calculate the next time-step.

3.2.4. Thermo fluid solver flowchart

The principal sequence of solving the thermo hydraulic network is shown in the flowchart given in Fig. 3.8. The following steps are required to solve a given fluid network for transient pressure, mass flow and temperature distribution:

1. Before the simulation starts the connectivity matrices $\mathbf{A}_{21}$ and $\mathbf{A}_{10}$ are automatically build from the user defined network topology that consists of multiple components and nodes for interconnection. They are build once per simulation run and are then stored for later usage in the flow- and thermo solver;

2. If the flow solver is called for the first time, system initial values for mass flow $\dot{\mathbf{M}}_0$ node pressure $\mathbf{p}_0$ and fluid temperatures τ_0 are derived from the simulation model GUI (Initial temperatures from component GUI and initial mass flow and pressure from the solver component GUI). Otherwise, the converged flow network solution from last time step is taken as solver initial condition;

3. With the initial values the first simulation model update step is calculated;

4. The pressure coefficient vector $\mathbf{K}$ and component outlet temperature T_o are calculated for each component and then forwarded to the thermo fluid solver;

5. In the solver component pressure coefficient matrix $\overline{\mathbf{K}}$ and the component output temperature vector τ_i are build from pressure coefficient vectors $\mathbf{K}$ and component outlet temperatures T_o, respectively;

6. The flow solver iteratively solves the network for component mass flows $\dot{\mathbf{M}}$, pressure differences $\Delta\mathbf{p}$ and nodal pressure $\mathbf{p}$ in terms of continuity and energy conservation;

7. If the solution converges the fluid mass flow, together with the connectivity matrix and the component outlet temperature is forwarded to the thermal network solver (Thermo Solver). Otherwise, the initial fluid mass flow is adapted or an error is thrown if the maximum number of iterations is reached;

8. The Thermo Solver computes the component inlet temperatures τ_i, for the next time step, from the connectivity matrices, component outlet temperatures and current component mass flow;

9. If any of the fluid temperatures in the network is out of the fluid properties bounds (too hot or too cold) NaN is returned and an error is thrown. Otherwise, the function call count is increased by one and the component mass flows $\dot{\mathbf{M}}$ and pressure drops $\Delta\mathbf{p}$, nodal pressure $\mathbf{p}$ and component inlet temperatures τ_i are output and the next time step can be calculated.

Note that for some time steps this sequence may be processed more than once e.g. at the first time step or if the flow direction changes. This is necessary because the initial mass flow direction is an estimate and the corrected flow distribution or a negative flow may cause a different pressure coefficient matrix $\overline{\mathbf{K}}$ resulting in a different flow network solution. This is especially important if components like one way valves are used which have a completely different pressure drop characteristics, depending on the sign of the fluid mass flow.
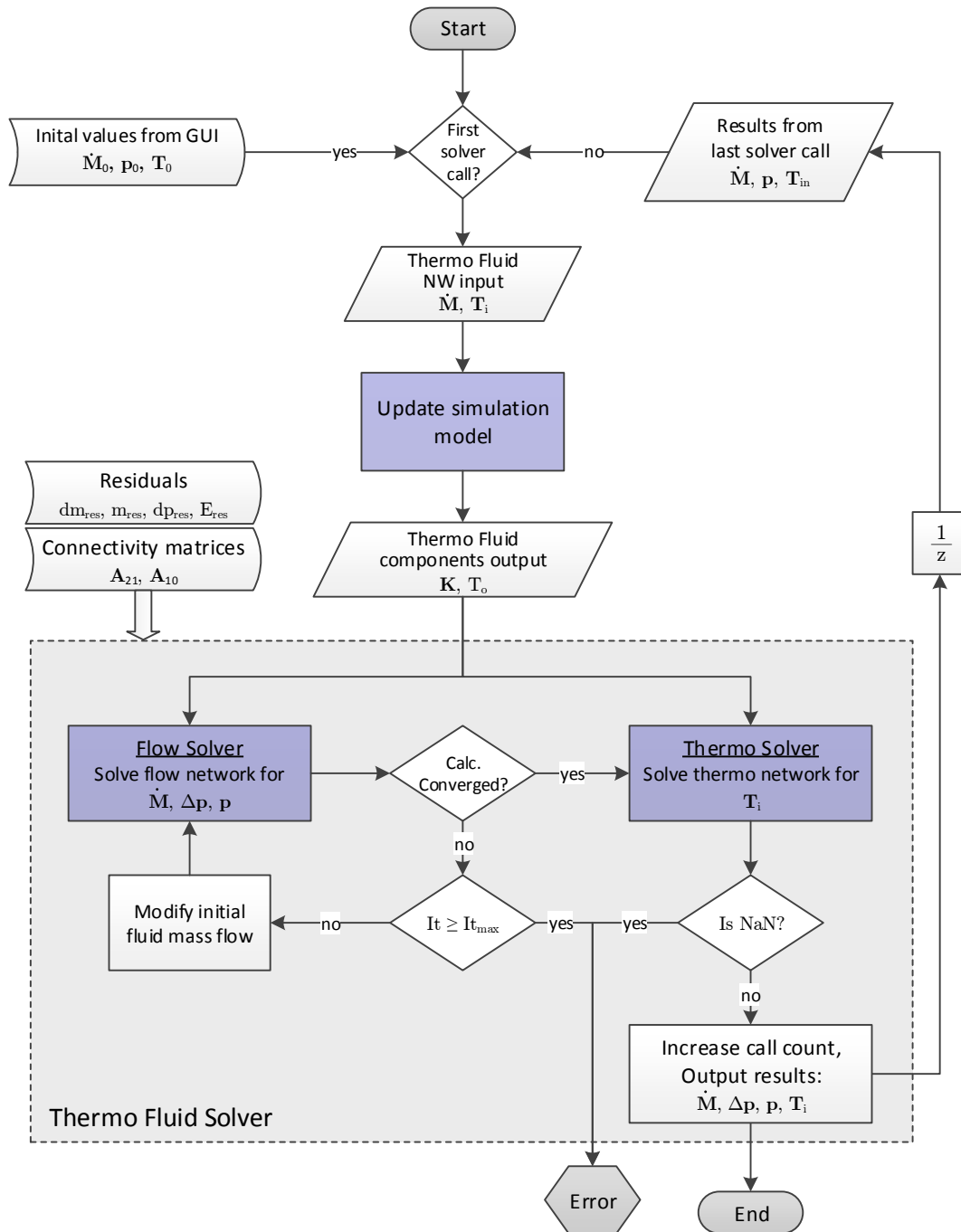
Figure 3.8.: Flowchart for solving the hydraulic and thermal network for one time step
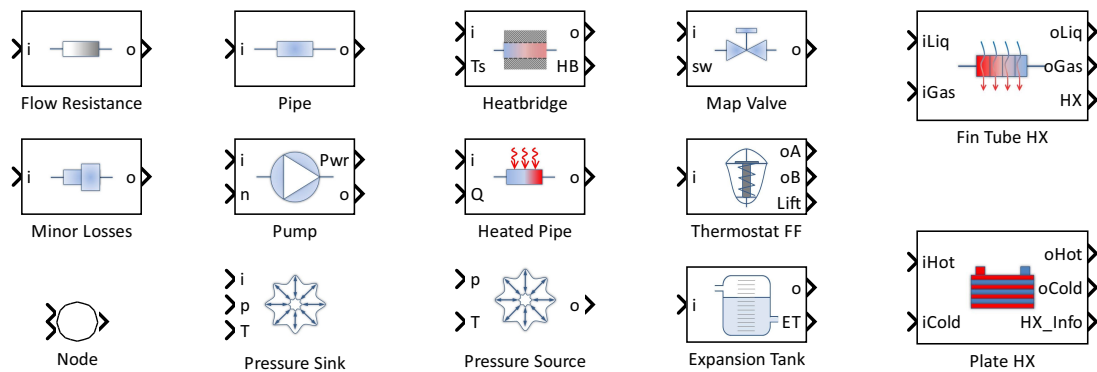
3.3. Fluid network components

The fluid network components described in this section can be used to build up a thermo fluid network, like shown in Fig. 3.9 for the example network which was already considered in the thermo fluid solver section 3.2. A valid network configuration requires a node between each of the components. This node can work as signal splitter or junction. The pressure source and sink components are also interpreted as nodes with a given temperature and pressure. Consequently, the network connectivity matrix is automatically derived from this node-component relationship.

Note that the network definition is independent from the direction of flow, since the components and nodes are only used to define the network and to provide pressure drop and heat transfer inputs to the solver.
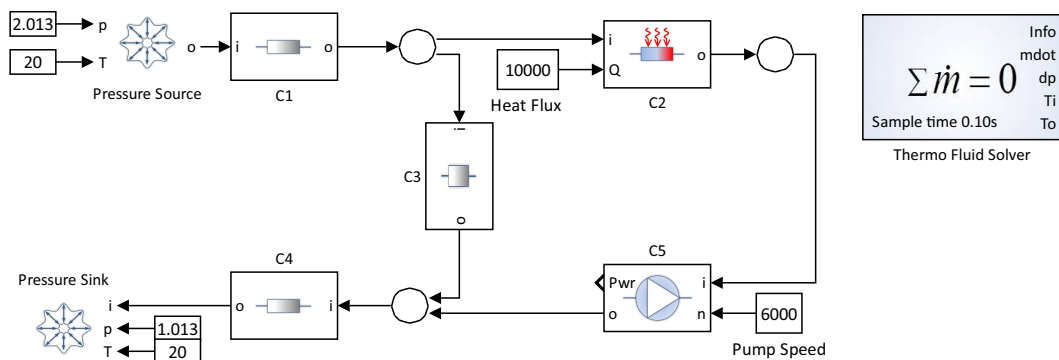
Figure 3.9.: Example Network setup with the Thermo Hydraulic Library Fluid Network Components.

Most of the underlying pressure drop/increase and heat transfer equations are introduced in the fundamentals chapter 2, thus the description of fluid network components will refer to and extend from this formulations. The network may consist of *flow resistances* like pipes and fittings and *pressure sources* like reservoirs and pumps to define the hydraulic behavior. To specify the *thermal behavior* of a flow network several heat sources, heat sinks and heat transfer components are available, as shown in Tab. 3.1. The corresponding fluid network components are implemented as a MATLAB/Simulink library which is depicted in Fig. 3.10.

Figure 3.10.: Thermo Hydraulic Library - Fluid network components.

Table 3.1.: Fluid network components overview

Component	Pressure drop	Pressure source	Heat storage	Heat transfer
Flow Resistance	✓			
Pump		✓		
Pressure Source		✓		
Minor Loss	✓			
Map Valve	✓			
Thermostat	✓			
Node				
Pipe	✓		✓	
Heated Pipe	✓		✓	✓
Heat Bridge	✓		✓	✓
Expansion Tank	✓		✓	
Fin Tube Heat Exchanger	✓		✓	✓
Plate Heat Exchanger	✓		✓	✓

The used correlations for pressure drop, pressure source, heat storage and heat transfer are explained in the following sections. Special components like heat exchanger and expansion tank are outlined in more detail.

3.3.1. Pressure drop

The hydraulic behavior of the coolant, oil and air network is modeled based on the assumption of a quasi-static behavior. Since the focus of the modeling lies on the thermal dynamics and not on transient pressure changing phenomena the quasi-static behavior is sufficient. This simplification allows a significantly less complex approach for the determination of the flow rates. The coolant and oil circuits are described using a hydraulic resistance network. As a simplification, the general form of the pressure difference characteristics for all components is described by a quadratic polynomial, as a function of mass flow:

$$\Delta p = a_2 \dot{m}^2 + a_1 \dot{m} + a_0. \tag{3.40}$$

This simplification is not limiting the application area since Eq. 2.90 shows that most flow resistances functions have a quadratic behavior (at least local).

For components that are representing a hydraulic resistance four different modeling approaches are available:

- Reference pressure drop point as in Eq. 3.42;
- Constant pressure drop polynomial as in Eq. 2.87;
- Darcy friction factor f as in Eq. 2.82 and;
- Dimensionless pressure loss coefficient ζ as in Eq. 2.83.

Reference pressure drop point

This approach requires a minimum amount of information. The specification of one reference pressure drop point defined by a reference volume flow $\dot{V}_{ref}$, pressure difference p_{ref} and fluid density $\rho_{ref}(T)$ is sufficient. From this parameters, a dimensionless loss coefficient is calculated as

$$\zeta = \frac{\Delta p_{ref}}{\dfrac{\rho \, v_{ref}^2}{2}} = \frac{\Delta p_{ref}}{\dfrac{\rho_{ref} \, \dot{V}_{ref}^2}{2 \, A^2}}. \tag{3.41}$$

Rearranging and combining with $\Delta p = \frac{\rho}{2}v^2 \, \zeta$ gives for the pressure difference formulation in vector form, as defined in Eq. 2.88:

$$\Delta p = \mathbf{K} \, \dot{\mathbf{m}}^2 \qquad \text{with} \qquad \mathbf{K} = \left[\frac{\rho_{ref}}{\rho} \frac{\Delta p_{ref}}{\dot{m}_{ref}^2} \quad 0 \quad 0 \right] \tag{3.42}$$

where ρ is the current temperature dependent fluid density.

Valve pressure drop

Valve components require a special approach since the pressure drop is not only a function of the flow, but also a function of the current valve opening. Therefore, the pressure drop characteristics is represented by a valve opening dependent pressure loss coefficient ζ, as shown in Fig. 3.11.
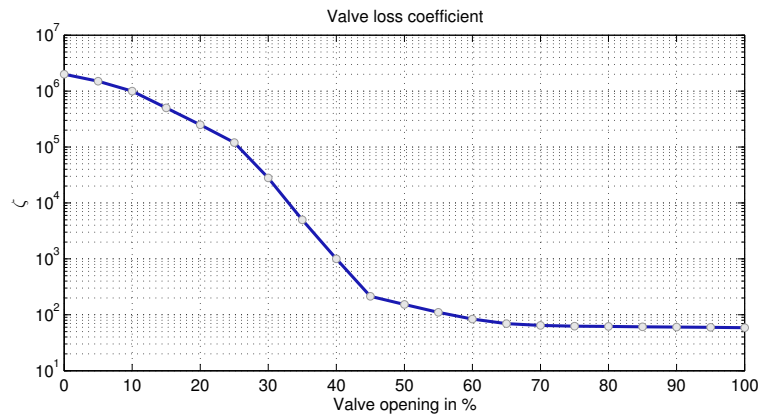
Figure 3.11.: Loss coefficient as a function of valve opening.

3.3.2. Pressure sources

Pressure sources and sinks are creating a pressure difference in the system thus, they are the major cause for fluid motion in a flow network. The presented toolbox supports two pressure source representations:

- Pump $\rightarrow$ Variable pressure source and;
- Pressurized reservoir $\rightarrow$ Static pressure source.

Pump

For the pump pressure sources a quasi-static behavior is assumed. Thus, no inertia effects from acceleration and deceleration of the pump impeller are taken into account.
The behavior of the pump component is strongly dependent on the rotational speed, fluid temperature and pump geometry. For description of the performance characteristics for existing pump designs *similarity laws* are used to form a second order polynomial, as shown in Eq. 2.96.

For the power consumption calculation three different approaches are available:

- Power coefficient polynomial $\hat{P}(\phi)$ as in Eq. 2.98;
- Constant efficiency and;
- Fluid flow dependent efficiency.

Pressurized reservoir

Static pressure sources (and sinks) like pressurized reservoirs are presumed to stay at a constant pressure level for the current time step and are therefore also independent from mass flow variations $(p \neq p(\dot{m}))$. Also the temperature of the fluid flow leaving the reservoirs is assumed to be static. The *static pressure* toolbox component is an integral part of the energy conservation equation (Eq. 2.67) and represents a *static pressure* element.

3.3.3. Heat storage

A heat storage represents the thermal capacity of a fluid control volume within a component in the thermo fluid network. The change of internal energy and temperature is balanced by using the simplified first law of thermodynamics for open systems, which is given in Eq. 2.15 as

$$\frac{dH}{dt} = \sum \dot{Q} + \Delta \dot{H}. \tag{3.43}$$

Energy is transferred from one heat storage to the other by an enthalpy flow $\dot{H}$. The heat flow $\dot{Q}$ may result from heat exchange with the surroundings and is zero for components without active heat transfer.

3.3.4. Heat transfer

In general there are two options to transfer heat between the fluid network and the environment:

- Prescribed heat flow $Q \neq Q(T)$ and;
- Model based heat transfer $Q = Q(\Delta T, A, h)$.

Prescribed heat flow

Prescribed heat flow from given inputs is used in the *Heated Pipe* toolbox component. It is the simplest form of describing heat input or output from the system, because of it's independence from flow conditions and temperature difference. This prescribed heat flow can be calculated from efficiency calculations or empirical data and can be directly used as $\dot{Q}$ input to the heat storage equation (Eq. 3.43).

Model based heat transfer

Model based heat transfer is used in the *heat bridge* toolbox component to calculate the heat flux between the solid and the fluid network.

The heat flow is calculated based on temperature difference, heat transfer area and heat transfer coefficient, as shown in Eq. 2.46 and Eq. 2.50, respectively.

For the heat bridge component three different ways to determine the heat transfer coefficient are distinguished:

- Dittus-Boelter Nusselt correlation as in Eq. 2.37;
- Gnielinski Nusselt correlation as in Eq. 2.39 and
- Custom Nusselt correlation as in Eq. 3.44.

Note that the Dittus-Boelter and Gnielinski equation is applied in the, for engineering problems most relevant, *turbulent flow* regime. Otherwise, the Nusselt correlations for laminar or transitional Reynolds numbers are used (Eq. 2.36 or Eq. 2.42).

The *custom Nusselt correlation* is a convenient way to fit a Nusselt correlation from heat flow measurements. For this purpose a generic, Reynolds Re and Prandtl Pr number dependent, Nusselt Nu correlation of the form

$$Nu = a \, Re^b \, Pr^c \tag{3.44}$$

is used, where a, b and c are tuning variables that may be fitted from heat flux measurement data in a least squares sense.

3.3.5. Heat exchanger

Modeling of heat exchangers leads to partial differential equations which are usually solved via *spatial discretization*, leading to a system of ordinary differential equations. A discretized heat exchanger example is shown in Fig. 3.12.

Each cell i has one dynamic state (the cell temperature $T_{c,i}$) for which a differential equation based on the fist law of thermodynamics for open systems (see Eq. 2.15) may be given as:

$$\frac{dH_{c,i}}{dt} = \Delta\dot{H}_{c,i} + \dot{Q}_{c,i} \quad \text{with} \quad \Delta\dot{H}_{c,i} = \dot{m} \int_{T_{c,i-1}}^{T_{c,i}} cp(T)\,\mathrm{d}T \quad \text{and} \quad T_{c,i} = f(H_{c,i}). \tag{3.45}$$

$T_{c,i-1}$ is either the coolant temperature of the previous cell or the heat exchanger coolant input temperature T_c. For each cell the thermal resistance analogy law, as depicted in
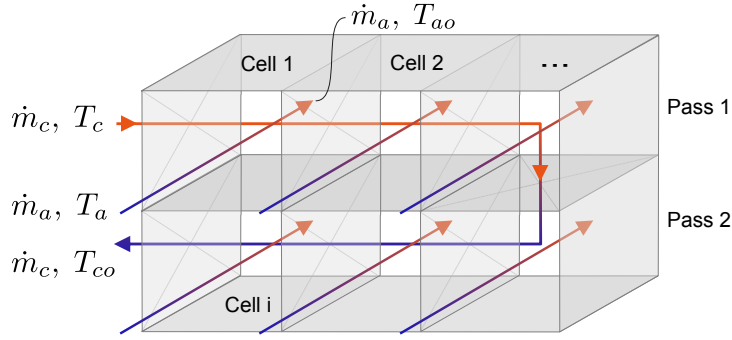
Figure 3.12.: Cell discretized, fin and tube heat exchanger modeling.

Fig. 2.11, is applied to describe the heat transfer between air and coolant by a thermal resistance network, as shown in Fig. 3.13:

$$\dot{Q}_{c,i} = \Delta T_{ln,i}\, R_i^{-1}. \tag{3.46}$$

$$\dot{Q}_{c,i} = \frac{\Delta T_{ln,i}}{R_i}$$

$$R_i = R_a + R_w + R_{c,i}$$
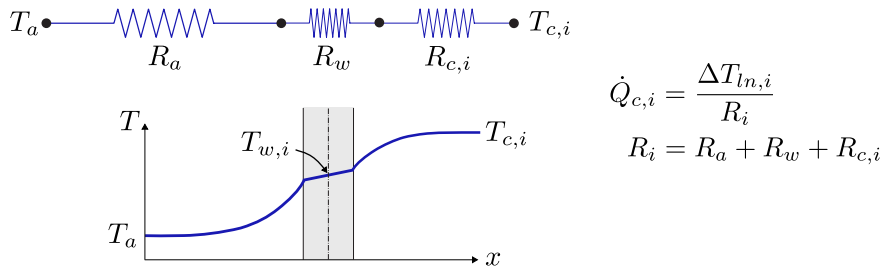
Figure 3.13.: Conduction (wall) and convection (air and coolant) resistance network for a single heat exchanger cell.

R_i is the overall resistance per cell and $\Delta T_{ln,i}$ is the logarithmic mean temperature difference. The resistance is calculated from a series connection of the *convection resistance* between the cooling air flow and the wall R_a, the *conduction resistance* in the heat exchanger wall R_w and the *convection resistance* between the coolant fluid flow and the wall $R_{c,i}$. It is given as

$$
\begin{aligned}
R_i &= R_a + R_w + R_{c,i} = \left(\frac{1}{h_a A_a}\right) + \left(\frac{l}{k A_w}\right) + \left(\frac{1}{h_c A_c}\right), \\
h_c &= f_c(\dot{m}_c, T_{c,i}), \quad h_a = f_a(\dot{m}_a, T_a),
\end{aligned}
\tag{3.47}
$$

where h_c is the fluid side heat transfer coefficient that is a function of coolant mass flow and temperature and can be calculated from Nusselt correlations, as shown in Fig. 2.8. Cell heat transfer area on coolant and air side (A_c, A_a) as well as the wall conduction resistance R_w, are known constant model parameters (same for each cell). To derive the air side heat transfer coefficient h_a, for heat exchangers with a louvered fin geometry, the *Chang and Wang* Nusselt correlation, as shown in Eq. 2.43, is used. The *mean*

temperature difference $\Delta T_{ln,i}$ between air and coolant is calculated for each cell from

$$\Delta T_{ln,i} = (\Delta T_{1,i} - \Delta T_{2,i}) \left(\ln \left| \frac{\Delta T_{1,i}}{\Delta T_{2,i}} \right| \right)^{-1} ,$$

$$\Delta T_{1,i} = T_a - T_{c,i} , \quad \Delta T_{2,i} = T_{ao,i} - T_{c,i} ,$$

$\quad$ (3.48)

where $T_{ao,i}$ is the cell specific air outlet temperature which is calculated from the quasi static analytical solution for the air temperature distribution along flow direction:

$$T_{ao,i} = T_{a,i} + \left(1 - e^{-\frac{h_a A_a}{\dot{m}_a c_{p,a}}} \right) (T_{w,i} - T_a) \tag{3.49}$$

where $T_{w,i}$ is the mean wall temperature of the cell, given as

$$T_{w,i} = (h_c A_c)^{-1} \dot{Q}_{c,i} + T_{c,i} .$$

Note that the calculation of $\dot{Q}_{c,i}$ from (3.46) is not explicit since $\dot{Q}_{c,i}$ also occurs on the right hand side of the equations. The influence showed up to be of minor importance in the present application, thus the wall temperature $T_{w,i}$ is calculated from $\dot{Q}_{c,i}$ of the last iteration (1/z operator in Simulink).

For each cell following assumptions are made for one time step:

- Homogeneous fluid (coolant) temperature;
- Homogeneous wall temperature and
- Variable air temperature (in direction of the flow).

3.3.6. Expansion tank

The expansion tank component calculates the system pressure based on thermal expansion of the fluid in the network. It consist of an air volume over a coolant volume, which is compressed as the system heats up and the fluid volume increases. As a boundary condition it is presumed that the air temperature equals the fluid temperature in the expansion tank and that the ambient air pressure stays constant during the simulation. The initial air volume $V_{a,ref}$ in the tank and initial coolant volume in the system $V_{c,ref}$ for a given temperature T and density ρ are used to calculate coolant volume V_c and air volume V_a for each time step as

$$V_c = V_{c,ref} \frac{\rho_{c,ref}}{\rho_c} \quad \text{with} \quad \rho = \rho(T),$$

$$V_a = V_{a,ref} + V_{c,ref} - V_c. \tag{3.50}$$

The mass of air m_a in the system is known at each time step, thus under the assumption of thermal and mechanical equilibrium we can calculate the air pressure p_a from the ideal gas law as

$$p_a = \frac{m_a R_a T_c}{V_a} \tag{3.51}$$

where R_a is the gas constant for air and T_c is the current coolant and air temperature under the assumption that $T_a \equiv T_c$.

3.4. Solid network components

For the transient simulation of complex thermal networks the *thermal resistance concept* and *lumped system analysis* approach, as presented in section 2.1.5, is exploited. According lumped mass and heat transfer blocks from the Simulink library implementation are shown in Fig. 3.14:
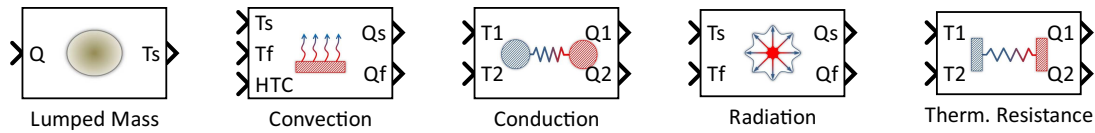
Figure 3.14.: Thermo Hydraulic Library - Solid network components.

Because a lumped system analysis is performed following assumption are made for each mass in the thermal network:

- Almost uniform temperature distribution within the mass with a Biot number $Bi < 1$ (as in Fig. 2.13) and;
- A solid with position dependent variation of temperature can be discretized into multiple lumped masses with an almost uniform temperature ($Bi < 1$).

In the following section the equations for a lumped mass heat storage and the heat transfer mechanisms that may occur between two lumped masses, are outlined.

3.4.1. Lumped mass

The lumped mass component works as energy storage and can be described with the first law of thermodynamics for closed systems. For solids the variation of the heat capacity with temperature and pressure can be neglected. Therefor the simplified form, as given in Eq. 2.14, is used:

$$m\,c\,\frac{dT}{dt} = \sum \dot{Q}.$$

$\sum \dot{Q}$ is the sum of the respective heat fluxes from heat input due to combustion, friction or electrical losses, or from heat transfer like convection or conduction. The lumped mass component can be interlinked with the Heat Bridge component, which is part of the fluid network, to calculate the heat flux from convection.

3.4.2. Heat transfer

For description of the heat transfer between lumped mass components in a thermal network the thermal resistance concept, as introduced in Eq. 2.51, is exploited. It is used to describe contact resistances, conductive heat transfer between lumped masses and convection and radiation with the ambient. It can be given as

$$\dot{Q} = \frac{\Delta T}{R} \quad \text{with} \quad \Delta T = T_i - T_j \tag{3.52}$$

where T_i and T_j are the temperatures of the two interconnected lumped masses, or the temperature of a lumped mass and the ambient air temperature, in case of convective heat transfer.

3.5. Airpath

The path of the cooling air flow that is entering at the vehicle grill, then passes through the heat exchangers and fans of the cooling package before leaving at the vehicle underbody, is called *airpath*.

Airpath analysis is used to determine the flow resistance, vehicle speed v and fan speed n dependent *air mass flow* through the radiators, as shown in Fig. 3.15, in order to calculate the heat exchanger performance, as shown in section 3.3.5.
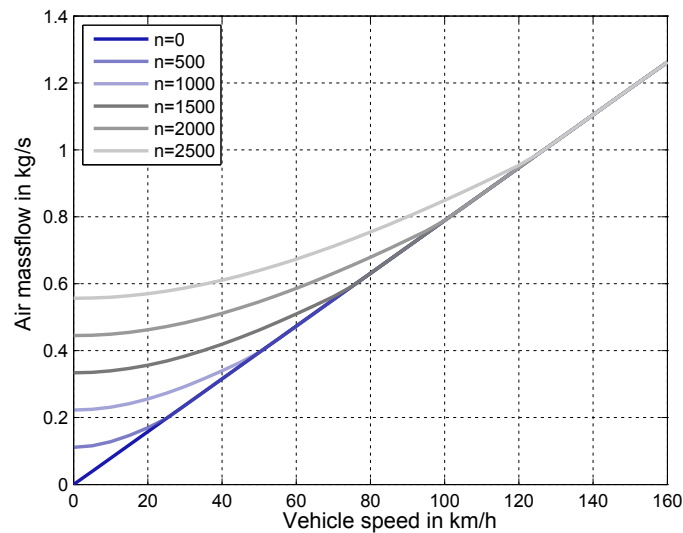
Figure 3.15.: Vehicle and fan speed dependent cooling air mass flow for a c-segment vehicle.

In Fig. 3.16 the toolbox components for the treatment of the cooling airflow are shown. It consists of a vehicle speed dependent pressure source called *Velocity pressure* and a fan activation dependent source called *Fan*. Flow resistances along the flow path may come directly from the heat exchanger component in the fluid network or can be defined by the *Flow resisitance* component (in series or parallel).
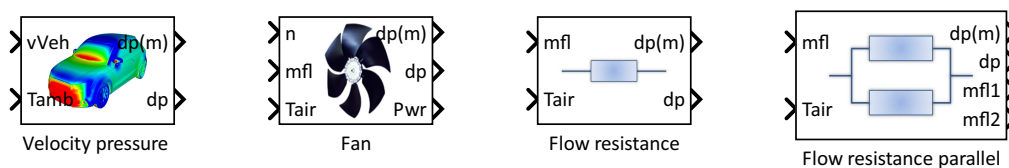
Figure 3.16.: Thermo Hydraulic library toolbox components for vehicle *airpath* modeling.

The air flow along a virtual stream tube through the vehicle underhood can be calculated by applying the energy equation, given in Eq. 2.67, to a control volume with one inlet (vehicle grill) and one outlet (underbody). Neglecting pressure difference from elevation yields for the energy equation

$$\left(p + \frac{\rho}{2}\, v^2\right)_{in} + \Delta p_p = \left(p + \frac{\rho}{2}\, v^2\right)_{out} + \Delta p_f. \tag{3.53}$$

73

In vehicle aerodynamics and 3D-CFD simulation it is common to describe the pressure distribution over a body with the dimensionless number C_p, called *pressure coefficient* which is defined as

$$C_p = \frac{p - p_\infty}{\frac{1}{2}\rho\, v_\infty^2} = \frac{\text{Static pressure}}{\text{Velocity pressure}}. \tag{3.54}$$

where p_∞, v_∞ and ρ are the respective static pressure, velocity and density of the free undisturbed stream and p is the static pressure at a specific point on the surface of a body. The pressure coefficient describes the relation between static and velocity pressure or how much of the dynamic pressure is converted into static pressure. Its maximum value is one, at the stagnation point[3], and zero if the pressure equals the free stream pressure. Also negative values can be reached if a slight negative static pressure difference occurs due to a local flow acceleration e.g.: at the car underbody as shown in Fig 3.17.
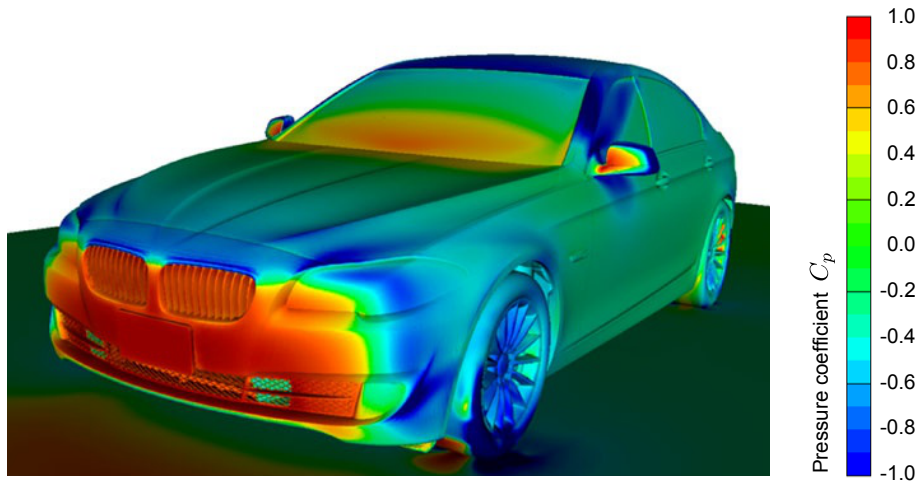
Figure 3.17.: Pressure coefficient distribution on a vehicle front [66].

With that in mind the pressure coefficient for the inlet and outlet of the airpath are defined as

$$C_{p,in} = \frac{p_{in} - p_\infty}{\frac{1}{2}\rho\, v_\infty^2} \quad \text{and} \quad C_{p,out} = \frac{p_{out} - p_\infty}{\frac{1}{2}\rho\, v_\infty^2}. \tag{3.55}$$

For vehicle applications the free stream velocity equals the driving speed of the vehicle $v_\infty = v_{veh}$. Rearranging Eq. 3.55 for p_{in} and p_{out} and combination with the energy equation (Eq. 3.53) gives

$$\frac{1}{2}\rho v_{veh}^2(C_{p,in} - C_{p,out}) + \frac{\rho}{2}\, v_{in}^2 + \Delta p_p = \frac{\rho}{2}v_{out}^2 + \Delta p_f. \tag{3.56}$$

---

[3]At the stagnation point the total velocity pressure of the free stream is converted into static pressure.

Transformation of this equation into a mass flow dependent form with $v = \frac{\dot{m}}{\rho A}$ yields

$$\frac{1}{2}\rho\, v_{veh}^2(C_{p,in} - C_{p,out}) + \left(\frac{\dot{m}^2}{2\rho\, A^2}\right)_{in} + \Delta p_p = \left(\frac{\dot{m}^2}{2\rho\, A^2}\right)_{out} + \Delta p_f. \tag{3.57}$$

For quasi static incompressible flow in a stream tube with one inlet and one outlet ($\dot{m}_{in} = \dot{m}_{out}$) the airpath equation simplifies further to

$$\frac{1}{2}\rho\, v_{veh}^2(C_{p,in} - C_{p,out}) + \left[\left(\frac{1}{2\rho\, A^2}\right)_{in} - \left(\frac{1}{2\rho\, A^2}\right)_{out}\right]\dot{m}^2 + \Delta p_p = \Delta p_f \tag{3.58}$$

where the left hand side of the equation accounts for the pressure increase due to driving speed (*Velocity pressure* component) and pressure increase due to fan activation Δp_p (*Fan* component), which is a function of fan speed, air temperature and mass flow, as shown in Eq. 2.96.

On the right hand side Δp_f is the overall pressure drop which accounts for the sum of friction losses along the stream tube. Flow resistance include among others; resistances due to inlet grill, heat exchangers and blocking by engine parts. To determine the overall pressure drop the solution of a simple flow network is usually required, as shown in Eq. 2.102. This network can be build up from *Flow resistance* components. With the overall flow resistance we can write for the pressure drop due to friction:

$$\Delta p_f = K_{tot}\, \dot{m}^2. \tag{3.59}$$

Finally, it can be seen that equation 3.58 leads to a second order polynomial which can be solved directly in terms of mass flow by a root finding algorithm.

<div style="text-align: right; font-size: 4em;">4</div>

Global vehicle simulation modeling

This chapter describes the global vehicle simulation model. The Future Hybrid demonstrator vehicle is used as example application. Firstly the overall vehicle and powertrain objectives and features are presented. Secondly the simulation modeling and co-simulation approach is described. Therefore the simulation model architecture and signal flow diagram are given. Then the thermal plant model is discussed in more detail. Regarding the conventional powertrain the cooling and lubrication circuits as well as the combustion engine thermal network are presented. Additionally the heat release and fuel consumption models are discussed. Afterwards the required thermal networks and fluid circuits for the thermal characterization of the electrical powertrain are outlined. Finally the Thermo-Fluid Library components are used for the software implementation in MATLAB/Simulink.

4.1. Future hybrid demonstrator vehicle

4.1.1. Overview

The AVL's "Future Hybrid[1]" demonstrator, as shown in Fig. 4.1, is based on a C-segment vehicle with an All Electric Range (AER) target of 30km (in the NEDC cycle), an acceleration from 0 to 100km/h in below 10sec and a certified CO_2 emission target of 35 gCO_2/km. The drive-train engineering task is driven by challenging component efficiency targets and intelligent operation strategies to achieve best CO_2 emission results, also in the charge sustaining mode. In this mode the battery SoC needs to be sustained when fulfilling the target limits of 79 gCO_2/km. This benchmark is directly relevant for customer perception of the vehicle's efficiency advantages in real-world customer drive cycles. In addition the transmission product cost must be kept min 10% below the industry benchmark. This should be achieved by utilizing only a single EM and by reducing hardware complexity. The targets require taking a holistic perspective of the drive train and its vehicle integration task along the development process by balancing of the key drive-train components.

---

[1]The vehicle is part of the future mobility lighthouse project "VECEPT" (Vehicle with cost efficient powertrain) founded by the Austrian government "Klima und Energie Fonds".

Figure 4.1.: Future Hybrid demonstrator vehicle [67].

The philosophy behind the PHEV drivetrain can be summarized as:

- "Best in Class" HEV regarding FC,
- Competitive constant velocity FC and
- "Best in Class" add-on costs for PHEV drivetrain.

To reach these objectives following key requirements can be identified:

Table 4.1.: Future hybrid demonstrator vehicle - Key requirements [14].

Top Level Specification	Unit	Description
Vehicle Class	-	C-segment (e.g. VW Golf MQB)
Vehicle Hybrid Architecture	-	Powersplit
Transmission	-	AVL transmission
ICE	-	1.2l, TGDI
CO_2 emission (Charge Sustaining Mode NEDC)	g/km	< 79 ($\equiv$ 3.2 l/100km)
Electric Range (AER in NEDC)	km	>30
Acceleration 0-100km/h (Hybrid)	s	<11
Max. velocity (ICE only)	km/h	>170

To fulfill the requirements listen in Tab. 4.1 a *power split* hybrid vehicle architecture, as shown in Fig. 4.2, is used. The Future Hybrid Transmission works as power split device which allows two power paths from the power sources to the wheels that can be either conventional (from ICE) or electrical. Since the electrical motor offers high torque at low speeds it is used to compensate the combustion engine's torque deficiency at low speeds. Therefore a smaller and simpler combustion engine with high efficiency can be used. The normal Otto cycle (high power density) is replaced by a Miller cycle [68] (low power density, less low-rpm torque, higher fuel efficiency). In a miller cycle engine the intake valve does not close at the beginning of the compression stroke. Thus the air/fuel mixture is pushed back into the intake port which reduces pumping losses and decreases engine power. This power loss is compensated by a turbocharger and an intercooler, resulting in

a lower intake charge temperature at a lower compression. The resulting NO_X emissions decrease and the ignition timing can be advanced for a higher combustion efficiency.
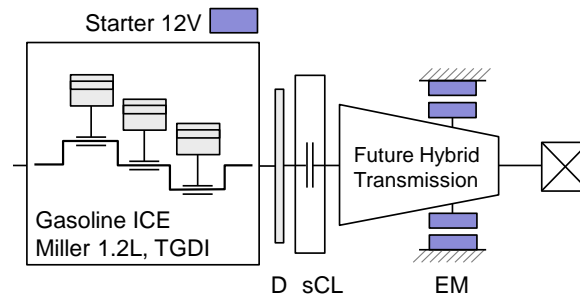
Figure 4.2.: Future Hybrid demonstrator vehicle powertrain configuration [67].

4.1.2. Future Hybrid transmission

The Future Hybrids vehicle comprises a state-of-the-art transmission and consist of only 4 shift elements, 1 EM (electric motor) and planetary gear sets. It is a compact and light weight transmissions with low production costs. The operation strategy which includes transient shifts is a key component for operating this automated transmissions [69]. It is capable of running in eCVT-mode, pure electrically and conventionally with parallel EM.

Eight different driving modes are available, as can be derived from the transmission schema depicted in Fig. 4.3:

- 5 parallel hybrid modes which can combine ICE and EM power,
- 2 electric driving modes to reduce EM torque demand and improve EM efficiency,
- 1 torque-split mode for ICE vehicle launch at low battery SoC.

The hybrid powertrain also supports following additional features, among others:

- Electric boost and recuperation,
- Charging at standstill with one clutch or in eCVT mode,
- Detaching the ICE during recuperation for better efficiency.
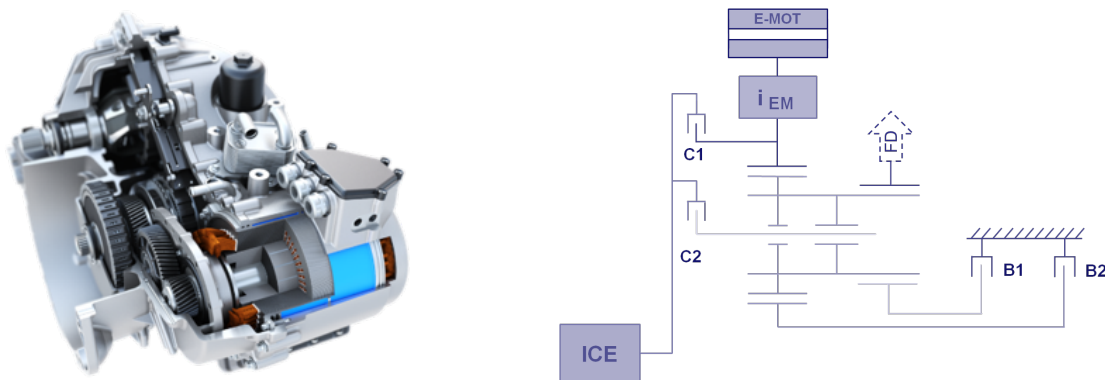
Figure 4.3.: Future Hybrid transmission drawing and schema [67].

4.2. Simulation model architecture

As mentioned in the introduction chapter (section 1.3.2) the complete vehicle needs to be considered for a comprehensive CO_2, emission and durability optimization approach. It is also required for the development of control strategies. Therefore a global vehicle simulation model is setup to consider the complete vehicle including all interactions between the subsystems. The complex interrelations between thermal management and dynamic vehicle behavior can be solved in terms of:

- Influence of the temperature on the powertrain efficiency (e.g.: higher gearbox and engine friction leads to a higher fuel consumption or higher ohmic battery losses at lower temperatures cause higher heat losses),
- Impact of the cooling system actuator power consumption on energy and fuel consumption, and therefore on the SoC dependent vehicle operating mode,
- Combined thermal and electrical battery aging influencing factors.

For the present work the global vehicle simulation model is split up into four main parts, as illustrated in Fig. 4.4:

- Boundary Conditions,
- Vehicle and Hybrid Control Unit (HCU),
- Thermal Management Controller,
- Thermal Plant.

Typically each engineering domain has it's established tools, therefore it is often required to perform a co-simulation [70, 71] to handle and synchronize the model data exchange. Since the thermal plant model, the thermal controller and the boundary conditions are implemented in the multi domain simulation tool MATLAB Simulink [72] it is sufficient to co-simulate it with the vehicle driveline simulation tool AVL-CRUISE [73] to build the global vehicle simulation model.

The simulation *boundary conditions* are ambient temperature, reference vehicle speed and road gradient. Drive cycle inputs are generated from statistically analyzed real world vehicle usage data. This statistical approach is called *usage space analysis* and is explained in more detail in section 6.3.1.

These boundary conditions are input to a virtual driver model, which is part of the *Vehicle and HCU* subsystem. The driver mode generates a load signal depending on the deviation between reference velocity and current vehicle velocity. From this load signal the *vehicle and HCU* model calculates temperature, road gradient and vehicle speed dependent driving resistances and the required torque to overcome the resistances and to follow the reference speed. The currently best torque split between electrical and conventional powertrain is calculated by a *mode rating* algorithm [74] in the HCU. Besides the driving torque additional torque may be requested from ICE (by the HCU) in order to charge the battery and to shift the engine operating point towards a significantly more efficient region (often called *load point shifting* [75]). In the powertrain models the actual torque outputs, under consideration of all resistances and efficiency losses, are calculated. Additionally, temperature and operating condition dependent heat losses are calculated and provided as input for the *thermal plant model*. Rejected heat is calculated from torque, speed and temperature dependent loss maps for conventional powertrain compo-
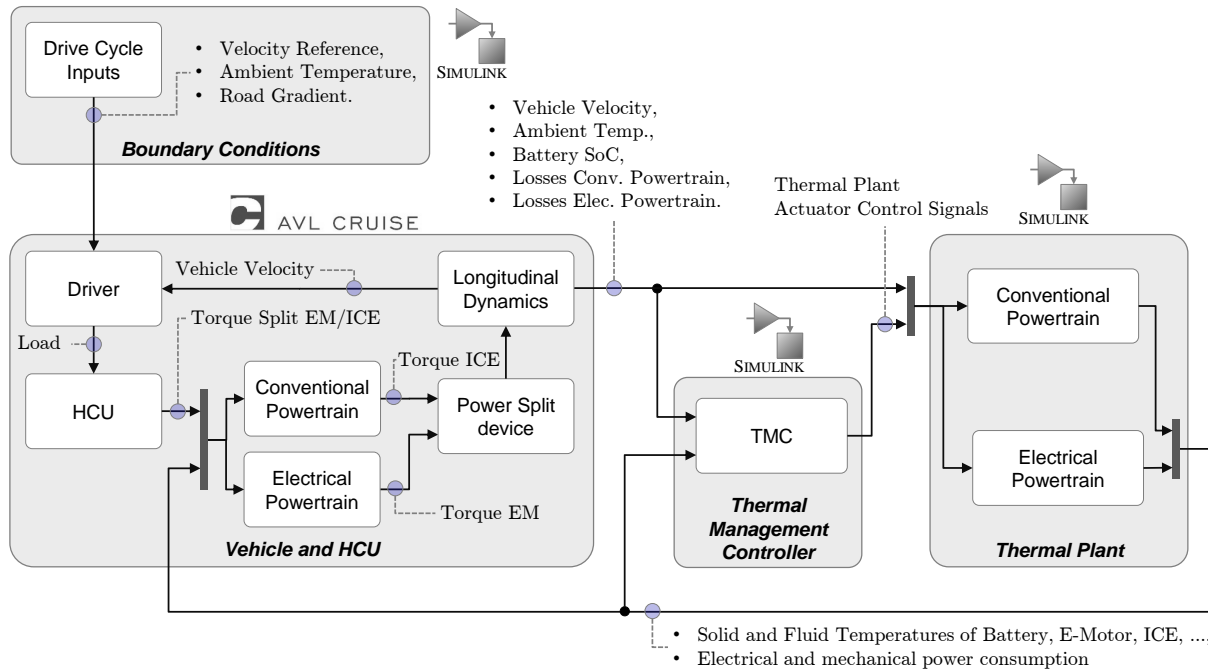
Figure 4.4.: Global vehicle simulation model subsystems, tools and signal flow overview.

nents (engine, gearbox and transmission) and from current, voltage, SoC and temperature dependent correlations for the electric powertrain. Torque generated or consumed by the conventional and electrical powertrain is split and converted by the *power split device.* The remaining driving Torque is balanced with the driving resistances in the *Longitudinal Dynamics* model. From the force balance contained therein the vehicle acceleration and the current vehicle speed is calculated. The task of the *Thermal Management Controller* is to keep, and not to exceed, defined temperature limits for all relevant components. For the combustion engine the strategy can be summarized as: "Run as hot as possible". This automatically reduces friction and minimizes parasitic losses from auxiliaries. Conversely, keeping all components of the electric powertrain always at the preferred low temperature level to avoid aging under any conditions (driving, parking, charging, etc.) will result in high energy consumption which is in contradiction to the efficiency targets. Therefore the Thermal Management Controler (TMC) control strategy is always a balance between efficiency and component durability. As inputs for the thermal controller, signals from the vehicle and HCU model feedback from the thermal plant are used. The required thermal system actuator control signals are provided as output. Detailed information about the Thermal Management Controller can be found in section 5.1.2.

The *thermal plant model,* consists of multiple cooling and lubrication circuits and lumped mass thermal networks for all relevant components. Heat rejection, vehicle speed and actuator control signals are considered for calculation of the fluid and component temperatures, flows and pressures. Also the mechanical and electrical power consumed for cooling and heating is calculated. This signals are feed back to the vehicle and HCU model for consideration in the vehicle fuel- and electric energy consumption, heat loss and efficiency calculation.

Thermal systems of electrified vehicles are increasing in complexity since additional electronic components require conditioning at various temperature levels. The analyzed PHEV thermal system consists of 5 major cooling and lubrication circuits, as shown in Fig. 4.5:

- High temperature ICE cooling,

- High temperature ICE lubrication,

- Low temperature AC chiller battery cooling,

- Low temperature electronics cooling (Inverter, E-Motor, Battery),

- Medium temperature gearbox lubrication.

Some of the cooling and lubrication circuits are connected via plate heat exchangers which are then called *oil coolers*. Thus the ICE oil cooler enables heat flux between the ICE cooling and lubrication circuit and the transmission oil cooler transfers heat between the transmission oil and electronics cooling circuit. The plate heat exchanger that connects the electronics cooling circuit with the refrigerant circuit is called chiller. It allows to decrease the temperature of the battery coolant below ambient temperature. In the airpath subsystem, as shown in Fig. 4.5, quantity and temperature of the cooling airflow is calculated. The cooling airpath also connects the AC system with the electronics cooling system and the ICE cooling system. Therefore the air is heated up as is flows through the condenser and low temperature heat exchanger before it enters the ICE heat exchanger.

Insight into the chosen thermal modeling approach for cooling/lubrication circuits and components in the conventional and electrical powertrain are given in section 4.3 and 4.4, respectively.

GBX	Gear Box	AC	Air Conditioning
OC	Oil Cooler	Cond	Condenser
LT	Low Temperature	HX	Heat Exchanger
HT	High Temperature	CAC	Charge Air Cooler
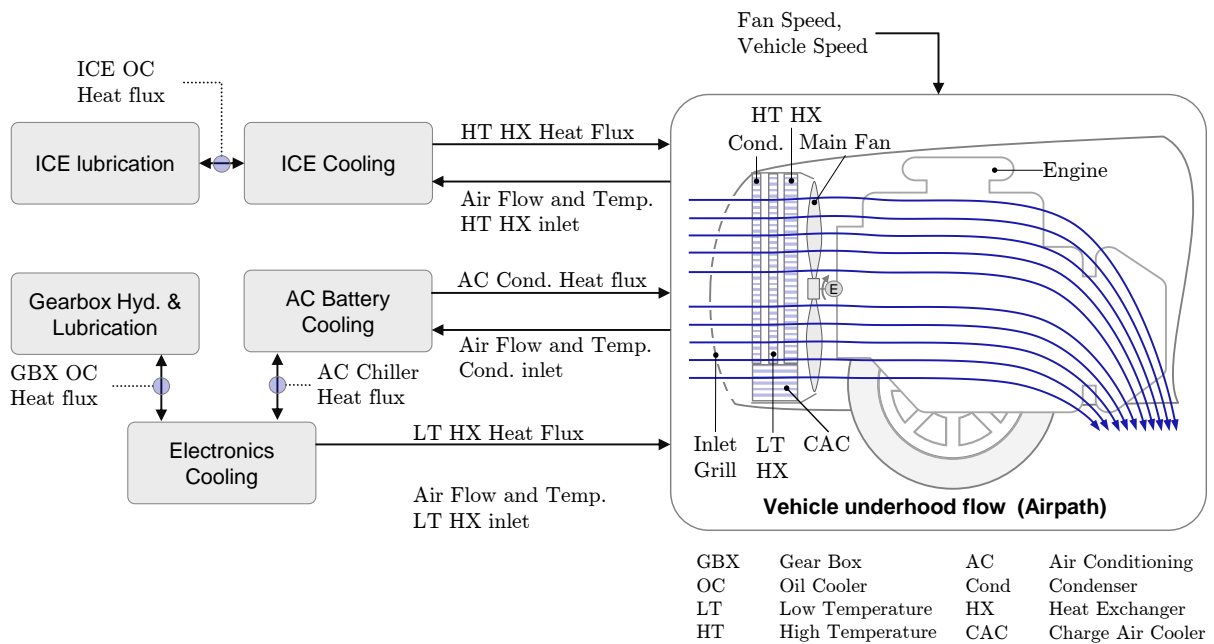
Figure 4.5.: Thermal plant model subsystem overview and signal flow.

4.3. Conventional powertrain

The central piece of the conventional powertrain thermal model is the combustion engine thermal network, which is described in section 4.3.1. Therefore, a network consisting of lumped masses and thermal resistances is used to balance and distribute heat in the combustion engine. Heat input to the thermal network origins from combustion wall heat flux and heat flux at the intake and exhaust port, as outlined in section 4.3.2. Additional solid and fluid heat input is generated by friction, as described in section 4.3.3. To prevent overheating of the engine structure cooling and lubrication circuits are used to reject heat to the ambient air, as described in section 4.3.4.

4.3.1. Thermal network

For the calculation of engine structure temperatures the heat flux due to combustion, friction and heat transfer between structure, coolant, oil and ambient air needs to be balanced. Since the thermal conditions are considered to be almost equal for each cylinder, it is generally sufficient to analyze only one representative cylinder. In order to assess engine temperature (e.g. liner temperature) dependent effects like fuel consumption (influenced by friction) and emissions it is necessary to describe the dynamic engine warm-up behavior in appropriate depth. Therefore the combustion engine is discretized into volumes of similar temperatures. This is required to qualify the engine structure for lumped system thermal analysis (as introduced in section 2.1.5). The chosen discretization granularity in this work is loosely based on the approach introduced by Samhaber [76]. It lies somewhere between the two proposed discretization levels coarse (4 lumped masses) and medium (14 lumped masses). Thus, for the analysis of the 3 cylinder Future Hybrid engine a thermal network that consists of 7 lumped *structural masses* and 5 *fluid masses* which are connected via 25 heat transfer resistances, is used. The lumped mass partitioning and the interconnecting thermal resistances are shown in Fig. 4.6. The structural masses are defined as

m_1 Piston and upper liner,

m_2 Cylinder head intake port side,

m_3 Cylinder head exhaust port side and turbo charger,

m_4 Lower liner and upper case,

m_5 Con-rod, crankshaft and lower case,

m_6 Cylinder head cover and camshafts and

m_7 Oil pan.

The fluid masses are defined as

m_{ci} Engine head, intake port coolant mass,

m_{ce} Engine head, exhaust port coolant mass,

m_{cb} Engine block coolant mass,

m_{op} Oil pan oil mass and

m_{ot} Turbo charger oil mass.
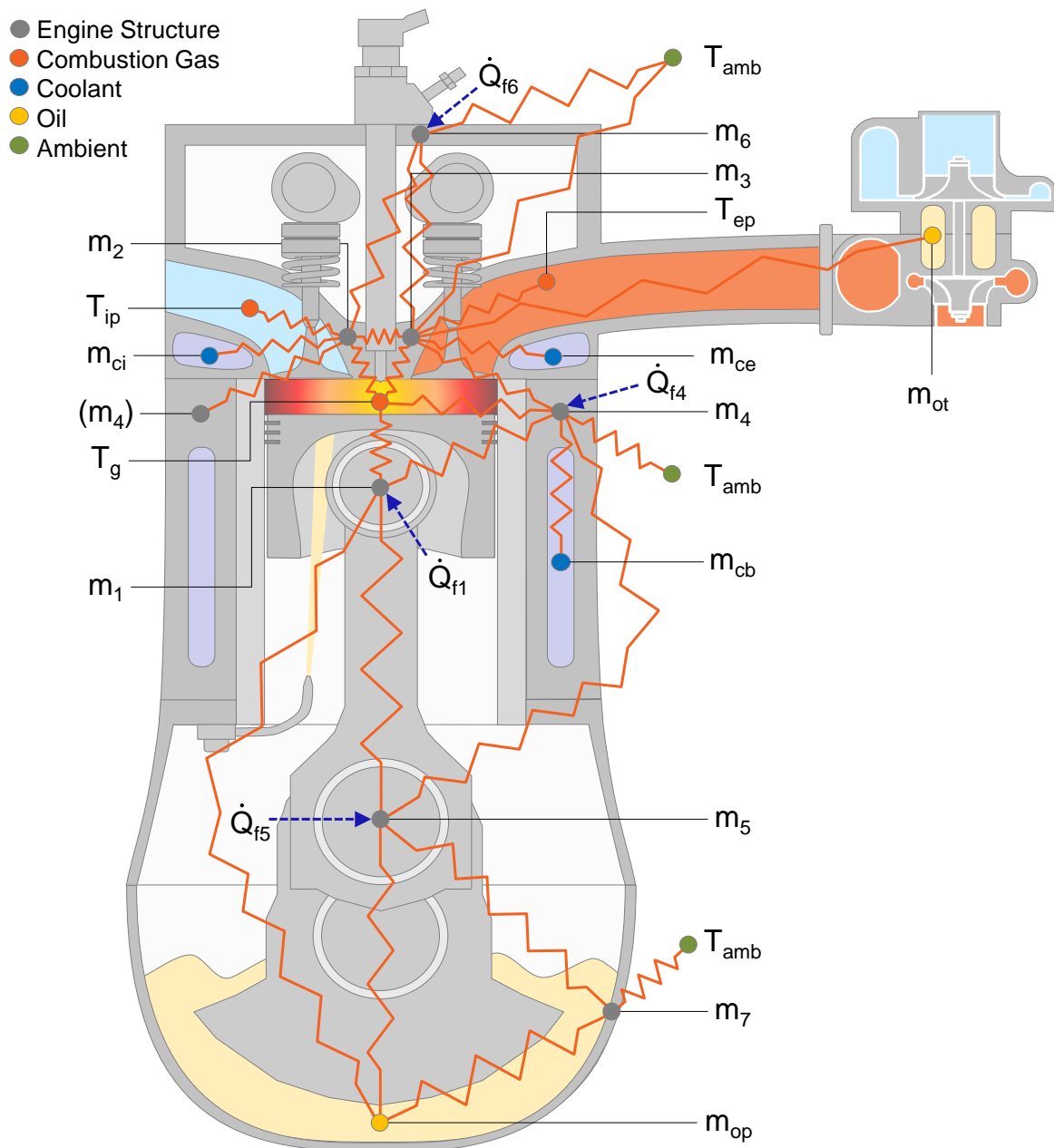
Figure 4.6.: Combustion engine lumped mass thermal network discretization and thermal resistances.

The transient thermal behavior (temperatures of the masses and heat fluxes) can be described by the first law of thermodynamics for closed and open systems, for the solid and fluid masses, as introduced in Eq. 2.14 and 2.15, respectively. In application of the thermal resistance concept, as can be recalled from Eq. 2.51, the equations for the solid structural masses can be given as

$$
\begin{aligned}
m_1\, c_1 \frac{dT_1}{dt} &= \frac{(T_4 - T_1)}{R_{4,1}} + \frac{(T_5 - T_1)}{R_{5,1}} + \frac{(T_{op} - T_1)}{R_{op,1}} + \dot{Q}_{g,1}, \\
m_2\, c_2 \frac{dT_2}{dt} &= \frac{(T_3 - T_2)}{R_{3,2}} + \frac{(T_{ci} - T_2)}{R_{ci,2}} + \frac{(T_4 - T_2)}{R_{4,2}} + \frac{(T_6 - T_2)}{R_{6,2}} + \dot{Q}_{g,2} + \dot{Q}_{ip}, \\
m_3\, c_3 \frac{dT_3}{dt} &= \frac{(T_{amb} - T_3)}{R_{amb,3}} + \frac{(T_2 - T_3)}{R_{3,2}} + \frac{(T_4 - T_3)}{R_{4,3}} + \frac{(T_6 - T_3)}{R_{6,3}} + \frac{(T_{ce} - T_3)}{R_{ce,3}} \\
&\quad + \frac{(T_{ot} - T_3)}{R_{ot,3}} + \dot{Q}_{ep} + \dot{Q}_{g,3}, \\
m_4\, c_4 \frac{dT_4}{dt} &= \frac{(T_{amb} - T_4)}{R_{amb,4}} + \frac{(T_{cb} - T_4)}{R_{cb,4}} + \frac{(T_1 - T_4)}{R_{4,1}} + \frac{(T_2 - T_4)}{R_{4,2}} + \frac{(T_3 - T_4)}{R_{4,3}} \\
&\quad + \frac{(T_5 - T_4)}{R_{5,4}} + \dot{Q}_{g,4}, \\
m_5\, c_5 \frac{dT_5}{dt} &= \frac{(T_1 - T_5)}{R_{5,1}} + \frac{(T_4 - T_5)}{R_{5,4}} + \frac{(T_{op} - T_5)}{R_{op,5}} + \frac{(T_7 - T_5)}{R_{7,5}} \quad, \\
m_6\, c_6 \frac{dT_6}{dt} &= \frac{(T_{amb} - T_6)}{R_{amb,6}} + \frac{(T_2 - T_6)}{R_{6,2}} + \frac{(T_3 - T_6)}{R_{6,3}}, \\
m_7\, c_7 \frac{dT_7}{dt} &= \frac{(T_{amb} - T_7)}{R_{amb,7}} + \frac{(T_{op} - T_7)}{R_{op,7}} + \frac{(T_5 - T_7)}{R_{7,5}},
\end{aligned}
\tag{4.1}
$$

and the equations describing the coolant and oil mass are given as

$$
\begin{aligned}
m_{ci}\, c_{ci} \frac{dT_{ci}}{dt} &= \frac{(T_2 - T_{ci})}{R_{ci,2}} + \dot{m}_{ci}(h_{ci,i} - h_{ci}), \\
m_{ce}\, c_{ce} \frac{dT_{ce}}{dt} &= \frac{(T_3 - T_{ce})}{R_{ce,3}} + \dot{m}_{ce}(h_{ci} - h_{ce}), \\
m_{cb}\, c_{cb} \frac{dT_{cb}}{dt} &= \frac{(T_4 - T_{cb})}{R_{cb,4}} + \dot{m}_{cb}(h_{cb,i} - h_{cb}), \\
m_{op}\, c_{op} \frac{dT_{op}}{dt} &= \frac{(T_1 - T_{op})}{R_{op,1}} + \frac{(T_5 - T_{op})}{R_{op,5}} + \frac{(T_7 - T_{op})}{R_{op,7}} + \dot{m}_{cb}(h_{op,i} - h_{op}), \\
m_{ot}\, c_{ot} \frac{dT_{ot}}{dt} &= \frac{(T_3 - T_{ot})}{R_{ot,3}} + \dot{m}_{cb}(h_{ot,i} - h_{ot}),
\end{aligned}
\tag{4.2}
$$

where T_1 till T_7 are the solid mass temperatures, T_{ci}, T_{ce} and T_{cb} are the coolant mass temperatures and T_{op} and T_{ot} are the oil mass temperatures. Parameters like component mass and conduction length, necessary for describing the thermal resistances R_*, are mainly derived directly from CAD data, as described in [76]. Remaining parameters are

derived from similar engines, using the AVL engine database and benchmark tool.

For resistances that connect two solid masses a constant conduction resistance (as shown in Eq. 2.51) can be used. The thermal resistance between solids and fluids is generally depending from the heat transfer coefficient which, in turn, is dependent from the current flow and temperature boundary conditions. Thus, for calculation of the convection resistance the solution of the thermo hydraulic network, for the cooling and lubrication circuit has to be known. The derivation of the required pressure drop and heat transfer correlations is shown in section 4.3.4. From known fluid velocity, temperatures and Nusselt correlations, as described in Eq. 2.35, the mean heat transfer coefficient and the temperature difference can be derived.

In Eq. 4.2 the heat flux from the combustion gas $\dot{Q}_{g,*}$ is calculated via Newton's law of cooling, as described in more detail in section 4.3.2. The intake and exhaust ports heat fluxes, $\dot{Q}_{ip}$, $\dot{Q}_{ep}$, are calculated as shown in section 4.3.2. Additional heat input from friction at piston $\dot{Q}_{f1}$, liner $\dot{Q}_{f4}$ and camshaft assembly $\dot{Q}_{f6}$ has to be considered in order to predict the correct engine warm-up behavior and fuel consumption. For the calculation of engine load, engine speed and temperature dependent friction heat losses a friction model, as shown in section 4.3.3, is used.

4.3.2. Heat release and fuel consumption

The combustion engine heat transfer between the combustion gas and the surrounding combustion chamber is commonly described by Newton's law of cooling, which can be recalled from section 2.1.3 as

$$\dot{Q}_w = h_w \sum_i A_{w,i} \left(T_g - T_{w,i} \right) \tag{4.3}$$

where i stands for the individual lumped engine masses, which are in contact with the combustion gas via the heat transfer surface area $A_{w,i}$. For the given thermal network these components are; piston, liner and cylinder head. In principle the combustion gas temperature T_g, the heat transfer coefficient h_w and the heat transfer area $A_{w,i}$ are crank angle dependent. But, for simplicity reasons, for all combustion chamber parts the same *cycle averaged* gas temperature T_g and heat transfer coefficient h_w is used to describe the convective heat transfer given in Eq. 4.3. The required wall surface temperatures $T_{w,i}$ of the cylinder walls are calculated in thermal network model, as shown in section 4.3.1, which is coupled with the heat release model.

Wall heat transfer h_w

Because of the complex flow and temperature boundary layer conditions in the combustion chamber the wall heat transfer coefficient h_w is found by using *Nusselt correlations*, which were initially derived by experiments. The most widely used wall heat transfer correlation is the formulation derived by Woschni [77]. Based on this approach Hohenberg [78] and Bargende [79] made improvements and adaptations for direct injection diesel engines and gasoline engines, respectively.

Intake and exhaust port heat transfer

In addition to the combustion chamber heat transfer, the heat transferred at the intake- and exhaust port needs consideration, because a significant amount of heat may be transfered there (depending on the operating condition). Almost all current correlations to describe the intake- exhaust port heat transfer rely on the formulations found by Zapf [80]. Based on stationary engine measurements he developed a Reynolds number and valve lift dependent Nusselt correlation for the intake- and exhaust port heat transfer coefficient, Nu_{ip} and Nu_{ep} respectively

$$
\begin{aligned}
Nu_{ip} &= 0.214\, Re^{0.68} \left(1 - 0.765 \frac{l_v}{D_i} \right), \\
Nu_{ep} &= 2.58\, Re^{0.5} \left(1 - 0.797 \frac{l_v}{D_i} \right),
\end{aligned}
\tag{4.4}
$$

where the term l_v/D_i represent the valve lift to valve seat inner diameter ratio.

Engine process simulation

The cycle averaged gas temperature T_g is derived for a combustion chamber energy balance within an engine process simulation [81]. Within the engine process simulation the thermal, fluid mechanical and chemical processes within the combustion chamber are analyzed. Due to the high flow turbulence and rapid changes in temperature, pressure and working gas composition the combustion process is highly nonlinear. Thus the gas temperature and wall heat transfer coefficient depend on space and time.

Many different engine modeling approaches ranging from *phenomenological* oriented approaches till *physics based* models exist. Depending on the spatial discretization of the combustion chamber the engine models are further categorized in *zero dimensional models*, where homogeneous conditions are assumed, and *one-or multidimensional models* where some of the state variables depend on space coordinates. Depending on the chosen modeling approach this calculations can be very time consuming.

In this work the commercial software tool AVL BOOST™[82] is used for engine process simulation. The calculation of the wall heat fluxes and calculation of intake- and exhaust port heat transfer coefficient are part of this simulation model. Also the fuel consumption, for any given operating condition, can be derived.

To allow an efficient integration into the global vehicle simulation model a reduced order model is requires. Therefor the engine process simulation model is furthermore used to generate *Indicated Mean Effective Pressure (imep)*, engine speed and temperature dependent heat flux and fuel consumption maps, as depicted in Fig. 4.7. These maps are then integrated into the vehicle driveline simulation model to calculate the operating point dependent fuel consumption and wall heat flux.

Mean effective pressure (*mep*) is a quantity that is used to describe the engine operating condition independent from the engine displacement, which allows comfortable comparison and assessment of different engines . The *mep* may be interpreted as the average pressure acting on a piston during the different portions of its cycle. It can be expressed
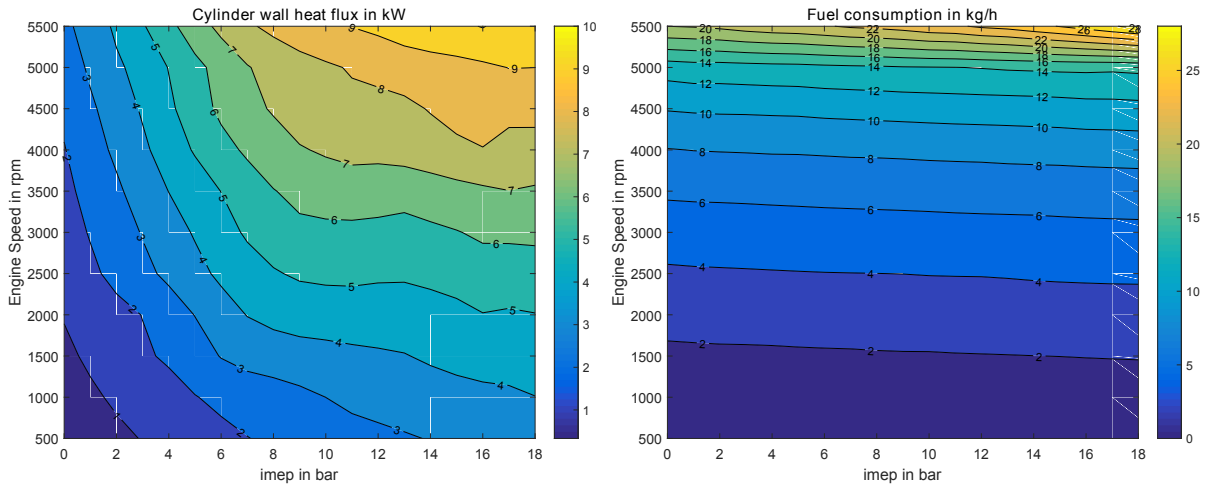
Figure 4.7.: Cylinder wall heat flux and Fuel Consumption map as a function of imep and engine speed for the engine at operating temperature.

in terms of engine torque as [81]

$$mep = \frac{2\pi\, n_R\, T_q}{V_d} \tag{4.5}$$

where

mep is the mean effective pressure in Pa,

n_R is the number of revolutions per work cycle (for a 4-stroke engine $n_R = 2$),

T_q is the engine torque in Nm,

V_d is the displacement volume in m^3.

Commonly used forms of the indicated pressure are:

$bmep$ is the mean effective pressure calculated from measured brake torque,

$imep$ is the net mean effective pressure calculated from in-cylinder pressure measurement over the complete engine cycle,

$fmep$ is the mean effective pressure loss due to friction.

In course of the global vehicle simulation the Brake Mean Effective Pressure (bmep) is calculated in the vehicle driveline simulation model from driving resistances. The Friction Mean Effective Pressure (fmep) is calculated from the friction model, as described in section 4.3.3. Consequently, the imep that needs to be provide by the engine to overcome driving resistances and friction is calculated from

$$imep = bmep + fmep. \tag{4.6}$$

4.3.3. Friction

For the prediction of engine friction losses Schwarzmeier [83] presented an approach for a combustion engine at operating temperature. It is based on experimental tribological research focusing on the assessment of part friction influences. The validity boundary

of the Schwarzmeier model is given as $T_{oil} > 40°C$. For the analysis of transient engine warm-up it is paramount that the full temperature range is covered by the friction model. Therefore, Reulein [84] suggested to extend the Schwarzmeier approach by an engine load and oil temperature dependent friction term:

$$p_{mfL} = C\frac{p_{me}}{T_{oil}^a}.$$

Finally, the Schwarzmeier friction model, extended by Reulein, which is valid for the cold engine as well as for the engine at operating conditions, can be given as shown in [85]:

$$
\begin{aligned}
fmep = fmep_x &+ C_1 \left(\frac{c_m}{T_{cw}^{1.68}} - \frac{c_{mx}}{T_{cwx}^{1.68}} \right) \\
&+ C_2 \left(\frac{p_{me}}{T_{cw}^{1.68}} - \frac{p_{mex}}{T_{cwx}^{1.68}} \right) + C_3 \left(\frac{(d\,n)^2}{T_{oil}^{1.49}} - \frac{(d\,n_x)^2}{T_{oilx}^{1.49}} \right) \\
&+ C_4 \left((1 + 0.012c_m)p_{me}^{1.35} - (1 + 0.012c_{mx})p_{mex}^{1.35} \right) \\
&+ C_5 \left(n^2 - n_x^2 \right) + C_6 \left(\frac{p_{me}}{T_{oil}^{1.49}} - \frac{p_{mex}}{T_{oilx}^{1.49}} \right)
\end{aligned}
\tag{4.7}
$$

where

$fmep$	is the friction mean effective pressure in Pa,
c_m	is the mean piston speed in m/s,
T_{cw}	is the cylinder wall (liner) temperature in °C,
p_{me}	is the mean effective pressure in bar,
d	is the mean conrod and main engine bearing diameter in m,
n	is the engine speed in $1/min$,
T_{oil}	is the engine oil temperature in °C,

with the mean piston speed c_m is defined as

$$c_m = \frac{s\,n}{30} \tag{4.8}$$

where s is the piston stroke. The term C_1 in Eq. 4.7 considers the oil temperature and piston speed dependent friction between piston and cylinder wall. Term C_2 considers the piston speed and engine load dependent friction of the piston assembly. The third term (C_3) accounts for the oil temperature and engine speed dependent conrod and main engine bearing friction losses. Part four (C_4) is used to consider the load and speed dependent losses of the fuel injection pump and part five (C_5) accounts for the auxiliaries (alternator and mechanical pumps and fans) power consumption, which is mainly engine speed related. The last part (C_6) reflects the influence of the engine load on bearing friction losses, at low engine oil temperatures.

For the prediction of engine friction at an arbitrary operating condition a reference condition is required (Reference values are indicated by the subscript x). The coefficients C_1, C_2, C_3, C_4, C_5 in Eq. 4.7 are calibrated in order to fit the engine friction measurements. For the given 3 cylinder engine the friction model fit is given in Fig 4.8. The coolant and oil temperature dependency, as shown in Fig. 4.9, indicates that the influence of the oil temperature on the fmep is significantly higher than those from the coolant temperature.
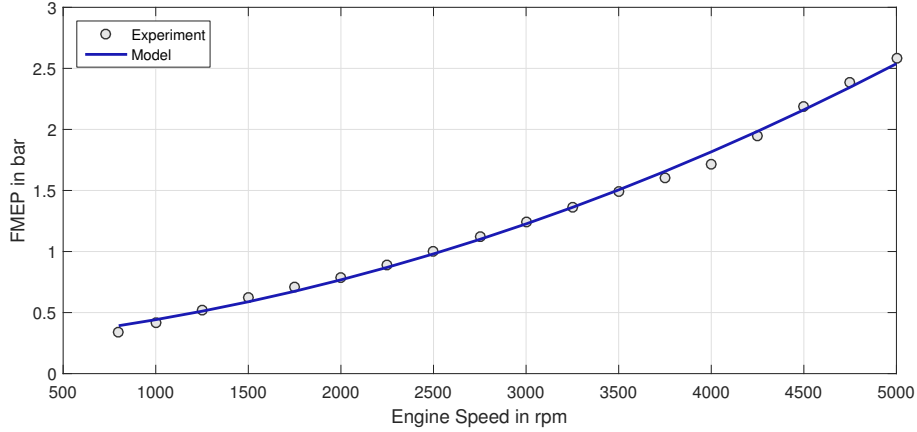
Figure 4.8.: Friction model verification for a TGDI engine at 90°C oil and water temperature and 110°C liner temperature.
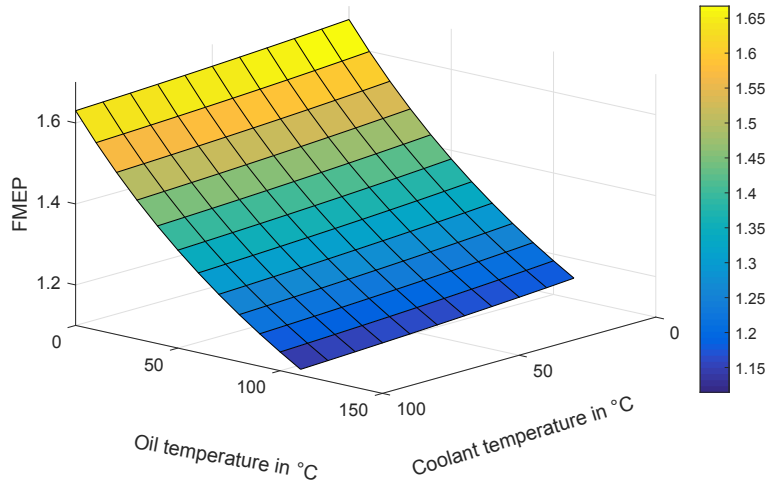
Figure 4.9.: Fluid temperature dependent friction map for a TGDI engine at an engine speed of 3000rpm and 45Nm torque.

With the presented friction model it is possible to predict the friction mean effective pressure, depending from operating point and thermal conditions (oil, water and liner temperature), in transient operation. The thermal conditions and the vehicle warm-up behavior are largely influenced by the friction heat loss. A large portion of the heat flux is going into the engine oil. Schwarzmeier proposed a correlation to calculate the oil friction heat flux under consideration of bearing, camshaft, crankshaft, piston assembly and oil pump friction as

$$
\dot{Q}_{foil} = \frac{V_D \, n \, 10^5}{120} \left[k_{oilx} \, p_{mfx} \qquad + C_1 \left(\frac{c_m}{T_{cw}^{1.68}} - \frac{c_{mx}}{T_{cwx}^{1.68}} \right) + C_2 \left(\frac{p_{me}}{T_{cw}^{1.68}} - \frac{p_{mex}}{T_{cwx}^{1.68}} \right) \right.
$$
$$
\left. + C_3 \left(\frac{(d \, n)^2}{T_{oil}^{1.49}} - \frac{(d \, n_x)^2}{T_{oilx}^{1.49}} \right) \quad + C_6 \left(\frac{p_{me}}{T_{oil}^{1.49}} - \frac{p_{mex}}{T_{oilx}^{1.49}} \right) \right] \tag{4.9}
$$

where V_D is the engine displacement volume and k_{oilx} is the oil heat flux portion for the given reference condition.

4.3.4. Cooling and lubrication

Modeling of the combustion engine cooling system requires consideration of the hydraulic and thermal behavior of the coolant and its connection to the oil and cooling air flow. Solution of the hydraulic flow network in therms of coolant flow, requires knowledge about flow resistances from piping and losses in components (engine head and block, heat exchanger,...). To make an a priori estimate about the flow distribution and quantity CAD data and 3D CFD simulations are used. For pipes as well as for simple minor losses like bends, diameter changes, junctions and other fittings the pressure drop characteristics can be derived with high accuracy from correlations found by experimental research, as mentioned in section 2.2.2.

The hydraulic resistance and the convective heat transfer coefficient in a complex engine cooling jacket can be found by using 3D-CFD. A transient coupling of 1D-CFD and 3D-CFD is theoretically possible but will result in unreasonably long calculations durations. Therefore a model order reduction from 3D to 1D-CFD is applied to reduce the required simulation wall clock time, without sacrificing the simulation quality.

All 3D-CFD simulations were conducted using in the commercial tool AVL FIRE in the version v2011.1 [86]. In Fig. 4.10 the calculation mesh is depicted which consists of the cylinder head, cylinder block, internal pipings as well as intake and outlet channels.
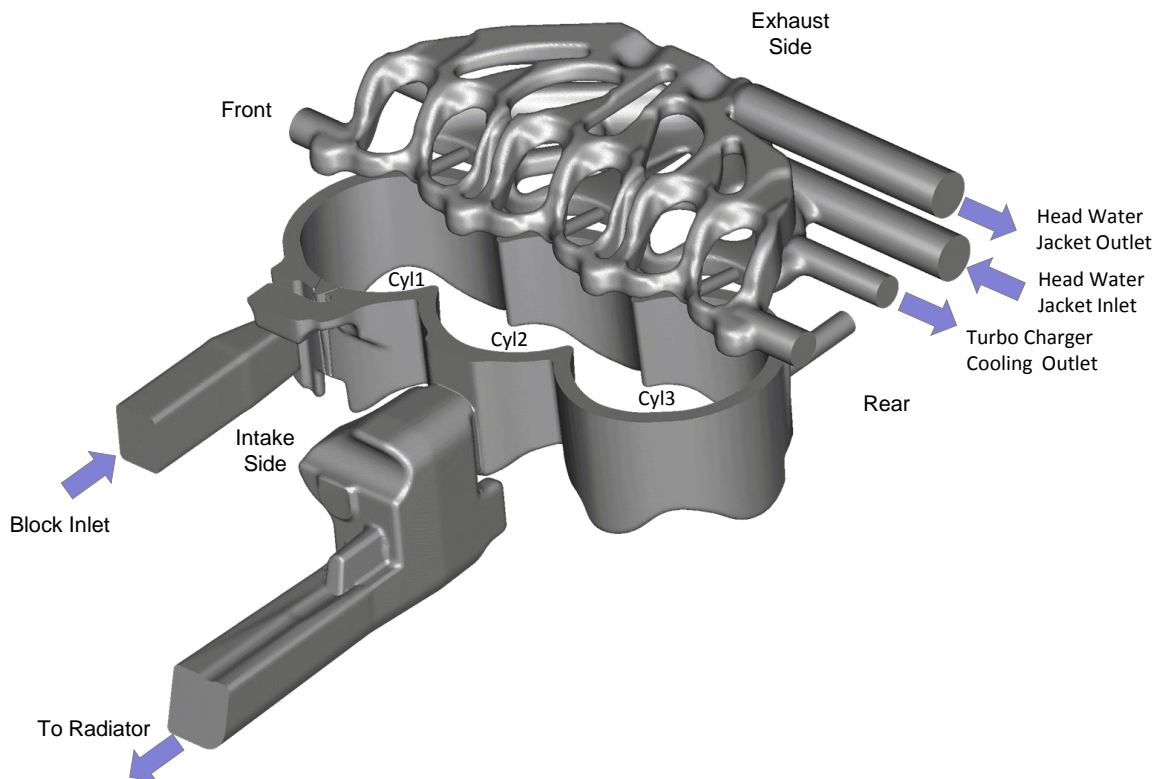
Figure 4.10.: Combustion engine water jacket 3D CFD calculation mesh [87].

Pressure drop

For the determination of the water jacket pressure drop multiple 3D-CFD simulations with a range of different boundary conditions are conducted. Therefore, volume flow and coolant inlet temperature at head and block are varied over the full operating range. Exemplary total pressure simulation results for the engine head and the block are depicted in Fig. 4.11.
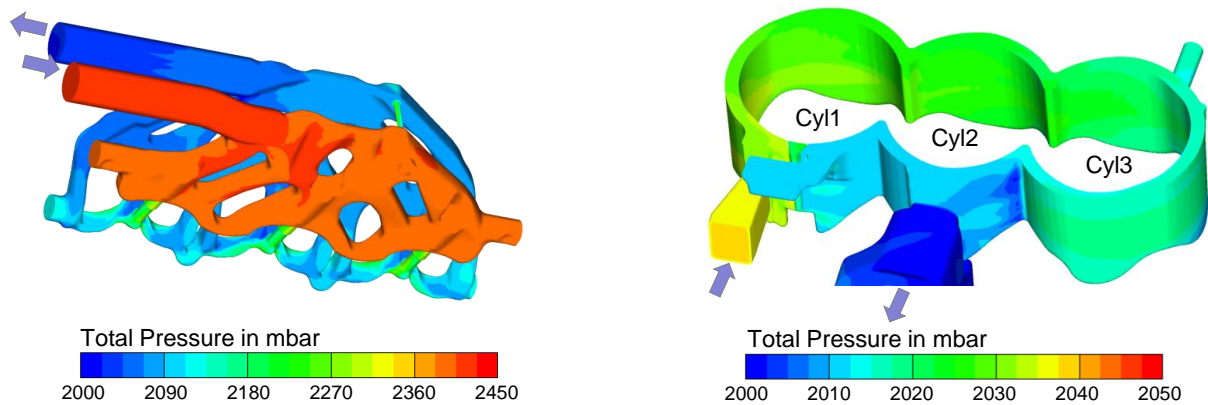
Figure 4.11.: Combustion engine water jacket 3D-CFD total pressure simulation results. Boundary conditions: volume flow rate at head 50l/min and at block 28l/min; coolant temperature at head and block inlet 90 °C; wall temperature ranging from 90 - 150 °C (from Finite element method (FEM) calculation) [87].

Some sort of model order reduction is required to find an equivalent 1D representation of the cooling jacket pressure drop.
From dimensional analysis [88] it can be found that the water jacket dimensionless pressure drop coefficient ζ (compare with Eq. 2.83), can be represented by a function ξ which is dependent from the Reynolds number Re (as introduced in Eq. 2.23):

$$\zeta = \xi(Re). \tag{4.10}$$

Therefore, a reduced oder model can be found by translating the pressure drop from simulation into a dimensionless form and correlating it with the Reynolds number. This function can then be used in the 1D-CFD cooling circuit simulations.

Heat transfer

Similar to the cooling jacket pressure drop calculation, 3D-CFD simulations were conducted under varying boundary conditions to determine the heat transfer coefficient in the head and block cooling channels. An exemplary simulation result for the local heat transfer coefficient is depicted in Fig. 4.12. To transfer the resulting local heat transfer coefficient into a simplified 1D representation a model order reduction is required. From dimensional analysis [6] it can be found that the mean dimensionless heat transfer coefficient, the *Nusselt number Nu* (as in Eq. 2.34), can be described by a function ψ which

is dependent from the Reynolds *Re* and Prandtl *Pr* number (as introduced in Eq. 2.23 and 2.29, respectively)

$$Nu = \psi(Re,\ Pr). \tag{4.11}$$

Therefore, the 1D representation of the water jacket heat transfer coefficient is found by fitting a function ψ such that with the resulting *mean* heat transfer coefficient the amount of transfered heat is equal to the resulting heatflux from 3D-CFD simulation. Since the engine structure is split up into multiple lumped masses, as shown in Fig. 4.6, one heat transfer correlation has to be found for each convection resistance (head intake side, head exhaust side and block). Thus, also the resulting heat flux from 3D-CFD simulation has to be split up accordingly to find the correct Nusselt correlation for each heat bridge.
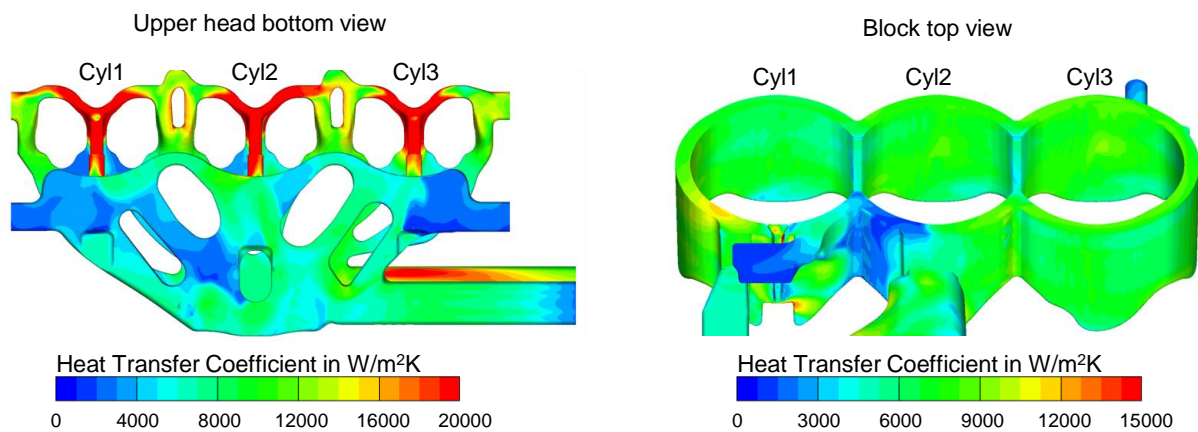
Figure 4.12.: Combustion engine water jacket 3d CFD heat transfer coefficient simulation results [87].

Cooling Circuit

The proposed methodology for the derivation of pressure drop and heat transfer of the engine cooling jacket is used together with discrete loss pressure drop formulations for pipes and channels to build up the complete cooling circuit. For components where no CAD data is available pressure drop and heat flux measurements or information from supplier data sheets are used to describe pressure drop and heat transfer characteristics.

The cooling circuit for the three cylinder turbo charged gasoline direct injection engine (TGDI) is depicted in Fig. 4.13.
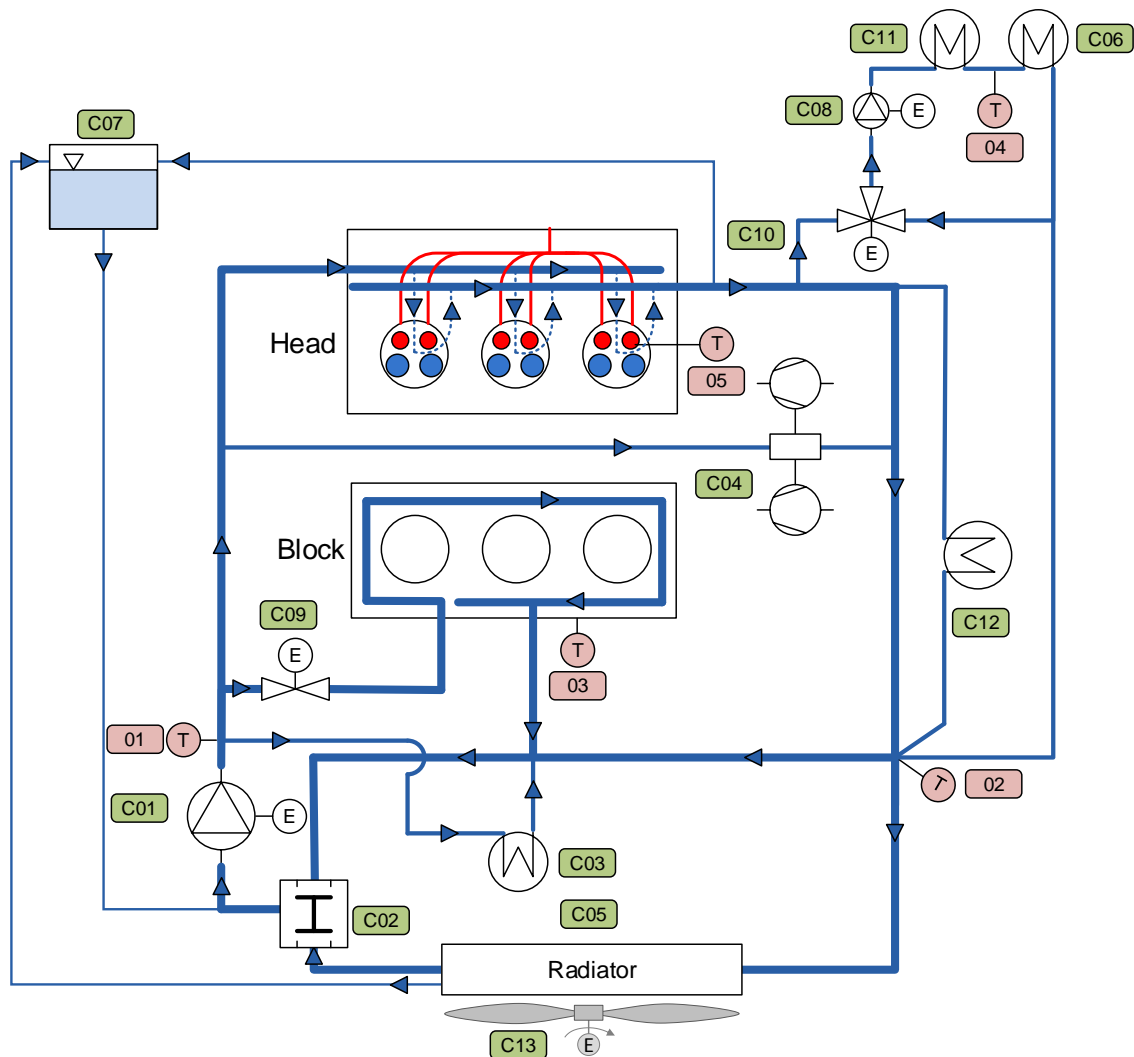
Figure 4.13.: Combustion engine high temperature cooling circuit and cabin heating.

Following components (maked with an upfront C in Fig. 4.13) are in the cooling circuit:

C01 Main coolant pump,

C02 Thermostat,

C03 Oil cooler,

C04 Turbo charger,

C05 ICE heat exchanger,

C06 Cabin heater,

C07 ICE expansion tank,

C08 Cabin heater pump,

C09 Crank case shut off valve,

C10 Cabin heater bypass valve,

C11 Electric coolant heater,

C12 Exhaust gas cooler,

C13 Main cooling fan,

and following temperature sensors (indicated by the symbol T in Fig. 4.13):

01 Coolant at main pump outlet,

02 Coolant at engine outlet,

03 Crank case metal,

04 Coolant at cabin heater inlet,

05 Cylinder head metal.

From a thermal management point of view following functionalities are implemented:

- **Split Cooling:** The flow distribution between head and block can be fully controlled by a shut off valve, thus allowing the block and liner to heat up faster to reduce friction losses [89];

- **Cabin heating:** In the proposed layout a cabin heater bypass valve is used to switch between cabin heating with hot coolant from the combustion engine (vehicle in conventional operating mode) and a Positive Temperature Coefficient (PTC) heater (vehicle in warm-up or electric operation mode). If the vehicle is in electrical operation mode the cabin heater pump is used;

- **Electric actuators:** Fully variable controllable electrical coolant pumps and fan allow to reduced the coolant flow rate at vehicle warm-up and at low load operating conditions. Thus the power consumption from cooling system actuators can be reduced and the vehicle warm-up is enhanced.

The MATLAB Simulink Toolbox TheLib, which is described in chapter 3, is used to setup and solve the thermo- and hydraulic network for flow and temperature distribution. In A.1 the actual high temperature cooling circuit simulation model is depicted.

HT Cooling Thermal modes

Due to electronically actuated pumps, valves and fan a number of different operating modes for engine cooling and cabin heating are possible. These operating modes are referenced as *Thermal Modes* further on. They also play an important role for the control system architecture definition, which is described in section 5.1.2. The high temperature cooling circuit thermal modes and functionalities are listed in Tab. 4.2 and the respective flow schemes are depicted in Fig. 4.14, where the abbreviations Ht, Wup, Heatg, Ar correspond to high temperature, warm-up, heating and afterrun, respectively.

Table 4.2.: High temperature cooling and heating *Thermal Modes*.

#	Mode Name	Cooling	Heating	Schema
0	HtWup0	No cooling required	No heating	4.14a
1	HtWup1	Engine head cooling	No heating	4.14b
2	HtWarm	head and block cooling	No heating	4.14c
3	HtWup0ElHeatg	No cooling required	PTC	4.14d
4	HtWup1Heatg	Engine Head cooling	PTC and ICE	4.14e
5	HtWarmHeatg	Head and Block cooling	ICE	4.14f
6	HtAr	Engine off, afterrun cooling	No heating	4.14b
7	HtArHeatg	Engine off, afterrun cooling	ICE residual heat	4.14e

The usage and activation criteria for the individual high temperature cooling thermal modes can be summarized as

Mode 0 The thermal mode *HtWup0* is used initially after engine coldstart. In this mode no active cooling is applied which means there is no forced fluid flow in the HT circuit in order to warm-up the engine and the fluids within the engine as fast as possible. The metal temperature of the cylinder head and crank case as well as the engine oil and EGR temperature are observed to prevent overheating.

Mode 1 In the thermal mode *HtWup1* the coolant flow is activated for parts of the circuit. The cylinder head is getting hot faster than the block because of the smaller heat capacity and the large combustion gas contact area. Therefore only the head is cooled in this operation mode (*split cooling*).

Mode 2 The thermal mode *HtWarm* is used after the engine warm-up is completed. Thus the liquids (oil and coolant), as well as the solids (block and head) are at operating condition. Therefore in this mode the auxiliaries are controlled such that the temperatures stay below the maximum temperature thresholds.

Mode 3 If cabin heating is required and if the vehicle is in pure electric operation mode or if the engine is still cold and no cooling is required the electric PTC heating mode *HtWup0ElHeatg* is used. Coolant is circulated through the cabin heater and PTC heater with the cabin heater pump only.

Mode 4 The thermal mode *HtWup1Heatg* is active when cabin heating is required and if the engine is still warming up. Heat dissipated from the ICE cylinder head is used for cabin heating. Additionally, to increase pax comfort, the PTC heater can be used to reach the cabin heater coolant inlet temperature setpoint faster.

Mode 5 If the combustion engine is at operating temperature enough energy is available for cabin heating. Therefore PTC heating is deactivated and only heat from combustion wall heat flux is used for cabin heating in the *HtWarmHeatg* thermal mode. In parallel the engine is cooled via the front end radiator.

Mode 6 The afterrun thermal mode *HtAr* is used to prevent overheating of bearings and the turbocharger after the engine stops. Therefore coolant is circulated through head and turbo charger.

Mode 7 Like mode 6 the *HtArHeatg* thermal mode is used to prevent damage from local overheating. Furthermore a cabin heating functionality, that uses the residual thermal energy of the system, is implemented.

(a) Mode 0

(b) Mode 1 and 6

(c) Mode 2

(d) Mode 3

(e) Mode 4 and 7

(f) Mode 5
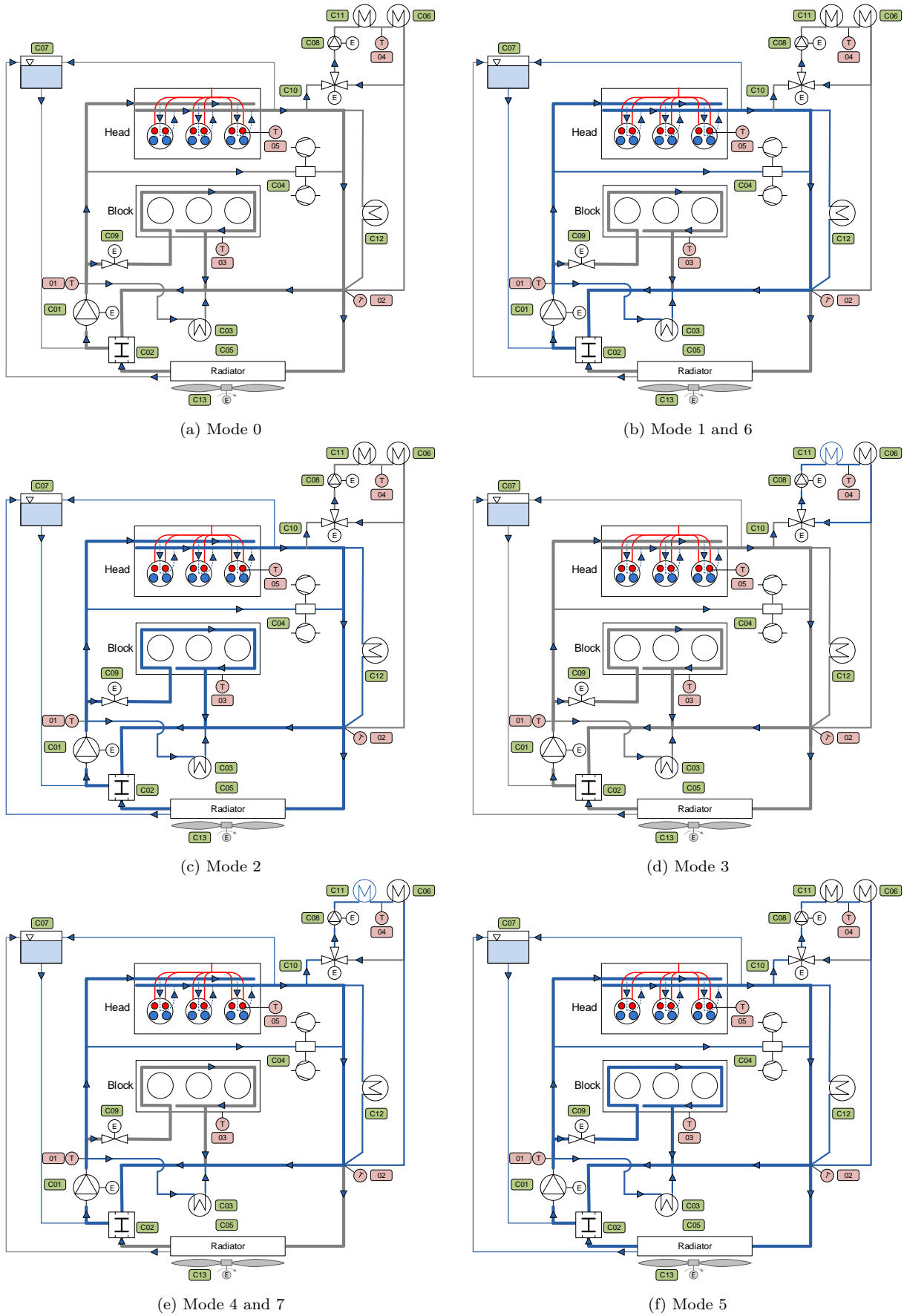
Figure 4.14.: Combustion engine cooling and cabin heating schemes for the individual thermal modes.

Lubrication Circuit

The lubrication circuit is used to cool and lubricate the engine bearings, camshaft and the piston. Heat can be rejected by the oilpan surface or via the oil cooler which transfers heat to the cooling circuit. Piston cooling jets are activated to enhance the cooling if the engine speed exceeds a certain threshold. The simulation model setup is similar to the methodology presented for the cooling circuit. It is also simulated with the Thermo-Fluid Library. Following components are part of the oil circuit:

C01 Engine Oil Pump,

C02 Oil cooler,

C03 Main Bearings,

C04 Conrod Bearings,

C05 Piston Cooling Jets,

C06 Chain Tensioner,

C07 Engine Head,

C08 Main Bearings,

and this sensor indicates the oil temperature:

01 Oil temperature at oil pan.
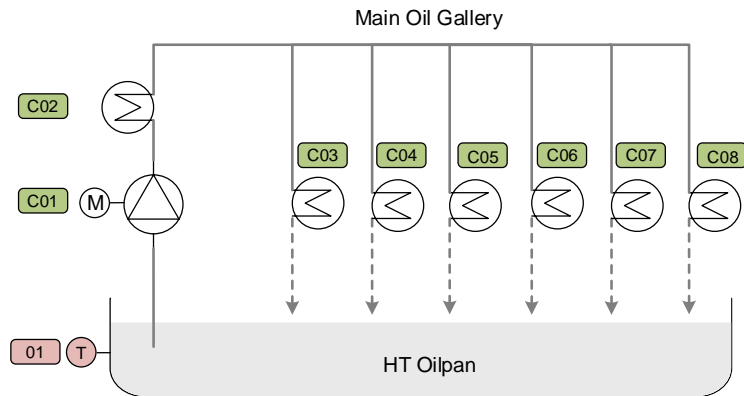
Figure 4.15.: Combustion engine lubrication system.

4.4. Electrical powertrain

4.4.1. Cooling and lubrication circuits

Low temperature electronics cooling circuit

The low temperature coolant circuit is used to cool the components of the electrical powertrain. Compared to the high temperature circuit the desired overall temperature level is much lower. For the electric machine and the power electronics a coolant temperature below 65 °C is desired. But for the battery a cell operating temperature of around 10 to 15°C would keep capacity decrease and the impedance increase low, although this temperature shows a higher power derating due to increased impedance compared to standard 30°C operation. So the compromise between life and operation conditions would be an operation in the window of 15 to 20°C [90]. This means that cooling of e-motor and battery together is only applicable if the ambient temperature is low and the e-motor is off or in a low power operation mode.
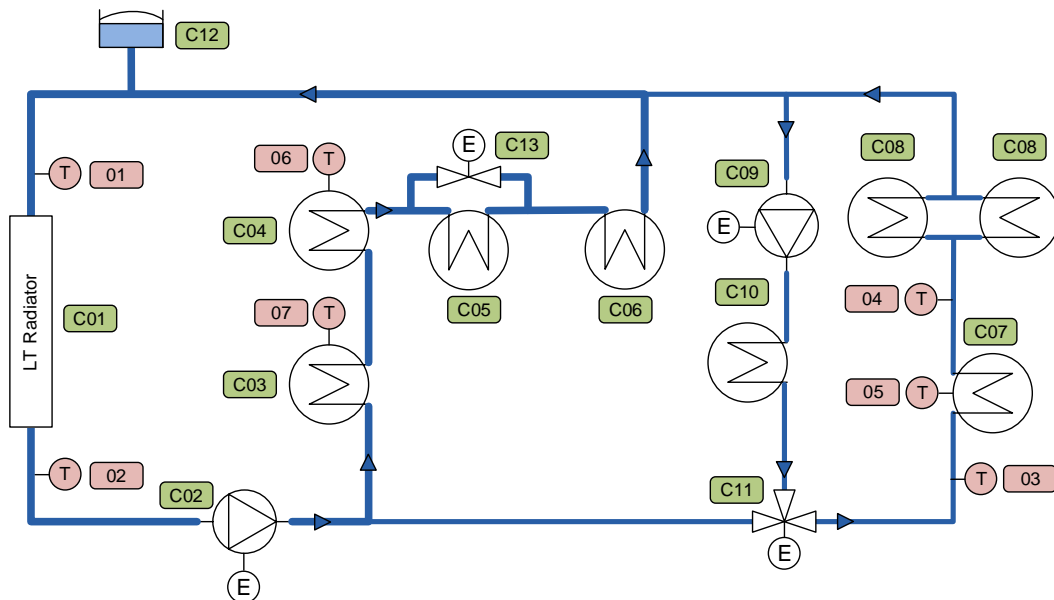
Figure 4.16.: Low temperature electric drivetrain cooling circuit

Low temperature cooling circuit components:

C01 Low temperature radiator,

C02 E-Motor pump,

C03 Power electronics,

C04 E-Motor,

C05 Transmission oil cooler (*TOC*),

C06 DC/DC converter,

C07 High voltage battery,

C08 Charger,

C09 Battery pump,

C10 Chiller,

C11 Electrical two-way valve,

C12 Membrane pressure regulator,

C13 TOC bypass valve.

Temperature Sensors T:

01 Coolant at LT HX inlet,	05 Mean battery cell,
02 Coolant at LT HX outlet,	
03 Coolant at battery inlet,	06 E-Motor stator copper winding,
04 Coolant at battery outlet,	07 Power electronics IGBT.

The actual low temperature cooling circuit model is build up from components of the Thermo-Fluid Library, as shown in Fig. A.2.

LT electronics cooling thermal modes

Due to electronically actuated pumps, valves and the connection to the air conditioning system via the chiller a number offer different operation modes for battery, EM and power electronics cooling are possible. They also play an important role for the control system architecture definition, which is described in section 5.1.2. The low temperature cooling circuit thermal modes and functionalities are listed in Tab. 4.3 and the respective flow schemes are depicted in Fig. 4.14, where the abbreviations Lt, Wup, Chrg, Chlr, HX, EM and PE correspond to low temperature, warm-up, charging, chiller, heat exchanger, e-motor and power electronics, respectively.

Table 4.3.: Low temperature cooling *Thermal Modes*

#	Mode Name	EM and PE	Battery	Schema
0	LtOff	No cooling required	No cooling required	4.17a
1	LtPwrElcWup	Pulsed pump operation	No cooling required	4.17b
2	LtPwrElcWarm	LT HX cooling	No cooling required	4.17c
3	LtPwrElcAndBattHx	LT HX cooling	Cooled via LT HX	4.17d
4	LtPwrElcAndBattChlr	LT HX cooling	Cooled via AC chiller	4.17e
5	LtBatChlr	No cooling required	Cooled via AC chiller	4.17f
6	LtChrgWup	No cooling required	Pulsed LT HX cooling	4.17g
7	LtChrgHX	No cooling required	Cooled via LT HX	4.17d
8	LtChrgChlr	No cooling required	Cooled via AC chiller	4.17f

The usage and activation criteria for the individual low temperature cooling thermal modes can be summarized as

Mode 0 If neither the battery nor the E-Motor or the transmission or the power electronics needs cooling the *LtOff* mode is active.

Mode 1 The thermal mode *LtPwrElcWup* is used during warm-up of the Power Electronic components, Battery and E-Motor. This function is also used when the ambient Temperature is higher than the coolant temperature. During this mode the E-Motor pump runs in pulsed operation mode in order to measure the correct coolant temperatures (no reliable sensor signal when there is no flow). There is no fluid exchange between the HV Battery and HV Electronics components. The gearbox oil temperature is monitored to prevent overheating (the oil temperature may reach up to 130°C).

Mode 2 When the coolant and the electronics components are warmed up the *LtPwrElctWarm* mode is active. This mode also requires that the either the battery needs no cooling or the cell temperature is lower than the temperature at the heat exchanger outlet.

Mode 3 During the thermal mode *LtPwrElcAndBattHx* the HV Electronics + EM, the Chargers and the HV Battery are cooled together via the low temperature heat exchanger. This function is enabled if the LT coolant temperature and the ambient temperature are low and the temperature difference between the cattery cells and the ambient air is high. This can be the case during, or shortly after, battery charging at low ambient temperature.

Mode 4 The *LtPwrElcAndBattChlr* thermal mode is active if both, the E-Motor or power electronics or transmission and the battery require cooling but the ambient or coolant temperature is too high for battery cooling. Therefore the low temperature cooling circuit is operated as two separate systems with no fluid exchange between them. The EM and PE are cooled via the HX and the battery is cooled via the AC chiller.

Mode 5 If only the battery requires cooling and the ambient temperature is too high the *LtBatChlr* mode is active. In this mode the battery is cooled via the AC chiller and the refrigerant circuit.

Mode 6 Charging of the battery causes an increase of the temperature. During this battery warm-up process the *LtChrgWup* mode is active and the pump is running in a pulsed operating mode.

Mode 7 If active cooling of the battery during charging is required and the ambient temperature is lower than the cell temperature the *LtChrgHX* mode is active.

Mode 8 If active cooling of the battery during charging is required and the ambient temperature is higher than the cell temperature the *LtChrgChlr* mode is active and the AC chiller is used as heat sink.

(a) Mode 0

(b) Mode 1

(c) Mode 2

(d) Mode 3 and 7

(e) Mode 4

(f) Mode 5 and 8

(g) Mode 6
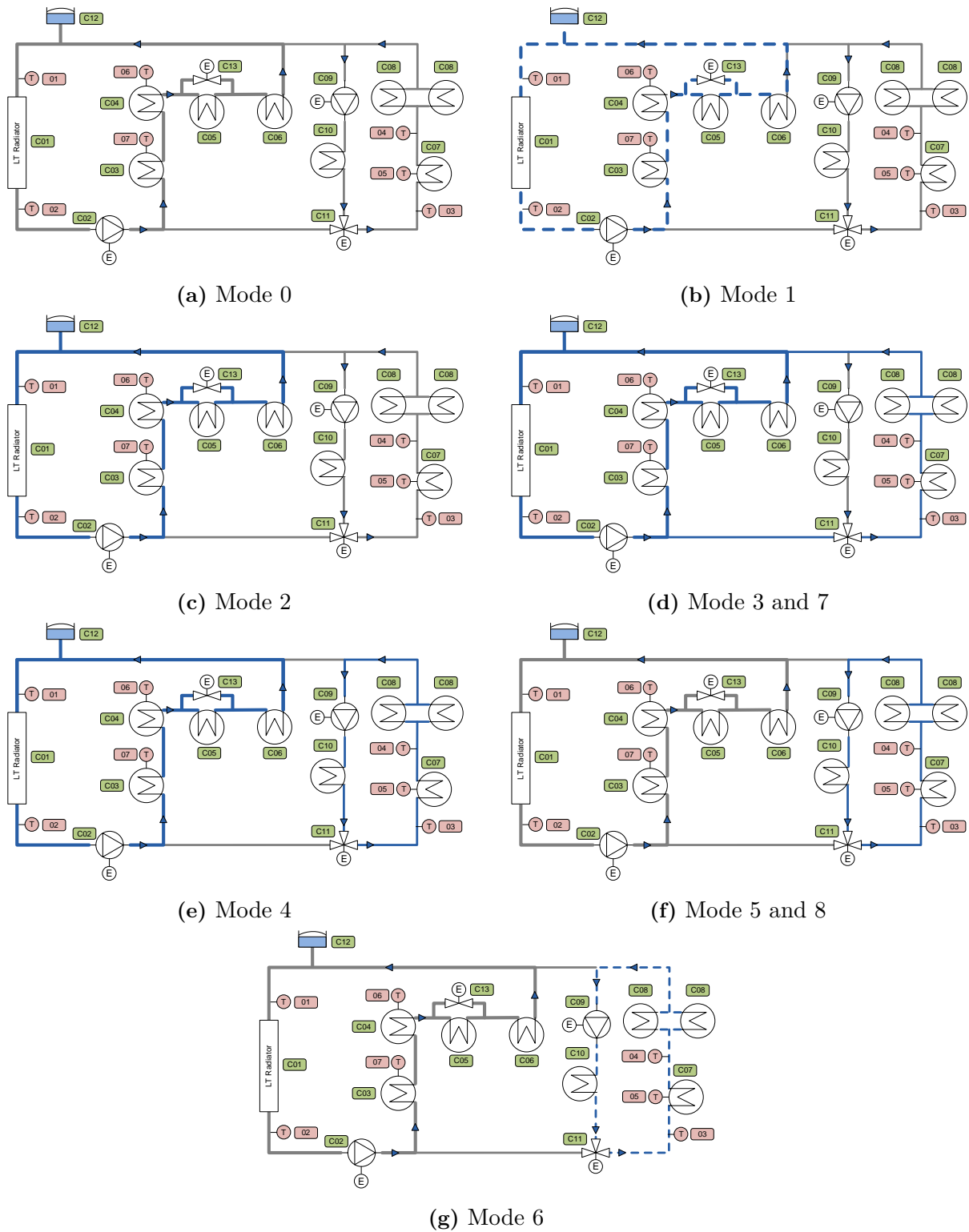
Figure 4.17.: Possible flow schemes of the low temperature electronics cooling circuit. Used for the definition of *thermal modes*.

Low temperature oil circuit

The task of the low temperature oil circuit is on the one hand to lubricate the gearbox and on the other hand to supply the gearbox hydraulics with oil for the clutch actuation. Therefore the oil circuit is split into the *low pressure (LP) gearbox lubrication* part and the *high pressure (HP) gearbox hydraulics* part, as depicted in Fig. 4.18. Heat losses from shifting and friction is rejected by the surface of the gearbox and oilpan and by the gearbox oil cooler which transfers heat between the low temperature cooling circuit and the low temperature oil circuit. The flow through the gearbox oil cooler can be bypassed on the cooling circuit side, which leads to a faster heat up of the engine oil and thus to reduced friction losses.
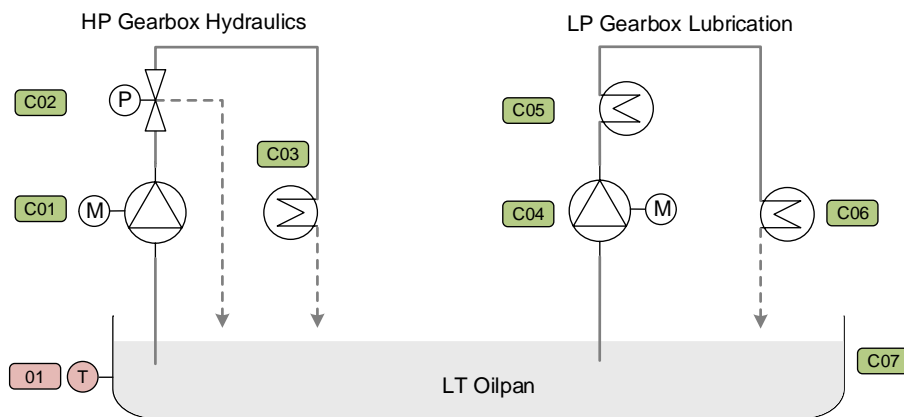
Figure 4.18.: Gearbox hydraulics and lubrication oil system.

Components:

C01 High pressure gear box (*GBX*) oil pump,

C02 Pressure relieve valve,

C03 Gearbox actuators,

C04 Low pressure GBX oil pump,

C05 Gearbox oil cooler,

C06 Gearbox lubrication,

C07 Oil pan.

Temperature Sensor *T*:

01 Oil at oilpan.

The simulation model setup is done in MATLAB Simulink by application of the Thermo-Fluid Library. Because of the purely mechanically actuated pumps and valves a thermal mode definition for the low temperature oil circuit is not required.

4.4.2. E-Motor and power electronics

An E-Motor of the *hybrid synchronous machine* (HSM) type is used in the vehicle. It is well suited for vehicle applications because of the following advantages [91]:

- Constant power over speed range,
- High torque per stator current,
- Efficiency over complete operating range,
- Low weight,
- Very low losses in the rotor, therefore no active cooling of the rotor is required.

Similar to the combustion engine the E-Motor thermal model relies on a lumped mass thermal network, as shown in Fig. 4.19. Due to the peculiarity of very low rotor heat losses the HSM thermal network only includes the stator thermal network. Because the E-Motor is rotationally symmetric it is sufficient to model only a small segment. Heat losses are scale down accordingly while the cooling jacket heat transfer area is in accordance with the full motor geometry. This leads to a thermal network that consists of five thermal masses which are defined as

m_{Cu} Copper windings in the stator, $\qquad$ m_J Cooling jacket,

m_{FeT} Iron in the stator teeth, $\qquad$ m_{co} Coolant in the cooling channel.

m_{FeY} Iron in the yoke,

and five thermal resistances (3 conduction and 2 convection resistances). The actual Simulink implementation of the HSM thermal network can be found in Fig. A.3.
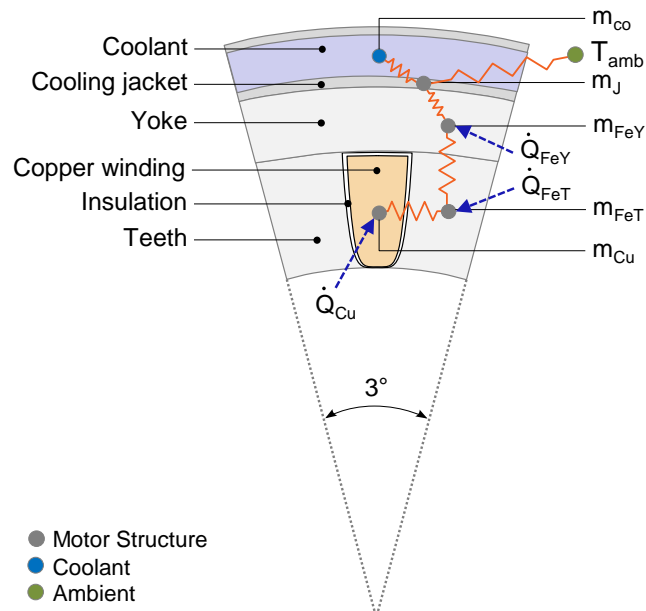
Figure 4.19.: The Hybrid Synchronous Electric machine (HSM) thermal network is build from 5 lumped masses which represent a 3° radial section of the stator.

The thermal network is calibrated to fit to the manufacturers measurements. Results for the E-Motor in S1[2] operation mode are depicted in Fig. 4.20. According to the manufacturer a maximum stator temperature of 137 °C is allow without power *derating*. Power derating means that the maximum allowed power capability of the E-motor is reduced below its rated maximum capability in order to avoid damage from overheating. Typically the derating function limits the maximum power capability linear from 100% at derating start temperature to 0% when the shut off temperature (165°C) is reached .
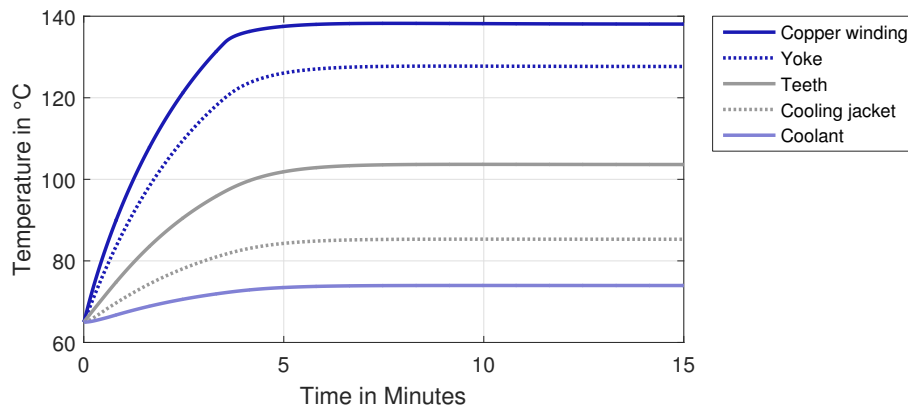
Figure 4.20.: Hybrid Synchronous Electric machine simulation results at S1 conditions; Speed 5400rpm, Torque 165Nm, Coolant inlet temperature 65 °C and Coolant flow 6 l/min.

For the thermal characterization of power electronics a model consisting of four thermal masses is used, as depicted in Fig. 4.21. The masses are defined as

m_{IGBT} Insulated Gate Bipolar Transistors, m_{ho} Housing,

m_{bp} Base Plate, m_{co} Coolant in the cooling channel.

For the calibration of the thermal network manufacturer measurements for the power electronics warm-up at S1 operating conditions are available. Therefore the model parameters are calibrated to fit the measurement results.
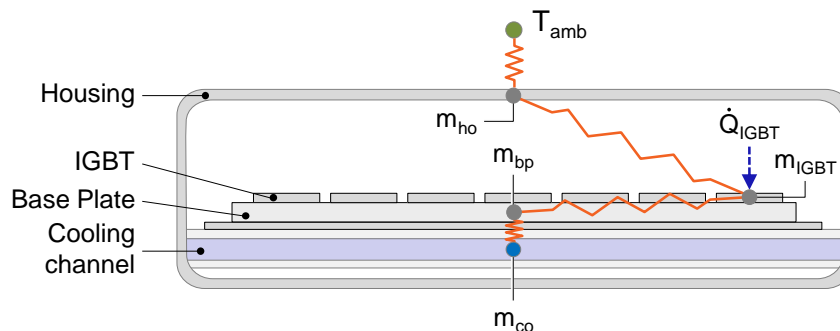
Figure 4.21.: Power Electronics lumped mass thermal network.

---

[2]S1 is the motor operating point with the highest load and torque (rated point) at the maximum coolant inlet temperature and the minimum allowed coolant flow that is approved for continuous operation.

4.4.3. Battery

For modeling of the traction battery only a black box model is available from the manufacturer. Therefore a fairly simple thermal mode setup is chosen, as shown in Fig. 4.22. The thermal network comprises two lumped thermal masses which are defined as

m_{cm} Battery cells, m_{co} Coolant in the cooling channel

and two thermal resistances which are fitted in least squares sense in accordance with simulation results from the black box model. The temperature, SoC, current and voltage dependent battery heat loss $\dot{Q}_{Batt}$ is calculated by the vehicle and HCU model. Since the main parameters of the battery like weight and specific heat capacity are known only the thermal resistances have to be found. The resulting model reproduces the thermal behavior with a sufficient level of detail and is valid in the full thermal and electrical operating range, as can be seen in Fig. 4.23.
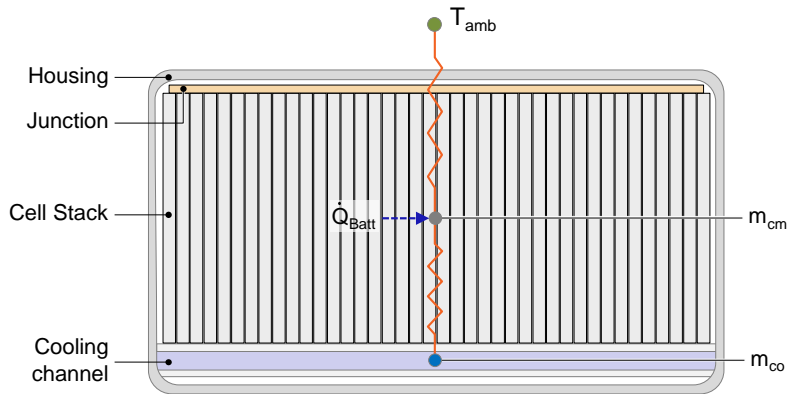
Figure 4.22.: High voltage battery lumped mass thermal network.
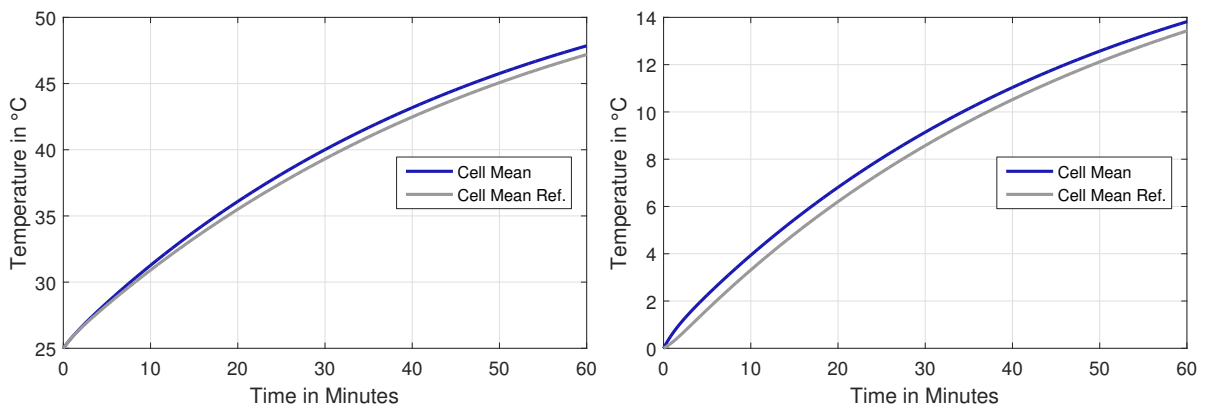
Figure 4.23.: Battery model calibration results for a constant battery powerloss of 2kW at 20 °C ambient temperature on the left hand side and constant battery powerloss of 500W at 0 °C ambient temperature on the right hand side.

106

4.5. Underhood flow

In course of the vehicle thermal management simulation knowledge about the underhood flow is required. As shown in Fig. 4.24, ambient air enters the vehicle at the vehicle inlet grill and passes the AC condenser, where it gets heated up if AC cooling of the battery and/or cabin is active. The condenser outlet air flows through the electronics cooling low temperature heat exchanger (LT HX), where again heat is rejected in case of electric or hybrid driving. Then the air flows through the ICE high temperature heat exchanger (HT HX) before it passes the engine structure where heat is transfered by convection at the engine surface. Finally the hot air leaves the car at the vehicle under bonnet. The flow quantity is mainly influenced by the driving speed and the main fan activation level.
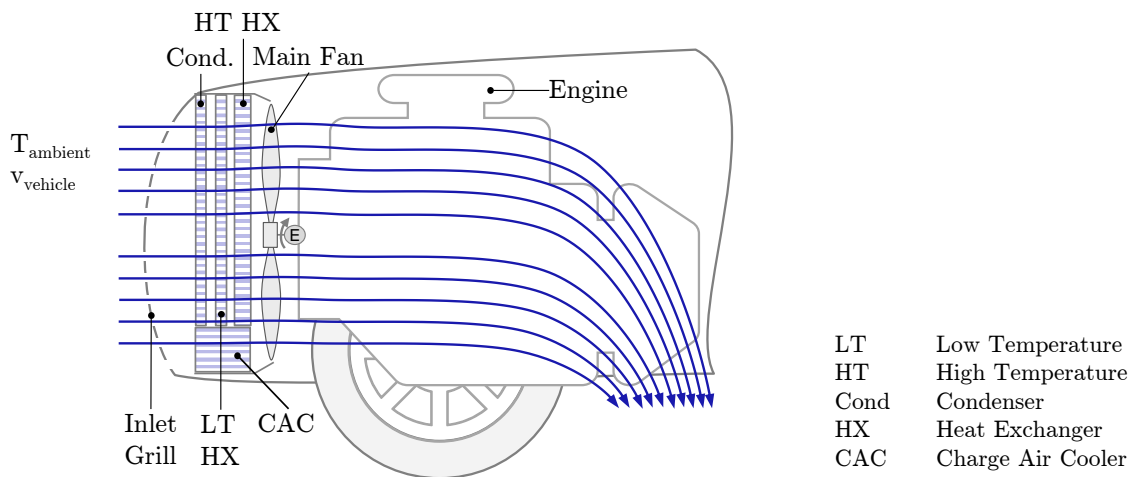
Figure 4.24.: Engine compartment underhood flow through the vehicle cooling package.

The underhood flow is modeled as so called *airpath* hydraulic resistance network, as shown in Fig. 4.25. Thermo-Fluid Library airpath components, as introduced in section 3.5, are used for software implementation. Flow resistances along the flow path are the inlet grill, AC Condenser (Cond.), high temperature heat exchanger (HT HX), low temperature heat exchanger (LT HX) and the engine. The charge air cooler (CAC) is considered as a parallel resistance in the air flow network. Pressure sources in the network are the velocity pressure from driving speed and the main fain, if activated. From the hydraulic resistances and the pressure sources a simple flow network is build up. The dimensionless pressure coefficients at inlet grill Cp_{in} and at the vehicle under bonnet Cp_{out} are required for calculation of the net velocity pressure increase. They are derived from 3D-CFD simulations. Pressure drop characteristics for the heat exchanger are available from component test bed measurements. For calibration and validation of the airpath model *in vehicle* wind tunnel air flow measurements, using a grid of miniature pitot tubes (called *ViF probes* [92]) at the condenser, are used.
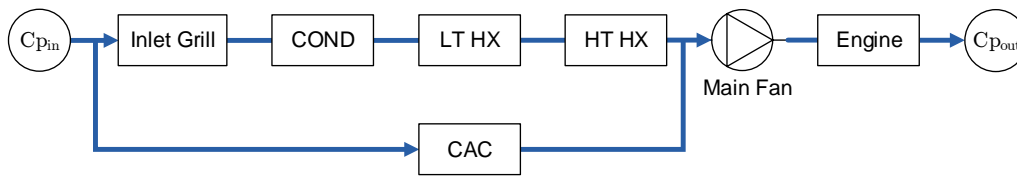
Figure 4.25.: Underhood airflow - airpath model.

The resulting air mass flow and temperature from the solution of the air network is used in the heat exchanger components for calculation of the heat rejection. Thus the air side heat transfer coefficient is found by using Nusselt correlations (as in Eq. 2.43) which are dependent from the Reynolds number (flow velocity influence) and Prandtl number (air temperature influence).

<div align="right">

5

</div>

Control

This chapter addresses the vehicle control system with emphasis on the thermal control system architecture and temperature control design.

The first part focuses on the control system architecture. A Vehicle Control Unit (VCU) including the HCU and the Transmission Control Unit (TCU) is outlined. Then detailed insight into a generic framework for the control of thermal auxiliaries, called Thermal Management Controller (TMC), is given. The second part of this chapter presents temperature control techniques: First a linear model predictive fan control approach for cooling of the vehicle electronics is outlined followd by a nonlinear Control Lyapunov Function based ICE pump control algorithm.

5.1. Control system architecture

5.1.1. Vehicle Control Unit

The Future Hybrid VCU [69], as depicted in Fig. 5.1, combines the functionality of the hybrid and transmission control unit into one common device. This has the advantage that both control units can directly command the powertrain actuators. Thus feedback loops and resulting time delays can be avoided. The VCU consists of two main function groups:

- HCU including the TMC,
- TCU.

The *HCU* selects the hybrid vehicle operating mode (e.g.: E-Drive, Conventional Drive, Boost,...) and provides the ICE and EM torque setpoints. Also the determination of the driver torque demand and powertrain thermal and auxiliary management is part of this Software (SW) function group. In case of quasi-static driving the HCU request are directly used as output of the control unit.

The *TCU* is responsible for the coordination of powertrain configuration changes which include functions like gear shifts and hybrid mode changes. In the transition phase the calculated driver torque demand and the powertrain torque split from HCU is modified to achieve a smooth transition between gear or hybrid modes while still fulfilling the driver torque demand. All operations are performed under consideration of limitations regarding power capability, response time, torque build up time and controllability.
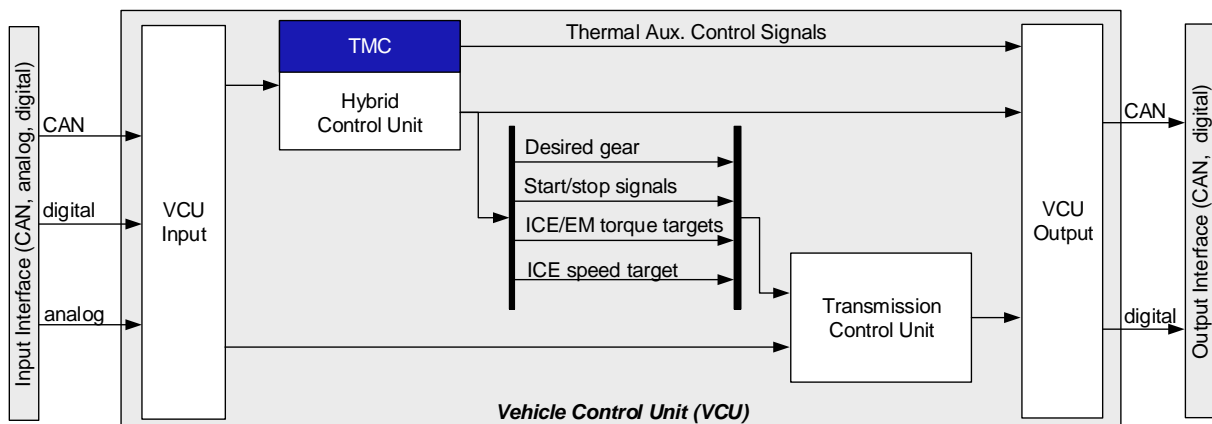
Figure 5.1.: VCU SW architecture [93].

Besides the HCU and TCU functionality the *VCU input* function group is used to collect and process incoming signals from Controller Area Network (CAN), analog and digital sources (e.g. sensors). Additional signals which are not available as control unit inputs are calculated and derived from maps or calculation models (e.g. traction torque, vehicle driving states, additional temperatures,...).

The function group *VCU output* gathers the output signals from the HCU (including the TMC) and TCU.

5.1.2. Thermal Management Controller

Basic Concept

The main objective of the *TMC* is to provide a generic framework for thermal auxiliary control that is flexible enough to be applicable for any vehicle configuration (CONV, EV, HEV, PHEV) and a broad range of control algorithms. Additionally, the hybrid mode selection shall be influenced depending on thermal rating signals.

To achieve this objectives a clustering of the thermal actuators is performed. The clustering is based on the present physically connection of cooling/lubrication circuits, as shown in Fig. 5.2.

Each circuit cluster consists of multiple thermal function groups, which correspond to the individual *thermal modes*. The thermal modes can be seen as a linguistic interpretation of the cooling/lubrication *system state*[1] and/or the currently requested thermal feature. For the Future Hybrid vehicle the high temperature ICE cooling and the low temperature electronics cooling circuit thermal modes are considered, as introduced in section 4.3.4 and 4.4.1, respectively.

In parallel each thermal function calculates an *individual set of actuator values* for the control of all actuators in the respective cooling/lubrication circuit. Each set of

---

[1]In thermodynamics states typically comprise temperature and pressure.

actuator values represents a tailored combination suitable for a certain system state and thermal feature. Selection of the currently best mode is performed by the *mode selection* algorithm. This algorithm selects the mode based on available inputs with respect to durability, efficiency and comfort. Definition of the mode selection criteria and thresholds is done in course of the *software system requirements* (SW Sys. Requirements) derivation together with the hybrid control unit requirements. Inputs for the mode selection may range from sensor and CAN bus signals over temperatures from calculation models and *thermal requests*[2] till predictive information about the upcoming route. Subsequently, the *Arbitrator* forwards the actuator signals from the selected mode under consideration of a hysteresis function which prevents switching between modes within a short time.

By introducing the thermal functions and thermal mode concept the challenging task of controlling actuators with a high number of interactions and dependencies is split into smaller pieces that are easier to handle. Instead of dedicated component control functions with many interactions and feedback loops, for each of the thermal systems a *central control logic* is introduced to select a comprehensive set of actuator control signals which is tailored towards the currently active thermal mode.
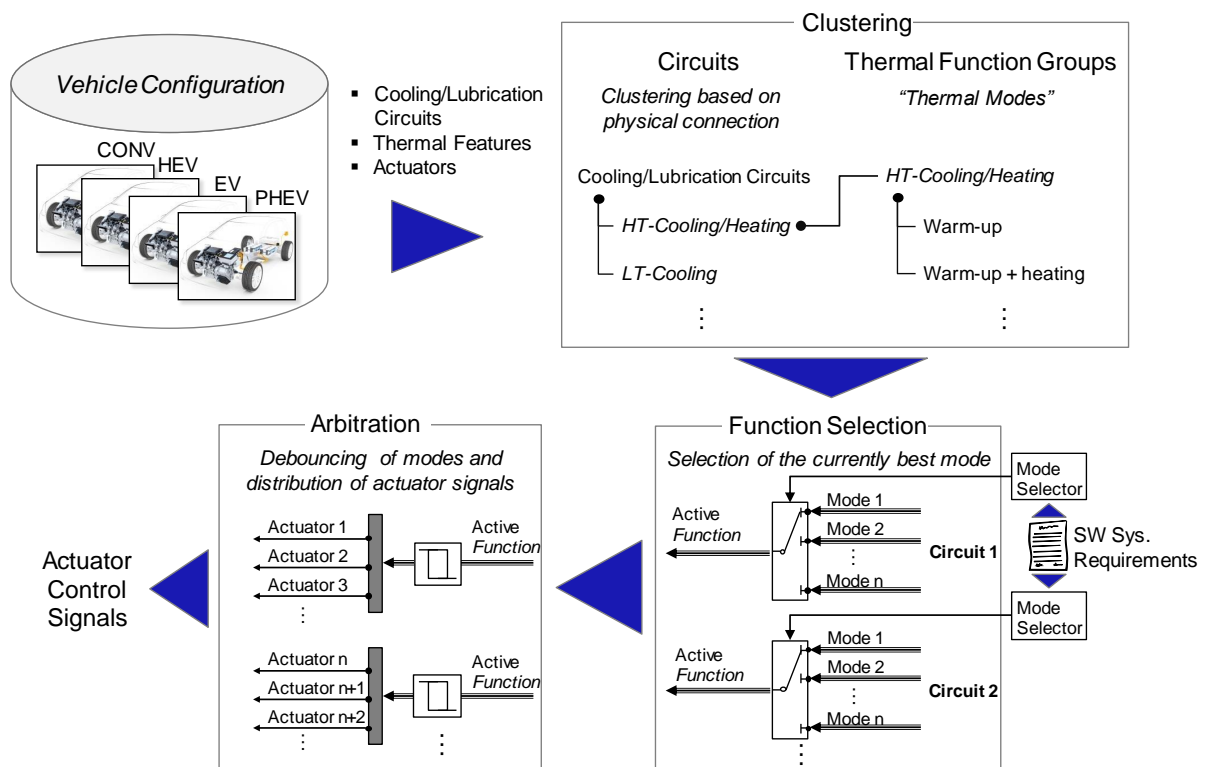
Figure 5.2.: Methodology for the development of a generic TMC.

---

[2]A thermal request is a component specific demand for heating or cooling.

Software Architecture Overview

The Thermal Management Controller software architecture is given in Fig. 5.3. It is separated into five main software function groups:

- VCU Input;
- Thermal Request Generation;
- Thermal Function Selection;
- Fan Control and
- Thermal Rating.

In the *VCU input* function group common inputs for the TMC are collected and additional signals are calculated. From this input the *Thermal Request Generation* function group derives component specific thermal requests and temperature setpoints. Under consideration of the VCU input signals, thermal requests and setpoints the *Thermal Function Selection* function group provides the thermal actuator control signals according to the currently active thermal function. In the *Fan Control* function group a common fan speed is derived from the individual cooling circuit fan speed requests, the current vehicle speed and ambient temperature. The *Thermal Rating* function group calculates rating values which influence the hybrid mode selection.
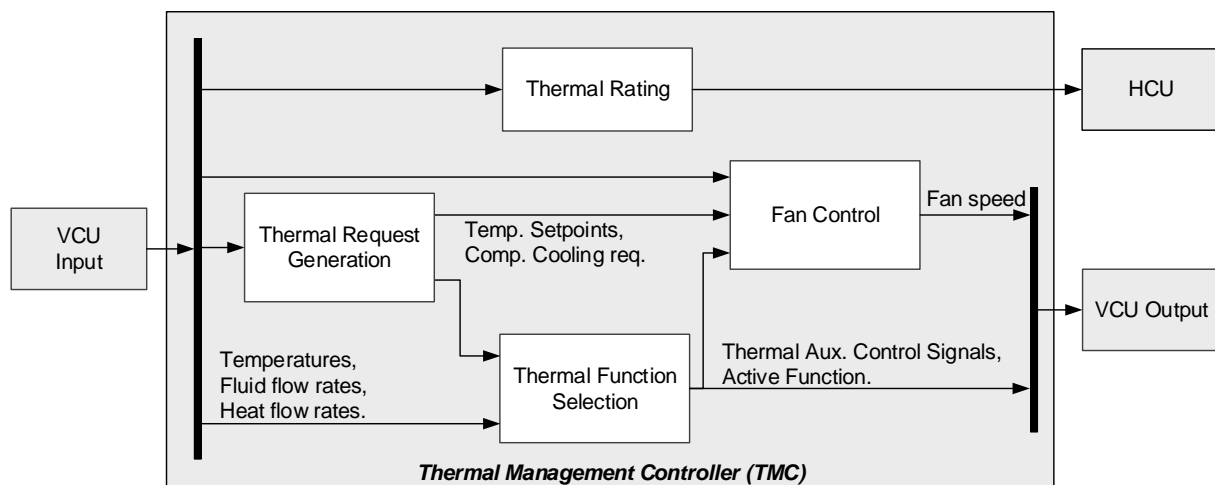
Figure 5.3.: Thermal Management Controller (TMC) SW architecture.

VCU Input

The Thermal Management SW function group in the VCU Input collects and calculates current temperatures, heat flows, fluid flows and temperature setpoints of components and fluids. The Thermal Management SW function group consists of three components:

- Electric Auxiliaries Detection;
- Heat flow Detection and
- Temperature Detection.

The *Electrical Auxiliaries Detection* SW component does the evaluation of current status, operation mode and power demand of electric auxiliary devices in hybrid vehicle and the calculation of fluid flow, and power demand, based on current operating point (rotation speed, valve setting, vehicle speed). In the *Heat Flow Determination* SW component calculation of the current waste heat generation of relevant components is carried out. The waste heat flow is derived from efficiency maps, electric resistance or current fuel consumption. The *Temperature Detection* SW component does the evaluation of temperature sensors and calculation of additional system temperatures and their corresponding temperature gradients. Exemplary, the Catalytic Converter (CAT) temperature is calculated. The temperature calculations are based on the first law of thermodynamics, using heat- and fluid-flow information.
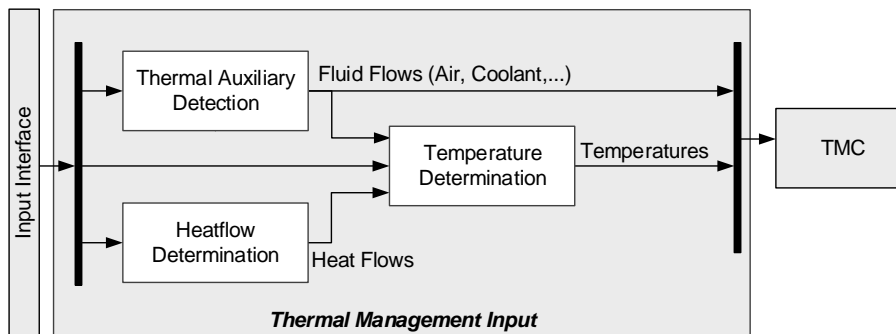
Figure 5.4.: Thermal management related SW function group in VCU input.

Thermal Request Generation

In the *Thermal Request Generation* SW function, as depicted in Fig. 5.5, component specific requests for cooling or heating are generated. Requests are formulated as integer values which are in accordance with linguistic representations. They are defined as *1=no thermal request*, *2=low priority thermal request* and *3=high priority thermal request*. In addition temperature setpoints are calculated which may vary with driving speed, load or ambient temperature. As example the cabin heater inlet temperature setpoint is depending on the current ambient air temperature. Thermal requests and setpoints are consequently used in the Thermal Function Selection and Fan Control function groups.
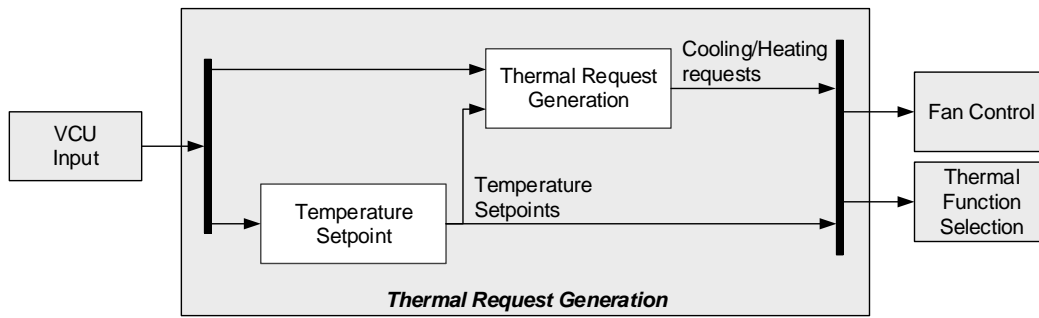
Figure 5.5.: Thermal Request Generation SW function group.

Thermal Function Selection

The *Thermal Function Selection* group contains SW function groups for each thermal circuit (cooling, lubrication,...) with electronically actuated auxiliaries. They are used to enable and select the currently best thermal management function. In Fig. 5.6 the Thermal Function Selection groups for the Future Hybrid vehicle cooling/lubrication circuits with electronically actuated auxiliaries are shown. In this function groups parameter sets for each thermal mode are calculated in parallel (exemplary shown for the HT cooling circuit in Fig. 5.7). Depending on the current vehicle state the control signal may origin from a defined constant value, from Bang-Bang controller, map based controllers or model based controllers. For the HT cooling circuit these signals include among others: Pump Speeds, Fan Speed request, Valve Settings and PTC heater activation.
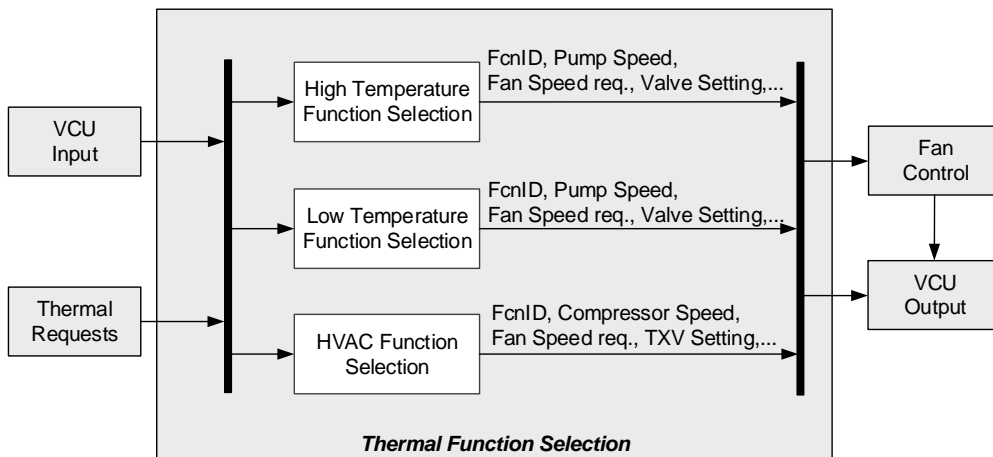
Figure 5.6.: Thermal Function Selection SW function group.

Selection of the output parameter set (and the according control approach) is done by the *Mode Selector* block. The Mode Selector comprises a control logic that selects the *best* thermal mode depending on the current system state (speed, torque, load, temperature,

pressure,...) and thermal requests. The best mode is considered to have the highest energy efficiency and lowest pollutant emission under the consideration of limitations regarding durability and aging. Definition of the control logic is done based on the thermal software system requirements. An example SW implementation in *MathWorks Simulink Stateflow* can be found in the appendix Fig. A.4.
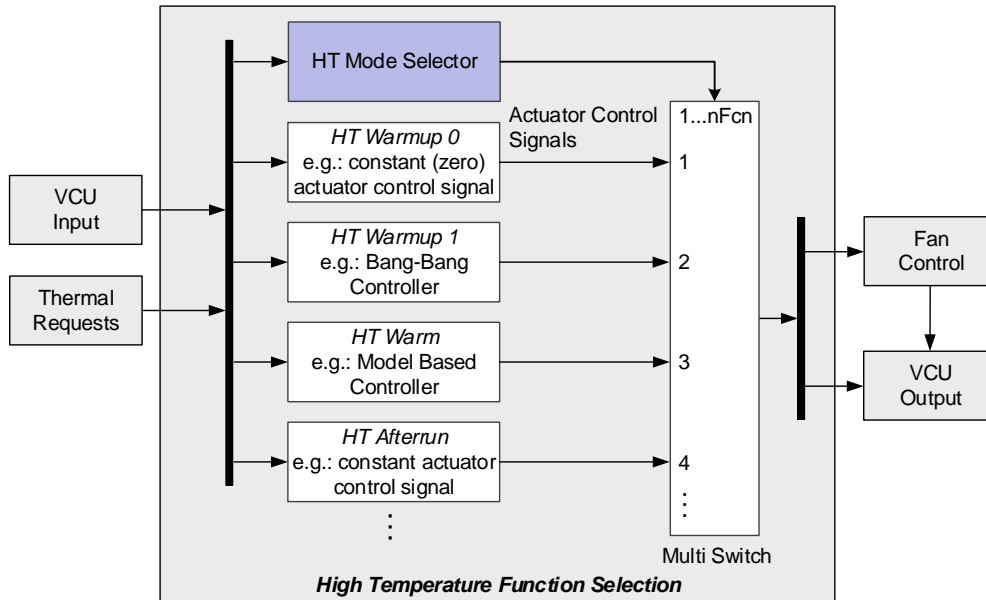
Figure 5.7.: High temperature cooling circuit Thermal Function Selection SW function group.

Fan Control

The *Fan Control* SW function group, as shown in Fig. 5.8, calculates the output fan speed. Determination of the fan speed needs consideration of all thermal circuits connected by a common air flow path.

In the *Fan Speed Arbitration* software component fan speed requests and ambient conditions like temperature and vehicle speed are considered together to derive a joint fan speed control signal. For the Future Hybrid vehicle fan speed request from the high temperature ICE cooling, low temperature electronics cooling and the HVAC system are considered.

Thermal Rating

The Thermal Management Controller can influence the HCU mode selection via thermal rating functions. As example the rating of the conventional driving mode may be promoted in order to keep the temperature of the CAT from dropping below the light off temperature threshold. This is important to avoid repeated cold start emissions.
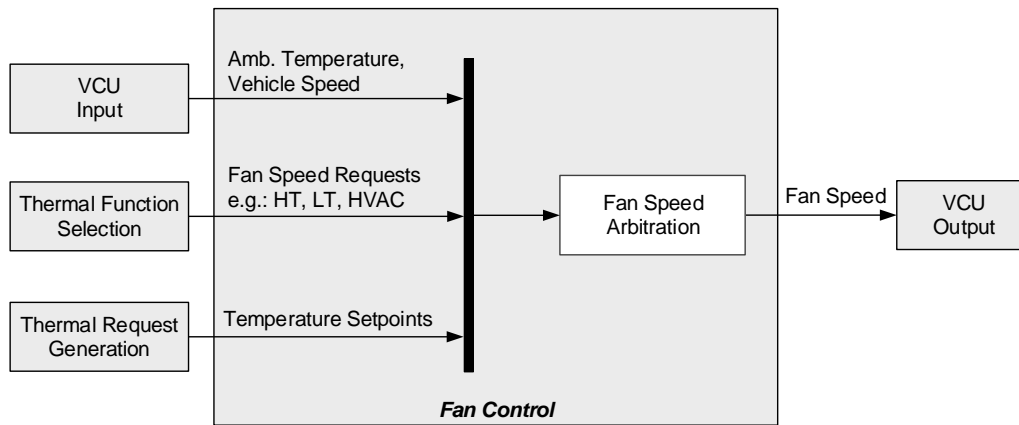
Figure 5.8.: Fan Control SW function group.

Thermal function selection Example ICE

In Fig. 5.9 an exemplary thermal function selection sequence for the ICE high temperature cooling, without heating, from vehicle warm-up till after-run is shown. Vehicle operation starts with a cold vehicle structure and fluids where no active cooling is required, thus the *HT Off* thermal function is activated. A number of conditions must be met to move to the *HT Warmup 1* thermal function. The most significant is the cylinder head structure temperature. If a certain threshold value is reached this function is enabled and fluid can flow through the cylinder head. The thermal function *HT Warm* is activated if the crank case temperature exceeds its threshold value. In this operating mode usually a closed loop control of the coolant or cylinder head temperature is enabled. After the engine is turned of and if the cylinder head temperature or the turbo charger temperature is above a certain level the coolant pump stays activated until the temperature drops below the safety temperature limit.
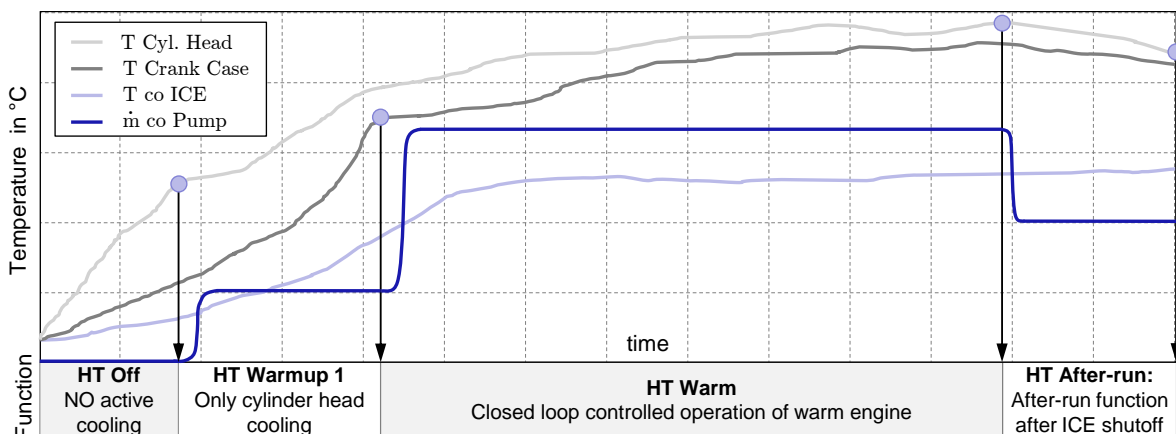
Figure 5.9.: Exemplary thermal function selection sequence for ICE cooling circuit with cabin heating deactivated.

5.2. Linear model predictive control

Standard implementations for cooling circuit control which are taken over from conventional cars with internal combustion engine usually involve a temperature based bang-bang control. This implementations are simple to implement but lead to oscillating temperatures. The present model based predictive control focuses on increasing electric cruising range and decreasing fuel consumption by reducing the power consumption for e-motor and power electronics cooling.

To meet hard temperature constraints usually safety offsets have to be introduced leading to increased cooling ventilation which results in a significantly higher power consumption mainly caused by the cooling package fan.

The proposed approach aims to enhance control performance in order to significantly reduce temperature safety margins in reference values resulting in a more efficient cooling and a lower power consumption. The approach involves a separation of the plant model into a linear and a nonlinear part, which is then advantageously used for control. The proposed control approach consists of a standard linear observer plus a linear model predictive control. Nonlinearities caused by the radiator are addressed separately.

A possible real-time execution on standard automotive hardware is also addressed. Results are shown on simulation examples, as well as on first testbed experiments.

5.2.1. Introduction

For reasons of simplicity and convenience classical control laws are currently applied for cooling. Using bang-bang control to regulate fluid temperature is simple but leads to limit cycles and overshoots for rapid load changes. Even conventional control approaches introducing more than two discrete fan speed levels (4 in the discussed example) share this disadvantage. Controlling fluid temperatures with a wax thermostat potentially also leads to a large over- or undershoots caused by the inertia of the wax. To compensate for overshoot and oscillations higher safety margins and lower setpoint temperatures are used. Increasing the average system fluid temperature level enhances cooling performance and helps to reduce the power required for the cooling system actuators. The rate of transferred heat from fluid to air for a heat exchanger is mainly based on mass flows, specific heat capacities and the temperature difference between cold and hot fluid. Thus a certain heat flux can be provided by higher mass flows and a lower temperature difference or lower mass flows and higher temperature difference. The latter approach is the preferred one since increasing mass flow directly translates to increased actuator (e.g. fan or pump) power demand. According to affinity laws for pumps and fans the consumed power is proportional to the cube of shaft speed [88]. The shaft speed is directly proportional to the flow increase. Hence the affinity law can be formulated as $\frac{P_1}{P_2} = (\frac{\dot{m}_1}{\dot{m}_2})^3$. This means an increase in flow ($\dot{m}_2$) by 10% increases the power requirement (P_2) by 33%. In other words, increasing the temperature difference rather than the flow saves roughly 25 Watts of power consumption per Kelvin setpoint increase. This statement holds for an average car at a medium load point equipped with a 500 Watts fan.

[94] show how to find the energy optimal solution for this problem for a known drive cycle. Therefore pump and fan are operating at a number of discrete speed stages only. [95] describe a model predictive control for the energy optimal solution controlling a cooling

circuit with pump and fan having a number of distinct operation stages. [96] show that decent temperature tracking can be performed by using a non-linear controller and a smart valve. Using a fully controllable fan in order to improve the control performance is recommended.

5.2.2. Plant model setup

Thermal circuit overview

The Future Hybrid low temperature electronics cooling circuit is subsequently used for setup of the mathematical model and the model predictive controller. As mentioned in section 5.1.2 control algorithms on component level are only active when all conditions for the corresponding thermal function are met. In case of the electronics cooling circuit MPC is active if the thermal mode *LtPwrElcWarm* or *LtPwrElcAndBattChlr* are enabled (as shown in Fig. 5.10 on the left and right hand side, respectively). Battery cooling is considered seperately. During this operating modes the considered cooling circuit consists of four heat source/sink components in series (C03 power electronics, C04 e-motor, C05 transmission oil cooler and C06 DC/DC converter). The power electronics is supplied with the coolest fluid directly after the heat exchanger. Afterwards the fluid gets heated up as it passes through the e-motor and the transmission oil cooler until it finally reaches the dc/dc converter. Pipes are connecting the powertrain components. They contain a substantial amount of coolant and need to be considered. A maximum coolant entry temperature of 65°C for the e-motor and power electronic units is specified by the manufacturer. The amount of air flowing through the heat exchanger, and thus the heat transfered from coolant to air, is mainly influenced by a given vehicle driving-speed and the fan-speed.

Figure 5.10.: Schematics of the low temperature electronics cooling circuit operating modes where the MPC algorithm is active.

Mathematical system model

Towards the mathematical model formulation following simplification is applied; the amount of heat loss and the thermal inertia of all electronic components are merged together in one component. This leads to a control oriented model consisting of ordinary differential equations. They allow an interpretation of the cooling circuit system as 4 lumped volumes: "*pipe 1*" (P1), "*motor*" (M), "*pipe 2*" (P2), "*heat exchanger*" (H).

They are connected in a loop, exchanging the coolant mass flow $\dot{m}_c$ as shown in Fig. 5.11. Engine and heat-exchanger point mass consider heat flows $\dot{Q}$, from losses and cooling respectively, in their energy balance.

Heat flows from motors, power electronic units and DC/DC-converter to the cooling circuit are denoted with $\dot{Q}_{()}$. A speed controlled pump drives the coolant mass flow $\dot{m}_c$. The air mass flow $\dot{m}_a$ at the heat exchanger air input is of temperature T_a. At the heat exchanger the heat flow $\dot{Q}_H$ is transferred from coolant to air side. Symbol v denotes the vehicle velocity.
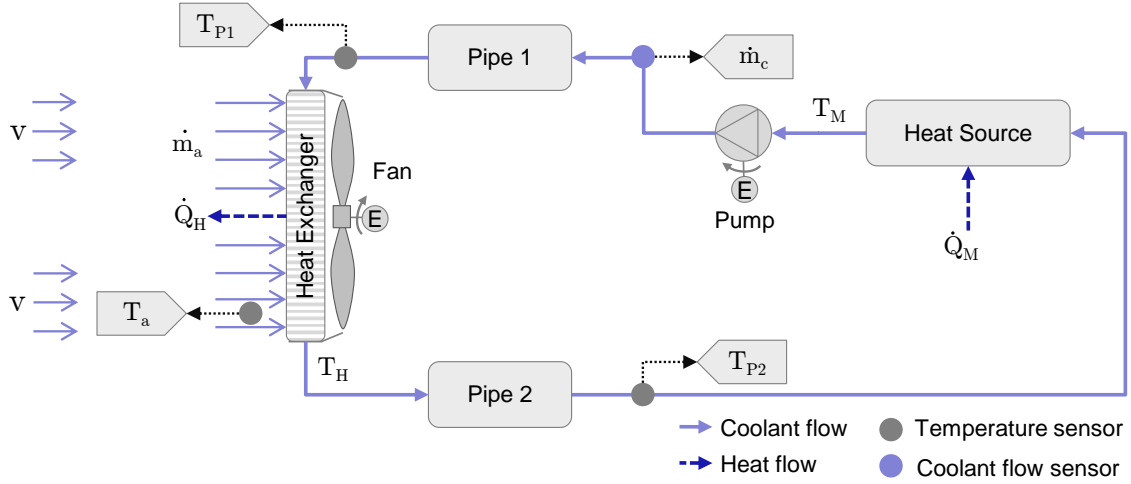
Figure 5.11.: Schematic of the simplified electronics cooling circuit.

Due to the simple flow setup equations for conservation of mass are straight forward to derive. Starting at the first law of thermodynamics for open systems we assume constant volumes with no accumulation. Additionally we neglect changes in potential and kinetic energy and changes of internal energy due to pressure changes and assume that no work is performed. With this common simplifications and assumptions we can state energy equilibrium for each lumped mass $m_{(k)}$ as

$$dH_{(k)} = \sum dm_{i,(k)} h_{i,(k)} + \sum dQ_j,$$
$$\text{with } \sum dm_{i,(k)} = 0 \tag{5.1}$$

with its enthalpy $H_{(k)} = T_{(k)} m_{(k)} c_{p,c}\left(T_{(k)}\right)$, its input and output mass flows $m_{i,(k)}$ and the corresponding specific enthalpies $h_{i,(k)} = T_{i,(k)} c_{p,c}\left(T_{i,(k)}\right)$. Subscript $(k) = \left\{P1, P2, M, H\right\}$ indicates the 4 volumes. For the sake of simplicity the dependence of the heat capacity of the temperature T is neglected and the specific heat capacity $c_{p,c}$ is assumed constant. Assuming constant masses $m_{(k)}$ and introducing heat capacities $C_{(k)} = m_{(k)} c_{p,c}$ the dynamic system equations can be written in a compact form as

$$
\begin{aligned}
C_{P1}\dot{T}_{P1} &= \dot{m}_c \left(h_H - h_{P1}\right) + K_H \left(T_a - T_H\right) \ , \\
C_M\dot{T}_M &= \dot{m}_c \left(h_{P1} - h_M\right) + \dot{Q}_M \ , \\
C_{P2}\dot{T}_{P2} &= \dot{m}_c \left(h_M - h_{P2}\right) + K_M \left(T_a - T_M\right) \ , \\
C_H\dot{T}_H &= \dot{m}_c \left(h_{P2} - h_H\right) + \dot{Q}_H(n, v, T_a, \dot{m}_c, T_{P2}) \ .
\end{aligned}
\tag{5.2}
$$

119

Symbol K denotes the product of the heat transfer coefficient h and the area A of the convective heat transfer to the ambient air having known temperature T_a. The control input w to the system is the fan speed n. The control output y which shall be controlled is the input temperature of the motor T_{P2}.

$\dot{Q}_M$ is assumed to be known (approximated/calculated from lookup tables or estimated by an observer). The calculation of $\dot{Q}_H$ is of more complex nature and will be outlined shortly in the following. As described in Eq. 3.45 - 3.49 first principle modeling of heat exchangers leads to partial differential equations which are usually solved via spatial discretization leading to a system of ordinary differential equations. This leads to a nonlinear plant model for input n, although (5.2) is linear with respect to input $\dot{Q}_H$. Assuming $\dot{m}_c$ constant even leads to a linear and time invariant (LTI) system. This fact will be exploited in the control approach. In the appendix Tab. A.1 specific numeric values for the plant parameters are listed.

5.2.3. Control

Objectives

Control objectives can be summarized as follows:

- Hard constraints on states and inputs have to be satisfied.
- Maximum performance in terms of control speed is an important target.
- Real-time execution on an embedded control unit must be possible.

Control concept

One common control approach to fulfill these challenging requirements is the use of so called *model predictive control* (MPC) as described in detail e.g. in [97, 98, 99, 100]. As shown in Fig. 5.12 the basic concept involves successive on-line optimization of the input control sequence (u_{k+1}) for a defined control horizon (N_c) taking into account the optimization criteria and constraints. From this optimal input sequence only the first sample is applied as control command. The main objective of the MPC in temperature control applications to is to reach the temperature setpoint without excessive oscillations and violation of temperature constraints.
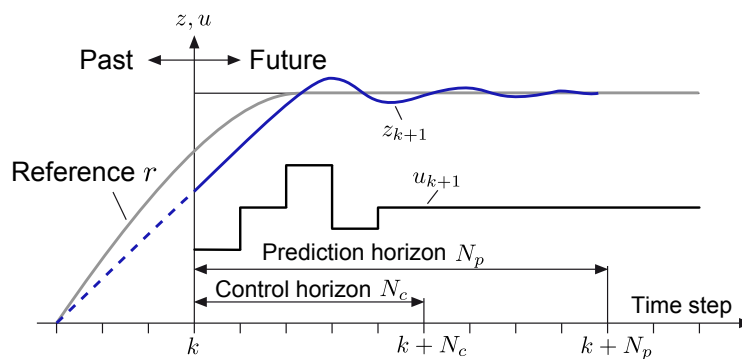
Figure 5.12.: Basic concept of a MPC approach [99].

Although there exist methods for controlling nonlinear plants using this approach (NMPC), having a linear plant leads to a reduced amount of required computing power and enables real-time execution on currently available hardware. In order to be able to apply linear MPC the plant model is split into a linear and a nonlinear dynamic part. At first we focus on the linear part with input $u = \dot{Q}_H$ to control output $z = T_{P2}$. In a second step we interpret the control command for $\dot{Q}_H$ as a setpoint for an underlying control loop handling the nonlinearity using an integrator and a feedback loop. Fig. 5.13 summarizes this approach. In a first step the mathematical plant model from (5.2) is
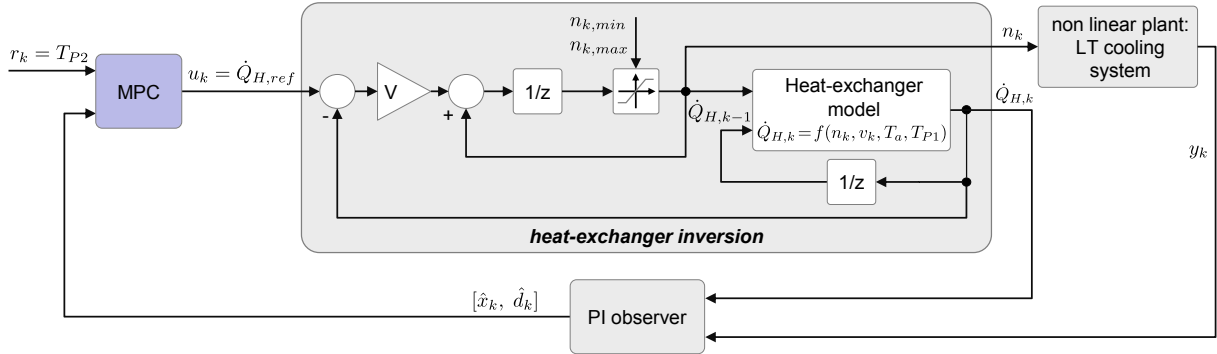
Figure 5.13.: Overview of the control concept consisting of the MPC, heat-exchanger inversion and interaction with the non linear plant model.

rewritten into the commonly used general form describing dynamic systems governed by linear differential equations in continuous time:

$$\begin{aligned} \dot{\mathbf{x}} &= \mathbf{A}\mathbf{x} + \mathbf{B}u + \mathbf{B}_d\mathbf{d} \\ z &= \mathbf{C}_z\mathbf{x} \end{aligned} \quad \text{with} \quad \mathbf{x}_0 = \mathbf{x}(t{=}0), \tag{5.3}$$

states $\mathbf{x} = \left[T_{P2}, T_M, T_{P1}, T_H\right]^T$, control input $u = \dot{Q}_H$, input of known disturbances $\mathbf{d} = \left[\dot{Q}_M, T_a\right]^T$ and output $z = T_{P2}$. Parameter matrices $\mathbf{A}$, $\mathbf{B}$, $\mathbf{B}_d$ and $\mathbf{C}_z$ follow from comparing (5.2) and (5.3).

Note that parameter matrix $\mathbf{A}$ depends on $\dot{m}_c$ leading to a linear *time variant* plant model. When applying time discretization on (5.3), which is a prerequisite to use MPC, additionally both input matrices in the time discrete form will depend on $\dot{m}_c$ (and the sample time of course). Although implementation of MPC for a linear time variant plant is possible, calculation of the time discretized plant parameters depending on $\dot{m}_c$ leads to unwanted calculation overhead. Parameter's time dependence will be addressed using an interpolation approach as outlined in section 5.2.3. For stating the MPC-problem $\mathbf{A}$ is assumed constant. Time discretization (as outlined in [101]) leads to a linear time invariant and discrete time plant model

$$\begin{aligned} \mathbf{x}_{k+1} &= \boldsymbol{\Phi}\mathbf{x}_k + \mathbf{H}u_k + \mathbf{H}_d\mathbf{d}_k \\ z &= \mathbf{C}_z\mathbf{x}_k \end{aligned} \quad \text{with} \quad \mathbf{x}_0 = \mathbf{x}(t{=}0). \tag{5.4}$$

Matrices $\boldsymbol{\Phi}$, $\mathbf{H}$, and $\mathbf{H}_d$ are derived from $\mathbf{A}$ (at a specific coolant mass flow), $\mathbf{B}$ and the used sampling rate t_s. The MPC formulation taking into account the reference signal r

is represented by

$$\min_{\Delta u_{0,...,N_c-1|k}} \mathbf{x}_{N_c|k}^T \mathbf{P} \mathbf{x}_{N_c|k} + \sum_{k=0}^{N_p-1} e_{k|k}^2 Q + \sum_{k=0}^{N_c-1} \Delta u_{k|k}^2 R$$

$$\text{w.r.t.} \tag{5.5}$$

$$e_{k|k} = r - z_{k|k}, \quad k = 0, 1, ..., N_p - 1,$$

$$u_{k|k} = u_{k-1|k} + \Delta u_{k|k}, \quad k = 0, 1, ..., N_c - 1,$$

$$\mathbf{x}_{k+1|k} = \mathbf{\Phi} \mathbf{x}_{k|k} + \mathbf{H} u_{k|k} + \mathbf{H}_d \mathbf{d}_{k|k}, \quad k = 0, 1, ..., N_p - 1,$$

$$z_{k|k} = \mathbf{C}_z \mathbf{x}_{k|k}, \quad k = 0, 1, ..., N_p - 1,$$

$$\mathbf{x}_{k+1|k}^{\min} \le \mathbf{x}_{k+1|k} \le \mathbf{x}_{k+1|k}^{\max}, \quad k = 0, 1, ..., N_p - 1,$$

$$u_k^{\min} \le u_{k|k} \le u_k^{\max}, \quad k = 0, 1, ..., N_c - 1,$$

$$\dot{u}_k^{\min} \le \dot{u}_{k|k} \le \dot{u}_k^{\max}, \quad k = 0, 1, ..., N_c - 1,$$

$$\Delta u_k = 0, \quad N_c \le k \le N_p.$$

where N_c is the control horizon, N_p the prediction horizon, $N_c \le N_p$, and $\mathbf{x}_{k+1|k}^{\min}$, $\mathbf{x}_{k+1|k}^{\max}$, $u_k^{\min}$, $u_k^{\max}$ the constraints for states and the input, respectively. The subscript $k+1|k$ denotes the value of the variable $k+1$ steps ahead of the current time instance k. Although in theory they reflect system parameters, from practical point of view Q and R are the design parameters for MPC-control. Terminal weight $\mathbf{P}$ (an additional design parameter) is derived by solving the discrete Riccati-equation as described in [98]. Note that the actual limitations $u_k^{\min}$, $u_k^{\max}$ can be derived from allowed minimum and maximum values of the fan speed, the actual states, the known disturbances and the vehicle speed using (3.46).

Observer

Usually there are two sensors available in a cooling circuit: one for x_1 and the other for x_3, but to use the MPC approach all states of the system need to be known at every time instance. Therefore an observer is used estimating the unmeasured states and reducing unwanted measurement noise. To enable zero offset tracking in the presence of modeling errors or constant disturbances either the controller or the observer has to be extended. Since extending the controller usually involves additionally solving anti-wind-up issues, the observer is extended avoiding these side effects. The proposed observer is extended to a so called *PI-observer* (as outlined in [102]) to additionally estimate a (const.) disturbance signal $\dot{Q}_M$. The feedback matrix $\mathbf{L} = \left[\mathbf{L}_P^T, L_I \right]^T$ of the observer

$$\begin{bmatrix} \hat{\mathbf{x}}_{k+1} \\ \hat{\mathbf{d}}_{k+1} \end{bmatrix} = \begin{bmatrix} \mathbf{\Phi} & \mathbf{H}_d \\ \mathbf{0} & \mathbf{E} \end{bmatrix} \begin{bmatrix} \hat{\mathbf{x}}_k \\ \hat{\mathbf{d}}_k \end{bmatrix} + \begin{bmatrix} \mathbf{H} \\ \mathbf{0} \end{bmatrix} u_k + \begin{bmatrix} \mathbf{L}_P \\ L_I \end{bmatrix} (\mathbf{y}_k - \hat{\mathbf{y}}_k)$$

$$\hat{\mathbf{y}}_k = \begin{bmatrix} \mathbf{C} & \mathbf{0} \end{bmatrix} \begin{bmatrix} \hat{\mathbf{x}}_k \\ \hat{\mathbf{d}}_k \end{bmatrix} \quad \text{with} \quad \mathbf{C} = \begin{bmatrix} 1, 0, 1, 0 \end{bmatrix} \tag{5.6}$$

is derived from an LQR feedback matrix of the respective extended dual plant. Note that, if the observer is executed using a shorter sampling time, compared to the MPC control, system matrices $\mathbf{\Phi}$, $\mathbf{H}$ and $\mathbf{H}_d$ have to be computed accordingly. Faster sampling of the

observer to a certain extend leads to reduced noise on the state estimates and will increase the overall control quality. In automotive control units 10, 20 or 100 ms are common data acquisition sampling times, which could be used for the observer.

Inversion of heat exchanger nonlinearity

The proposed MPC control computes a virtual control signal $u = \dot{Q}_H$, but the real plant input $w = n$ is the fan speed. Unfortunately (3.46) cannot be solved for n analytically. A possible approach to overcome this drawback is to derive n depending on $\dot{Q}_H$, $\hat{\mathbf{x}}$, $\hat{d}$ and v via a simple feedback loop as outlined in Fig. 5.13. Gain V has been tuned by hand using worst case approximations. The inversion loop is iterated a defined number of times after observer update calculation (10 to 30 iterations have been used in the simulation examples). Note that here solving for n and iterating (3.46) is done simultaneously.

In Fig. 5.14 the influence of fan speed and thus of air mass flow variation on the heat exchanger performance is depicted for a number of fluid (coolant and air) Entrance Temperature Differences (ETDs) and a coolant volume flow of 8 liters per minute. From this illustration it becomes evident that a higher ETD helps to improve the heat exchange performance without increasing the air mass flow.
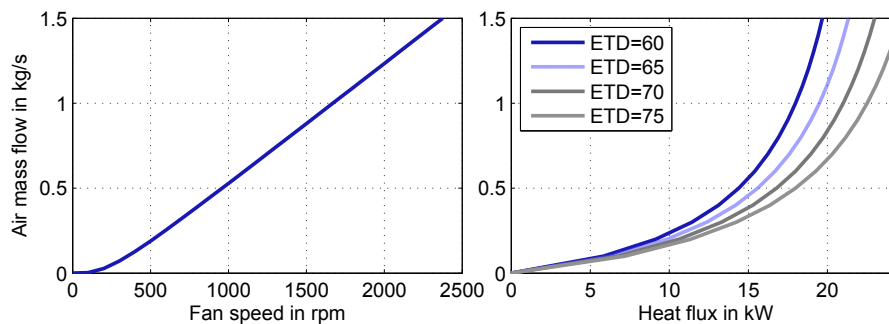
Figure 5.14.: Left: Air mass flow in dependence of fan speed; Right: Relation between heat exchanger air mass flow and heat flux for different fluid ETD.

Limitations and extensions of the approach

Up to now the matrices of the continuous time linear model (5.3) have been assumed time-invariant. This assumption restricts using the approach for constant coolant mass flows only. To apply the control concept for varying coolant mass flows the following practical extensions are proposed:

- instead of using one discrete time LTI model, two models are used: one for minimum and one for maximum coolant mass flow.
- Two observers are operated, one for each plant model. Estimation of state and disturbance signals are interpolated according to the actual coolant mass flow.
- Two MPC control signals are calculated, one for each model. The final requested heat flow at the heat exchanger is also interpolated according to the actual coolant mass flow.

Validation of this extension using simulation and testbed experiments will be shown in the following chapter.

5.2.4. Simulation

Simulation was performed using a non linear cooling system model as plant model together with the presented control concept derived from the linear system description given in (5.2). Fig. 5.13 summarizes the structure of the resulting simulation model. To simulate a real live driving behavior the air mass flow has to be a function of driving speed and fan activation level. This is implemented using the energy equation as shown in 3.53. The drive cycle dependent heat losses (disturbances) of the e-components where calculated using efficiency data from component supplier together with a powertrain simulation tool. Boundary conditions for the simulations where as follows;

Table 5.1.: Simulation boundary conditions

Var	Value	Unit	Description of parameters
$\dot{m}_c$	0.13	kg/ sec	coolant mass flow
T_a	30	°C	ambient air temperature
T_{setp}	50	°C	control value temperature setpoint

Two different control concepts have been assessed based on real live drive cycle simulations: first the presented MPC approach and second a conventional fan control applying constant fan speed levels (4 different levels in the discussed example) at specified temperature ranges. Simulation result are depicted in Fig. 5.15.

Analysis of the results for MPC shows an excellent control performance. Noticeable is the robust temperature tracking capability regardless of the dynamic drive cycle behavior with its rapid changes in driving speed (air mass flow) and heat losses (disturbance) as shown in Fig. 5.15 plot 1-5. Careful inspection of the left hand side bottom plot in Fig. 5.15 shows a slight Temperature undershoot after 100 minutes. This is because the air mass flow coming from the current driving speed is resulting in a heat flux that is already exceeding the MPC target heat dissipation as shown in Fig. 5.15 plot 3 on the left hand side.

Comparison of MPC with the conventional control (Fig. 5.16) shows that, even though 4 discrete fan speed levels where used, the temperature tracking performance of the MPC cannot be reached and oscillations occur. Limiting the possible fan speeds to discrete values in general causes higher fan speed peaks which are more expensive in terms of energy consumption. The reason for this is that the consumed power is proportional to the cube of fan speed, as described in section 5.2.1. Together with the throughout lower ETD the conventional controlled fan is consuming almost twice the amount of energy compared to MPC as shown in Fig. 5.16.
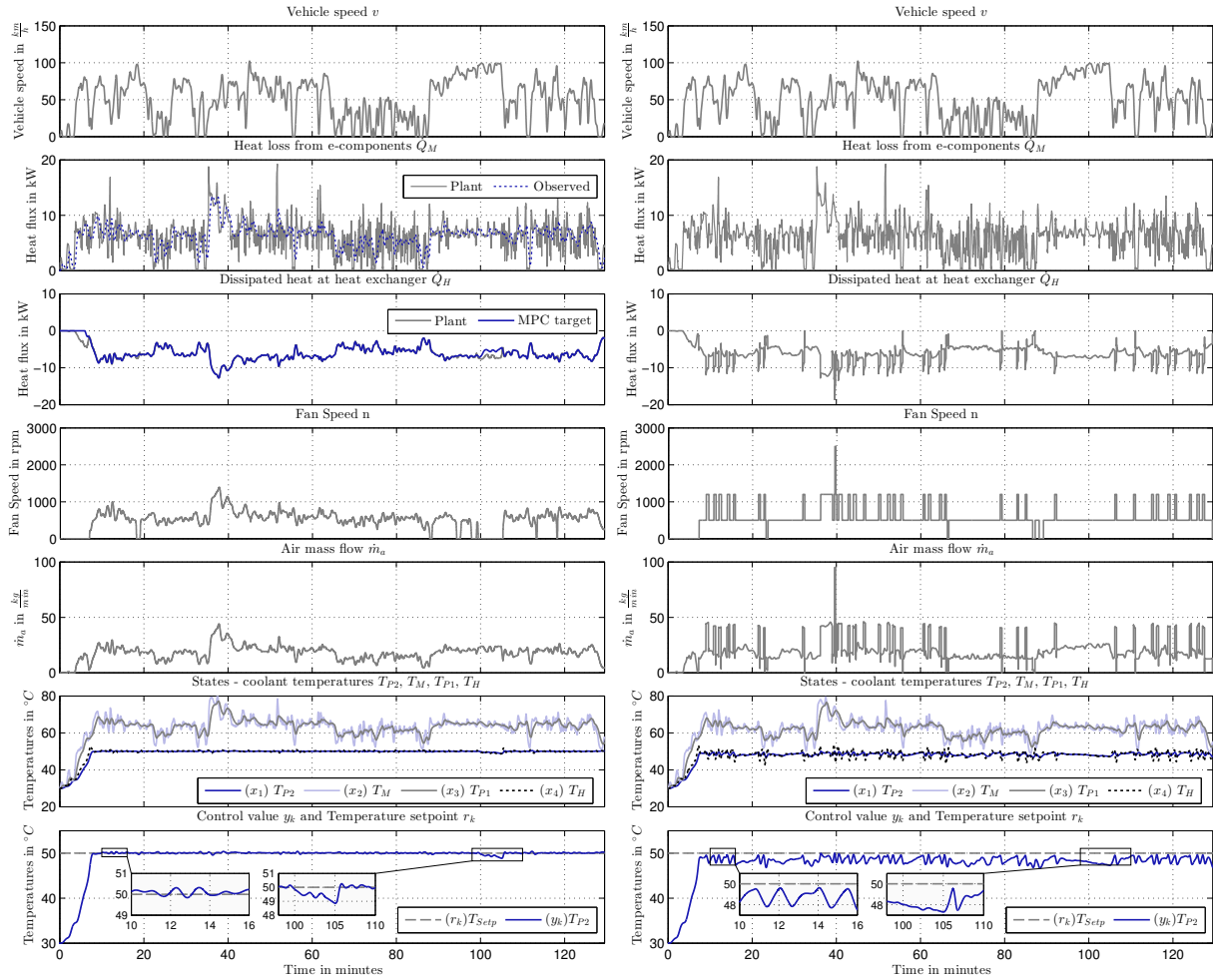
Figure 5.15.: Simulation results for a real live drive cycle with proposed MPC approach (left) and with conventional control applying defined constant fan speeds (right).
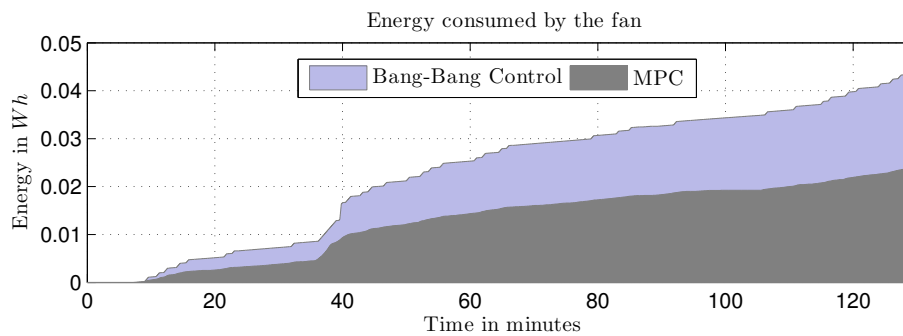
Figure 5.16.: Comparison of cumulated fan energy consumption for conventional control and MPC.

5.2.5. Testbed operation

Testbed setup

Since an experimental vehicle was not available, a slightly modified testbed setup was used for model parameter identification (mainly heat exchanger) to demonstrate the practical feasibility of the control approach.

A schematic of the testbed configuration is shown in Fig. 5.17.

At the testbed a single heat source covers the sum of all heat sources from the electric components. In addition to the simulation model setup convective heat transfer between the pipes and the surrounding air is considered ($\dot{Q}_{conv}$). Because the limiting front motor entrance temperature is not measured in the testbed configuration the heat source entrance temperature the estimated signal is used for control. Therefore the control set-point temperature has to be reduced in order to meet the 65°C coolant inlet temperature target of the e-motor at the front axle.

Figure 5.17.: Testbed setup for concept validation.

Testbed facility was a wind tunnel that includes a coolant conditioning unit and is capable of testing full scale automotive cooling systems as illustrated in Fig. 5.18.

Figure 5.18.: Wind tunnel and conditioning unit at the VIRTUAL VEHICLE Research Center.

Measurement results

Measurements have been conducted using a testbed conditioning unit and a wind tunnel to demonstrate the applicability of the presented MPC control approach for a full scale

automotive cooling system. In the experiments a constant heat loss of 20kW and a constant coolant mass flow was used. Results are depicted in Fig. 5.19.

Note that there was a strong nonlinear behavior of the used fan: At low fan speed demand values small changes in the fan speed control signal already caused huge changes in air mass flow. As a consequence air mass flows between 0 and 10 kg/min could not be applied. In the experiment the time to warm-up the system is therefore longer than necessary, since too much heat is rejected at the heat exchanger from approximately minute 7 to 11. With increasing fan demand and air mass flow the control performance improves and the heat exchanger heat flux can be controlled as requested by MPC. Finally, after 15 minutes the temperature reaches the desired maximum value and shows almost no overshoot which assures a high cooling efficiency.
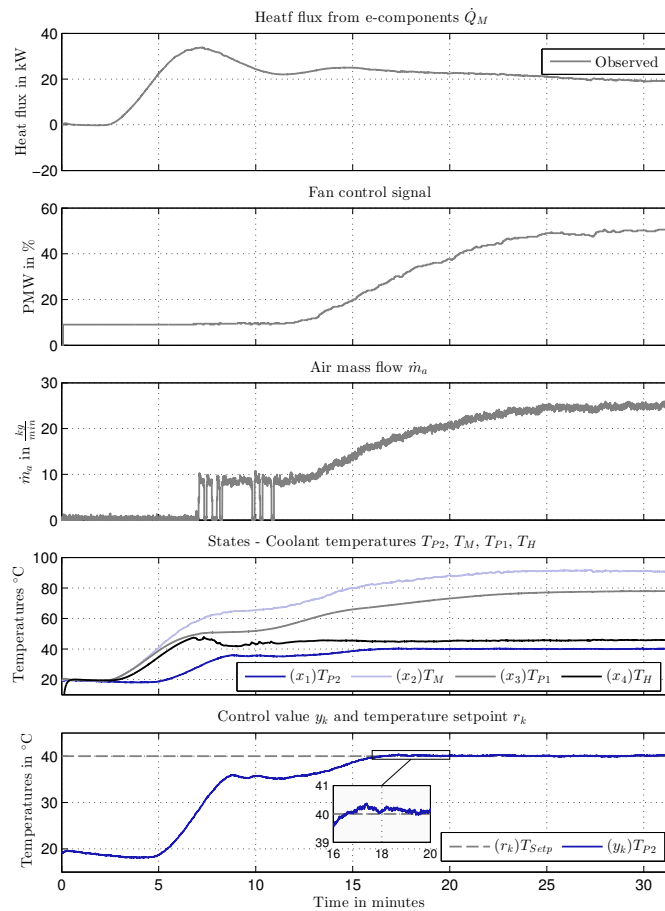
Figure 5.19.: Measurement results for MPC controlled fan at constant heat loss conditions

5.2.6. Summary and Conclusion

For a standard cooling circuit a plant model has been derived, consisting of a linear and a nonlinear part. This enables the straight forward use of a linear observer and a linear model predictive control for the linear part of the plant. The nonlinear part is addressed separately. The resulting new control approach has been validated in simulation as well as on test bed. Simulation results from a transient real life test cycle show big potential of

the proposed control strategy for saving energy spend in the cooler fan. A first successful application on testbed proved feasibility of the control concept regarding robustness.

Due to the special control layout real-time execution on a state of the art automotive control unit is not an issue. In contrast to automotive cooling circuit control schemes currently used in cars the proposed approach offers direct consideration of state and actuator constraints, better performance and finally less power consumption at the fan.

5.2.7. Outlook

The proposed control approach has been demonstrated for cooling circuits with all components connected in series but allows straight forward extension to more complex (branched) cooling layouts comprising switch valves. In such cases the hydraulic and thermal network towards coolant mass flows and mixing temperature can be solved applying appropriate methods available in literature ([103] or [104]).

Additional consideration of the pump speed in the control law could be used to reduce the heat flux at the heat exchanger and to decrease pump energy consumption and to reduce temperature undershooting.

Measurements showed that the cooling system warm-up behavior could be enhanced by using a different fan actuator that allows better control at the low air mass flow range from $0 - 10 kg/min$. Alternatively, an open loop fan control strategy could be used if low air mass flow is requested in the initial warm-up phase.

5.3. Nonlinear control

5.3.1. Introduction

Regarding the thermal system actuators in the vehicle the ICE coolant pump is the biggest energy consumer besides the air conditioning (AC) compressor and the main vehicle fan. The Future Hybrid vehicle is equipped with a 400W electrical water pump for engine cooling. For reasons of simplicity and convenience classical control laws like Bang-Bang control or a map based control approach are applied for temperature control. Using a Bang-Bang control is simple but it leads to unwanted overcooling (the temperature drops significantly below the setpoint temperature) and temperature oscillations at rapid load and cooling power changes. As mentioned in section 5.2.1 the radiator cooling capacity is dependent from heat transfer coefficients of air ($f(\dot{m}_c)$) and coolant side ($f(\dot{m}_c)$) as well as on the temperature difference. Thus an increasing cooling request can be fulfilled by increasing the heat transfer coefficients or increasing the temperature difference. Since a higher heat transfer coefficient requires an increase in flow rate, which goes along with a cubic[3] increase in actuator power (fan and/or pump), the highest possible temperature difference is demanded.

The highest allowable coolant temperature in the combustion engine depends on the boiling temperature of the fluid on the one hand but more important on the temperature of the critical engine parts (e.g. valve bridge temperature). Thus in the following section the control setpoint is formulated in terms of the engine solid temperature.

---

[3] $\frac{P_1}{P_2} = (\frac{\dot{m}_1}{\dot{m}_2})^3$

5.3.2. Plant model setup

Thermal circuit overview

The Future Hybrid high temperature ICE cooling circuit is subsequently used for setup of the mathematical model and design of a Control Ljapunov Function (CLF) [105, 99]. As mentioned in section 5.1.2 control algorithms on component level are only active when all conditions for the corresponding thermal function are met. In case of the ICE cooling circuit the CLF based control is active if the thermal mode *HtWarm* or *HtWarmHeatg* are enabled (as shown in Fig. 5.20 on left and right hand side, respectively). During this operating modes the considered cooling circuit consists of two main heat source components in parallel; heat from the cumbustion engine head and block structure and heat transfered by the engine oil cooler (C03).

Engine and oil cooler are connected in parallel. They are supplied with the coolest fluid directly after the heat exchanger (C05) and the coolant pump (C01). Then both fluid flows are mixed again before reaching the thermostatic valve (C02). In the baseline vehicle a *wax* thermostatic valve is implemented. The containing wax melts and increases in volume as the coolant heats up. Due to the expansion forces the valve opens and allows flow through radiator (C05) while closing the bypass branch in return. A maximum engine head coolant outlet temperature of 115°C, and a maximum valve bridge temperature of 270 °C are specified by the manufacturer.

The amount of air flowing through the heat exchanger, and thus the heat transfered from coolant to air, is mainly influenced by a given vehicle driving speed and the fan speed.
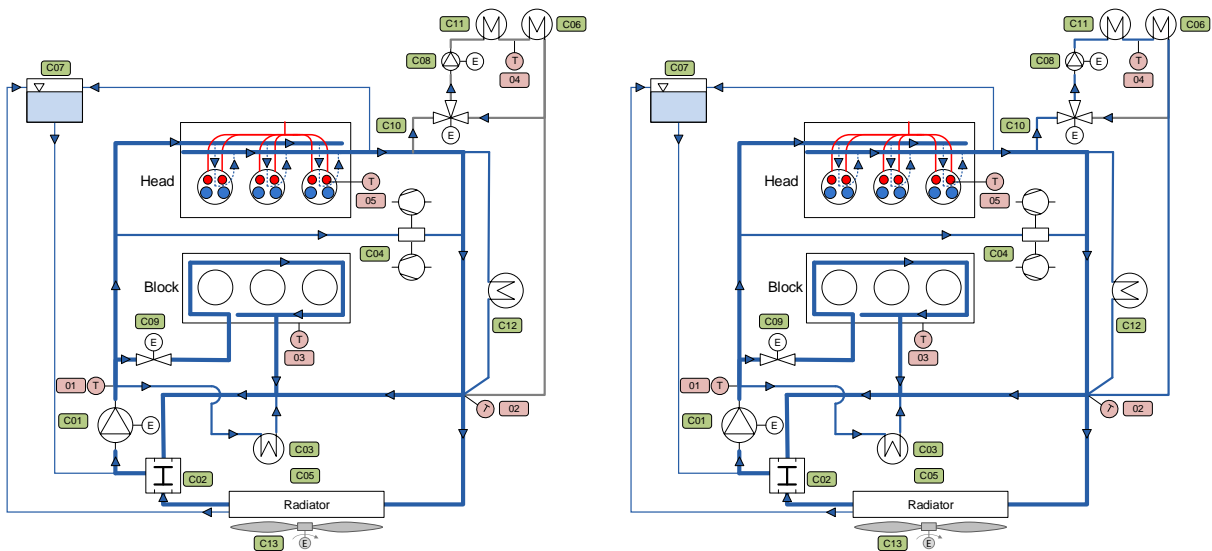
Figure 5.20.: Schematics of the ICE cooling circuit operating modes where the CLF based control is active.

Mathematical system model

Towards the mathematical model formulation the following assumptions are applied;

- The cooling circuit is equipped with an electrically controllable bypass valve which allows opening and closing of the bypass and radiator branch, independent from the current coolant temperature;

- The bypass branch is closed and the entire coolant flow is going through the radiator. This is no hard restriction since the controller and it's mathematical system model are not used during engine warm-up;

- Engine head and block are represented by one coolant lumped mass (T_e) and one solid lumped mass (T_s);

- Heat loss due to combustion $\dot{Q}_g$ and friction $\dot{Q}_f$ are assumed to be known and are used as input and

- Sensors for measuring all system states are available. This assumption is true in case of the Future Hybrid demonstrator vehicle, but it may not hold for series production vehicles. Thus an observer as outlined in section 5.2.3 may be used.

This leads to a control oriented model consisting of ordinary differential equations. They allow an interpretation of the cooling circuit system as 4 lumped masses: "*engine coolant*" (e), "*engine solid*" (s), "*radiator*" (r), "*oil*" (o). They are connected in a loop, exchanging the coolant mass flow $\dot{m}_c$ as shown in Fig. 5.21. Heat input from combustion gas and friction are denoted as $\dot{Q}_g$ and $\dot{Q}_f$, respectively. Convective heat flow from solid to coolant, oil to coolant and air to coolant are denoted as $\dot{Q}_{sc}$, $\dot{Q}_{co}$ and $\dot{Q}_r$, respectively. Note that the arrows in Fig. 5.21 define the positive direction of the heat flow. Thus a negative $\dot{Q}_{()}$ indicates a change in heat flow direction. A speed controlled pump drives the coolant mass flow $\dot{m}_c$. The air mass flow $\dot{m}_a$ at the heat exchanger air input is of temperature T_a. Symbol v denotes the vehicle velocity.
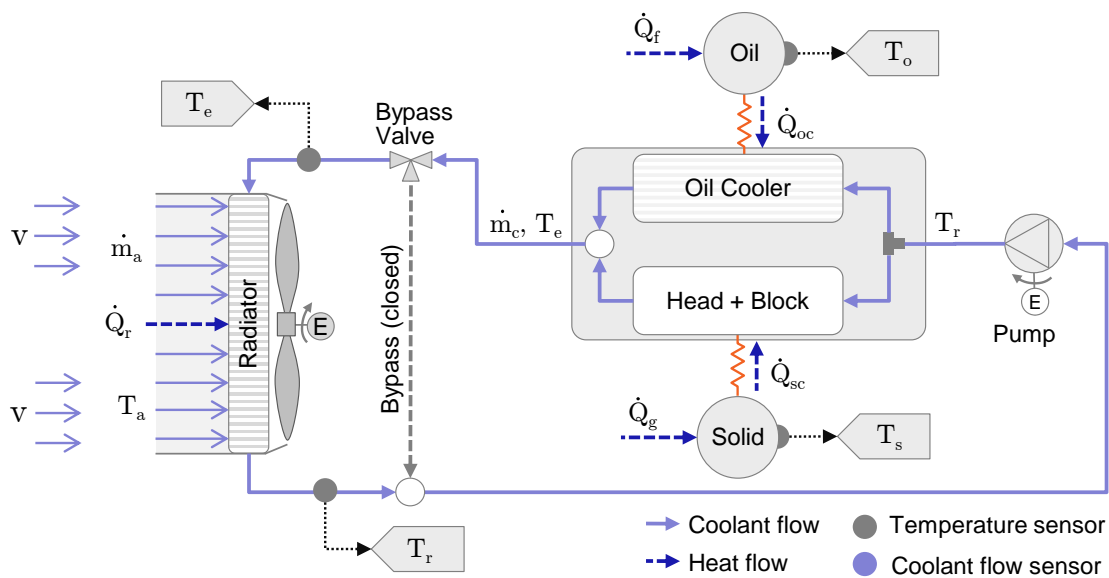
Figure 5.21.: Schematic of the simplified ICE cooling circuit.

This simplified flow setup together with common assumptions regarding the energy conservation law and fluid properties (as given in section 5.2.2) allows to state the energy

equilibrium for each lumped mass $m_{(k)}$ as

$$dH_{(k)} = \sum dm_{i,(k)} h_{i,(k)} + \sum dQ_j, \quad \text{with} \quad \sum dm_{i,(k)} = 0 \tag{5.7}$$

with its enthalpy $H_{(k)} = T_{(k)} m_{(k)} c_{p,c}$, its input and output mass flows $m_{i,(k)}$ and the corresponding specific enthalpies $h_{i,(k)} = T_{i,(k)} c_{p,c}$. Subscript $(k) = \{e, s, r, o\}$ indicates the 4 volumes. Assuming constant masses $m_{(k)}$ and introducing heat capacities $C_{(k)} = m_{(k)} c_{p,c}$ allows writing the dynamic system equations in a compact form as

$$
\begin{aligned}
C_e \dot{T}_e &= \dot{m}_c \left(h_r - h_e \right) + K_s \left(T_s - T_r \right) + K_o \left(T_o - T_e \right) , \\
C_s \dot{T}_s &= K_s \left(T_r - T_s \right) + \dot{Q}_g , \\
C_r \dot{T}_r &= \dot{m}_c \left(h_e - h_r \right) + K_r \left(T_e - T_a \right) , \\
C_o \dot{T}_o &= K_o \left(T_e - T_o \right) + \dot{Q}_f .
\end{aligned}
\tag{5.8}
$$

T_a is a the known ambient air temperature. The control input u to the system is the coolant mass flow $\dot{m}_c$ which is a function of the pump speed n. The control output y which shall be controlled is the *mean engine solid temperature T_s*.
$\dot{Q}_g$ and $\dot{Q}_f$ are assumed to be known inputs (e.g.: calculated from the currently injected amount of fuel and from friction maps or estimated by an observer).

Symbol $K_{()}$ denotes functions describing the convective heat transfer between coolant and engine structure (K_s), coolant and oil (K_o) and coolant and ambient air (K_r). The calculation of the heat transfer functions is of more complex nature and will be outlined shortly in the following. As described in Eq. 3.45 - 3.49 first principle modeling of heat exchangers leads to partial differential equations which are usually solved via spatial discretization leading to a system of ordinary differential equations. Alternatively, it is possible to fit heat transfer functions from complex simulation models which are not as accurate as the spatial discretized model but are capable of predicting transfered heat in the right magnitude. Fig. 5.22 shows the quality of the identified heat transfer function for describing the heat transfer between fluid and engine solid. The static heat transfer functions for K_s, K_o and K_r can be given as

$$
\begin{aligned}
K_s &= k_1 \alpha_1 \dot{m}_c T_e^{b_1} , \\
K_o &= k_2 \alpha_2 \dot{m}_c + \dot{m}_o^{b2} k_3 , \\
K_r &= k_4 \dot{m}_c + k_5 \dot{m}_a^{b_3} .
\end{aligned}
\tag{5.9}
$$

The constant coefficients k_1, k_2, k_3, k_4, k_5, b_1, b_2 and b_3 are fitted in a least-squares sense with MATLAB's `fminsearch` optimization function for Design of Experiments (DoE) input sequences consisting of a full factorial combination of all relevant fluid mass flows and temperatures. $\dot{m}_c$ and $\dot{m}_a$ are the oil and coolant mass flow which are assumed to be known because the oil pump is mechanically powered and thus the mass flow is calculated from an engine speed and temperature dependent map. The air mass flow is calculated from a vehicle velocity and fan speed dependent map. Coefficients α_1 and α_2 are used to specify the coolant flow distribution between ICE engine structure (block and head) and the oil cooler ($\alpha_1 + \alpha_2 = 1$). This coefficients are almost constant (for the warm engine) and can be derived from cooling system layout analysis.
Substitution of Eq. 5.9 into Eq. 5.8 leads to a nonlinear plant model for input $\dot{m}_c$.
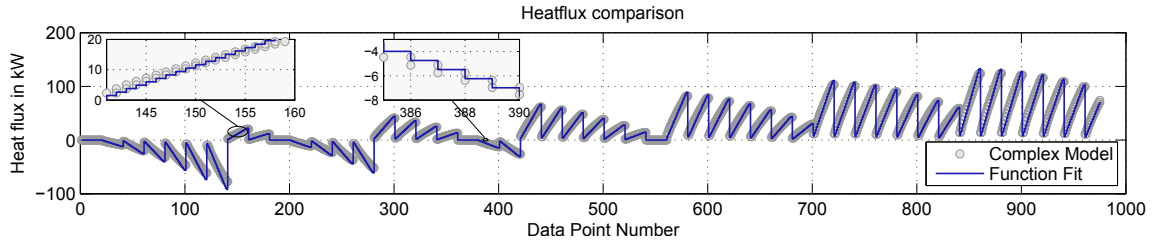
Figure 5.22.: Engine ↔ coolant HTC fit for various flow and temperature conditions.
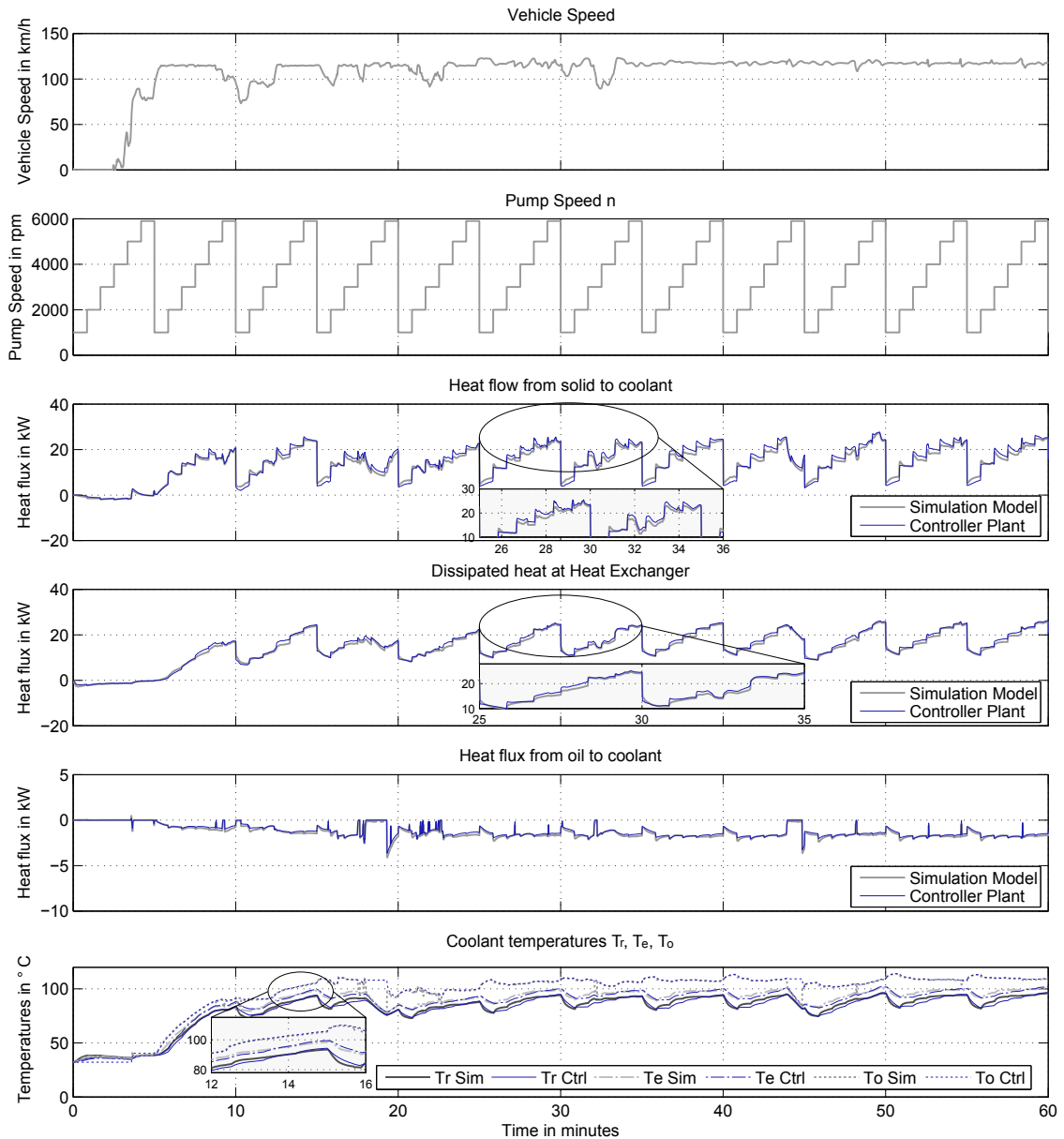
Figure 5.23.: Detailed high temperature cooling simulation model versus controller plant model.

Comparison of simulation results for the controller plant model and the complex simulation model (as shown in Fig. 5.23) show a satisfactory agreement. Thus the developed mathematical model is capable of describing the essential dynamic behavior of the system under given assumptions (bypass branch closed, no wax thermostat,...).

5.3.3. Control

The nonlinear characteristics of thermo fluid systems implies the usage of a nonlinear control law. It is used for stabilization of the solid engine mass temperature.

Besides the stability analysis Ljapunov's direct method can be used for control synthesis [106, 105, 107]. Such synthesis is called CLF $V(\mathbf{x})$, which applies the control vector $\mathbf{u}$ of a nonlinear plant

$$\dot{\mathbf{x}} = \mathbf{f}(\mathbf{x}, \mathbf{u}) \tag{5.10}$$

to minimized the radial unbound Ljapunov-function $V(\mathbf{x})$ such that the inequality

$$\dot{V}(\mathbf{x}) < 0 \tag{5.11}$$

is valid for all $\mathbf{x} \neq 0$. Based on the Ljapunov's stability law the determined control input $\mathbf{u}(\mathbf{x})$ forms a control loop

$$\dot{\mathbf{x}} = \mathbf{f}(\mathbf{x}, \mathbf{u}(\mathbf{x})) \tag{5.12}$$

with an asymptotically stable equilibrium point.
Subsequently, the following definition and conditions are used to find a valid CLF [107].

Definition 5.1. Control-Ljapunov-Function. *Considered is a system of the form*

$$\dot{\mathbf{x}} = \mathbf{f}(\mathbf{x}, \mathbf{u}), \quad \mathbf{x} \in I\!\!R^n, \quad \mathbf{u} \in I\!\!R^m,$$

with the equilibrium point $\mathbf{x}_R = \mathbf{0}$ with $\mathbf{u} = \mathbf{0}$. Then a continuously differentiable function $V(x)$ is called Control-Ljapunov-Function if following conditions are met:

1. *$V(\mathbf{0}) = 0$,*
2. *$V(\mathbf{x}) > 0$ for all $\mathbf{x} \neq \mathbf{0}$,*
3. *$V(\mathbf{x}) \rightarrow \infty$ for $|\mathbf{x}| \rightarrow \infty$,*
4. *There exists a $\mathbf{u}(\mathbf{x})$ which satisfies $\dot{V}(\mathbf{x}) < 0$ for all $\mathbf{x} \neq 0$.*

For the system given in Eq. 5.8 with $\mathbf{u} = \mathbf{0}$ it can be shown that $\mathbf{x}_R = \mathbf{0}$ is an equilibrium point of the system. Moreover it can be stated that the system is in an equilibrium point if all temperatures are equal and the heat flux from combustion and friction disappears.

Following definition 5.1 a control law shall be designed which stabilizes the system around the equilibrium point T_d which corresponds to the desired engine solid temperature. Therefore the tracking error dynamics $\dot{e}_s$ is introduce as an *additional system state* defined as

$$\dot{e}_s = (\dot{T}_s - \dot{T}_d), \tag{5.13}$$

and the related tracking error

$$e_s = (T_s - T_d). \tag{5.14}$$

For a constant desired temperature $\dot{T}_d$ Eq. 5.13 simplifies to

$$\dot{e}_s = \dot{T}_s. \tag{5.15}$$

For the system defined by Eq. 5.8 and Eq. 5.15 a CLF satisfying conditions 1-3 from definition 5.1 can be given as

$$V(e) = \frac{1}{2}e_s^2 \tag{5.16}$$

with the derivative

$$\dot{V}(e) = e_s\dot{e}_s. \tag{5.17}$$

Substituting Eq. 5.15 into Eq. 5.17 and using T_s from Eq. 5.8 together with K_s from Eq. 5.9 yields

$$\dot{V}(e) = \frac{e_s}{C_s}\left(\dot{Q}_g + k_1\alpha_1\dot{m}_c(T_r - T_s)T_e^{b_1}\right). \tag{5.18}$$

Consequently a control input $\dot{m}_c$ that satisfies the condition $\dot{V}(e) < 0$ for all $\mathbf{x} \neq 0$ can be determined as

$$\dot{m}_c = \frac{-C_1C_se_s - \dot{Q}_g}{\alpha_1k_1(T_r - T_s)T_e^{b1}} \tag{5.19}$$

where coefficient C_1 is a weighting factor for influencing the impact of the tracking error e_s on the control input calculation. Back substitution of $\dot{m}_c$ as in Eq. 5.19 into Eq. 5.18 yields

$$\dot{V}(e) = -C_1e_s^2 \tag{5.20}$$

which means the derivative of the Ljapunov function is negative definite for all $C_1 > 0$ and $e_s \neq 0$. Consequently the tracking error equilibrium point $e_R = 0$ is asymptotically stable. Performance and applicability of the control law is investigated in the following section with the help of numerical simulation studies.

5.3.4. Simulation

Simulation was performed using the global vehicle simulation model, as presented in chapter 4, as nonlinear plant model together with the presented control concept derived from the nonlinear system description given in Eq. 5.8. Fig. 4.4 summarizes the structure of the resulting simulation model. To simulate a real live driving behavior a representative customer drive cycle, found by cluster analysis, is used as input for the system. Boundary conditions for the simulations where as follows;

Table 5.2.: Simulation boundary conditions

Var	Value	Unit	Description of parameters
T_a	$30.9 - 31.5$	°C	ambient air temperature
T_{setp}	130	°C	control value temperature setpoint
SoC_{init}	50	%	initial battery SoC

Two different control concepts have been assessed based on real live drive cycle simulations; firstly the presented CLF approach, secondly a conventional pump control applying constant pump speed levels (4 different levels in the discussed example) at specified temperature ranges. Simulation results are depicted in Fig. 5.24.

Analysis of the results for CLF shows an excellent control performance. Noticeable is the good temperature tracing capability regardless of the dynamic drive cycle behavior with its rapid changes in driving speed (air mass flow) and heat losses (disturbance) as shown in Fig. 5.24 plot 1-5. The solid temperature undershoots on the left hand side bottom plot in Fig. 5.24 are mainly caused by the maximum allowed coolant temperature difference ($12\,°C$) between engine inlet and outlet. This specification was used as lower saturation boundary condition for the coolant mass flow. Upper saturation boundary condition is the maximum achievable coolant mass flow which is available from cooling system layout simulations.

Comparison of CLF based control with the conventional control (Fig. 5.25) shows that, even though 4 discrete pump speed levels where used, the temperature tracking performance of the CLF based control cannot be reached and oscillations occur. The transient behavior of the coolant temperature is closely coupled to the solid temperature, thus comparison of the CLF based control with the conventional control (Fig. 5.25, row 6) shows that the CLF keeps the coolant temperature at an overall higher level. Limiting the possible pump speeds to discrete values in general causes a higher average pump speed which is more expensive in terms of energy consumption and leads to overcooling at transient load changes.

Together with the throughout higher ETD the pump consumes one third less energy by using CLF based control compared to conventional control, as shown in Fig. 5.25.

5.3.5. Summary and Conclusion

For a common ICE cooling circuit a nonlinear plant model consisting of four differential equations and three algebraic heat transfer functions has been derived. This encourages the usage of a nonlinear control law which is based on Ljapunov's stability theorem. The resulting new control approach has been validated by means of a global vehicle simulation to consider all relevant interactions with other vehicle subsystems (e.g. powertrain). Simulation results from a transient real life test cycle show big potential of the proposed control strategy for saving energy spend in the ICE coolant pump. Due to the fairly simple control law a real-time execution on a state of the art automotive control unit is not an issue. In contrast to automotive cooling circuit control schemes currently used in cars the proposed approach offers better performance and finally less power consumption at the pump.

5.3.6. Outlook

The proposed control approach has been demonstrated for a cooling circuit equipped with a bypass valve which is always open (full flow over the radiator) when the vehicle cooling system is on the *warm* operating mode. Together with the limitation regarding the maximum coolant temperature difference between engine inlet and outlet this was causing unwanted overcooling in some situations. Closing the bypass valve during this

situations would rapidly reduce the radiator heat flux and diminish the engine coolant in- and outlet temperature difference. Therefore future work will consider controlling the bypass valve to improve the tracking performance and to decrease the pump power consumption even further. Additional consideration of the fan speed in the control law could be used to reduce the heat flux at the heat exchanger and to decrease fan energy consumption.
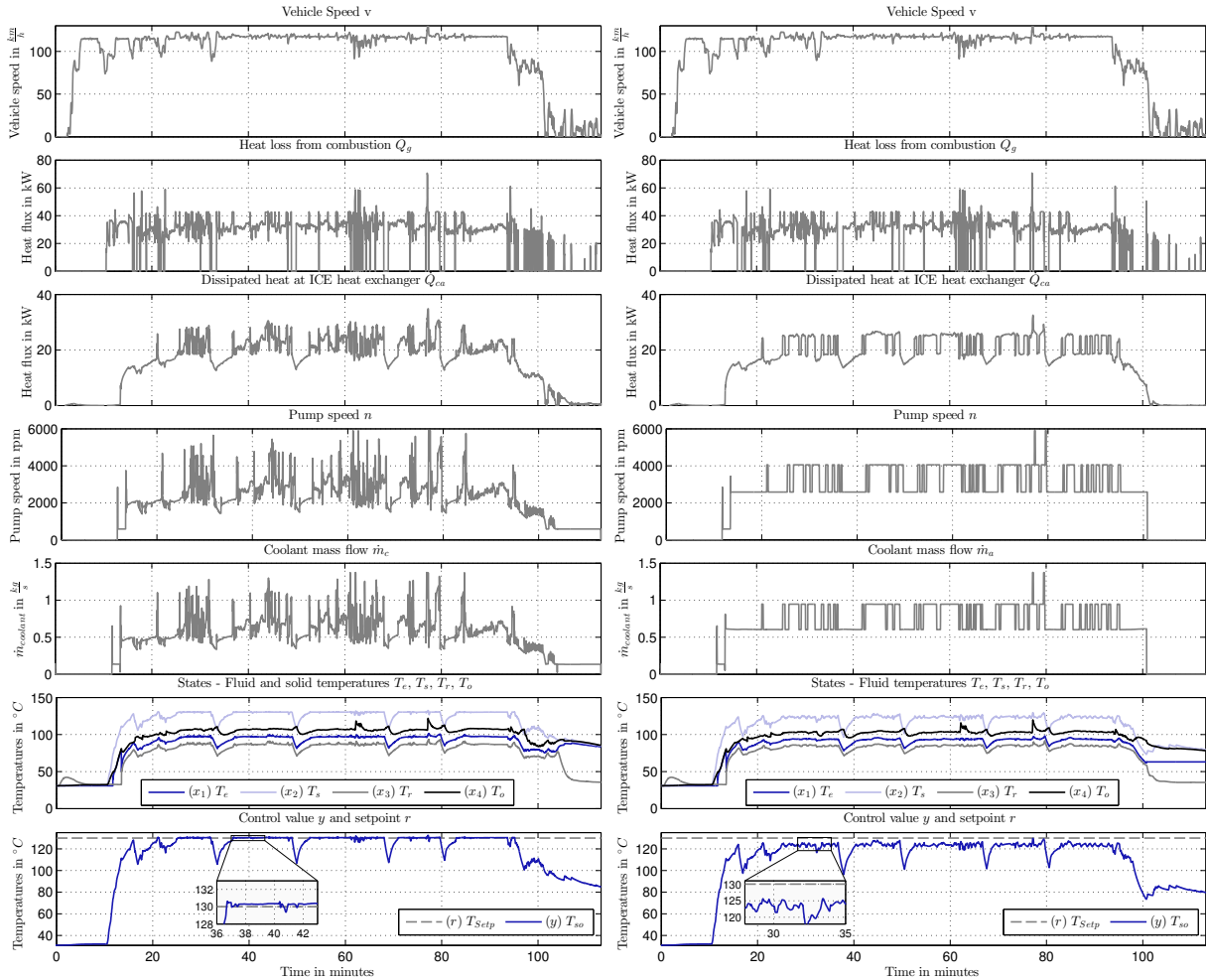
Figure 5.24.: Simulation results for a real live drive cycle with proposed CLF approach (left) and with conventional control applying defined constant pump speeds (right).
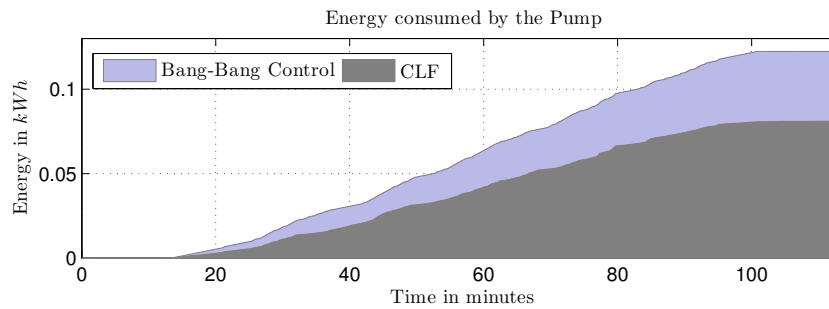
Figure 5.25.: Conventional control versus CLF; cumulated pump energy consumption.

6

Lifetime thermal performance assessment

One of the main contributions of this thesis is a methodology for the assessment of different thermal management features and control strategies under real-world conditions. In the previous chapters a framework for a thermal management controller and a thermo fluid systems simulation toolbox were presented. They reflect key pieces of the global vehicle simulation model which is used in this chapter to analyze the lifetime thermal behavior. First the lifetime thermal analysis methodology is explained. Afterwards details on the statistical approach, used for identifying representative drive cycles and ambient profiles, are outlined. Finally the lifetime thermal performance, in terms of energy consumption and durability, of the Future Hybrid vehicle is addressed for a number of control approaches and hardware configuration variants.

6.1. Introduction

The layout of the thermal system and its control strategy need to find a balance of efficiency and component durability under consideration of a representative annual usage profile. In order to support this development process a methodology is introduced that allows the assessment of energy consumption together with lifetime estimations for sensitive components like the traction battery. For lifetime analysis one of the key requirements are short simulation run-times without sacrificing the model accuracy and fidelity. Thus simulation of 365 consecutive days, á 24 hours, is not a realistic option. In the present approach custom drive cycles are identified from real-world driving by means of cluster analysis. These drive cycles are a statistically significant representation of the real user behavior. This drive cycles together with according ambient temperature profiles are used as input for the global vehicles simulation model, as introduced in chapter 4. The global vehicles simulation model allows assessing the resulting component temperature traces and the energy consumption under consideration of different thermal control strategies and hardware configurations. This comprehensive approach supports the selection of the system design and its operational control with special respect to aging and energy efficiency, already in the early phases of the vehicle development process.
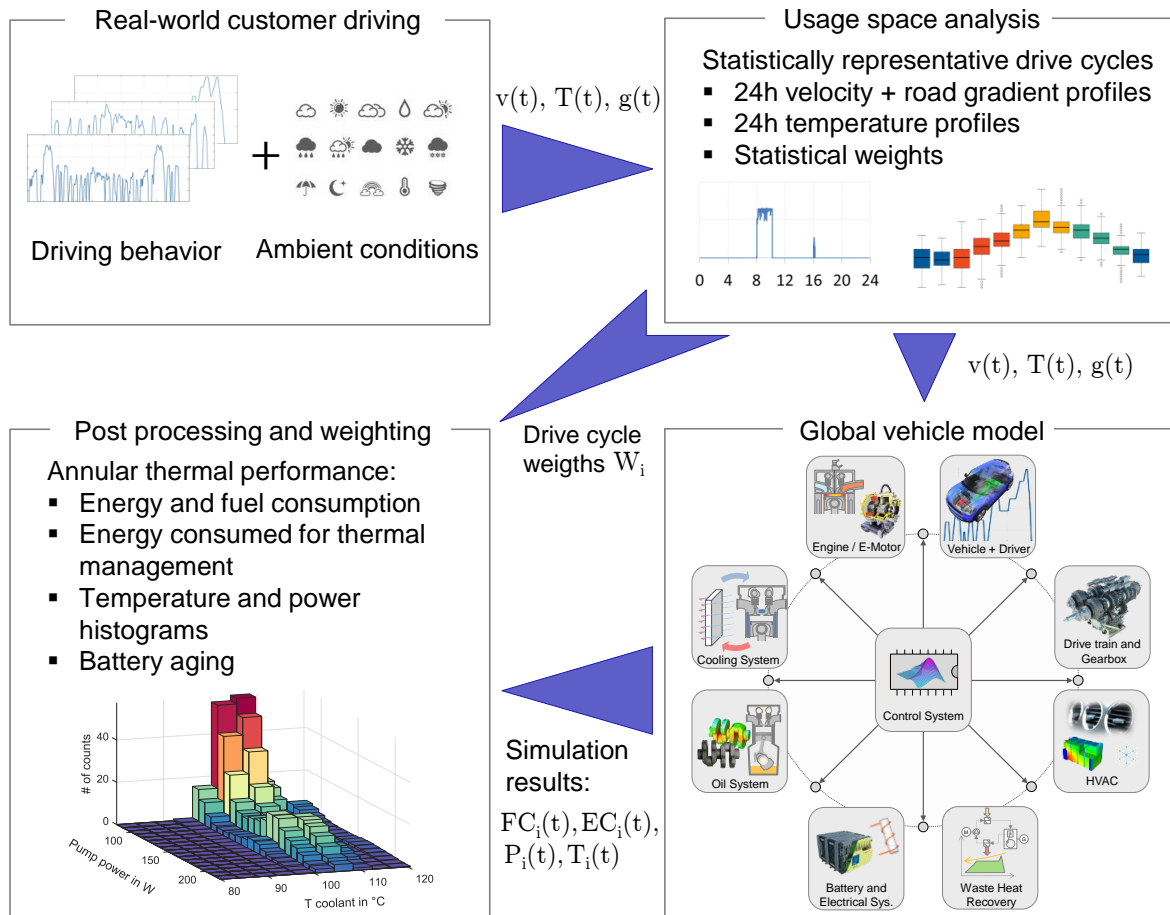
Figure 6.1.: Methodology for assessment of the annual thermal performance based on real customer behavior [108].

6.2. Methodology

In Fig. 6.1 the methodology overview is depicted. The key to reduce the computation time is a smart composition of the drive cycle and ambient temperature portfolio. Therefore a so-called usage space analysis (as described in section 6.3.1) is used. In [108] this approach was applied to simulate the lifetime thermal performance of a HEV. Drive cycle measurement data, taken from a full year real-world customer driving, together with annual ambient temperature profiles for a set of relevant locations is used as input. The output is a statistically representative subset of 24 hour drive cycles (velocity $v(t)$ and road gradient $g(t)$) and temperature $T(t)$ profiles, including vehicle standstill and park conditions. Factorial recombination of drive cycles and temperature profiles provide the input for the coupled global vehicle model. Simulation results like fuel and energy consumption $(FC_n(t), EC_n(t))$ as well as component temperatures $(T_n(t))$ and power consumption $(P_n(t))$ are analyzed within the post-processing tool. Each of the individual drive cycles i represents, with a certain weight W_i, the annual vehicle usage behavior. Assessment of the overall annual thermal performance (e.g.: energy and fuel consumption, hours above a temperature threshold, number of temperature peaks per year, aging,...) requires further weighting of the results. Weights can be adopted from the statistical drive

cycle and temperature profile analysis or weights may be altered to cover extreme vehicle usage behavior to a greater extend. Finally, the sum of the weighted results reflects the annual thermal performance of the vehicle.

6.3. Usage space analysis

Usage space analysis is a methodology developed by AVL [109] to analyze customer driving, engine operation and vehicle usage patterns. Moreover, it can be used to identify representative customer reference cycles. For the development, validation or simulation of a given system (or subsystem) a thorough knowledge of the usage of this system is required. The presented methodology is used to derive the global vehicle usage. Outcomes of the analysis are mean and extreme customer cycles, which represent the vehicle usage based on the given database. Objective of the usage space analysis is to be as representative as possible with respect to the underlying database and to minimize the information loss due to the proposed data reduction process. A more realistic result in terms of lifetime analysis is created by identification of not only one representative cycle but a set of mean and extreme representative drive cycles. One big advantage of the presented approach over fully synthetic drive cycles is that the selected duty cycles are valid in any case since they are built up from measured trips. These drive cycles might also be used in other kinds of vehicle simulations or further vehicle usage dependent analysis.

6.3.1. Statistical analysis

For statistical analysis a representative set of trips, which were measured in the target vehicle at different locations, are used. The individual trips are combined together (full factorial) in order to create 24 hour duty cycles, including driving, parking and idle phases. Following assumptions were made:

- Two trips per day,
- Driving start times and durations according to database and
- Parking durations according to database.

Under these assumptions a full set of random 24 hours drive cycles is created. So called *usage parameters* are calculated for the description of the vehicle usage. The most relevant usage parameters are shown in Tab. 6.1. For every 24 hour drive cycle, the usage parameters are calculated to describe their position in the usage space.

Table 6.1.: Set of relevant usage parameters

Usage Space Parameter	Description of parameters
Time ignition on	Total duration of ignition on
Time fraction vehicle moving	Time in which the vehicle is moving
Mean trip length	Mean duration of one single trip
Mean vehicle speed	Average vehicle speed during ignition on
Mean of power	Average traction power during ignition on
Number power cycles	Number of power cycles per hour during ignition on
Mean AP position	Mean of accelerator pedal position during ignition on
Time fraction positive AP changes	Duration with positive acceleration pedal changes

Cluster analysis

To reduce the number of representative drive cycles to a minimum, a cluster analysis is performed. The cluster algorithm *Partitioning Around Medoids (PAM)*, as shown in [110], is used to identify groups in the high dimensional usage parameter space. It partitions the dataset of n objects into k clusters, which are both provided as input to the algorithm. A dissimilarity matrix is used to minimize the overall dissimilarity between a representative drive cycle in the center of the cluster (medoid) and each cluster member. The following cost function $F(x)$ is used to solve the problem

$$F(x) = \text{minimize} \sum_{i=1}^{n} \sum_{j=1}^{n} d_{i,j} z_{ij} \tag{6.1}$$

where $d_{i,j}$ is the dissimilarity measurement between two cluster members (i and j). z_{ij} ensures that only elements from the same cluster are considered in the cost function. The optimization is performed under the constraints that; every single objective is assigned to one cluster and only one cluster; every entity is assigned to its medoid that represents the cluster; exactly k clusters are used; decision variables (z_{ij}) assume just the values of 0 or 1. The dissimilarity matrix is calculated using the Euclidean distance between points, as described in Eq. 6.2 and Eq. 6.3.

In $I\!R^2$ the definition of the Euclidian distance $d_{1,2}$ between two points, denoted by subscripts 1 and 2, yields

$$d_{1,2} = (\Delta x^2 - \Delta y^2)^{1/2}, \quad \text{with} \quad \Delta x = x_1 - x_2 \quad \text{and} \quad \Delta y = y_1 - y_2, \tag{6.2}$$

where Δx and Δy describe the distance between point 1 and point 2 in direction of coordinates x and y, respectively. The Euclidian distance between two points in $I\!R^p$ can be written as

$$d_{1,2} = \left(\sum_l \Delta x_l^2 \right)^{1/2} \quad \text{with} \quad \Delta x_l = x_{1,l} - x_{2,l} \quad \text{and} \quad l = 1 \ldots p, \tag{6.3}$$

where p denotes the number of dimensions of the usage space.

Principal component analysis

One further step is to reduce the high dimensional usage space and to emphasis the main variation for visualization and interpretation of the cluster analysis results. Therefore a technique called *Principal Component Analysis (PCA)*([111, 112]) is used. The mathematical procedure is also known as *Singular Value Decomposition*. This methodology allows the identification of principal directions in which the data varies. In this work the two most significant components are interpreted as "Load" and "Dynamics". In the 2D example, given in Fig. 6.2, first the PCA direction of the maximum variance (PC_1) is identified. Afterwards the data is rotated in direction of the principal components. Because the PCA transformation ensures that the horizontal axis PC_1 has the most variation, the second axis can be dropped to reduce the order.

1. Find direction with max. variance

2. Rotate data in direction of principal components

3. Order reduction by dropping second axis (PC2)
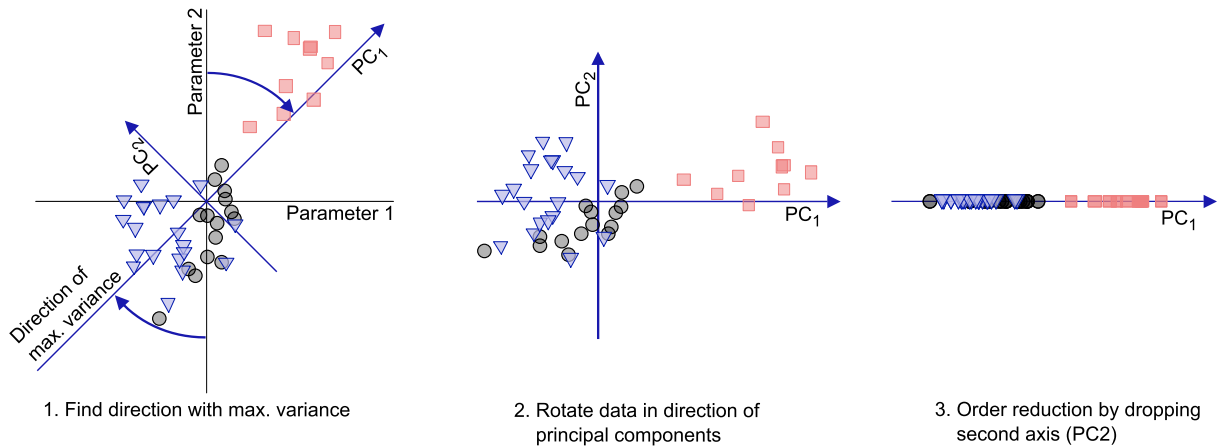
Figure 6.2.: Principal component analysis approach for reduction of dimensions [108].

6.3.2. Drive cycles

For the given dataset, the principal components, load and dynamics explain 64% of the total variance. Therefore, by concentrating on the first two principal components the essential information is preserved for the graphical representation. The locations of the main groups, in terms of principal components, load and dynamics, are shown in Fig. 6.3. Red stars are indicating the medoids (centers) of the grouped data. The drive cycles related to the medoids are taken as the representative reference daily duty cycles for these groups. Four main groups (clusters) were identified which represent the following usage behavior:

- **Group 1** represents the low load and low dynamics group (main operation: city driving);
- **Group 2** represents the high load and low dynamics group (main operation: highway/ regional driving);
- **Group 3** represents the low load and average dynamics group (main operation: city driving) and
- **Group 4** represents the average load and high dynamics group (main operation: mountain driving).

In addition to the main clusters, extreme clusters were identified, to account for vehicle usage outside of the normal operating range. Therefore, the usage space representing 90% typical customer data and the usage space representing 10% of extreme data were identified. For the 10% extreme customer data the cluster analysis is repeated to ensures that the analyzed customer cycles are mean representatives regarding the extreme behavior. The three extreme customer group medoids, as shown in Fig. 6.4, represent the following usage behavior:

- **Extreme group 1** represents the low load and low dynamics group (city driving);
- **Extreme group 2** represents the high load and high operation time/ low dynamic group (highway/ regional driving) and
- **Extreme group 3** represents the average load and high dynamic group (mountain driving).
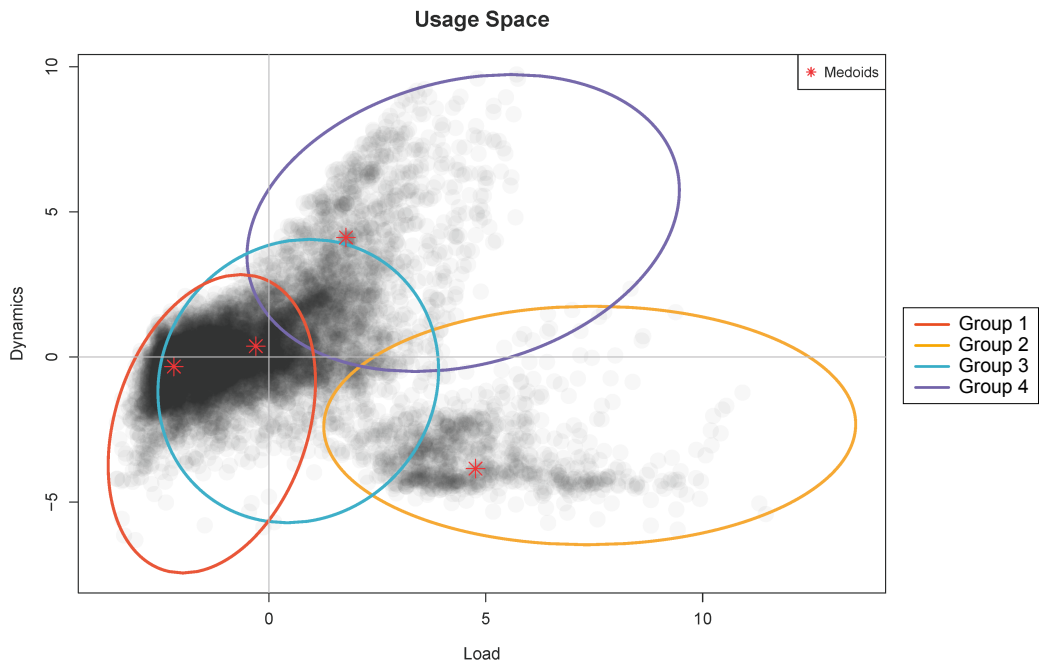
Usage Space

Figure 6.3.: Main clusters in the usage space. The principal components *Load* and *Dynamics* represent 64% of the point variability [108].

Usage Space (Extreme Data)
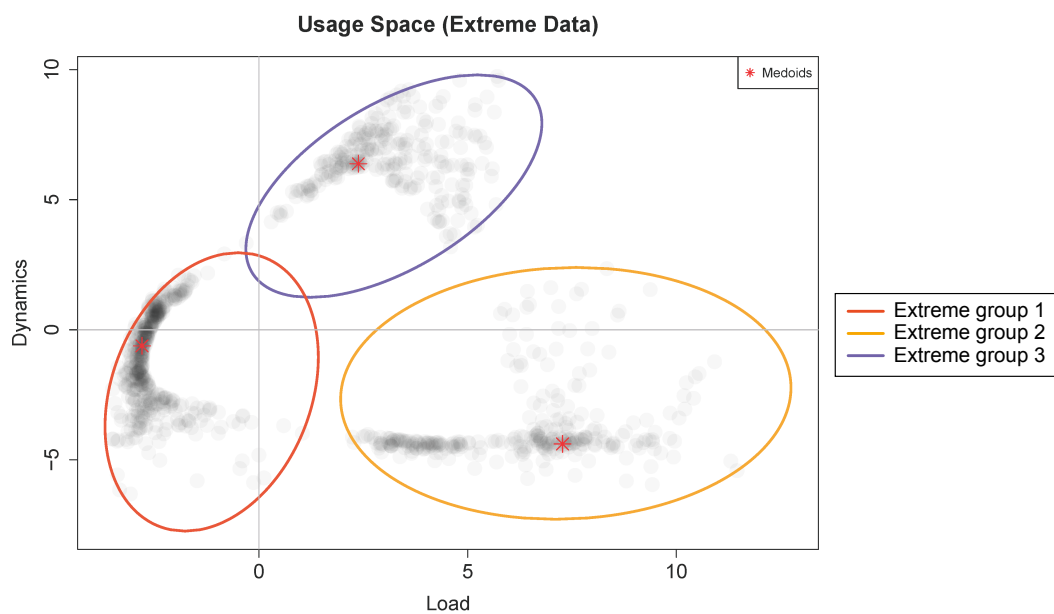
Figure 6.4.: Extreme clusters in the usage space. This clusters represent 10% of the customer data [108].

In total seven 24 hour drive cycles were identified. Example drive cycle velocity profiles are shown in Fig. 6.5 and in the appendix Fig. A.5. Note that all reference cycles also include a corresponding road gradient to reflect the altitude change.
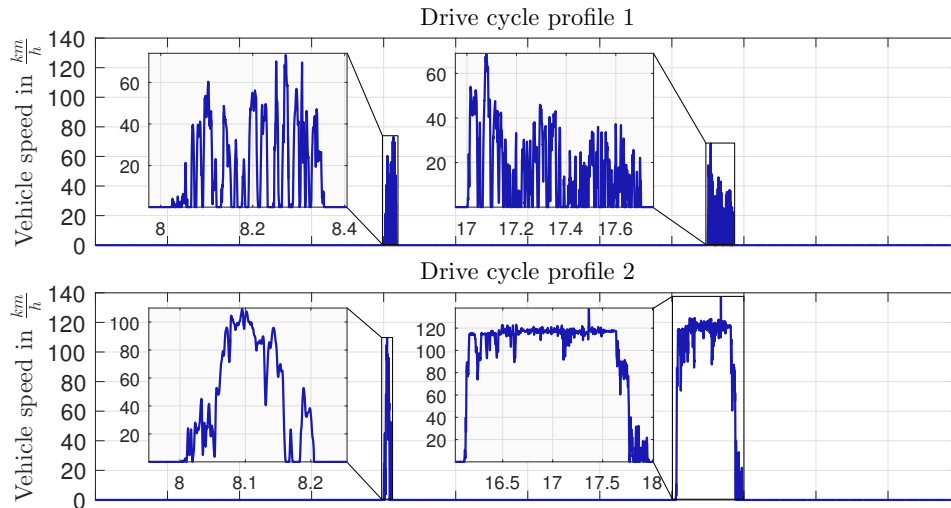
Figure 6.5.: Example for 24h reference drive cycles. Top: low load and low dynamics city driving. Bottom: high load and low dynamics highway driving.

6.3.3. Ambient temperature profiles

In addition to representative drive cycles also representative ambient profiles are required to consider the vehicle usage location accordingly. Therefore, historical weather data from *The Weather Underground* database [113] was used. In this database temperature, ambient air pressure, humidity and other information are available in a half hour resolution for more than 60.000 cities around the world. For ambient temperature profile analysis, the historical data from 2013 and 2014 for the cities Birmingham, Madrid and Paris were used, as shown in Fig. 6.6.
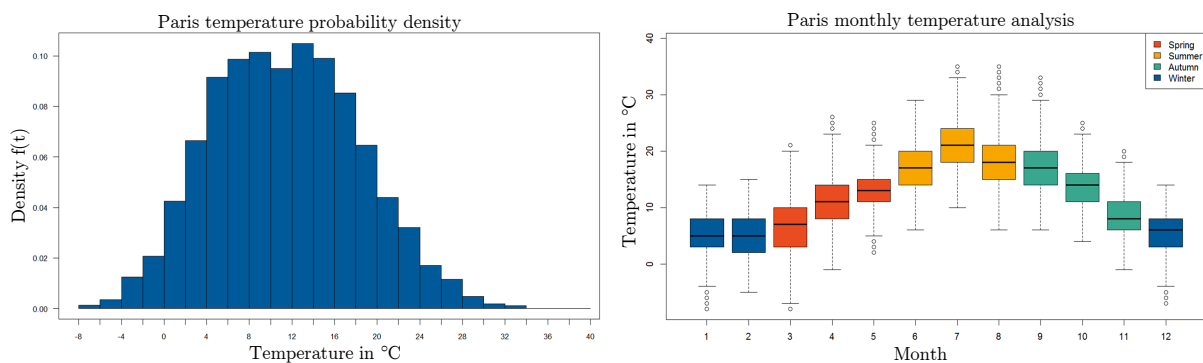
Figure 6.6.: Detailed analysis of temperature distribution and monthly average temperature in Paris (years 2013 and 2014).

Due to different day-to-day measurements, the time channel was transformed to a uniform time track with nearest neighborhood method as shown in [114]. The 12 calendar months are separated into four three-month periods using the meteorological seasons:

- Spring (February, March, April);
- Summer (May, June, July);
- Autumn (August, September, October) and

- Winter (November, December, January).

From statistical analysis of all selected city's temperature profiles it became evident that autumn and spring show similar ambient conditions and can be merged together. Mean profiles per city and season were identified and merged together if they show similarity. In addition to the mean representative ambient temperature profiles, the most extreme profiles in terms of maximum and minimum temperature were selected. In the end, the analysis shows six different temperature profiles; four profiles representing the mean temperature conditions, one profile for maximum temperature and one profile for minimum temperature, as given in Fig. 6.7 and Fig. 6.8.
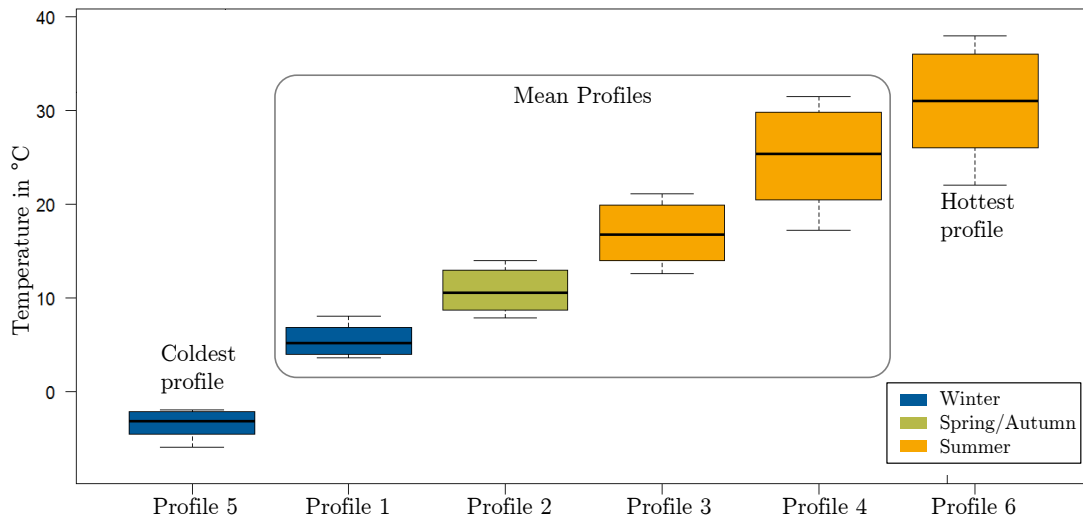
Figure 6.7.: Final temperature profile clusters after combination of similar seasonal temperature profiles for the cities Birmingham, Paris and Madrid.
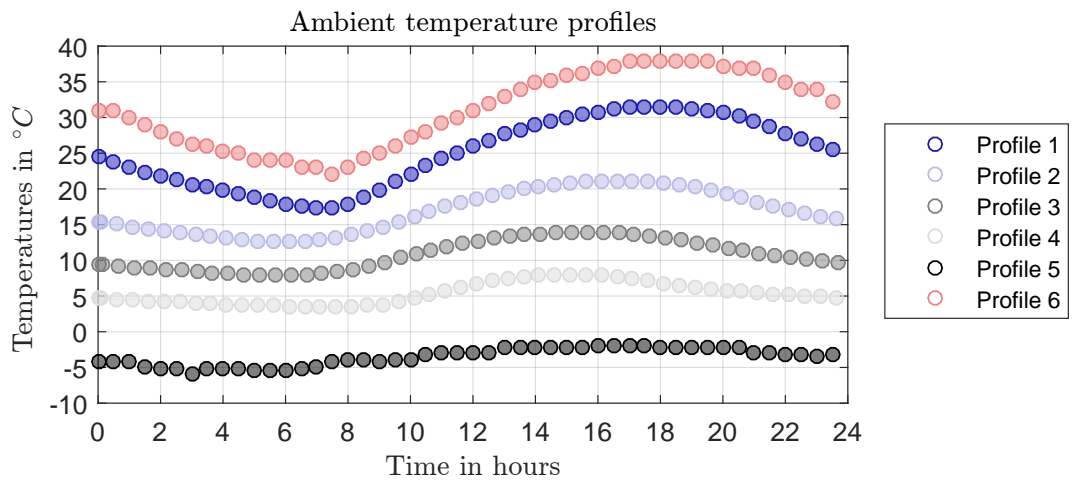
Figure 6.8.: Final 24h temperature profiles for lifetime thermal analysis.

The seasonal temperature profiles of the individual cities were merged as follows:

- **Profile 1:** Combination of Birmingham, Madrid and Paris winter;
- **Profile 2:** Combination of Birmingham spring and Paris autumn;
- **Profile 3:** Mix of Madrid spring/autumn with Birmingham and Paris summer;
- **Profile 4:** Madrid summer;
- **Profile 5:** Extreme profile reflecting minimum of Birmingham winter and
- **Profile 6:** Extreme profile reflecting maximum of Madrid summer.

6.3.4. Weighting

Each ambient temperature profile and driving profile correlates to a certain probability of occurrence. The drive cycle weights, as shown in Tab. 6.2, were directly adopted from the cluster analysis results.

Table 6.2.: Drive cycle weights.

	Customer profiles	Weight	Weight per day	Distance in km	Weighted distance in km
Mean profiles	Reference day 1	91%	36.4%	18.2	6.6
	Reference day 2		9.1%	194.6	17.7
	Reference day 3		36.4%	28.6	10.4
	Reference day 4		9.1%	47.7	4.3
Extreme profiles	Extreme reference day 1	9%	4.0%	8.8	0.4
	Extreme reference day 2		3.0%	276.8	8.3
	Extreme reference day 3		2.0%	41.9	0.8
					48.6

The weighting for the extreme ambient profiles, as shown in Tab. 6.3, was increased from less than one percent to five percent in order to have additional safety margins for assumptions towards battery durability and energy consumption of the cooling system. All mean temperature profiles are assumed to have the same probability and thus the same weight.

Table 6.3.: Ambient profile cycle weights.

	Ambient profiles	Weight	Weight per profile
Mean profiles	Profile 1	95%	23.8%
	Profile 2		23.8%
	Profile 3		23.8%
	Profile 4		23.8%
Extreme profiles	Profile 5	5%	2.5%
	Profile 6		2.5%

For obvious reasons the energy and fuel consumption of a PHEV for a certain drive cycle is also strongly depending on the *initial battery SoC*. Analysis of the charging behavior [115] revealed that more than 44% of dutch PHEV drivers charge their battery for *more than 85%* of the battery capacity. This implies that it is likely that the battery is driven almost empty. Asides from this peak at 80-90% charging capacity the charging frequency of the remaining 56% PHEV drivers was evenly distributed.

In the last row of Tab. 6.2 the mean daily vehicle driving distance is given by ≈50km per day. Therefore if the driver is starting with a full battery (90% SoC ≡ 8kWh) at day one, he will (in average) start day two with a half depleted battery (50% SoC ≡ 4kWh) under the premise that the vehicle consumes $\approx 8 \ \frac{kWh}{100km}$. Subsequently, recharging would be required at the end of day two. This allows to the assumption that the vehicle's initial SoCs 90% and 50% are evenly distributed over the year, leading to a SoC weight factor $w_{c,i} = 50\%$ for both cases.

In summary, *seven drive cycles* combined with *six ambient profiles* and *two start SoC's* yield a total simulation task of *84* full days for the assessment of the lifetime thermal behavior. The individual overall weights W_i for each day (subscript i) are calculated from the product of the probability for the ambient profile $w_{a,i}$, the driving profile $w_{p,i}$ and initial SoC $w_{c,i}$ as

$$W_i = w_{a,i} \ w_{p,i} \ w_{c,i}. \tag{6.4}$$

Weighting allows certain flexibility and can be adopted depending on the desired engineering statement. It is notable that lifetime assumptions for different locations and markets can simply be made by tuning the individual weights without the need to recalculate the drive cycles.

6.4. Sample assessment

With the global vehicle simulation model, which can be recalled from chapter 4 - Fig. 4.4, and drive cycle boundary conditions, temperature profiles and weights from usage space analysis (section 6.3) all required parts are available to run a *lifetime thermal performance analysis.*

For demonstration purpose the Future Hybrid global vehicle simulation model (including powertrain, HCU, TMC and thermal plant) is considered. The example assessment comprises one base model and five variants with different hardware configurations, control setpoints for battery chiller cooling and pump/fan control algorithms.

Objective of the assessment is to reduce the annual *vehicle energy consumption* by reducing the energy required for conditioning of the ICE and the electric powertrain. Because reduced battery cooling may also influence the battery lifetime, battery aging is also considered in the analysis. Therefore a Lithium-ion battery cell aging model [116], developed in course of a joint research project[1] between the VIRTUAL VEHICLE Research center and AVL List GmbH, is used for post-processing. The aging model requires cell temperature T_{cell}, charge SoC, Open Circuit Voltage (OCV) and current I related to time t for calculation of the State of Health (SoH) after completing the drive cycle as

$$SoH = f(T_{cell}(t), \, SoC(t), \, OCV(t), \, I(t)). \tag{6.5}$$

The SoH is consequently used to calculate the damage ($da = 100\% - SoH$) and the number of possible stress cycles np under this conditions $np = 1/da$. Since one profile corresponds to one day division of np by 365 yields the cell lifetime in years.

6.4.1. Variant description

The *Base* simulation model is used as starting point for modifications. It corresponds to the global vehicle simulation model given in chapter 4. Conventional control strategies (bang-bang control or map based control) are used together with a conservative battery cooling strategy, requiring chiller cooling if the battery temperature reaches more than 25°C.

Differences between the base model and the variants are given in (Tab. 6.4) and can be summarized as:

Variant 1 uses a relatively simple bypass valve instead of the conventional wax thermostat. It allows to open the radiator flow path while closing the bypass branch and vice versa. Therefore, if the radiator branch is open the ICE coolant pump has full control over heat rejection in engine and radiator. A CLF based pump control algorithm, as shown in section 5.3, is used to track an average engine temperature setpoint.

---

[1]project name: *ALICe*

Variant 2 features the same hardware and control algorithm changes as Variant 1. Additionally the start of the battery chiller cooling setpoint is moved towards 30°C.

Variant 3 uses the same bypass valve as Variant 1 and 2 but a bang-bang control with multiple discrete levels for the ICE pump, in contrast to the CLF based control.

Variant 4 corresponds to the base variant but with battery chiller cooling disabled. This does not mean that the battery is not cooled at all because cooling via the low temperature cooling system is still available.

Variant 5 uses a model predictive fan control algorithm, as presented in section 5.2. Otherwise the configuration is equal to the base variant.

Table 6.4.: Overview of variants

Hardware / Control strategy	Base	Variant 1	Variant 2	Variant 3	Variant 4	Variant 5
ICE bypass valve		✔	✔	✔		
ICE pump bang-bang control				✔		
ICE pump CLF control		✔	✔			
Start battery chiller cooling at 30°C			✔			
No battery chiller cooling					✔	
Model predictive fan control						✔

6.4.2. Assessment results

First step of the assessment is to run all of the drive cycle, ambient temperature and SoC combinations for each of the six configurations. This yields a total number of 504 simulated days à 24h. At this point it shall be noted that the simulation batch jobs are submitted and coordinated by a central batch job coordinator. The simulations are also qualified for parallel computing since all days are independent from each other. Without parallelization the computation of one day takes roughly 50 minutes ($RTF = 0.035$) on a mobile workstation with 16GB of RAM. Parallelization (6 instances of MATLAB running) helps to reduce the simulation duration to 20 minutes per day ($RTF = 0.014$). Consequently, one variant takes roughly 28 hours to complete, if only one notebook is available. These calculation time statements are valid for a simulation time step of 0.001 seconds for the CRUISE powertrain and HCU model and 0.2 seconds for the thermal plant. Simulation results are logged with a frequency of 1Hz. One logfile contains ≈330 timeseries and 580 model parameters.

Sample simulations results for Variant 2 (drive cycle 2, ambient profile 1 and 50% initial SoC) are shown in Fig, 6.9. The drive cycle starts at midnight. During the first couple of hours the ambient temperature decreases and the vehicle fluids are also cooled down accordingly. At around 8am the first (relatively short) drive cycle of the day starts and the temperature of the fluids increases (mainly in the low temperature electronics cooling circuit). Afterwards the vehicle is in park position again until the second trip of the day starts at around 4pm. During the second trip the battery SoC drops below the charge sustaining threshold, therefore ICE operation time increases and the fluids and solids get heated up. If the low temperature thermal function $F_{LT} = 4$ is active, chiller

cooling is enabled and energy for running the ac compressor is consumed, as depicted in Fig 6.9 - plot 4 and 6. The high temperature cooling circuit thermal function $F_{HT} = 2$ corresponds to the *warm* engine operating mode, thus temperature is controlled according to the setpoint. In Variant 2 the mean engine temperature is controlled, as depicted in Fig. 6.9 - plot 5. Cumulated energy consumption for the main consumers, ICE pump, LT pump and AC compressor are depicted in the bottom plot of Fig. 6.9. After the second trip of the day the vehicle is in park condition again and the fluids and solids are slowly cooling down towards ambient temperature.
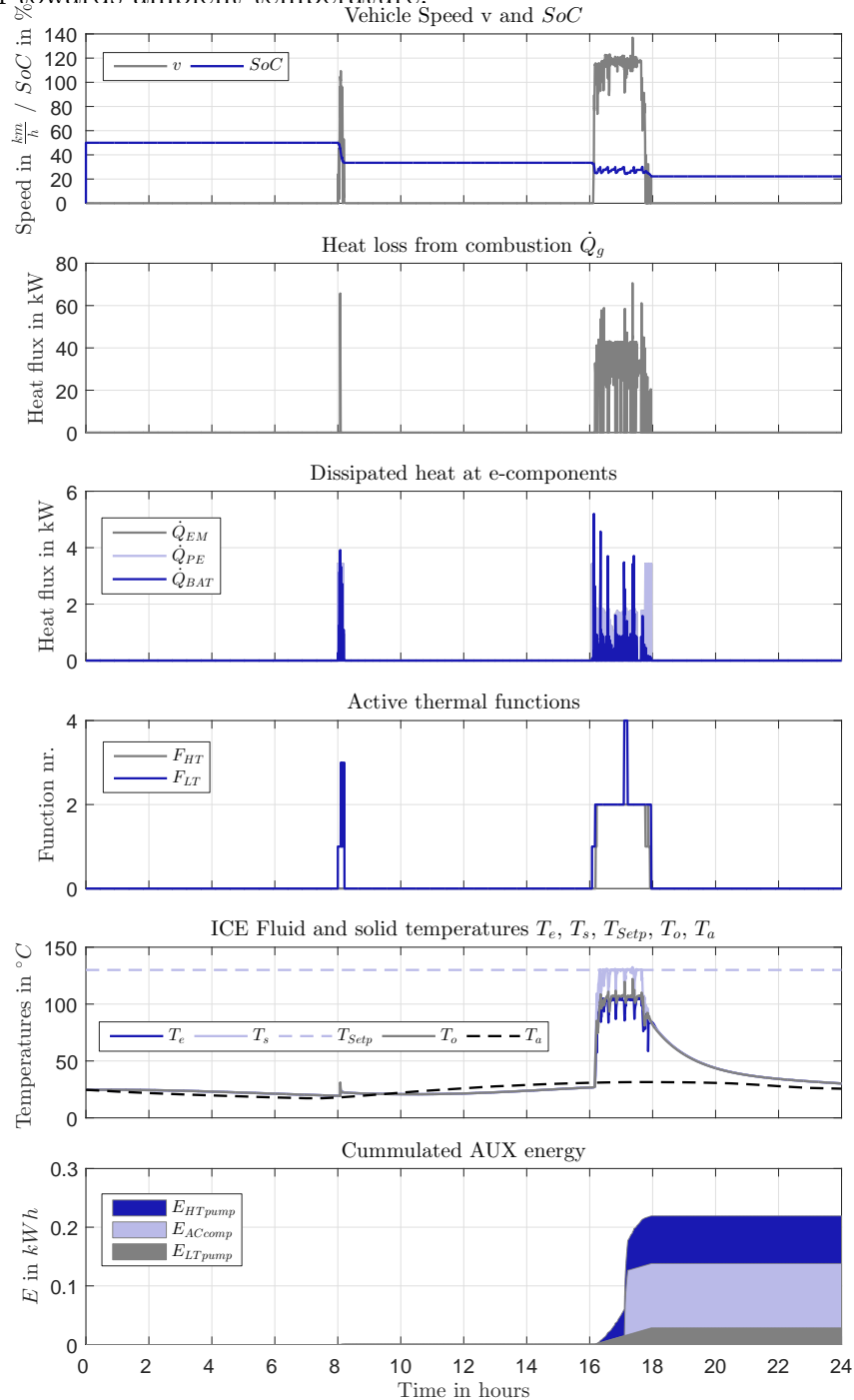
Figure 6.9.: Variant 2 example results for drive cycle 2 with ambient profile 1 and 50% start SoC.

Annual energy consumption

Five different variants have been assessed by means of lifetime thermal analysis. Results presented in this section reflect auxiliaries (AUX) and vehicle energy consumption under statistically representative conditions for a typical year of vehicle operation in the cities Paris, Birmingham and Madrid. Therefore, if not other specified, weights given in Tab. 6.3 and Tab. 6.2 were used for post-processing (SoC weights were always 50%).

Simulation results for the *Base* model AUX annual energy consumption are depicted in Fig. 6.10. Analysis of the results show that the main consumers are the ICE coolant pump and the AC compressor. Note that the compressor energy consumption for cabin conditioning was not considered.

AUX energy consumption in kWh

AUX energy consumption in %
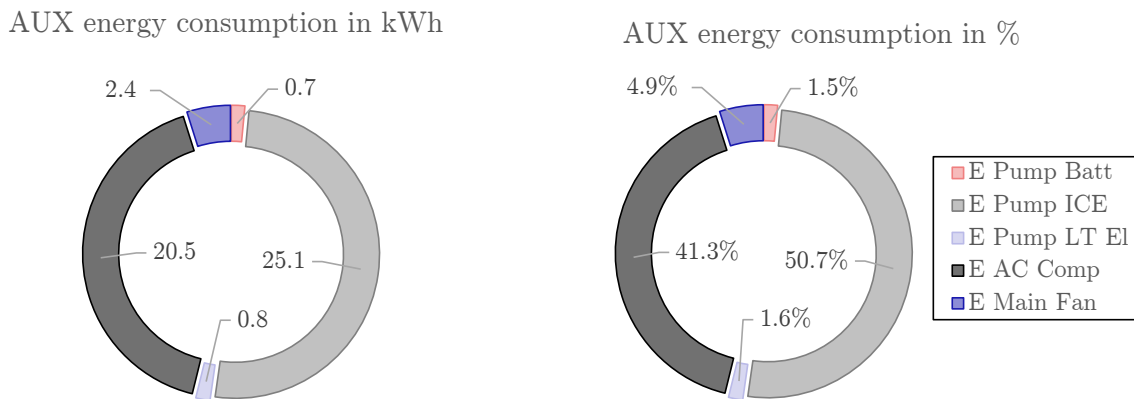
Figure 6.10.: Base auxiliaries energy consumption in absolute values (left) and as a percentage (right).

In *Variant 1* a CLF based ICE pump control algorithm was used together with a bypass valve to reduce the pump energy consumption. Results given in Fig. 6.11a indicate that a reduction of the ICE pump energy consumption by 86% was achieved. Thus the AC compressor is now causing 73% of the total AUX energy consumption.

Variant 2 (6.11b) features a higher chiller activation setpoint for battery cooling in additional to the CLF based pump control. In addition to the reduced ICE pump power consumption the AC compressor power consumption was reduced by 77%.

Variant 3 (6.11c) uses a conventional bang-bang control based strategy together with a bypass valve to reduce the pump energy consumption. 74% pump energy reduction was achieved. That is 12% less than with the comparable model based controller used in Variant 1 and 2.

In *Variant 4* (6.11d) the battery chiller cooling was deactivated leading to zero energy consumption for the AC compressor. The LT pump power consumption increased by 36% because the battery was more frequently cooled by LT electronics cooling system.

Variant 5 (6.11e) uses a predictive strategy to control the main vehicle fan leading to a reduction of fan energy consumption by 40%.

AUX energy consumption in kWh

AUX energy consumption in %

(a) Variant 1

(b) Variant 2

(c) Variant 3

(d) Variant 4

(e) Variant 5
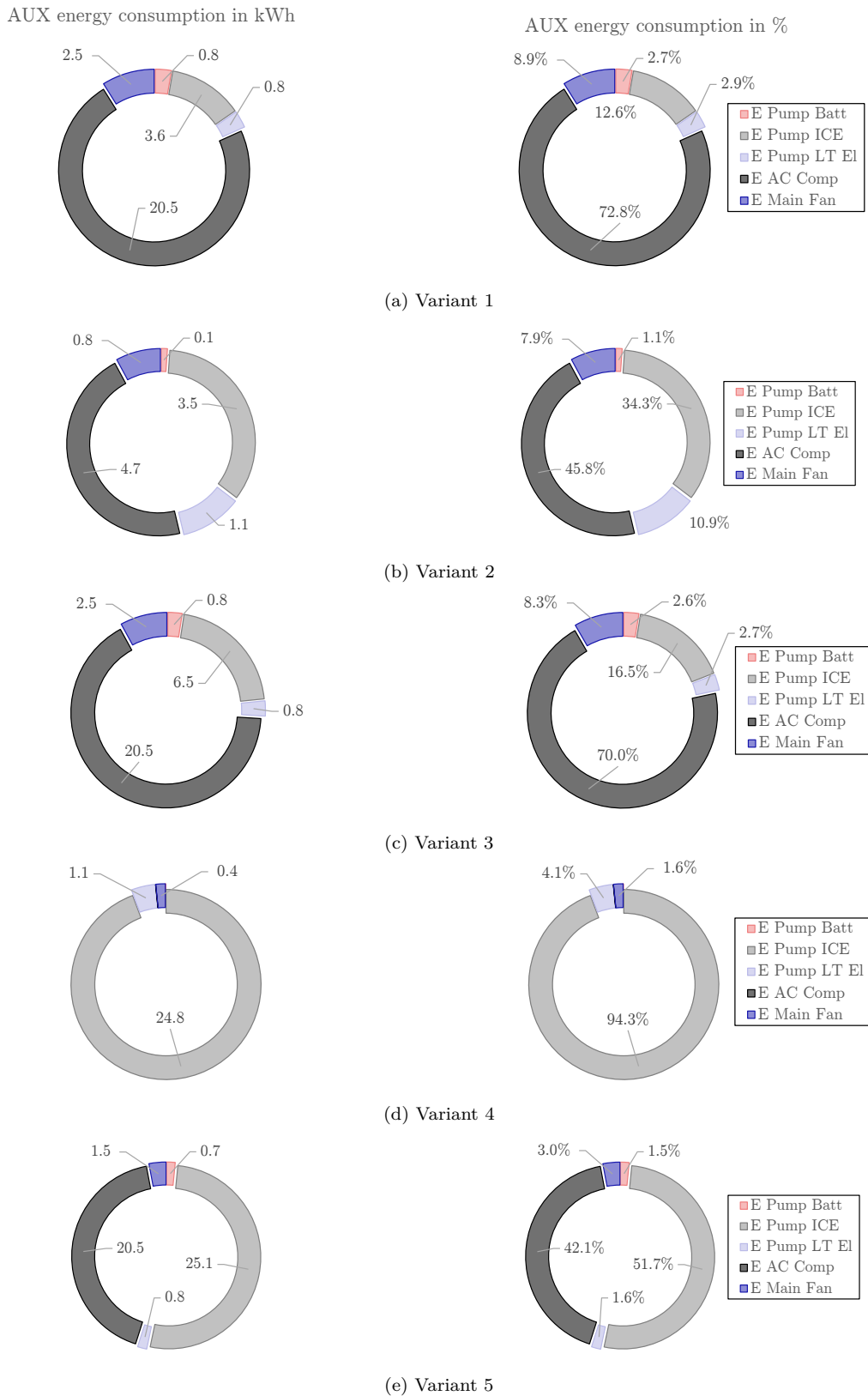
Figure 6.11.: Auxiliaries energy consumption in absolute values (left) and as a percentage (right).

The comparison of the AUX energy consumption and the achievable reduction potential relative to the base vehicle are given in Fig. 6.12
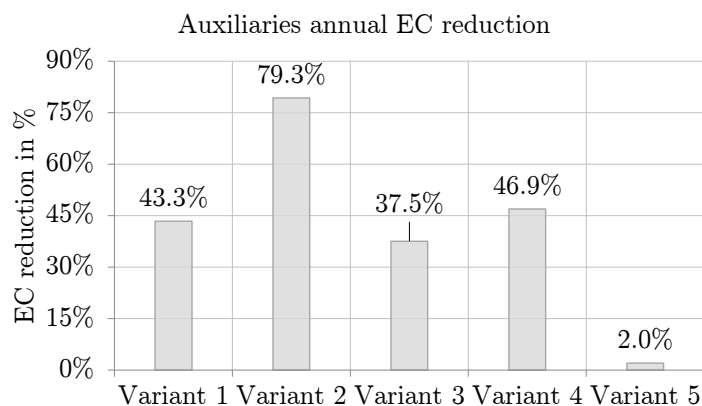
Figure 6.12.: Auxiliaries annual energy consumption assessment results.

Consequently, the reduced auxiliary energy consumption leads to an improved overall vehicle efficiency. The achieved energy consumption reduction on vehicle level is depicted in Fig. 6.13. Results show that a maximum efficiency increase of 2.2% (Variant 1) is possible with a CLF based control strategy, without sacrificing battery cooling. The bypass valve together with conventional control shows an energy reduction potential of 1.9% (Variant 3). Vehicle operation without battery chiller cooling reveals an energy reduction potential of 2.4% (Variant 4). Shifting the battery chiller cooling activation level up for 5°C, as in Variant 2, yields additional 1.8% improvement over Variant 1.
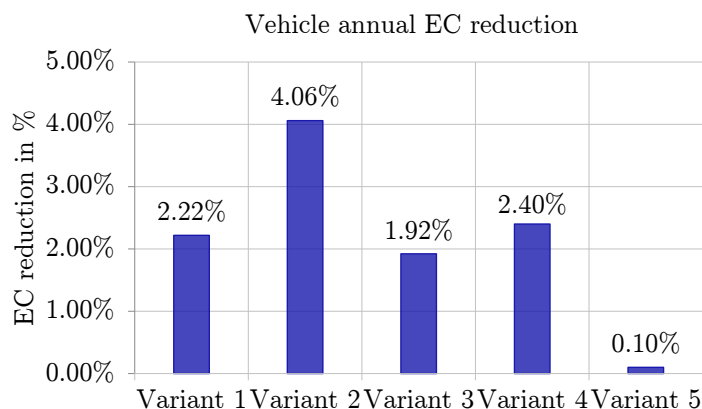
Figure 6.13.: Vehicle annual energy consumption assessment results.

Battery aging

Vehicle annual energy consumption analysis showed that modification concerning the battery cooling system offer high potential for energy consumption reduction. In order to predict the influence of cooling system modifications, results from the global vehicle simulation model were used as input for SoH calculations, as outlined in Eq. 6.5. Results regarding the expected battery lifetime, as given in Fig. 6.14, were derived by projection and weighting of the drive cycle dependent SoH results. The lifetime reduction due to modifications in hardware or battery cooling is given in Fig. 6.15. Results show that the battery has a lifetime expectation of 13.8 years and that it is *not drastically reduced*, even if the vehicle is operated without battery chiller cooling (Variant 4). It is noteworthy that the analysis was performed for (realistic) moderate European climate conditions where extremely hot and cold conditions are rare. 5% extreme ambient conditions were considered in the analysis. Even though the damage during these days is high, the weight is very low, thus having low impact on the overall battery lifetime.

If the weights for extreme ambient conditions are increased the battery lifetime analysis results (Fig. 6.16) show a significant lifetime reduction (4.3%) for the variant without battery cooling compared to Variant 2 where battery cooling starts at a higher setpoint.
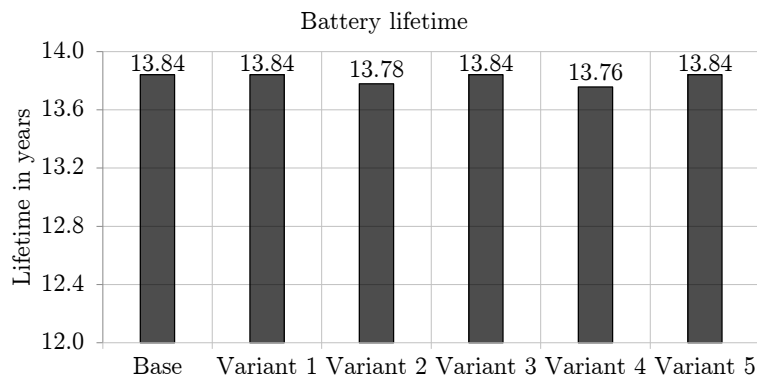
Figure 6.14.: Battery lifetime overview with weights chosen according to statistical analysis.
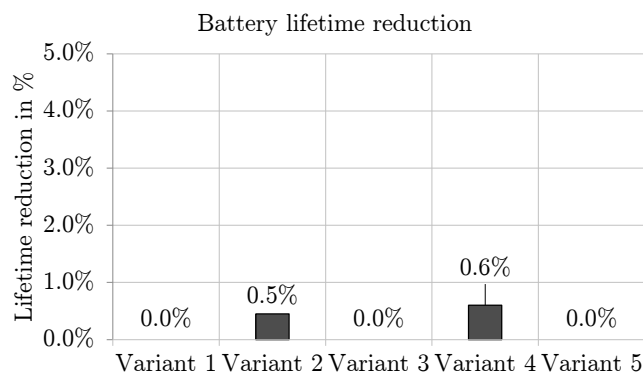
Figure 6.15.: Percentage of battery lifetime reduction with weights chosen according to statistical analysis.

Battery lifetime reduction
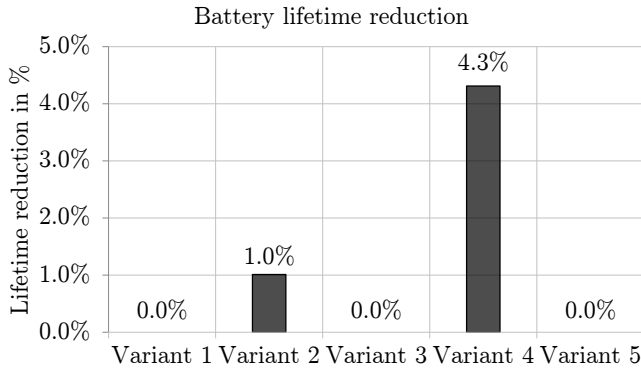
Figure 6.16.: Percentage of battery lifetime reduction with ambient weights chosen to reflect worst case conditions.

7

Conclusion and Outlook

This chapter concludes the findings and results and gives an outlook on upcoming work as well as recommendations for future research activities in the field of vehicle thermal/energy management simulation, control and assessment. Furthermore, other fields of application are discussed.

7.1. Results review

Thermo-Fluid Library

A MATLAB/Simulink based Thermo-Fluid Library (TheLib) for the simulation of fluid circuits (coolant, oil, air) and lumped mass thermal networks has been developed. Many different cooling/lubrication circuits and lumped mass thermal networks, in a number of different configurations and arrangements, have been setup with a small subset of available toolbox software components, which underlines the usability of the tool. The consistent physics based modeling approach made a good description of the system possible before it was build, allowing to predict the impact of design and control strategy changes. The model setup with TheLib is straight forward and allows to represent any thermo-fluid network in a clear structure. With the help of a custom thermo flow solver, the Simulink user interface is decoupled from the solution of the network. Therefore fluid flow direction changes and stagnant fluids are no obstacle, in spite of the causal signal propagation nature of MATLAB/Simulink. Currently 17 licensed users from three different companies are working with TheLib. Up to now the toolbox has been used within 12 research projects and engineering services. A user with some thermodynamics and MATALB/Simulink background is typically familiar with the usage of the toolbox after one day, which speaks for a generally good user acceptance. Straightforward linkage to control system software and controller design helped to reduce the complexity and to speed up the entire development process. This was especially important for the development of model based controllers, where full system insight is paramount. It is also possible to provide the project members or customers with a black-box (s-function) version of the model, hence there is no need to buy expensive software licenses to consider thermo-fluid simulation in other fields of application. The widespread usage of MATLAB/Simulink and the fact that the toolbox comes without any additional licenses fees helps to increase it's popularity. In course of the lifetime thermal analysis simulation is has been proven that the library is capable of handling heat transfer at zero/stagnant flow well. This fact

is essential for the simulation of real vehicle usage, especially for PHEVs where frequently parts of the powertrain and the corresponding thermal systems are deactivated while the vehicle moves. The simulation runtime of the tools is satisfying. For the quite complex thermal plant model, given in chapter 4, without co-simulation of the powertrain model a RTF of 0.02 was reached, which is fast enough for running lifetime analysis in adequate time. Outcome of recent work showed that - with minor modifications - thermal systems created with TheLib are qualified for hardware target code generation. This makes usage on a HiL testbed possible.

Thermal control

A thermal management controller, intended to serve as generic framework for the control of thermal auxiliaries, has been developed in the course of this work. The introduction of the thermal functions / thermal mode concept helped to split the challenging task of controlling actuators with a high number of interactions and dependencies into smaller pieces that are easier to handle. Instead of dedicated component control functions with many interactions and feedback loops for each of the thermal systems a *central control logic* (called mode selector) was introduced to select a comprehensive set of actuator control signals, which is tailored towards the currently active thermal mode. By means of this approach it was made possible to use multiple different control concepts for one actuator, depending on the currently active thermal mode and system state. Moreover, the exchange of controllers, for tests and variant studies, was simplified because interactions with other systems and actuators are coordinated by the central control logic, regardless of the used control algorithm. Even though in the present work only one vehicle variant (PHEV) has been discussed, usage of this framework in two different projects, one considering a pure electric vehicle and the other considering a conventional vehicle, has proven its generic nature. Use of model based control algorithms for temperature tracking showed that - compared to conventional control - higher overall fluid temperatures with less over- or undershoots can be achieved. Consequently, higher radiator ETDs were leading to an improved cooling performance without an expensive (in terms of energy consumption) increase in fluid flow, caused by a fan or a pump.

Lifetime thermal analysis

In order to support the vehicle development process a simulation tool was introduced that allows the assessment of energy consumption together with lifetime estimations for sensitive components. Custom drive cycles extracted from real-world driving offered a convincing way to understand, how the average (and also the extreme) customer is using the vehicle. Resulting drive cycles and boundary conditions allow the assessment of energy consumption and durability under realistic conditions. This is an important fact especially in connection with the upcoming vehicle typ approval test (RDE) focusing on emission and energy consumption for *real world driving*, rather than for synthetic drive cycles. Results from lifetime thermal analysis showed that there is potential for improving the vehicle energy consumption (1.9 - 2.2%) by using a bypass valve instead of a wax thermostat in the ICE cooling circuit. Furthermore the results revealed that using a model based ICE pump control over a conventional controller results in 12% less pump

energy consumption and 0.3% less annual vehicle energy consumption. Conversely, the lifetime thermal analysis showed that even though it was possible to reduce the fan energy consumption by 40% with a predictive control approach, the overall impact on the vehicle energy consumption was too small to show much improvement. Because it is tempting to develop and test new hardware or control algorithms for conditions, where a high benefit is expected, such effects are often overestimated regarding their potential during real world driving. That is why knowledge and consideration of the actual vehicle usage plays an important role during the vehicle development process. Reducing or dropping the battery chiller cooling and therefore the AC compressor activation also showed good improvement potential. Results for aging confirmed that for this kind of vehicle under the given boundaries regarding load cycles and climatic conditions (moderate European climate), a refrigerant cooled battery may not be required. But increasing the share of extreme climate condition led to a recognizable drop in battery lifetime when no battery chiller cooling was available. This implies that selection of the best suitable kind of battery cooling system and its required control setpoint are subject to the individual usage profile and the desired battery lifetime.

It can therefore be concluded that the presented framework supports the selection of the system design and its operational control with special respect to aging and energy efficiency, already in the early phases of the vehicle development process.

7.2. Recommendations for further research

Future work on the simulation toolbox will concentrate on testing of hardware implementations and code clean up to make every toolbox component available for target code generation.

Currently an important engine development target is the reduction of NO_X emissions, thus to asses the impact of modifications (e.g.: different hybrid or engine control strategies, CAT heating devices,...) on emissions a suitable engine and exhaust gas after-treatment is required. Hence, future activities will include coupling of the thermal system simulation with an engine model that is capable of predicting raw emissions on the one hand and runs fast enough for long lasting lifetime analysis simulations on the other hand.

Further extensions of the toolbox functionality by a toolset for refrigerant circuit modeling and a generic vehicle cabin model are future topics as well. By these extensions the mutual influence of battery chiller cooling and cabin conditioning could be predicted and used for AC system energy efficiency assessment and development of control strategies aiming at passenger comfort.

During the development of the Future Hybrid concept the demand for battery heating arose, because at low temperatures the battery's power capability was limited, so the preferred vehicle operating modes were not available, consequently leading to a deterioration of driveability, efficiency or pollutant/noise emission. Therefore a close examination of possible battery heating concepts it is recommended for future studies.

The gearbox plays a central role in modern hybrid vehicles because it is always active, independent from the currently active power source. Since the gearbox efficiency is strongly

depending on its actual temperature level (oil and structure), upcoming work should consider approaches for decreasing gearbox losses by enhancing the gearbox warm-up.

In course of the present lifetime thermal analysis battery charging at the plug was not considered, because it was assumed that charging is done mainly overnight without any impact on following day's battery starting temperature and charge. This assumption seemed to be correct in terms of energy consumption for cooling. However, the temperature and power boundary conditions at battery charging may influence the battery aging process (e.g. high current charging at low temperatures causes accelerated aging). For that reason it is recommended to consider battery charging in the composition of vehicle drive cycles and load profiles in future work.

A

Appendix

A.1. Fluid network models

Figure A.1.: Thermo-fluid model of the HT cooling circuit using *TheLib* MATLAB/Simulink library components

Figure A.2.: Thermo-fluid model of the LT cooling circuit using *TheLib* MATLAB/Simulink Library components

A.2. Solid network components
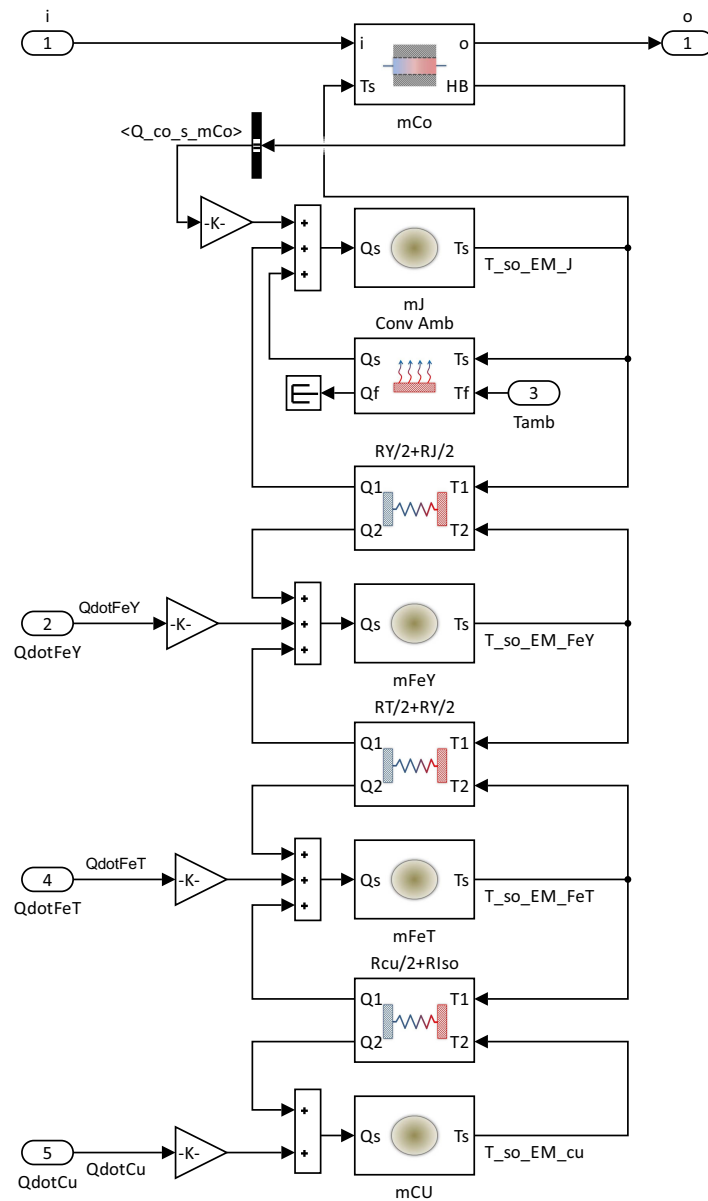
Figure A.3.: Thermal network of the HSM e-motor using *TheLib* MATLAB/Simulink Library components

A.3. Flow solver source code

```matlab
1  function [Hnew, Qnew, dq, dE, it, status] = FlowSolver(K,ncomp,nnodes,...
2      dpM,Q0,H0,p0,A12,A21,resdQ,rescQ,resE,ItMax,A10)
3
4  % Initialization of matrices
5  A11_0_diag = zeros(1,ncomp);
6  A11_diag = zeros(1,ncomp,'double');
7  A22 = zeros(size(A21,1));
8  x = zeros(ncomp + nnodes,1,'double');
9  RHS = zeros(ncomp + nnodes,1,'double');
10 LHS = zeros(ncomp + nnodes,0)*zeros(0,ncomp + nnodes);
11 Qnew = zeros(ncomp,1,'double');
12 Hnew = zeros(nnodes,1,'double');
13 Qold= zeros(ncomp,1,'double');
14 Hold = zeros(nnodes,1,'double');
15 dq = zeros(nnodes,1,'double');
16 dE0 = zeros(ncomp,1);
17 dE = dE0;
18 it = int16(0);
19 status = zeros(1,1);
20 IxSource  = zeros(ncomp,1);
21 q_out = zeros(nnodes,1);
22 % Quadratic pressure difference approach for pressure sources/sinks
23 expo = 2;
24 n = expo.*ones(ncomp,1);
25 pow = [n n-1 n-2];
26 pow_min_1 = pow-1;
27 % Input error checking
28 if length(dpM)~= 3*ncomp || max(isnan(dpM)) > 0
29     error('Component pressure drop input vector contains NaNs');
30 else
31     % Build matrices for nA11 calculation
32     Nq = diag(repmat([expo expo-1 expo-2 ]',ncomp,1));
33     Kq = zeros(ncomp, ncomp*(expo+1));
34     for kk = 1:length(K)
35         Kq(kk,(kk-1)*3+1:(kk-1)*3+3)= K(kk,:);
36     end
37     Mq = reshape((abs([Q0 Q0 Q0]).^pow_min_1)',3*ncomp,1);
38     A11 = diag(Kq*Mq);
39     nA110 = diag(Kq*Nq*Mq);
40     % Initial energy balance error
41     dE0 = A11*Q0 +  A12*H0 + A10*p0;
42     % Initial mass balance error
43     dq0 = A21*Q0 - q_out;
44     dQsum = 1;
45     while dQsum > resdQ || sum(abs(dq)) > rescQ || sum(abs(dE)) > resE
46         % First iteration
47         if it == 0
48             dE = dE0;
49             dq = dq0;
50             Qold = Q0;
51             Hold = H0;
52             nA11 = nA110;
```

```matlab
53            % build the left hand side of the matrix equation
54            LHS = [nA11 A12 ; A21 A22];
55            % build the right hand side of the matrix equation
56            RHS = [-dE; -dq];
57            % Solve the equation
58            x = (LHS'*LHS)\(LHS'*RHS);
59            % Generate updated states
60            Qnew = Qold + x(1:ncomp);
61            Hnew = Hold + x(ncomp+1:end);
62            % Change of pressure head compared to last step
63            dQsum = (Qnew-Qold)'*(Qnew-Qold);
64            Qold = Qnew;
65            Hold = Hnew;
66        % Check if max number of iterations are reach
67        elseif it >= ItMax
68            status = 1;    % Set status to 1 for later error handling
69            break;
70        else
71            % Build the new matrices
72            Mq = reshape((abs([Qnew Qnew Qnew]).^pow_min_1)',3*ncomp,1);
73            A11 = diag(Kq*Mq);
74            nA11 = diag(Kq*Nq*Mq);
75            % New energy balance error
76            dE = A11*Qnew +  A12*Hnew + A10*p0;
77            % New mass balance error
78            dq = A21*Qnew - q_out;
79            % build the left hand side of the matrix equation
80            LHS = [nA11 A12 ; A21 A22];
81            % build the right hand side of the matrix equation
82            RHS = [-dE; -dq];
83            % Solve the equation LHS*x = RHS:
84            %      LHS    *   x  =  RHS
85            % |nA11  A12 |   |dQ|    |-dE|
86            % ----------  *  -- =  --
87            % |A21    0  |   |dH|    |-dq|
88            x = (LHS'*LHS)\(LHS'*RHS);
89            % Generate updated states
90            % Qnew = Qold + dQ
91            Qnew = Qold + x(1:ncomp);
92            % Hnew = Hold + dH;
93            Hnew = Hold + x(ncomp+1:end);
94            % Compute residuals
95            dQsum = (Qnew-Qold)'*(Qnew-Qold);
96            % Store results for next iteration
97            Qold = Qnew;
98            Hold = Hnew;
99            % Check validity of mass flow output vector
100            if max(isnan(Qnew))>0
101                status = 2;
102                break;
103            end
104        end
105        it = it + 1;
106    end
107 end
```

A.4. Thermo solver source code

```matlab
1  function [T_comp_in_output, T_out_node]  = ...
2      ThermoSolver(ncomp,nnodes,A21,T0,m_output,T_comp_out,h,A10)
3
4  % Initialization of thermo solver variables
5  An21 = zeros(size(A21),'double');
6  Aout = zeros(size(A21),'double');
7  Hdot = zeros(ncomp,1);
8  Ain = zeros(size(A21),'double');
9  h_out = zeros(nnodes,1,'double');
10 % Connectivity matrix with respect to flow direction
11 An21 = A21*sign(diag(m_output));
12 An10 = diag(sign(m_output))*A10;
13 % Matrices to identify components that receive or provide flow to a node
14 Ain  = An21 > 0;
15 Aout = An21 < 0;
16 Aout0 = An10 < 0;
17 % Enthalpy flows out of the components
18 Hdot = interp1(h(:,1),h(:,2),T_comp_out).*abs(m_output);
19 % Specific enthalpy at node outlet h = sum(Hdot_in)/sum(mdot_in)
20 h_out = (Ain*Hdot)./(Ain*abs(m_output));
21 % Mixture temperature at node outflow
22 T_out_node = interp1(h(:,2),h(:,1),h_out);
23 % Condsideration of static temperature sources
24 T_comp_in_output = Aout'*T_out_node + Aout0*T0;
25 % Check if out of fluid property validity range
26 if max(isnan(T_comp_in_output))>0
27     error(['Fluid Temperature are NaN' ...
28     '-> Check if fluid temperatures are out of bounds.']);
29 end
```

A.5. High temperature cooling mode selection control logic
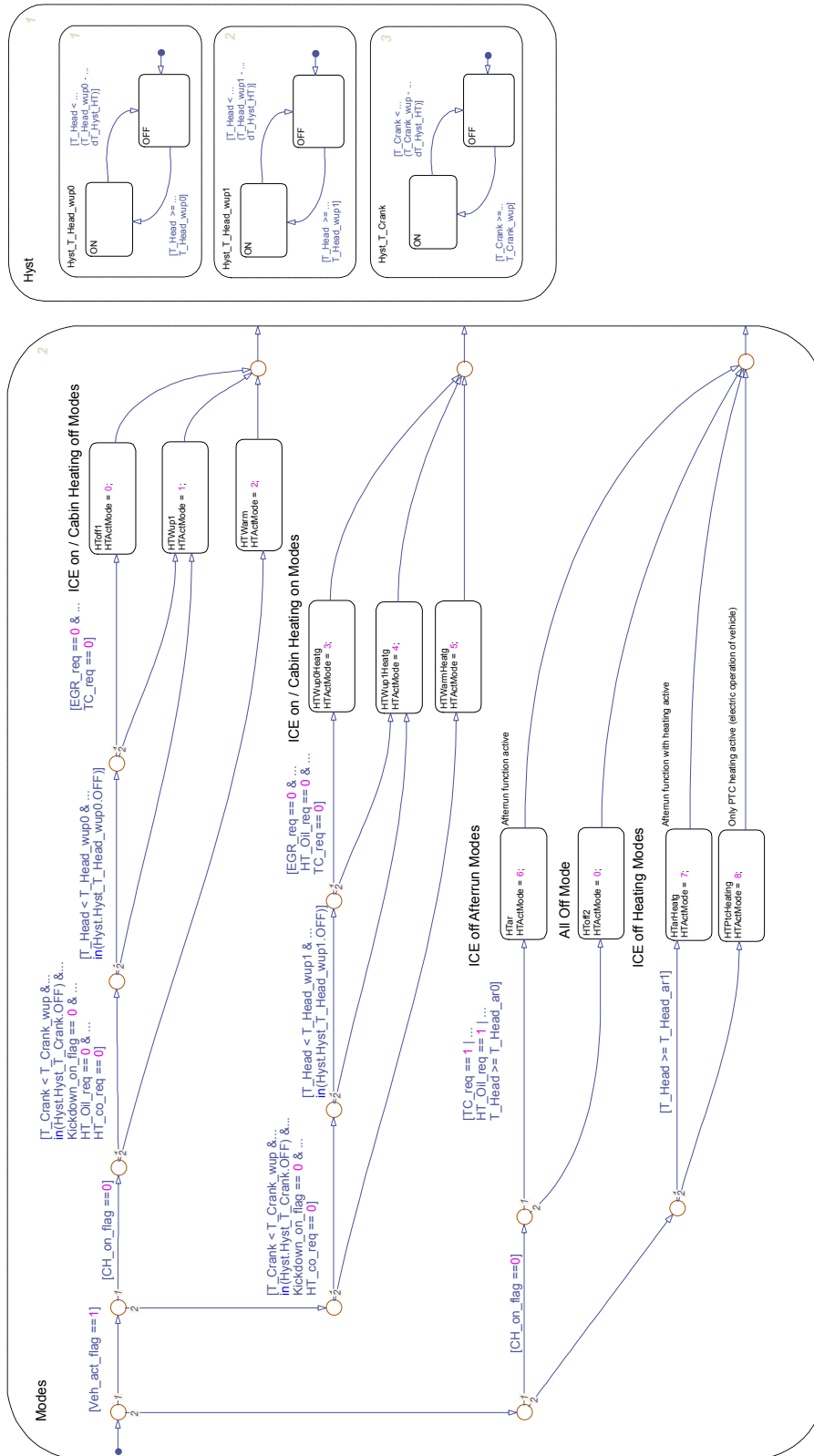
Figure A.4.: HT cooling mode selection control logic in Stateflow.

A.6. MPC plant parameters

Table A.1.: Plant and control parameters

Var	Value	Unit	Description of parameters
$\dot{m}_c$	$0.1 \ldots 2$	kg/ sec	coolant mass flow
$\dot{m}_a$	$0 \ldots 1$	kg/ sec	air mass flow at heat exchanger
$\dot{Q}_H$		J/ sec	heat flow from coolant to air
$c_{p,c}$	3417	J/kg/K	specific heat of coolant (assumed const.)
$c_{p,a}$	1.16	J/kg/K	specific heat of air (assumed const.)
A_a	4.12	m^2	area of convective heat transfer at heat exchanger air side
A_c	0.67	m^2	area of convective heat transfer at heat exchanger coolant side
m_{P1}	5.76	kg	mass of lumped mass "*pipe 1*"
m_{P2}	5.42	kg	mass of lumped mass "*pipe 2*"
m_H	3	kg	mass of lumped mass "*heat exchanger*"
m_M	2.3	kg	mass of lumped mass "*motor*"
T_a	30	°C	ambient air temperature
v	$0 \ldots 20$	m/ sec	vehicle speed
t_s	2	sec	sampling rate MPC
N_p	4	samples	control horizon
N_c	35	samples	prediction horizon
$\hat{R}_{ii}$	$10^{[0,0,0]}$		input weighting factor for the observer
$\hat{Q}_{ii}$	$10^{[1,-4,0,6]}$		state weighting factor for the observer
R	1	-	input weighting factor for MPC
Q	10^6	-	error weighting factor for MPC
u_{max}	30	kW	for MPC
u_{min}	0	kW	for MPC
y_{max}	51	°C	for MPC
y_{min}	$-\infty$	°C	for MPC

[1] test bench configuration

A.7. Usage space analysis
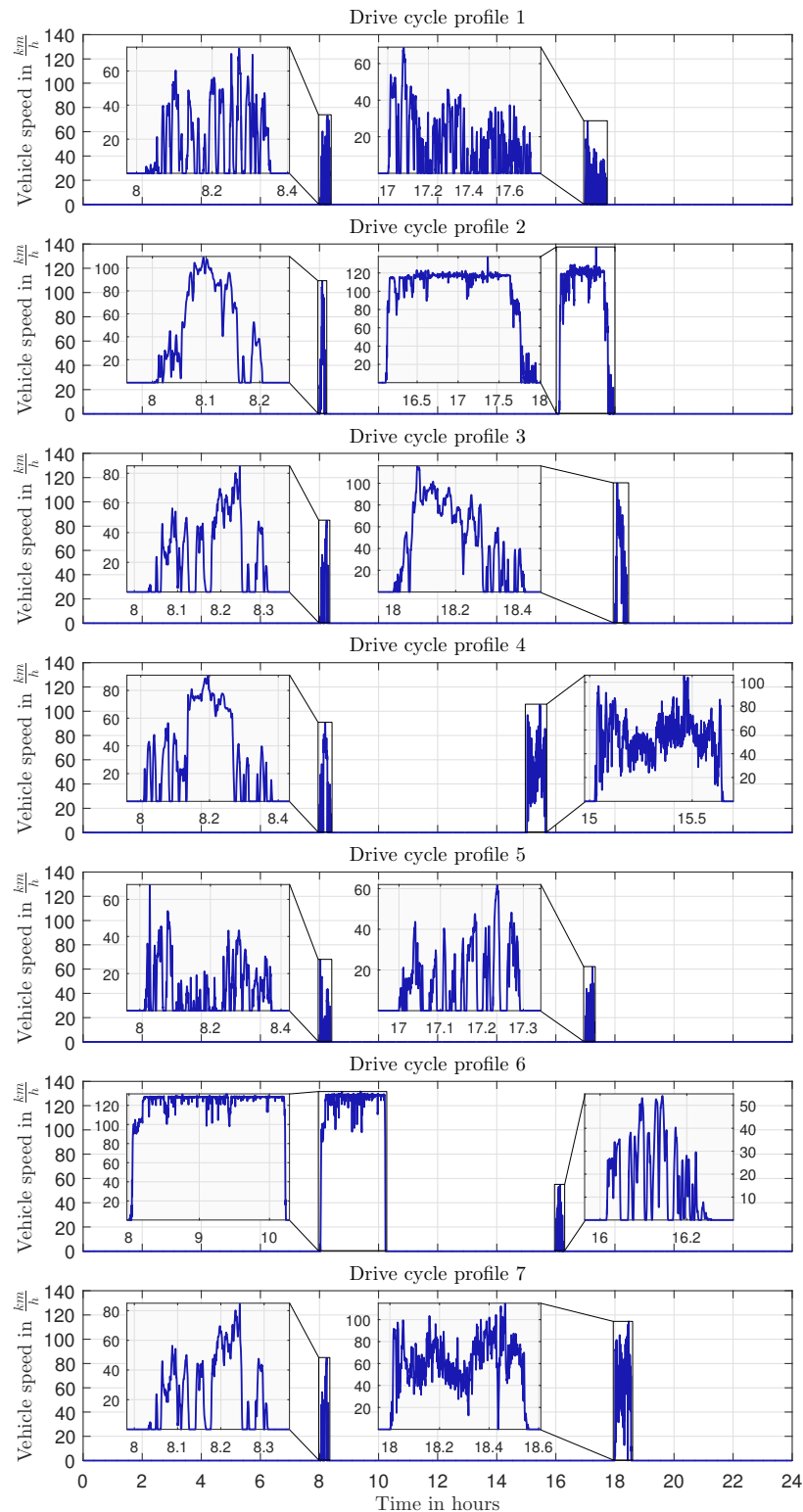
Figure A.5.: 24h reference drive cycles. Cycle profile 1-4 are normal drive cycles (90% of the customer data). Cycles 5-7 represent extreme cases (10% of customer vehicle usage).

Acronyms

AC	air conditioning
AER	All Electric Range
AUX	auxiliaries
bmep	Brake Mean Effective Pressure
CAN	Controller Area Network
CAT	Catalytic Converter
CLF	Control Ljapunov Function
CO_2	Carbon Dioxide
DoE	Design of Experiments
ECU	Engine Control Unit
EM	Electric Motor
ETD	Entrance Temperature Difference
EV	Electric Vehicle
FC	fuel consumption
FEM	Finite element method
fmep	Friction Mean Effective Pressure
HCU	Hybrid Control Unit
HEV	Hybrid Electric Vehicle
HiL	Hardware in the Loop
HT	high temperature
HTC	heat transfer coefficient
HVAC	Heating Ventilation and Air Conditioning
ICCT	International Council on Clean Transportation
ICE	Internal Combustion Engine
imep	Indicated Mean Effective Pressure
LT	low temperature
LTI	linear and time invariant

LZI	Linear zeitinvariant
MPC	Model Predictive Control
NEDC	New European Drive Cycle
NO_X	Nitrogen Oxide
OCV	Open Circuit Voltage
PAM	Partitioning Around Medoids
PCA	Principal Component Analysis
PEMS	Portable Emission Measurement System
PHEV	Plug-in hybrid electric vehicle
PTC	Positive Temperature Coefficient
RDE	Real Driving Emissions
RTF	real time factor
SoC	State of Charge
SoH	State of Health
SW	Software
TCU	Transmission Control Unit
TheLib	Thermo-Fluid Library
TMC	Thermal Management Controler
VCU	Vehicle Control Unit
VTMS	Vehicle Thermal Management Systems
xCU	Control Unit

Symbols

$\mathbf{A}_{10}$ fixed pressure node connectivity matrix

$\mathbf{A}_{12}$ connectivity matrix

A_f free flow area

A heat transfer area

$\mathbf{A}$ state matrix of the continuous time system

α flow distribution ratio

$a_{\{0...2\}}$ pressure drop polynomial coefficients

Bi Biot number

$\mathbf{B}$ input matrix of the continuous time system

β thermal expansion coefficient

$b_{1...3}$ constant exponent

$\mathbf{C}$ output matrix of the continuous time system

Cp pressure coefficient

$\mathbf{C}_z$ output matrix of the discrete time system

C heat capacity

c specific heat capacity

Δ difference or change

$\mathbf{D}$ feedthrough matrix of the continuous time systems

$\mathbf{D}_z$ feedthrough matrix of the discrete time system

D impeller diameter

d_h hydraulic diameter

$\hat{\mathbf{d}}$ estimated disturbance vector

$\mathbf{d}$ vector of known disturbances

E energy

ϵ pipe surface roughness height

e controller error

F_m mass conservation equation

F_p energy conservation equation

f friction factor

Gr Grashof number

g acceleration due to gravity

$\mathbf{H}$ input matrix of the discrete time system

$\mathbf{H}_d$ input matrix of known disturbances in discrete time

$\dot{H}$ enthalpy flux

H enthalpy

$h_{\{e,i,n,r,...\}}$ specific fluid enthalpy

h_f pressure head loss from friction

h_m pressure head loss from minor losses

h_p pressure head from pump or fan

h overall heat transfer coefficient

I electric current

$K_{\{s,o,r\}}$ heat transfer function

$\overline{\mathbf{K}}$ pressure coefficient matrix

$\mathbf{K}$ pressure coefficient vector

K pressure coefficient

k thermal conductivity

$k_{1...5}$ constant coefficients

L conduction length

$\mathbf{L}$ observer parameter matrix

r controller reference value

l length

$\dot{\mathbf{M}}$ network mass flow vector

$\overline{\mathbf{M}}$ mass flow matrix

μ dynamic viscosity

m mass

$\dot{\mathbf{m}}$ mass flow vector

$\dot{m}$ mass flow

N_c control horizon

N_p prediction horizon

Nu Nusselt number

ν kinematic viscosity

n rotational speed

$\hat{P}$ dimensionless power coefficient

Pr Prandtl number
P power
Φ dimensionless flow coefficient
Ψ dimensionless head coefficient
$\mathbf{p}_0$ network fixed node pressure vector
$\mathbf{p}$ network node pressure vector
p pressure
$\boldsymbol{\Phi}$ state matrix of the discrete time system

Q heat
$\mathbf{q}$ network node in- and outflow vector
$\dot{Q}$ heat flow

Re Reynolds number
R heat transfer resistance
ρ density

Tq torque
T temperature
$\dot{T}$ temperature time derivative

U internal energy function
u input vector in discrete time

Vd engine displacement volume
$\dot{V}$ volume flow
V controller gain
v vehicle velocity
$V(*)$ Ljapunov function of state $*$

W work

x position or length
$\mathbf{x}$ state vector
$\hat{\mathbf{x}}$ estimated state vector

$\mathbf{y}$ output vector in continuous time

ζ dimensionless pressure drop coefficient
$\mathbf{z}$ output vector in discrete time

List of Figures

List of Tables

Bibliography

[1] M. Genger, Instationäre Kühlsystemoptimierung: Optimierung eines Fahrzeugkühlsystems im instationären Betrieb aufgrund der Anforderungen des Thermomanagements, FVV-Vorhaben Nr. 772, FVV, Stuttgart, 2004. (cited on page 1.)

[2] T. Schütz, Hucho - Aerodynamik des Automobils: Strömungsmechanik, Wärmetechnik, Fahrdynamik, Komfort, 6th Edition, Springer Vieweg, 2013. (cited on page 1.)

[3] H. Petutschnig, Entwicklung einer Simulationsmethodik zur Abbildung des thermischen Managements von Motor und Fahrzeug, Ph.D. thesis, Technischen Universität Graz, Graz (Mar. 2007). (cited on pages 2 and 12.)

[4] S. Park, A Comprehensive Thermal Management System Model for Hybrid Electric Vehicles, Ph.D. thesis, The University of Michigan (2011).
URL http://deepblue.lib.umich.edu/handle/2027.42/84563 (cited on page 2.)

[5] C. Haupt, Ein multiphysikalisches Simulationsmodell zur Bewertung von Antriebs-und Wärmemanagement-konzepten im Kraftfahrzeug, Ph.D. thesis, Universität München (2013).
URL http://mediatum.ub.tum.de/doc/1114641/file.pdf (cited on page 2.)

[6] D. Ghebru, Modellierung und Analyse des instationären thermischen Verhaltens von Verbrennungsmotor und Gesamtfahrzeug, Ph.D. thesis, Karlsruher Institut für Technologie, Karlsruhe (Apr. 2013). (cited on pages 2 and 92.)

[7] M. Tizianel, Energy Flow Chart - Sankey Diagramm (Aug. 2016). (cited on pages 2 and 177.)

[8] A. Traussnig, M. Stolz, Vehicle Thermal Management Simulation Method Integrated in the Development Process from Scratch to Prototype, in: SAE 2014 World Congress & Exibition, 2014. doi:10.4271/2014-01-0668. (cited on page 3.)

[9] S. Hausberger, Anforderungen durch die kommende „Real Drive Emissions (rde)" Gesetzgebung für PKW (Mar. 2016). (cited on pages 5 and 9.)

[10] Austrian environment agency, Particle emissions trend (PM10).
URL http://www.umweltbundesamt.at/pm10/ (cited on page 5.)

[11] CO2 emissions from new passenger cars in the EU: Car manufacturers' performance in 2014, White paper, International Council on Clean Transportation europe (Jul. 2015).
URL http://www.theicct.org/sites/default/files/publications/ICCTbriefing_EU-CO2_201507.pdf (cited on pages 5, 6, and 177.)

[12] Uwe Tietge, Nikiforos Zacharof, Peter Mock, Vicente Franco, From laboratory to road - A 2015 update of official and "real-world" fuel consumption and co2 values for passenger cars in europe, White paper, international council on clean transportation europe (Sep. 2015).
URL http://www.theicct.org/laboratory-road-2015-update (cited on pages 6, 7, 8, and 177.)

[13] Regelung Nr. 101 der Wirtschaftskommission der Vereinten Nationen für Europa (UN/ECE) (Dec. 2010).
URL http://eur-lex.europa.eu/LexUriServ/LexUriServ.do?uri=OJ:L:2012:138:0001:0077:DE:PDF (cited on page 7.)

[14] A. Traussnig, Waltenberger, Michael, Klima, Bernd, Ennemoser, Andreas, Konzeptbewertung und Auslegung der thermischen Betriebsstrategie in einem HEV, Stuttgart, 2013. (cited on pages 8, 78, 177, and 181.)

[15] Bill Canis, Richard K. Lattanzio, Adam Vann, Brent D. Yacobucci, Volkswagen, Defeat Devices, and the Clean Air Act: Frequently Asked Questions, CRS Report (Feb. 2016).
URL https://www.fas.org/sgp/crs/misc/R44372.pdf (cited on page 8.)

[16] Handelsblatt, Volkswagen-Markenchef Herbert Diess: Neues VW-Elektroauto soll bis zu 600 Kilometer fahren. (cited on page 10.)

Bibliography

[17] E. Chen, Hybrid electric vehicle thermal management system, cIB: B60H1/00; B60K1/00; B60L11/00 (Jan. 2013). URL `http://worldwide.espacenet.com/publicationDetails/biblio?FT=D&date=20130101&DB=&locale=&CC=US&NR=8346422B2&KC=B2&ND=1` (cited on page 11.)

[18] D. Gabriel, S. J. Kotre, Power electronics cooling for a hybrid electric vehicle (Sep. 2002). URL `http://worldwide.espacenet.com/publicationDetails/biblio?FT=D&date=20020917&DB=&locale=en_EP&CC=US&NR=6450275B1&KC=B1&ND=4` (cited on page 11.)

[19] G. Major, M. Utter, Thermal Management of Cabin and Battery Pack in Hev/Phev/Bev Vehicles, cIB: H01M10/50 (Sep. 2012). URL `http://worldwide.espacenet.com/publicationDetails/biblio?FT=D&date=20120906&DB=&locale=en_EP&CC=US&NR=2012225341A1&KC=A1&ND=5` (cited on page 11.)

[20] V. Negandhi, D. Jung, J. Shutty, Active thermal management with a dual mode coolant pump, SAE International Journal of Passenger Cars - Mechanical Systems 6 (2). `doi:10.4271/2013-01-0849`. (cited on page 11.)

[21] S. Park, A Comprehensive Thermal Management System Model for Hybrid Electric Vehicles., Ph.D. thesis, University of Michigan (2011). URL `http://hdl.handle.net/2027.42/84563` (cited on page 11.)

[22] B. Zhou, X. Lan, X. Xu, X. Liang, Numerical model and control strategies for the advanced thermal management system of diesel engine, Applied Thermal Engineering 82 (2015) 368–379. `doi:10.1016/j.applthermaleng.2015.03.005`. URL `http://www.sciencedirect.com/science/article/pii/S1359431115002197` (cited on page 11.)

[23] M. H. Salah, T. H. Mitchell, J. R. Wagner, D. M. Dawson, Nonlinear-Control Strategy for Advanced Vehicle Thermal-Management Systems, IEEE Transactions on Vehicular Technology 57 (1) (2008) 127–137. `doi:10.1109/TVT.2007.901892`. (cited on page 11.)

[24] M. H. Salah, P. M. Frick, J. R. Wagner, D. M. Dawson, Hydraulic actuated automotive cooling systems—Nonlinear control and test, Control Engineering Practice 17 (5) (2009) 609–621. `doi:10.1016/j.conengprac.2008.10.016`. URL `http://www.sciencedirect.com/science/article/pii/S0967066108001871` (cited on page 11.)

[25] M. H. Salah, T. H. Mitchell, J. R. Wagner, D. M. Dawson, A Smart Multiple-Loop Automotive Cooling System - Model, Control, and Experimental Study, IEEE/ASME Transactions on Mechatronics 15 (1) (2010) 117–124. `doi:10.1109/TMECH.2009.2019723`. (cited on page 11.)

[26] P. Setlur, J. R. Wagner, D. M. Dawson, E. Marotta, An advanced engine thermal management system: nonlinear control and test, IEEE/ASME Transactions on Mechatronics 10 (2) (2005) 210–220. `doi:10.1109/TMECH.2005.844707`. (cited on page 11.)

[27] X. Tao, K. Zhou, A. Ivanco, J. Wagner, H. Hofmann, Z. Filipi, A Hybrid Electric Vehicle Thermal Management System - Nonlinear Controller Design, SAE Technical Papers 2015-April (April). `doi:10.4271/2015-01-1710`. (cited on page 11.)

[28] T. Wang, J. Wagner, Advanced automotive thermal management – Nonlinear radiator fan matrix control, Control Engineering Practice 41 (2015) 113–123. `doi:10.1016/j.conengprac.2015.04.004`. URL `http://www.sciencedirect.com/science/article/pii/S0967066115000702` (cited on page 11.)

[29] M. Khodabakhshian, L. Feng, J. Wikander, Fuel Saving Potential of Optimal Engine Cooling System, Society of Automotive Engineers, 2014. (cited on page 11.)

[30] B. Zhou, X. Lan, X. Xu, X. Liang, Numerical model and control strategies for the advanced thermal management system of diesel engine, Applied Thermal Engineering 82 (2015) 368–379. `doi:10.1016/j.applthermaleng.2015.03.005`. URL `http://www.sciencedirect.com/science/article/pii/S1359431115002197` (cited on page 11.)

[31] A. Karnik, D. Pachner, A. M. Fuxman, D. Germann, M. Jankovic, C. House, Model Predictive Control for Engine Powertrain Thermal Management Applications, 2015. `doi:10.4271/2015-01-0336`. URL `http://papers.sae.org/2015-01-0336/` (cited on page 11.)

[32] S. S. Butt, R. Prabel, R. Grimmecke, H. Aschemann, Nonlinear model-predictive control for an engine cooling system with smart valve and pump, in: Methods and Models in Automation and Robotics (MMAR), 2014 19th International Conference On, 2014, pp. 520–525. `doi:10.1109/MMAR.2014.6957408`. (cited on page 11.)

[33] M. Khodabakhshian, L. Feng, J. Wikander, Predictive control of the engine cooling system for fuel efficiency improvement, in: 2014 IEEE International Conference on Automation Science and Engineering, 2014, pp. 61–66. `doi:10.1109/CoASE.2014.6899305`. (cited on page 11.)

184

[34] Blago Minovski, Study of Software System Integration for Transient Simulation of Future Cooling System for Heavy Truck Applications (2013).
URL `http://publications.lib.chalmers.se/records/fulltext/185292/185292.pdf` (cited on pages 12 and 13.)

[35] Gamma Technologies, ECU Testing and Calibration with GT-SUITE Plant Models.
URL `https://www.gtisoft.com/wp-content/uploads/2015/01/SiL.pdf` (cited on page 12.)

[36] Mentor Graphics, Accurate 1d Thermo - Fluid Simulation in Real - Time Environments.
URL `https://www.mentor.com/products/mechanical/engineering-edge/volume3/issue1/accurate-1d-thermo-fluid-simulation` (cited on page 13.)

[37] H. C. V. Ness, Understanding Thermodynamics, dover ed Edition, Dover Publications Inc., New York, 1983. (cited on page 15.)

[38] E. W. Lemmon, M. L. Huber, M. O. McLinden, NIST reference fluid thermodynamic and transport properties–REFPROP, version, 2002.
URL `http://www.bldrdoc.gov/srd/upload/REFPROP9.pdf` (cited on pages 16 and 59.)

[39] I. H. Bell, J. Wronski, S. Quoilin, V. Lemort, Pure and pseudo-pure fluid thermophysical property evaluation and the open-source thermophysical property library coolprop, Industrial & Engineering Chemistry Research 53 (6) (2014) 2498–2508. `arXiv:http://pubs.acs.org/doi/pdf/10.1021/ie4033999`, `doi:10.1021/ie4033999`.
URL `http://pubs.acs.org/doi/abs/10.1021/ie4033999` (cited on pages 16 and 59.)

[40] Cengel, Heat Transfer a Practical Approach Si Ve, 3rd Edition, Mcgraw Hill Higher Education, New Delhi etc., 2006. (cited on pages 16, 19, 21, 22, 23, 25, 29, 30, and 177.)

[41] Y. Cengel, R. Turner, J. Cimbala, Fundamentals of Thermal-Fluid Sciences, 4th Edition, McGraw-Hill Education, New York, 2011. (cited on pages 17 and 177.)

[42] Y. A. Cengel, Heat Transfer: A Practical Approach, 2nd Edition, Mcgraw-Hill, Boston, 2002. (cited on page 18.)

[43] John H. Lienhard IV, John H. Lienhard V, A Heat Transfer Textbook, 3rd Edition, Phologiston Press, Cambridge Massachusetts, 2008. (cited on pages 20, 22, 24, and 177.)

[44] E. Buckingham, On Physically Similar Systems. Illustrations of the Use of Dimensional Equations, Physical Review 4 (4) (1914) 345–376. `doi:10.1103/PhysRev.4.345`. (cited on page 20.)

[45] F. M. White, Fluid Mechanics, 7th Edition, McGraw-Hill Higher Education, Singapore; Boston; Burr Ridge etc., 2011. (cited on pages 25, 33, 34, 35, 36, and 177.)

[46] VDI Heat Atlas, 2nd Edition, Springer-Verlag Berlin Heidelberg, 2010. (cited on pages 24, 25, and 26.)

[47] Martin H, Vorlesung Wärmeübertragung I (1990). (cited on page 25.)

[48] M. Kaviany, Principles of Heat Transfer, Wiley-Interscience, New York, 2001. (cited on page 26.)

[49] A. D. D.-I. V. Gnielinski, Ein neues Berechnungsverfahren für die Wärmeübertragung im Übergangsbereich zwischen laminarer und turbulenter Rohrströmung, Forschung im Ingenieurwesen 61 (9) (1995) 240–248. `doi:10.1007/BF02607964`.
URL `http://link.springer.com/article/10.1007/BF02607964` (cited on page 26.)

[50] P. Konakov, A New Correlation for the Friction Coefficient in Smooth Tubes, Berichte der Akademie der Wissenschaften der UdSSR 51 (1946) 51. (cited on page 26.)

[51] Y.-J. Chang, C.-C. Wang, A generalized heat transfer correlation for Iouver fin geometry, International Journal of Heat and Mass Transfer 40 (3) (1997) 533–544. `doi:10.1016/0017-9310(96)00116-0`.
URL `http://www.sciencedirect.com/science/article/pii/0017931096001160` (cited on page 27.)

[52] J. Dong, J. Chen, Z. Chen, W. Zhang, Y. Zhou, Heat transfer and pressure drop correlations for the multi-louvered fin compact heat exchangers, Energy Conversion and Management 48 (5) (2007) 1506–1515. `doi:10.1016/j.enconman.2006.11.023`.
URL `http://www.sciencedirect.com/science/article/pii/S0196890406003608` (cited on pages 28 and 177.)

[53] Günter Brenn, Transportprozesse 2 CHE.718 (2010). (cited on pages 32 and 177.)

[54] O. Reynolds, A. W. Brightmore, W. H. Moorby, Papers on mechanical and physical subjects, Cambridge [Eng.] : The University Press, 1900.
URL `http://archive.org/details/papersonmechanic03reynrich` (cited on page 33.)

[55] L. F. Moody, Friction factors for pipe flow, Trans. Asme 66 (8) (1944) 671–684. (cited on page 37.)

Bibliography

[56] D. S. Miller, Internal Flow Systems, BHRA, Fluid Engineering Centre, 1990. (cited on pages 37 and 39.)

[57] I. E. Idelchik, Handbook of Hydraulic Resistance, 3rd Edition, Jaico Publishing House, Mumbai; New York, N.Y., 2005. (cited on pages 37 and 39.)

[58] P. F. Boulos, K. E. Lansey, B. W. Karney, Comprehensive Water Distribution Systems Analysis Handbook for Engineers and Planners, second edition Edition, MWH Soft, Incorporated, 2006. (cited on pages 37 and 52.)

[59] D. Clamond, Efficient Resolution of the Colebrook Equation, Industrial & Engineering Chemistry Research 48 (7) (2009) 3665–3671. doi:10.1021/ie801626g.
URL http://dx.doi.org/10.1021/ie801626g (cited on page 37.)

[60] Tom Davis, Moody Diagram (Mar. 2008).
URL http://www.mathworks.com/matlabcentral/fileexchange/7747-moody-diagram (cited on pages 38 and 177.)

[61] H. Dixon, Fluid Mechanics and Thermodynamics of Turbomachinery, 6th Edition, Elsevier, 2010. (cited on page 40.)

[62] H. Cross, Analysis of flow in networks of conduits or conductors, University of Illinois. Engineering Experiment Station. Bulletin; no. 286.
URL http://www.ideals.illinois.edu/handle/2142/4433 (cited on page 45.)

[63] E. Todini, S. Pilati, Computer Applications in Water Supply: Vol. 1—systems Analysis and Simulation, Research Studies Press Ltd., Taunton, UK, UK, 1988, pp. 1–20.
URL http://dl.acm.org/citation.cfm?id=61052.61053 (cited on pages 45, 51, and 52.)

[64] Automatic Code Generation - Simulink Coder - MathWorks Deutschland.
URL http://de.mathworks.com/products/simulink-coder/?s_cid=wiki_simulink_3 (cited on pages 48 and 49.)

[65] R. Fletcher, Practical Methods of Optimization, John Wiley & Sons, 2013. (cited on page 53.)

[66] T. Schütz, Hucho - Aerodynamik des Automobils: Strömungsmechanik, Wärmetechnik, Fahrdynamik, Komfort, Springer-Verlag, 2013. (cited on pages 74 and 177.)

[67] AVL List GmbH, AVL Future Hybrid - "Lighthouse" of future mobility - Hybrid Vehicle Powertrain System - avl.com (2016).
URL https://www.avl.com/-/avl-future-hybrid-lighthouse-of-future-mobility (cited on pages 78, 79, 177, and 178.)

[68] A. Al-Sarkhi, J. O. Jaber, S. D. Probert, Efficiency of a Miller engine, Applied Energy 83 (4) (2006) 343–351. doi:10.1016/j.apenergy.2005.04.003.
URL http://www.sciencedirect.com/science/article/pii/S0306261905000474 (cited on page 78.)

[69] P. Teufelberger, M. Yolga, M. Ringdorfer, E. Korsunsky, Optimierte Regelung integrierter Hybridgetriebe, MTZ - Motortechnische Zeitschrift 77 (9) (2016) 36–41. doi:10.1007/s35146-016-0088-2.
URL http://link.springer.com/article/10.1007/s35146-016-0088-2 (cited on pages 79 and 109.)

[70] M. Benedikt, Eine Kopplungsmethode für die nicht-iterative Co-Simulation, Dissertation, Graz University of Technology, Graz (2013). (cited on page 80.)

[71] G. Stettinger, M. Benedikt, M. Horn, J. Zehetner, Modellbasierte Echtzeit-Co-Simulation: Überblick und praktische Anwendungsbeispiele, e & i Elektrotechnik und Informationstechnik 132 (4-5) (2015) 207–213. doi:10.1007/s00502-015-0305-6.
URL http://link.springer.com/article/10.1007/s00502-015-0305-6 (cited on page 80.)

[72] MATLAB and Simulink Toolbox, release 2011b 32bit. (cited on page 80.)

[73] AST, AVL CRUISE™.
URL https://www.avl.com/cruise (cited on page 80.)

[74] M. Stolz, B. Knauder, P. Micek, W. Ebner, E. Korsunsky, P. Ebner, Unifying Approach to Hybrid Control Software, in: G. Meyer, J. Valldorf (Eds.), Advanced Microsystems for Automotive Applications 2011, Springer Berlin Heidelberg, Berlin, Heidelberg, 2011, pp. 69–78.
URL http://link.springer.com/10.1007/978-3-642-21381-6_7 (cited on page 80.)

[75] D. Görke, Untersuchungen zur kraftstoffoptimalen Betriebsweise von Parallelhybridfahrzeugen und darauf basierende Auslegung regelbasierter Betriebsstrategien, Ph.D. thesis, Springer Fachmedien Wiesbaden, Wiesbaden (2016).
URL http://link.springer.com/10.1007/978-3-658-14163-9 (cited on page 80.)

[76] Samhaber Christof, Simulation des thermischen Verhalten von Verbrennungsmotoren, Dissertation, Technischen Universität Graz, Graz (Sep. 2002). (cited on pages 83 and 85.)

[77] G. Woschni, A universally applicable equation for the instantaneous heat transfer coefficient in the internal combustion engine, Tech. rep., SAE Technical paper (1967).
URL http://papers.sae.org/670931/ (cited on page 86.)

[78] G. Hohenberg, Experimentelle Erfassung der Wandwarme in Kolbenmotoren (Experimental acquisition of the wall heat in piston engines), Ph.D. thesis, Habilitation Thesis, Technical University of Graz (1980). (cited on page 86.)

[79] M. Bargende, Ein Gleichungsansatz zur Berechnung der instationären Wandwärmeverluste bei Ottomotoren, Ph.D. thesis, TH Darmstadt, Darmstadt (1991). (cited on page 86.)

[80] H. Zapf, Beitrag zur untersuchung des Wärmeübergangs während des Ladungswechsels im Viertakt-Dieselmotor, Motortechnische Zeitschrift MTZ 30 (1969) 461–465. (cited on page 87.)

[81] R. Pischinger, M. Klell, T. Sams, Thermodynamik der Verbrennungskraftmaschine, Springer-Verlag, 2009. (cited on pages 87 and 88.)

[82] AST, AVL BOST (2013). (cited on page 87.)

[83] M. Schwarzmeier, Der Einfluß des Arbeitsprozeßverlaufs auf den Reibmitteldruck von Dieselmotoren., Ph.D. thesis, TU München, München (1992). (cited on page 88.)

[84] C. Reulein, Simulation des instationären Warmlaufverhaltens von Verbrennungsmotoren., Ph.D. thesis, TU München, München (1998). (cited on page 89.)

[85] G. P. Merker, C. Schwarz, Grundlagen Verbrennungsmotoren: Simulation der Gemischbildung, Verbrennung, Schadstoffbildung und Aufladung, Springer-Verlag, 2009. (cited on page 89.)

[86] AVL List GmbH, FIRE (2011). (cited on page 91.)

[87] A. Bodor, Future hybrid PHEV 3d CFD water cooling analysis, Internal report, Graz (Sep. 2013). (cited on pages 91, 92, 93, and 178.)

[88] B. R. Munson, A. P. Rothmayer, T. H. Okiishi, Fundamentals of Fluid Mechanics, 7th Edition, John Wiley & Sons, Incorporated, 2012. (cited on pages 92 and 117.)

[89] P. Steinberg, Wärmemanagement des Kraftfahrzeugs IV: Entwicklungsmethoden, Konzepte und Innovationen des Wärmemanagements im Kraftfahrzeug, expert verlag, 2005. (cited on page 95.)

[90] W. Prochazka, G. Pregartner, M. Cifrain, Design-of-experiment and statistical modeling of a large scale aging experiment for two popular lithium ion cell chemistries, Journal of The Electrochemical Society 160 (8) (2013) A1039–A1051.
URL http://jes.ecsdl.org/content/160/8/A1039.short (cited on page 99.)

[91] A. Mathoy, Abschlussbericht Antriebsentwicklung Projekt COASTER, Tech. rep., BRUSA Elektronik AG, Sennwald (2004). (cited on page 104.)

[92] B. Lechner, Virtual Vehicle: Testing & Validation (2016).
URL http://www.v2c2.at/services/testing-validation/ (cited on page 107.)

[93] AVL List GmbH, AFE2641 Future Hybrid VCU SW Architecture Document, Tech. rep., AVL List GmbH, Graz (Oct. 2013). (cited on pages 110 and 178.)

[94] F. Kitanoski, A. Hofer, A contribution to energy optimal thermal management for vehicles, IFAC Proceedings Volumes (IFAC-PapersOnline) (2010) 87–92 doi:10.3182/20100712-3-DE-2013.00121. (cited on page 117.)

[95] A. Hofer, F. Kitanoski, Energy efficient model predictive control of a cooling system, International Journal Automation Austria 19 (2) (2011) 49–61. (cited on page 117.)

[96] M. Salah, T. Mitchell, J. Wagner, D. Dawson, Nonlinear-Control Strategy for Advanced Vehicle Thermal-Management Systems, IEEE Transactions on Vehicular Technology 57 (1) (2008) 127–137. doi:10.1109/TVT.2007.901892. (cited on page 118.)

[97] M. Steinberger, Automatisierung meachatronischer Systeme (2014). (cited on page 120.)

[98] J. B. Rawlings, D. Q. Mayne, Model Predictive Control : Theory and Design, 5th Edition, Madison, Wis. Nob Hill Pub. cop., 2015. (cited on pages 120 and 122.)

[99] J. Adamy, Nichtlineare Systeme und Regelungen, Springer-Verlag, 2014, google-Books-ID: 7SIeBAAAQBAJ. (cited on pages 120, 129, and 178.)

Bibliography

[100] L. Wang, Model Predictive Control System Design and Implementation Using MATLAB®, Springer Science & Business Media, 2009, google-Books-ID: PphumLcKPi4C. (cited on page 120.)

[101] G. F. Franklin, M. L. Workman, D. Powell, Digital Control of Dynamic Systems, 3rd Edition, Addison Wesley Longman, Inc., 1997. (cited on page 121.)

[102] Y. Lui, Robust Nonlinear Control Design with Proportional-Integral-Observer Technique, PhD-Thesis, Universität Duisburg-Essen (2011). (cited on page 122.)

[103] X. Zou, J. A. Jordan, M. Shillor, A dynamic model for a thermostat, Journal of Engineering Mathematics 36 (4) (1999) 291–310. `doi:10.1023/A:1004587425961`. (cited on page 128.)

[104] T. Mitchell, M. Salah, J. Wagner, D. Dawson, Automotive Thermostat Valve Configurations: Enhanced Warm-Up Performance, Journal of dynamic systems, measurement, and control 131 (4). (cited on page 128.)

[105] H. K. Khalil, Nonlinear Control, Global Edition, Pearson Education Limited, 2015, google-Books-ID: lXWx-CQAAQBAJ. (cited on pages 129 and 133.)

[106] O. Föllinger, Nichtlineare Regelungen, Bd.1, Grundbegriffe, Anwendung der Zustandsebene, Direkte Methode, 8th Edition, De Gruyter Oldenbourg, München u.a., 1998. (cited on page 133.)

[107] J. Adamy, Nichtlineare Regelungen, Springer Berlin Heidelberg, Berlin, Heidelberg, 2009. (cited on page 133.)

[108] A. Traussnig, W. Jansen, H. Petutschnig, S. Steiner, P. Gruen, A Simulation Approach for Vehicle Life-Time Thermal Analysis Applied to a HEV Battery System, Tech. rep., SAE Technical Paper (2016).
URL `http://papers.sae.org/2016-01-0201/` (cited on pages 138, 141, 142, and 178.)

[109] K. Denkmayr, H. Hick, U. Sauerwein, Die Load-Matrix, MTZ - Motortechnische Zeitschrift 64 (11) (2003) 924–930.
`doi:10.1007/BF03227139`.
URL `http://dx.doi.org/10.1007/BF03227139` (cited on page 139.)

[110] B. S. Everitt, S. Landau, M. Leese, D. Stahl, Cluster Analysis, John Wiley & Sons, 2011. (cited on page 140.)

[111] I. Jolliffe, Principal component analysis, Wiley Online Library, 2002.
URL `http://onlinelibrary.wiley.com/doi/10.1002/9781118445112.stat06472/full` (cited on page 140.)

[112] K. Fukunaga, Introduction to Statistical Pattern Recognition, Academic Press, 2013. (cited on page 140.)

[113] The Weather Underground, Inc., The Weather Underground (2016).
URL `www.wunderground.com` (cited on page 143.)

[114] M. N. Murty, V. S. Devi, Pattern Recognition: An Algorithmic Approach, Springer Science & Business Media, 2011, google-Books-ID: uBWD3HnzYFUC. (cited on page 143.)

[115] J. C. Spoelstra, Charging behaviour of Dutch EV drivers.
URL `http://dspace.library.uu.nl/handle/1874/297327` (cited on page 146.)

[116] M. Cifrain, Alterung von Traktionsbatterien, ViF Magazin (17, 2014-II). (cited on page 147.)

Armin Traussnig

Dipl.-Ing. (FH),

Bauernfeldstraße 30
A-8020 Graz
✉ *armin.traussnig@gmail.com*

--- **Persönliche Daten**

Geboren	10.03.1985, Wolfsberg
Staatsangehörigkeit	Österreich
Familienstand	verheiratet
Kinder	Sohn 2 Jahre, Tochter 5 Monate

--- **Berufserfahrung**

10/2012 -jetzt **Senior Researcher (Vollzeit)**,
Kompetenzzentrum - Das Virtuelle Fahrzeug Forschungsgesellschaft mbH, Graz, Area B / Thermo & Fluid Dynamics.
Researcher und Projektleiter im Bereich F&E Fahrzeug Thermomanagement, Fokus: Modellierung und Simulation komplexer Gesamtfahrzeugsysteme vebunden mit dem Entwurf von Steuer- und Regelungskonzepten

01/2010 -10/2012 **Junior Researcher (Vollzeit)**,
Kompetenzzentrum - Das Virtuelle Fahrzeug Forschungsgesellschaft mbH, Graz, Area B / Thermo & Fluid Dynamics.

08/2010 -jetzt **Analysis Engineer (Teilzeit)**,
AVL List GmbH, Graz, CFD Analysis / Engineering and Technology Powertrain Systems.
Mitarbeit in Forschungsprojekten und Teilprojektleitung in Dienstleistungsprojekten, Fokus: Entwicklung eines generischen Thermomanagement Controllers; Entwicklung einer Methodik zur Bewertung von Regelstrategien und Thermomanagementmaßnahmen im Sinne von Jahresenergiebedarf für real world driving.

09/2008 -01/2009 **Praktikant**,
MTU-Aero Engines, München, Testing and Control department.

10/2004 -05/2005 **Grundwehrdienst**,
StbKp/MilKdo Ktn., Wolfsberg.

--- **Ausbildung**

02/2011 -jetzt **Doktorand**,
Technischen Universität Graz / Institut für Regelungs- und Automatisierungstechnik, Graz,
Fokus: Modellierung, Simulation und Regelung von thermischen Gesamtfahrzeugsystemen.

04/2009 -09/2009 **Diplomarbeit**,
AVL List GmbH, Graz,
Untersuchung der Effizienz von alternativen Kühlkonzepten unter Berücksichtigung aerodynamischer Effekte.

08/2007 -01/2008 **Auslandssemester**,
Hogeschool van Amsterdam, Amsterdam / Netherlands.
Bereich: Luftfahrt und Aviation

10/2005 -09/2009 **Studium**,
Fachhochschule Joanneum, Graz.
Luftfahrt und Aviation, Zweig Luftfahrttechnik.
Fokus: Modellbildung und Simulation von Thermo Fluid Systemen

09/1999	**Berufsbildende höhere Schule**,
-06/2004	*HTL für Maschineningenieurswesen*, Wolfsberg, Ausbildungsschwerpunkt: Automatisierungstechnik. Matura

Publikationen

[1] A. Traussnig, M. Stolz, and M. Horn, MPC Based Fan Control for Automotive Applications, presented at the 8th IFAC International Symposium on Advances in Automotive Control, Norrköping, Sweden, 2016.

[2] A. Traussnig, W. Jansen, H. Petutschnig, S. Steiner, and P. Gruen, A Simulation Approach for Vehicle Life-Time Thermal Analysis Applied to a HEV Battery System, SAE Technical Paper, Detroit World Congress, 2016.

[3] A. Traussnig, M. Stolz, M. Waltenberger, and T. Lemke, Simulationsmethodik zur Bewertung von Thermomanagement-Maßnahmen, presented at the SIM-VEC - Simulation und Erprobung in der Fahrzeugentwicklung, Baden-Baden, 2014.

[4] A. Traussnig, H. Petutschnig, A. Ennemoser, M. Stolz, and M. Tizianel, Vehicle Thermal Management Simulation Method Integrated in the Development Process from Scratch to Prototype, SAE Technical Paper, Detroit World Congress, 2014.

[5] A. Traussnig, Michael Waltenberger, B. Klima, and A. Ennemoser, Konzeptbewertung und Auslegung der thermischen Betriebsstrategie in einem HEV, presented at the 2. VDI-Konferenz Thermomanagement für elektromotorisch angetriebene PKW, Stuttgart, 2013.

[6] A. Traussnig, Energy and Thermal Management Simulation of an Advanced Powertrain, presented at the 8th A3PS-Conference - Eco-Mobility 2013, Wien, 11-Mar-2013.